Experimental Investigation and Constitutive Modeling of Metallic Honeycombs in Sandwich Structures

by

Dirk Mohr

Diplom-Ingenieur
University of Karlsruhe, 1999

Master of Science
Massachusetts Institute of Technology, 2000

Submitted to the Department of Civil and Environmental Engineering
in partial fulfillment of the requirements for the degree of
Doctor of Philosophy in Applied Mechanics
at the
MASSACHUSETTS INSTITUTE OF TECHNOLOGY
September 2003

Author .....
Impact and Crashworthiness Laboratory
August 30, 2003

Certified by .....
Professor Tomasz Wierzbicki
Thesis Supervisor

Certified by .....
Professor Lorna J. Gibson
Thesis Reader

Accepted by .....
Professor Heidi Nepf
Chairman, Departmental Committee on Graduate Students

Experimental Investigation and Constitutive Modeling of Metallic Honeycombs in Sandwich Structures

Dirk Mohr

Submitted to the Department of Civil and Environmental Engineering
on August 30, 2003 in partial fulfillment of the requirements for the degree of
Doctor of Philosophy in Applied Mechanics

Abstract

Traditionally, honeycomb sandwich structures are designed in the elastic range, but recent studies on the crushing of sandwich profiles have shown their potential in crashworthiness applications. Thin sandwich sheets also hold a promise for widespread use in automotive industry because standard sheet metal forming technology could be used to produce double-curvature sandwich shell structures. The crashworthiness and formability of sandwich structures are critically dependent on the behavior of the sandwich core under large plastic deformation. In this thesis, a new biaxial testing device has been developed for the reliable characterization of the mechanical behavior of cellular materials. Using this device, the macroscopic phenomenology and the underlying microstructural deformation mechanisms of thin-walled aluminum honeycomb have been studied experimentally for combined out-of-plane shear and normal loading. Furthermore, numerical simulations of the experiments have been performed where the cell walls of the specimen microstructure have been discretized with fine shell element meshes. Based on the experimental and numerical results, a finite-strain rate-independent orthotropic constitutive model for metallic honeycombs has been formulated and implemented into commercial finite element software. The good agreement of the model predictions with the experimental results encourages the use of this constitutive model for applications involving large plastic out-of-plane deformation. On the structural scale, the model has been used to predict the crushing response of a thin-walled sandwich profile with a micro-cell stainless steel honeycomb core.

Thesis Supervisor: Tomasz Wierzbicki
Title: Professor of Applied Mechanics

Contents

Appendices

List of Figures

List of Tables

Acknowledgements

It is a pleasure to thank Professor Wierzbicki for his continuous support and advice throughout my work at his Impact and Crashworthiness Laboratory (ICL). Thanks are due to Professor Gibson for her valuable suggestions and encouraging feedback. I am grateful to Professor Anand for his excellent teaching of the plasticity of solids and his interest in my research. Thanks also to Professor Wooh for serving on my thesis committee.

Special thanks are due to my colleague Dr. Mulalo Doyoyo. Our many discussions over the past two have had an important influence on my approach to research. I am deeply indebted to Stephen Rudolph for adding his engineering know-how and his inestimable help in designing and machining of the experimental equipment. I am grateful to our group's secretary Sheila McNary for her immediate help whenever I needed it. Altogether, I could not have asked for a better environment to conduct this research on honeycomb than the one at the ICL.

I have also benefited from the help of other students and visitors at MIT, notably Nicoli Ames, Georgios Constantinides, Emilio Silva and Dr. Marc Mainguy as well as my colleagues at the ICL. I would like to thank Franz Heukamp who was always available to listen and comment on my ideas. I highly appreciated the close collaboration with BMW and the patience of my colleague Stefan Henn, whenever I focused on honeycomb instead of working on fracture.

And finally, I would like to thank my family for their great moral support – at distance and while visiting me here in Boston. In particular, I would like to thank my wife Fadoua for her love, support and encouragement during our graduate studies between Paris and Seattle.

Chapter 1

Introduction

Crashworthiness and low weight are structural properties central to designing and developing high quality passenger cars. The crashworthiness of a transportation vehicle, measured by the degree of injury of its passengers under accidental impact loads, is often achieved at the expense of additional weight. For instance, locally increasing the thickness of thin-walled structural members typically yields the desired crashworthiness in a straightforward way, but it also increases their weight. Wierzbicki and co-workers conducted extensive research on how to increase the crashworthiness and decrease the weight at the same time (e.g. Santosa, 1999; Chen, 2001; Kim, 2001). Their results clearly demonstrated that the use of low-density filler materials such as metallic foams or metallic honeycombs can lead to the desired ultralight crashworthy body-in-white. Based on the analytical framework of the crushing mechanics of foam-filled and thin-walled structures (Wierzbicki and Abramowicz, 1983; Abramowicz and Wierzbicki, 1988; Abramowicz and Wierzbicki, 1989; Santosa *et al.*, 2000), Chen and Wierzbicki (2001) optimized thin-walled structures for crush loading and found that the right choice of ultralight fillers may increase the mechanical energy absorbed per unit weight (of the structure) by up to 300%. In a similar approach, Kim *et al.* (2002) carried out the weight and crash optimization of three dimensional 'S-frame' components, both analytically and numerically, and concluded that filling the otherwise hollow S-frame with 5%-relative

density aluminum foam while reducing the wall thickness doubles its specific energy absorption. With regards to sandwich structures, Santosa and Wierzbicki (1998) investigated the crashworthiness of prismatic columns and demonstrated that replacing traditional sheet metal by aluminum sandwich panels results in weight savings ranging from 25-50%.

Given the potential merits of cellular solids in applications involving large deformation, reliable modeling technique is crucial for their success in industrial applications. So far, analytical and numerical studies on metallic honeycomb typically made use of a simple heuristic constitutive model where the stress-strain relationship for each pair of work conjugate components of the stress and strain tensors are prescribed in an independent manner. In other words, no interaction between the components of the stress tensor is taken into account. Wierzbicki (1997) questioned this assumption and undertook a series of experiments to determine the interaction of normal and shear stresses acting on metallic honeycomb. In particular, he focused on 'combined out-of-plane loading', a loading condition highly relevant to practical applications. The microstructure of metallic honeycombs is composed of parallel thin-walled hexagonal tubes and thus, its mechanical properties must be described with respect to its three orthotropy axes: there are the strong tubular or T-direction and two so-called in-plane directions (W and L). Combined out-of-plane loading is defined by normal stresses acting in the T-direction along with shear stresses in the T-W or T-L-plane. Wierzbicki's results revealed the complexity of testing metallic honeycombs under combined out-of-plane loading; depending on the height of the specimen, different failure modes were observed: short specimens underwent shear buckling, intermediate specimens developed diagonal shear bands while tall specimens deformed by non-uniform compression at the holding grips and rigid body rotation of the undeformed central block. Other experimentalists reported premature failure of the bond between the honeycomb and loading platens when performing shear lap tests according to the ASTM Standard C273 (Hexcel, 1997).

Due to the experimental challenges in testing metallic honeycomb, only little is known about their response to large multiaxial deformation. Honeycombs are widely used by the aeronautical industry, but their focus is predominantly on the elastic behavior. The in-plane behavior of honeycombs, i.e. combined loading in the W-L-plane,

can be studied on the basis of two-dimensional beam models. Thus, besides analytical expressions for elastic properties, closed-form solutions for the macroscopic yield loci under in-plane loading could be derived (Klintworth and Stronge, 1988). Furthermore, Papka and Kyriakides (1999) developed a new jig for the biaxial testing of honeycombs under combined in-plane loading. However, their device is not suitable for the testing under combined out-of-plane loading. It is believed that understanding the in-plane behavior of honeycombs provides insight into the mechanics of metallic foams (Andrews and Gibson, 2001; Chen and Fleck, 2001), but most engineering applications for honeycombs require understanding of the out-of-plane behavior. Typically, the energy dissipation under out-of-plane loading is by two orders of magnitude higher than under in-plane loading. With respect to out-of-plane loading, Wierzbicki (1984) derived a closed form solution that describes the crushing behavior of metallic honeycombs subjected to uniaxial compression along the T-direction. Wierzbicki's classical solution predicts the mean crushing stress based on the microstructural properties such as cell size and cell wall material.

This thesis investigates the mechanical behavior of metallic honeycomb subjected to large *combined* out-of-plane displacements. The core task is the development of appropriate experimental techniques. Petras and Sutcliffe (2000) introduced the 'Arcan apparatus in its clamped configuration' to determine the strength envelope of brittle Nomex honeycomb, whereas Doyoyo and Wierzbicki (2000) extended Arcan's concept of butterfly-shaped specimens (Arcan *et al.*, 1978) to metallic foams and honeycombs. Here, we show from theoretical analysis that the reliable use of the Arcan apparatus in the clamped configuration requires the measurement of an additional force component, which leads to substantial changes of the testing method. Two generations of biaxial testing devices have been co-developed by the present author. The first, an enhanced version of Doyoyo and Wierzbicki's equipment, measures all force components while it applies a biaxial displacement field on a butterfly-shaped specimen. The initial yield envelope is determined using this method. The second apparatus, specifically designed to investigate the post-yield behavior of cellular solids, applies combinations of large normal and shear displacements to a rectangular sandwich specimen. The plasticity of a thin-walled aluminum honeycomb is studied in detail. In addition to the physical

experiments, finite element analyses (virtual experiments) are performed to gain further insight into the microstructural behavior under combined out-of-plane loading. The honeycomb microstructure of a sandwich specimen is carefully discretized with three-dimensional shell elements that obey an elastic-plastic material law and then subjected to large displacement loadings, closely following the experimental setup.

The experimental results, physical and virtual, provide the basis for the development of an orthotropic three-dimensional finite-strain rate-independent phenomenological constitutive model for thin-walled metallic honeycomb. The constitutive model incorporates the interaction of normal and shear stresses. The experimental results revealed the importance of this interaction: its neglect under combined loading could overestimate the energy absorption by as much as 100%. A conical yield surface in the out-of-plane shear and normal stress space describes the crushing behavior of metallic honeycomb. The plastic flow is taken to occur in the direction of the minimum principal stress. Geometrically self-similar hardening accounts for the densification under large volume changes. A computational procedure is developed and implemented into a commercial finite element code. As a first application, we use the computational model to simulate the experiments under combined out-of-plane loading.

Another application of the constitutive model is shown for sandwich structures. First, we conduct a series of crush tests on double-cell profiles made of the Hybrid Stainless Steel Assembly (HSSA), a thin sandwich sheet with a low density steel fiber core. Theoretical analysis reveals that a shear-folding mechanism is responsible for the remarkably short folding wavelength of the crushed soft-core sandwich profiles. Subsequently, the shear crushing strength of HSSA fiber cores is compared to metallic honeycombs. A finite element simulation of the crushing of a thin honeycomb sandwich profile is performed to demonstrate the superior mechanical performance of honeycombs in crashworthiness applications.

This thesis proceeds in several steps. Chapter 2 begins with the theoretical and numerical analysis of the Arcan apparatus in the clamped configuration and presents the design of the Enhanced Arcan Apparatus (EAA) as well as its use for the determination of initial yield loci for aluminum honeycomb. In Chapter 3, we develop and apply the

Universal Biaxial Testing Device (UBTD) to investigate the response of metallic honeycomb under large out-of-plane displacements. In a similar manner, virtual experiments are performed in Chapter 4, where the macroscopic response curves are found from numerical simulation of the microstructural response. In Chapter 5, the development of a three-dimensional constitutive model is detailed. Furthermore, having implemented the constitutive model into a finite element code, we simulate the physical and virtual experiments performed in Chapters 3 and 4. Chapter 6 discusses the crashworthiness of sandwich structures. The crushing of soft-core sandwich profiles is treated experimentally and analytically, before the constitutive model is used in the finite element simulation of the crushing of a honeycomb sandwich structure. The careful comparison of the results demonstrates the advantages of stainless steel honeycomb cores over stainless steel fiber cores. Finally, Chapter 7 summarizes this work and suggests future tasks along this line of research on honeycomb.

Chapter 2

Determination of initial yield of butterfly-shaped specimens using the Enhanced Arcan Apparatus (EAA)

2.1 Introduction

The cellular microstructure of a honeycomb is composed of a network of joined, parallel, thin-walled hexagonal tubes (Fig. 1). As a result, honeycombs are strongly orthotropic, thereby providing a high mechanical performance per unit weight under shear and normal loading in the tubular direction. This loading condition, also referred to as combined out-of-plane loading, is typical for most engineering applications of honeycombs. Examples involving large deformations are the stamping and deep drawing of flat honeycomb sandwich panels or the crushing of sandwich profiles. Among the three orthotropy axes of the honeycomb microstructure (denoted as T, W, and L), the tubular or T-direction is the strongest direction (Fig. 1). The variation in internal energy under loading in the T-direction is typically by one to two orders of magnitude higher than under loading along the weaker in-plane directions (W and L).

The textbook by Gibson and Ashby (1997) presents a comprehensive summary on the state of the art of honeycomb mechanics. The in-plane behavior of honeycombs can

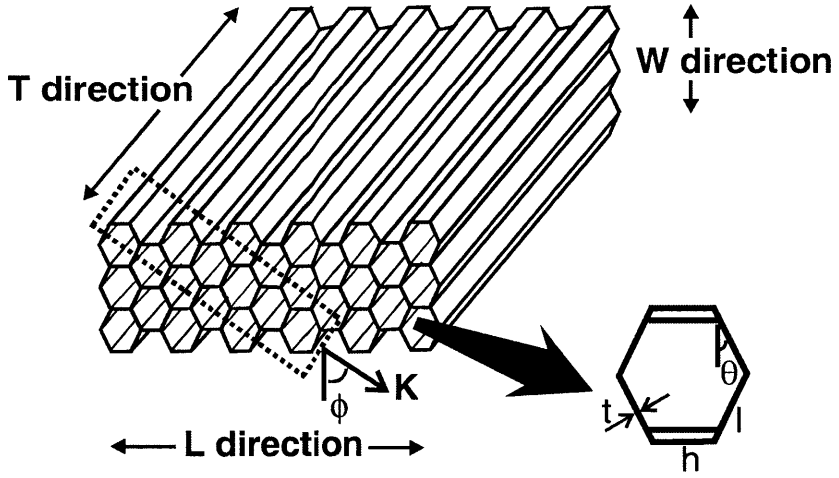

Fig. 1. A schematic of a honeycomb with a hexagonal microstructure.

be studied on the basis of two-dimensional beam models. Using this approach, Klintworth and Stronge (1988) derived closed-form solutions for the micromechanical boundary value problems defining the macroscopic yield loci for in-plane loading. The response of a metallic honeycomb to uniaxial compressive loading in the T-direction was studied in detail by various authors and an analytical expression for the mean crushing stress was presented by McFarland (1963) and Wierzbicki (1983).

However, only little is known about the mechanical behavior of metallic honeycombs under combined out-of-plane loading. Standard testing techniques such as the combined compression-torsion Taylor-Quiney tests on cylindrical specimens are not suitable for honeycombs, where the orthotropy axes are aligned with the Cartesian coordinate system. Papka and Kyriakides (1999) developed a new jig for the testing of honeycombs, composed of a set of four perpendicular plates that can move relative to each other. Their tests contributed to the understanding of the in-plane biaxial behavior of honeycombs, but were not suitable to study the interaction of normal and shear stresses in the out-of plane direction. Others performed biaxial out-of-plane tests on honeycomb plates glued to loading platens and found that the load-displacement responses depended on the height of

the specimen (Wierzbicki, 1997); different failure modes characterized the response: short specimens underwent shear buckling, intermediate specimens developed diagonal shear bands while tall specimens deformed by non-uniform compression at the holding grips. Other experimentalists reported premature failure of the bond between the honeycomb and loading platens when performing shear lap tests according to the ASTM Standard C273 (Hexcel, 1997).

Recent findings indicate that the use of the Arcan apparatus in the clamped configuration is most suitable for the biaxial testing of honeycombs. Petras and Sutcliffe (2000) used the Arcan apparatus to determine a failure surface for brittle Nomex honeycomb. Using a similar test setup, Chen and Fleck (2001) studied size effects in foams under multiaxial loading. Doyoyo and Wierzbicki (2003) employed the Arcan apparatus to determine the yield loci of ductile aluminum foams. They also suggested this approach for the biaxial testing of honeycombs (Doyoyo and Wierzbicki, 2000). The underlying idea is to perform fully displacement-controlled tests, thereby bypassing problems due to the localization of deformation in cellular solids. This testing technique shall be explored here and developed further to investigate the behavior of metallic honeycombs.

We begin with the analysis of the Arcan apparatus in the clamped configuration, which leads to an important finding: the reliable testing in the clamped configuration requires the measurement of two force components, a fact that has been overlooked by the researchers cited above. Consequently, the Enhanced Arcan Apparatus (EAA) is developed incorporating an additional load cell. Using the EAA, biaxial tests are performed on aluminum honeycomb butterfly specimens. The results provide useful insight into the mechanical behavior of aluminum honeycomb butterfly specimens under combined loading. Microstructural mechanisms are described and the initial yield envelope for these microstructural tests is determined both for combined compression and shear as well as combined tension and shear.

2.2 Analysis of the Arcan apparatus

2.2.1 Background

The Arcan test was developed to produce a uniform state of plane-stress in solid specimens (Arcan *et al.*, 1978). While this test was primarily suited for the biaxial testing of fiber-reinforced materials (Arcan et al., 1978, Voloshin and Arcan, 1980, Hung and Liechti, 1999), recent developments have shown that the Arcan apparatus can also be used to determine the biaxial properties of cellular solids.

The main component of the Arcan test is a butterfly-shaped specimen, which is joined on either side to two half-circular grips (Fig. 2). The grips are connected to a universal testing machine at the top and bottom, respectively. The grips together with the butterfly specimen form a circular disk with two anti-symmetric cutouts. Originally, Arcan *et al.* (1978) proposed this test as a monolithic Arcan specimen, where the grips and the butterfly specimen are cut out of a single plate. Thus, no joints were necessary between the butterfly specimen and the grips. Here, we will consider the test set-up with separate grips and a removable butterfly specimen. The choice of the joint between the Arcan grips and the universal testing machine allows for an important distinction between two configurations:

1. Standard Arcan Test. The joint between the Arcan grips and the testing machine has a single bolt. Horizontal and vertical displacements are controlled at the joint, but rotations of the grips are still allowed (Fig. 3(a)). This configuration corresponds to the initial design by Arcan *et al.* (1978).
2. Clamped Arcan Test. The joint between the Arcan grips and the testing machine has two bolts or any other joint that prohibits rotations. Thus, not only the horizontal and vertical displacements are controlled, but also the rotation of the grip is zero (Fig. 3(b)).

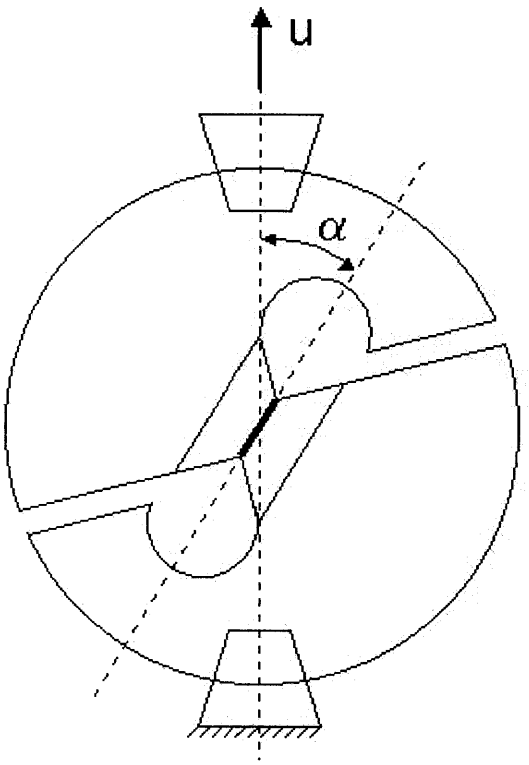

Fig. 2. Arcan test setup with butterfly specimen, Arcan grips, and fixtures

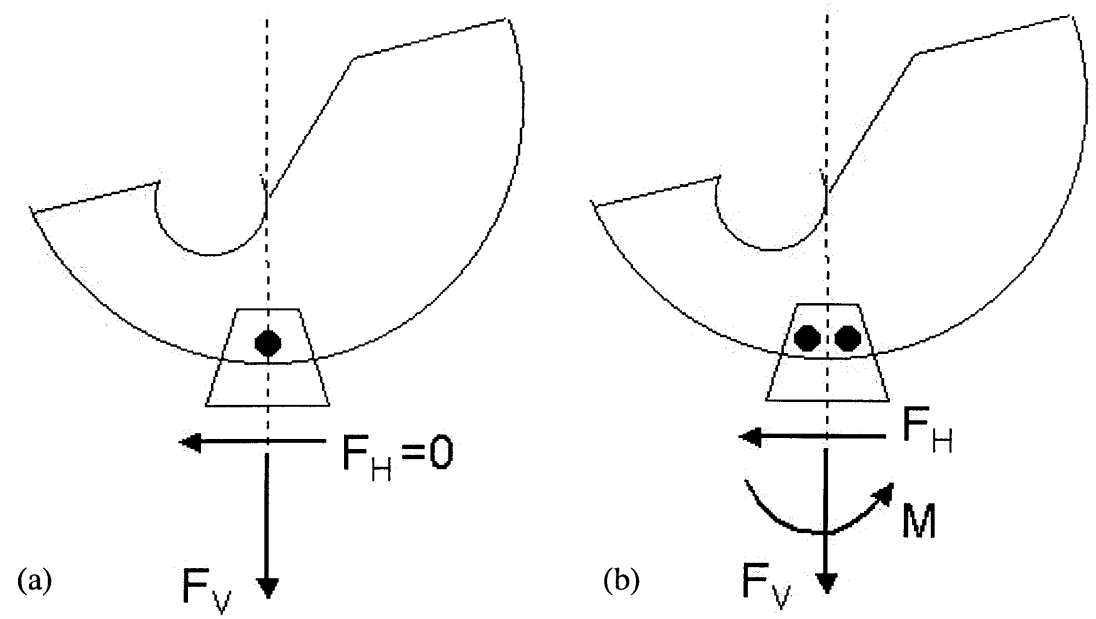

Fig. 3. Joint between the uniaxial testing machine and the Arcan grips for the (a) standard and (b) clamped configuration.

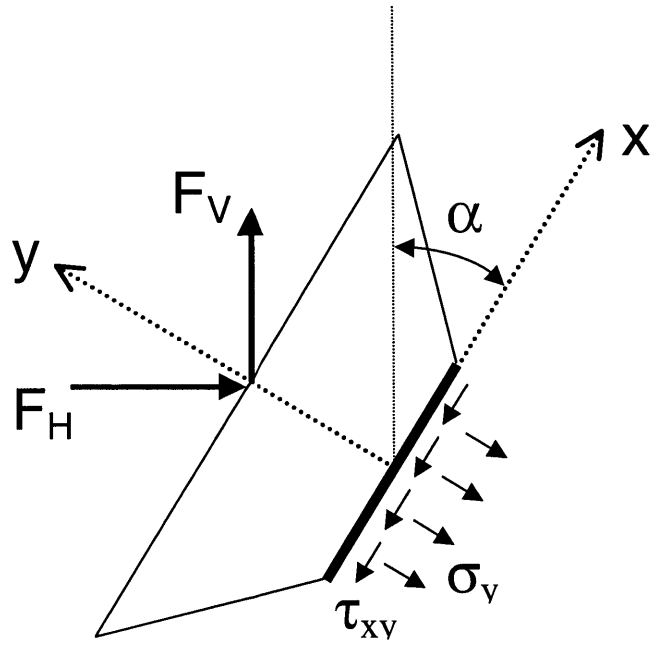

Fig. 4. Mean shear and normal stresses in the 'significant section' (force equilibrium, moment equilibrium not shown)

From a practical point of view, the clamped configuration is more convenient since the grips are rigidly connected with the testing machine and thus, the replacement of the butterfly specimen is very easy. Another advantage of the clamped configuration becomes apparent when testing cellular solids. Cellular solids are in general very soft as compared to the stiff metal grips. A problem frequently observed throughout the testing of these materials is that the deformation tends to localize in undesirable regions when using the unclamped setup. Doyoyo and Wierzbicki (2000; 2003) showed that this issue could indeed be overcome by using the clamped configuration. Expecting good stress uniformity, Petras and Sutcliffe (2000) used the clamped configuration for their biaxial testing on the Nomex honeycomb core of a sandwich panel.

The basic concept behind both configurations is that the Arcan test set-up has a well-defined section, usually referred to as the *significant section*, where the stresses are expected to be uniform. Figure 2 shows the significant section as a bold line at the center

of the butterfly specimen. This uniformity is achieved by an appropriate choice of the geometrical parameters of the butterfly specimen in accordance with the tested material and the biaxial loading angle. Another outcome of the butterfly-shaped geometry is that the stresses at the significant section are the highest and thus, failure or initial yield is most likely to occur there.

The mean shear stress, τ_{xy}, and the mean normal stress, σ_y, at the significant section are defined in a local coordinate system, where the x-axis is parallel and the y-axis is perpendicular to the significant section (Fig. 4). Both components can be directly determined from the forces that are transmitted by the joints between the Arcan grips and the testing machine (Figs. 3 and 4). We refer to the force that acts along the positive axis of the universal testing machine as the *vertical force,* F_V. The force perpendicular to the vertical one is referred to as the *horizontal force*, F_H. The angle between the fixed axis of the testing machine (vertical axis) and the direction of the significant section (local x-axis) is referred to as the biaxial loading angle α, while A denotes the cross-sectional area of the significant section.

Based on the global static equilibrium, Arcan *et al.* (1978) give the following expressions for the (mean) stresses in the significant section for the standard configuration:

$$\sigma_y^0 = \frac{F_V}{A}\sin\alpha \tag{1}$$

$$\tau_{xy}^0 = \frac{F_V}{A}\cos\alpha \tag{2}$$

It is important to note that although the horizontal displacements are prohibited at the top and bottom of the standard Arcan apparatus, the horizontal force still remains zero (Fig. 3(a)). This is a consequence of the momentum equilibrium equation. In fact, momentum equilibrium about any arbitrary point yields $M = F_H\, h$, where h is the distance between the top and bottom joint (Fig. 3 only shows the bottom joint). Since all rotations are free at the joints, the moment M must be zero and thus, $F_H = 0$.

In the case of the clamped configuration, the rotations at the joint between the Arcan grips and the testing machine are prohibited and thus, F_H can take non-zero values (Fig. 3 (b)). The expressions for the (mean) normal and shear stresses in the significant section must be corrected by adding a term that takes the effect of the horizontal force into account:

$$\sigma_y = \frac{F_V}{A}\sin\alpha - \frac{F_H}{A}\cos\alpha \tag{3}$$

$$\tau_{xy} = \frac{F_V}{A}\cos\alpha + \frac{F_H}{A}\sin\alpha \tag{4}$$

From an experimental point of view, it is essential to know whether the influence of the horizontal force can be neglected or not. It is also important to note that the measurement of the horizontal force would require an additional load cell. The standard load cell of a universal testing machine can only measure F_V, but not F_H, and it is common practice to ignore the measurement of the horizontal force (and thus neglect the second term in Eqs. (3) and (4)).

In the following subsections, we discuss the importance of measuring the horizontal force, which exists when using the Arcan apparatus in the clamped configuration. We derive a theoretical model that predicts the (mean) shear and normal stresses for orthotropic, linear-elastic materials. Based on this model, the hypothesis of a negligible horizontal force is checked and the corresponding error functions are shown for different engineering materials. Also, we will use the finite element method to support the results found from the theoretical analysis.

2.2.2 Theoretical analysis

Since the stiffness of the Arcan grips is much higher than the stiffness of the specimen, we assume the Arcan grips to be rigid in the subsequent analysis. This can be either guaranteed by the choice of different materials for the specimen and the grips, e.g. metallic foam and steel, or by the choice of different thicknesses for the specimen and

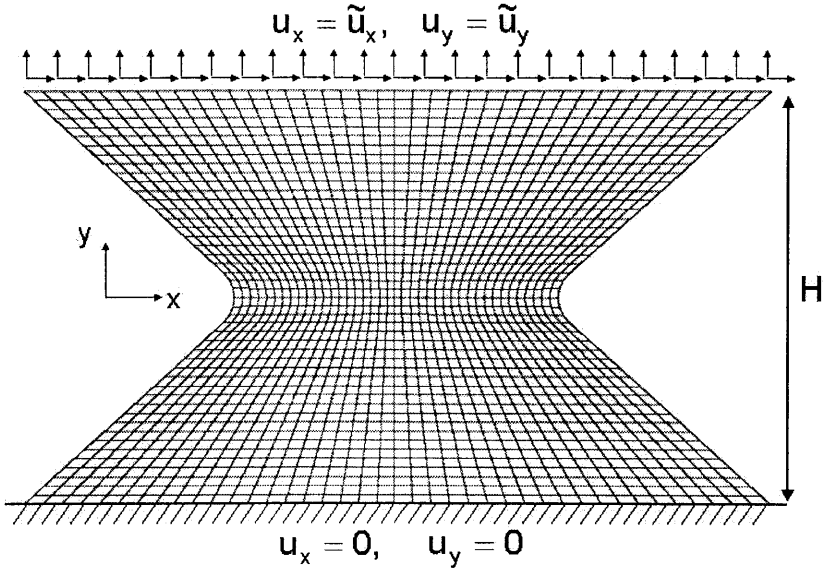

Fig. 5. Finite element mesh with displacement boundary condition

grips. Because of the combination of 'rigid grips' and 'rigid joints' between the grips and the testing machine (Fig. 3 (b)), the displacement field at the boundaries of the specimen is known. Thus, we will consider a butterfly specimen with a uniform displacement field on its boundaries as a simplified system (Fig. 5).

Given a uniform displacement field $(\tilde{u}_x, \tilde{u}_y)$ at the top boundary of the butterfly specimen, we assume the following kinematically admissible displacement field within the specimen,

$$u_x(y) = \frac{\tilde{u}_x}{2} + \frac{\tilde{u}_x}{H} y \tag{5}$$

$$u_y(y) = \frac{\tilde{u}_y}{2} + \frac{\tilde{u}_y}{H} y \tag{6}$$

where H is the height of the butterfly specimen (Fig. 5). The proportional loading path is defined by the biaxial loading angle α:

$$\tan\alpha = \frac{\tilde{u}_y}{\tilde{u}_x} \tag{7}$$

Next, assuming small deformations, we calculate the strain in the local x-direction, ε_x, the strain in the local y-direction, ε_y, and the shear distortion, γ_{xy}, in the significant section as:

$$\varepsilon_x = \frac{\partial u_x}{\partial x} = 0 \tag{8}$$

$$\varepsilon_y = \frac{\partial u_y}{\partial y} = \frac{\tilde{u}_y}{H} \tag{9}$$

$$\gamma_{xy} = \frac{\partial u_x}{\partial y} + \frac{\partial u_y}{\partial x} = \frac{\tilde{u}_x}{H} \tag{10}$$

The hypothesis of a negligible horizontal force implies that the resultant force on the top of the specimen points into the direction of the vertical force (Fig. 4). Using simple vector algebra, the hypothesis can be expressed as a fixed ratio between the shear and normal stresses:

$$\tan\alpha = \frac{\varepsilon_y}{\gamma_{xy}} = \frac{\sigma_y}{\tau_{xy}} \tag{11}$$

The left-hand side of the above equation is a kinematic relationship that results from the assumed displacement field. As for the right-hand side, it relates the ratio of the strains, ε_y and γ_{xy}, to the corresponding ratio of the stresses, σ_y and τ_{xy}. Thus, the right part of the above equation puts a restriction on the material behavior. In other words, the hypothesis of a negligible horizontal force is only true if the material law satisfies the above equation.

Next, we introduce an orthotropic material law that defines the relationship between stresses and strains under plane-stress conditions:

$$\begin{Bmatrix} \sigma_x \\ \sigma_y \\ \tau_{xy} \end{Bmatrix} = \begin{bmatrix} \overline{Q}_{11} & \overline{Q}_{12} & \overline{Q}_{16} \\ \overline{Q}_{12} & \overline{Q}_{22} & \overline{Q}_{26} \\ \overline{Q}_{16} & \overline{Q}_{26} & \overline{Q}_{66} \end{bmatrix} \begin{Bmatrix} \varepsilon_x \\ \varepsilon_y \\ \gamma_{xy} \end{Bmatrix} \tag{12}$$

We used the notation of composite mechanics, where $[\overline{Q}_{ij}]$ denotes the stiffness matrix of an orthotropic lamina in plane stress conditions (e.g. Swanson, 1997). For simplicity, we will restrict our discussion to the general case of orthotropic materials, where the material axes are aligned with the local x- and y-directions. This restriction guarantees that the shear and normal components are uncoupled, and thus $\overline{Q}_{16} = \overline{Q}_{26} = 0$. Since the particular choice of the displacement field implies that $\varepsilon_x=0$, Eq. (12) can be used to relate the strain and stress ratios as:

$$\frac{\sigma_y}{\tau_{xy}} = \beta_y \frac{\varepsilon_y}{\gamma_{xy}} \tag{13}$$

where β_y is a constant of proportionality. We define β_y as the *stiffness ratio*, obtained by dividing the normal modulus $\overline{Q}_{22}$ by the shear modulus $\overline{Q}_{66}$:

$$\beta_y := \frac{\overline{Q}_{22}}{\overline{Q}_{66}} \tag{14}$$

Comparing Eqs. (11) and (13) allows us to reformulate the hypothesis of a negligible horizontal force as a direct constraint on the material law. The hypothesis of a negligible horizontal force is only true if the stiffness ratio is equal to one:

$$F_H = 0 \quad \text{if} \quad \beta_y = 1.0 \tag{15}$$

In the special case of isotropic materials, we have the stress-strain relationships

$$\left.\begin{aligned} \varepsilon_x &= \frac{\sigma_x}{E} - \nu\frac{\sigma_y}{E} \\ \varepsilon_y &= \frac{\sigma_y}{E} - \nu\frac{\sigma_x}{E} \\ \gamma &= 2(1+\nu)\frac{\tau_{xy}}{E} \end{aligned}\right\} \tag{16}$$

Assuming $\varepsilon_x = 0$ yields

$$\left.\begin{aligned} \varepsilon_y &= (1-\nu^2)\frac{\sigma_y}{E} \\ \gamma_{xy} &= 2(1+\nu)\frac{\tau_{xy}}{E} \end{aligned}\right\} \tag{17}$$

and hence, we find the stiffness ratio as a function of the Poisson's ratio ν:

$$\beta_y = \frac{2(1+\nu)}{1-\nu^2} = \frac{2}{1-\nu} \tag{18}$$

Clearly, the condition $\beta_y = 1.0$ (Eq. (15)) is not satisfied for most isotropic materials and thus, the shear and normal stresses in the significant section depend on the horizontal force.

For orthotropic materials, e.g. unidirectionally fiber reinforced composites, two stiffness ratios are defined in the testing plane:

$$\beta_1 = \frac{Q_{11}}{G_{12}} = \frac{\mathrm{E}_{11}}{\mathrm{G}_{12}(1-\nu_{12}\nu_{21})} \tag{19}$$

and

$$\beta_2 = \frac{Q_{22}}{G_{12}} = \frac{\mathrm{E}_{22}}{\mathrm{G}_{12}(1-\nu_{12}\nu_{21})} \tag{20}$$

where E_{11} and E_{22} denote the Young's moduli in the direction of the fibers and perpendicular to the fibers, respectively. G_{12} is the corresponding in-plane shear modulus and ν_{12} and ν_{21} are the corresponding Poisson's ratios. The first stiffness ratio, β_1, must satisfy condition (15) when the fibers are oriented perpendicular to the significant section, or, in other words, when a 1-2 specimen is tested. The second, β_2, must be used for 2-1 specimens, where the fibers are parallel to the significant section. Table 1 shows the values of β_y for different fiber reinforced composites, Nomex honeycomb, and isotropic aluminum foam. The stiffness ratio can take very high values. For a unidirectional, fiber reinforced composite AS4/PEEK, the ratio β_2 is as high as 19.2. Clearly, the hypothesis of a negligible horizontal force is not valid.

For engineering purposes, it is necessary to quantify the error due to the neglect of the horizontal force in the measurements. We will quantify this error in terms of the shear

	Theoretical Analysis					Numerical Analysis		
	E_{11} [MPa]	E_{22} [MPa]	G_{12} [MPa]	ν_{12} [-]	β_y [-]	K_{yy}[N/mm]	K_{xx}[N/mm]	β_y^* [-]
Aluminum Foam (Alporas, ρ^*/ρ=9.5%)	90	90	35	0.3	2.9	420	151	2.8
E-glass/epoxy (1-2), V_f=0.6	40,300	6,210	3,070	0.2	13.2	-	-	-
E-glass/epoxy (2-1), V_f=0.6	40,300	6,210	3,070	0.2	2.0	-	-	-
AS4/PEEK (1-2)	128,700	10,200	6,200	0.3	19.4	508,300	29,440	17.3
AS4/PEEK (2-1)	128,700	10,200	6,200	0.3	1.7	46,610	25,400	1.8
Nomex Honeycomb (ρ^*/ρ=17.5%)	159	-	34	0.4	4.7	-	-	-

Table 1: Results of the analytical and numerical analysis. The elastic properties of the unidirectionally fiber reinforced composites are taken from Swanson (1997) and Hung and Liechti (1999). Specimens with the fiber direction in the local y-direction or x-direction are referred to as "1-2" and "2-1", respectively. The fiber volume ratio is denoted as V_f. For the foam and honeycomb, ρ^*/ρ denotes the relative density.

and normal stresses in the significant section. In addition to the real stresses, τ_{xy} and σ_y, we introduce the hypothetical stresses, τ_{xy}^0 and σ_y^0, that are found when the horizontal force is assumed to be zero (see Eqs. (1) and (2)).

The real force F_V, measured by the universal testing machine, can be expressed in terms of the real stresses by

$$F_V = \tau_{xy} A\cos\alpha + \sigma_y A\sin\alpha \tag{21}$$

Applying Eqs. (1) and (2), we can express the hypothetical stresses as a function of the real stresses by

$$\tau_{xy}^0 = \tau_{xy}\cos^2\alpha + \sigma_y \sin\alpha\cos\alpha \tag{22}$$

$$\sigma_y^0 = \tau_{xy}\sin\alpha\cos\alpha + \sigma_y \sin^2\alpha \tag{23}$$

If we introduce the material law in the above equations, we can obtain the following expressions for the error in the hypothetical stresses:

$$e(\tau_{xy}) := \frac{\tau_{xy}^0 - \tau_{xy}}{\tau_{xy}} = (\beta_y - 1)\sin^2\alpha \quad \text{for } \tau_{xy} \neq 0 \tag{24}$$

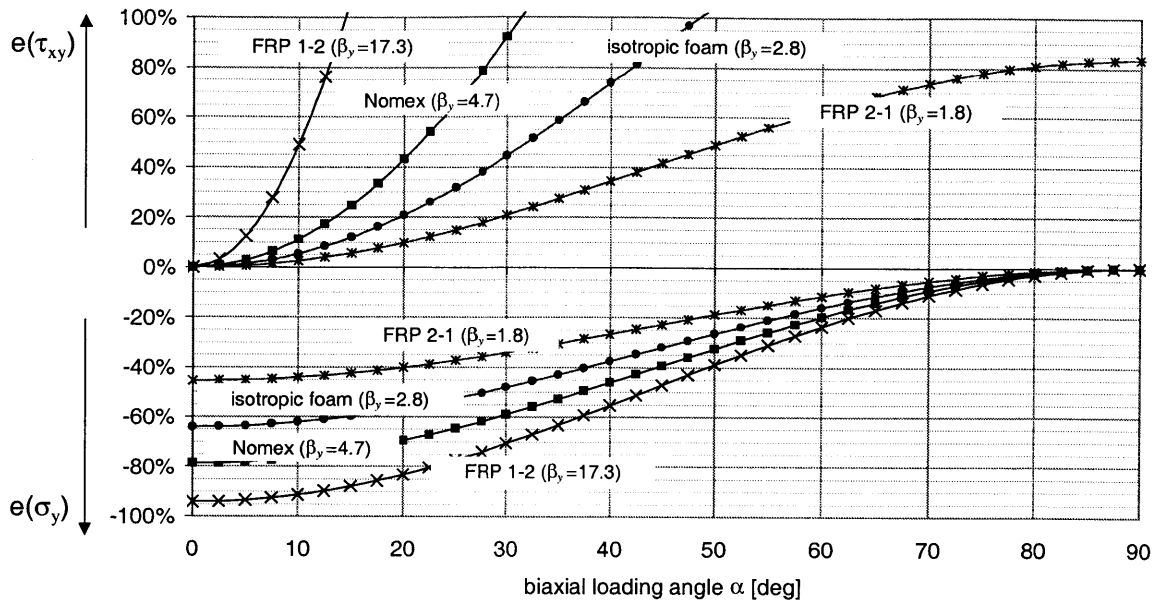

Fig. 6. Error in the shear stress $e(\tau_{xy})$ and in the normal stress $e(\sigma_y)$ as a function of the biaxial loading angle for various materials

$$e(\sigma_y) := \frac{\sigma_y^0 - \sigma_y}{\sigma_y} = \left(\frac{1}{\beta_y} - 1\right)\cos^2\alpha \quad \text{for } \sigma_y \neq 0 \tag{25}$$

These ratios provide us with a direct measure of the error in the stresses that are obtained from an Arcan test in the clamped configuration. The error in the stresses is not only a function of the stiffness ratio β_y, but also a function of the biaxial loading angle α. If the condition in Eq. (15) is satisfied, it implies that the hypothetical stresses are equal to the real stresses. Unless this condition is satisfied, one can claim that there exists an error in the hypothetical stresses.

Figure 6 shows the errors, $e(\tau_{xy})$ and $e(\sigma_y)$, as functions of the loading angle for different materials. For a given angle, there is either a significant error in the shear stresses or in the corresponding normal stresses. The only cases of a good measurement of either components are for $\alpha=0$ and $\alpha=90$. At these loading angles, the error curves presented in Fig. 6 are not defined. These stress states, based on the simplified

displacement field correspond to pure shear and pure normal stress, respectively. As a consequence, the hypothetical stresses are equal to the real stresses and thus, the absolute errors in the stresses are zero. With respect to β_y, the results demonstrate the interesting nature of Eqs. (24) and (25). Since for most engineering materials, we have $\beta_y >> 1$, the maximum error in the normal stresses is always below 100%. But the maximum error in the shear stresses, as shown by Eq. (24), increases linearly with β_y. Thus, for unidirectionally reinforced composites, maximum relative errors in the shear stresses of the order of 1000% can be observed!

Specifically, for orthotropic materials, e.g. honeycomb or fiber reinforced composites, the results found from an Arcan test in the clamped configuration must be interpreted with care, unless the horizontal force is known.

Remark. Although the focus of this section is the measurement of the two stress components τ_{xy} and σ_y, we like to note that this theoretical analysis may also be used to give a first approximation of the second normal stress, σ_x. Using the orthotropic material law (Eq. (12)) and the strain field given by Eqs. (8), (9) and (10), we obtain that $\sigma_x = \frac{\overline{Q}_{12}}{\overline{Q}_{22}}\sigma_y$. Thus, for isotropic materials, a first approximation for the relationship between the two normal stresses is $\sigma_x = \nu\sigma_y$. For an orthotropic material we have $\sigma_x = \nu_{21}\sigma_y$ and $\sigma_x = \nu_{12}\sigma_y$ for the 1-2 and 2-1 specimen, respectively.

2.2.3 Numerical analysis

The results from the theoretical analysis are based on the assumption of a simplified displacement field that does not take the specific geometry of the butterfly specimen into account. The objective of the additional numerical analysis is to perform the error analysis for a typical butterfly specimen geometry. We note that the simplicity of the theoretical displacement field allowed for a direct formulation of the hypothesis of a negligible horizontal force in terms of the elastic material constants, i.e. a formulation on

the material level. By contrast, the formulation within this section will be made for the butterfly structure, i.e. on the structural level. Thus, instead of the material stiffness matrix, we introduce the structural stiffness matrix $[K_{ij}]$ for the butterfly specimen that relates the forces and displacements that act on the top boundary of the specimen:

$$\begin{Bmatrix} F_x \\ F_y \end{Bmatrix} = \begin{bmatrix} K_{xx} & K_{xy} \\ K_{yx} & K_{yy} \end{bmatrix} \begin{Bmatrix} \tilde{u}_x \\ \tilde{u}_y \end{Bmatrix} \tag{26}$$

Analogously to Eq (11), we write the hypothesis of a negligible horizontal force as:

$$\tan\alpha = \frac{\tilde{u}_y}{\tilde{u}_x} = \frac{F_y}{F_x} \tag{27}$$

We use the implicit solver of LS-DYNA, Version 960 (LSTC, 2001), to perform linear elastic finite element analyses of the butterfly specimen for various materials. Figure 5 shows the spatial discretization of the butterfly specimen with 4-node elements. We assume plane-stress conditions along the plane of the butterfly specimen. The height H of that specific butterfly specimen was 46.5 mm, the out-of-plane thickness was 5 mm and the corresponding length of the significant section was 33.15 mm.

The structural stiffness constants K_{xx} and K_{yy} are determined from calculations with $(\tilde{u}_x, \tilde{u}_y) = (0.0\,mm, 0.001\,mm)$ and $(\tilde{u}_x, \tilde{u}_y) = (0.001\,mm, 0.0\,mm)$, respectively. Table 1 summarizes the results of the numerical analyses. An analysis with $(\tilde{u}_x, \tilde{u}_y) = (0.001\,mm, 0.001\,mm)$ confirms that $K_{xy}=K_{yx}=0$ for the isotropic and orthotropic materials considered. Thus, compared to the material matrix (Eq. (11)), the structural matrix of the butterfly specimen (Eq (23)), $[K_{ij}]$, takes a diagonal form. Therefore, the algebraic form of the hypothesis of a negligible horizontal force as well as the error functions at the structural level are similar to the theoretical expressions in Eqs. (15), (24), and (25), when β_y^*, defined as

$$\beta_y^* = \frac{K_{yy}}{K_{xx}} \tag{28}$$

is used instead of β_y. A comparison between β_y and β_y^* (Table 1) shows that the differences are small. This supports the choice of the displacement field that has been

assumed for the theoretical analysis. Additionally, the validity of the error functions shown in Fig. 6 is fully confirmed by the numerical analysis.

2.2.4 Application: Correction procedure

The conclusion drawn from the previous analysis is that the effect of the horizontal force has to be taken into account when the Arcan apparatus is used in the clamped configuration. One solution to this problem is to modify the testing equipment and record the horizontal force during the experiment. This is probably the only possible way when large inelastic deformations are investigated. However, for tests that are exclusively performed in the elastic regime, e.g. the determination of the failure surface of brittle materials, the results of the theoretical analysis can be used to correct the measured data *a posteriori*. In the following paragraph, we describe a procedure used to correct the data from tests in which the horizontal force was not measured.

Petras and Sutcliffe (2000) used a flat specimen connected to the circular grips rather than the butterfly specimen. In their derivation, they applied Eqs. (1) and (2) which are only valid if the horizontal force is negligible. As an example, we consider the correction of the failure surface of the Nomex honeycomb with a core density of 128 kg/m^3, which was studied by the mentioned authors. For a given data point in the stress space that was found based on the hypothesis of a negligible horizontal force, $(\tau_{xy}^0, \sigma_y^0)$, we can determine the corrected data point, (τ_{xy}, σ_y), by transforming the error functions (24) and (25):

$$\tau_{xy} = \frac{\tau_{xy}^0}{(\beta_y - 1)\sin^2\alpha + 1} \tag{29}$$

$$\sigma_y = \frac{\sigma_y^0}{\left(\frac{1}{\beta_y} - 1\right)\cos^2\alpha + 1} \tag{30}$$

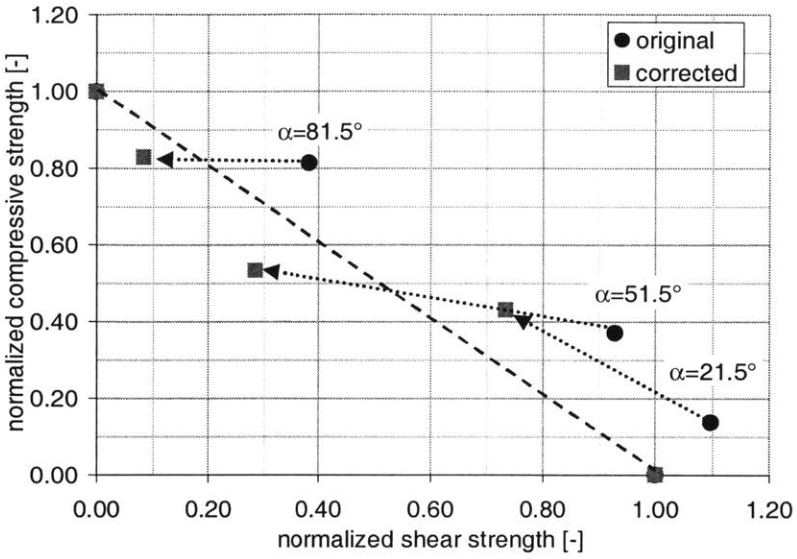

Fig. 7. Stress states at failure for Nomex honeycomb under biaxial loading. The arrows show the shifting of the data points due to the correction procedure (β_y=*4.7*). The straight line is the linear failure criterion suggested by Petras and Sutcliffe (2000).

The Young's modulus in the *out-of-plane direction* of that Nomex honeycomb is E_{22}=*159 MPa*, the corresponding transverse shear modulus is G_{12}=*34 MPa* (Petras, 1998). Thus, the material stiffness ratio is approximately $\beta_y \approx 4.7$.

Figure 7 shows both, the original and the corrected data in normal stress versus shear stress space. The arrows in Fig. 7 demonstrate the significant shifts of the corrected data points in the stress space. The corrected results still confirm the linear failure criterion of Petras and Sutcliffe. However, it must be noted that corrected results are more consistent with this criterion, as the points are clearly closer to the failure envelope. Also, two of the corrected data points now lie inside the failure envelope. This shows that the Petras and Sutcliffe failure surface is no longer a conservative criterion with respect to strength sensitive applications as it might be required in e.g. aircraft design.

2.2.5 Conclusion

Both the theoretical and finite element analysis of the Arcan test setup show that the original formulas for the stresses derived for the standard configuration cannot be applied when the Arcan apparatus is used in the clamped configuration.

In the standard configuration with a single pin joint, only a vertical force acts on the Arcan apparatus. By contrast, in the case of the clamped configuration, an additional horizontal force is present. Based on the hypothesis of a negligible horizontal force, error functions for the shear and normal stresses have been derived for isotropic and orthotropic materials. The results show that unless the material stiffness ratio of normal and shear modulus is equal to one, neglecting the horizontal force results in a significant error in the stresses. An evaluation of the error function for various engineering materials demonstrates, that, depending on the biaxial loading angle, significant errors arise in the stresses derived from the assumption of a negligible horizontal force.

From an experimental point of view it is concluded that besides the vertical force that acts on the Arcan apparatus in the clamped configuration, the horizontal force must be measured. For the special case that the elastic properties are known before testing and that the specimen is tested in the linear elastic regime (for example, the determination of the failure surface of brittle materials), the results from the force measurement can be corrected analytically. Previously published biaxial failure data of Nomex honeycomb was used to show the significance of this procedure.

2.3 Design of the Enhanced Arcan Apparatus (EAA)

The use of the Arcan test for cellular solids requires the modification of the *single-pin loading* mechanism of the standard design (Fig. 2(a)) to a *multiple-pin* or *clamped loading* mechanism (Fig. 2(b)). As demonstrated in the previous section, clamping generates an additional *horizontal* force perpendicular to the *vertical* force that is measured by the universal testing machine. Here, present the Enhanced Arcan Apparatus (EAA), a modification of the equipment developed by Doyoyo and Wierzbicki (2000; 2003). The EAA incorporates an additional load cell to measure the horizontal force.

Besides directly measuring the horizontal force at the fixtures, there are various ways to measure the effect of the horizontal force. Basically any additional force measurement is sufficient to quantify the effect of clamping. However, for the current design, it was beneficial to measure the force F_y that acts perpendicular to the significant section (force parallel to the y-direction in Fig. 4). The following formulae relate the average stresses along the significant section to the measured force components ($0 \le \alpha < 90^\circ$):

$$\sigma_y = \frac{F_y}{A} \tag{31}$$

$$\tau_{xy} = \frac{F_x}{A} = \frac{F_V}{A\cos\alpha} - \frac{F_y}{A}\tan\alpha \tag{32}$$

where A denotes the cross-section area of the significant section, and α is the biaxial loading angle between the loading axis and the direction parallel to the significant section. Figures 8 and 9 show the details of the EAA including the integrated load cell, which measures the normal load. Instead of directly connecting both sides of the butterfly-shaped specimen to the Arcan grips, a movable plate supported by four low friction cylindrical roller bearings is inserted between the upper Arcan grip and the specimen, allowing the plate to slide perpendicular to the significant section of the specimen (y-axis). All other translational and rotational degrees of freedoms of this plate are prohibited. Now, an additional load cell can be placed between the movable plate and

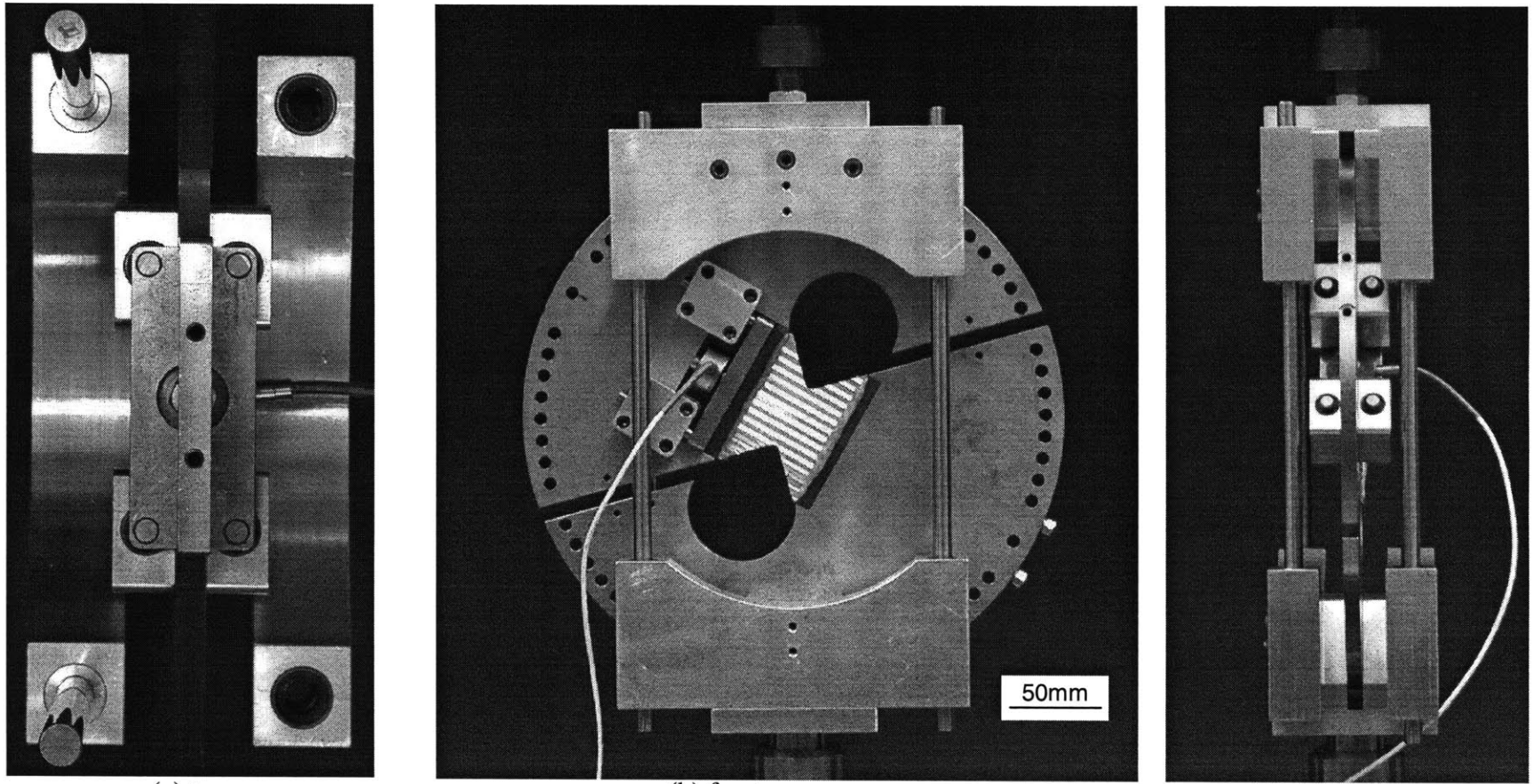

(a) top (b) front (c) side

Fig. 8. Views of the enhanced Arcan apparatus.

the upper Arcan grip. By connecting this load cell with both parts, the plate can no longer move along the y-direction. Instead, the normal force is measured.

The decision of measuring the additional force 'inside' the Arcan apparatus, i.e. not at the fixtures, is advantageous in that it also allows for another improvement of the design. Instead of clamping either Arcan grip to the universal testing machine, a closed apparatus is built. The idea is to join the two grips together such that the horizontal force is directly transmitted from one Arcan grip to the other. Similar to residual stresses, the horizontal force persists inside the apparatus although it does not generate any reaction force at the fixtures. Thus, the undesirable horizontal loading of the vertical load cell can be avoided and secondly the stiffness of the testing jig can be increased. Here, we adopt the following design: two pairs of parallel 'guide plates' as shown in Fig. 8, are mounted onto the Arcan grips. Each guide plate consists of two solid aluminum plates and two stiff low friction cylindrical roller bearing guides, allowing for a linear motion between the two solid parts. Precision steel pins in combination with three screws achieved an almost rigid connection between the solid aluminum parts of the guide plates and the Arcan grips. Thus, these guide plates guarantee that the upper and lower grips of the Arcan

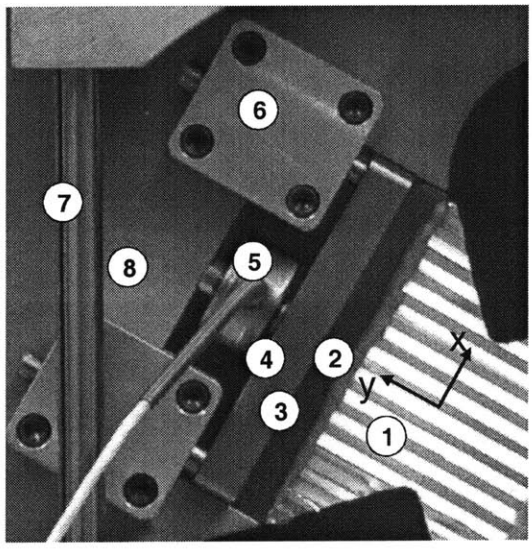

Fig. 9. Detail of the enhanced Arcan apparatus. 1-butterfly specimen, 2-epoxy layer, 3-intermediate steel grip, 4-movable steel plate, 5-integrated load cell, 6-roller bearings for moving plate, 7-cylindrical roller guidance of guidance system, 8-upper Arcan grip.

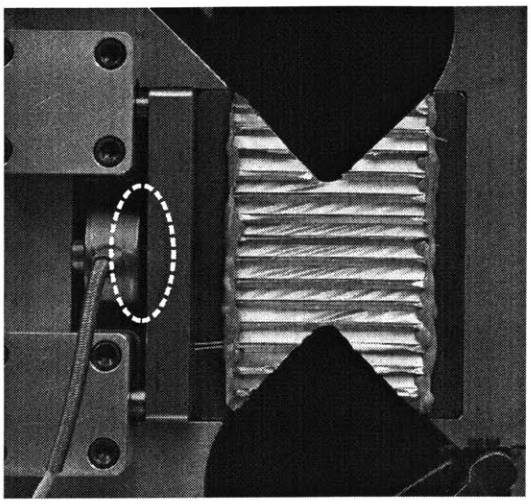

(a)

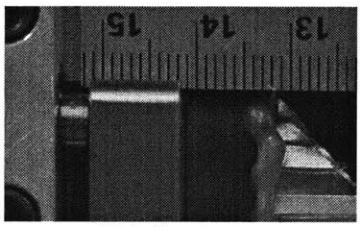

(b) before test

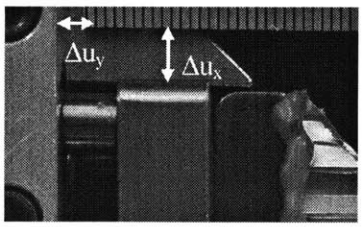

(c) during test

Fig. 10. Test set-up for 'pure shear'. By disconnecting the movable plate from the integrated load cell (a), normal displacements are allowed during a shear test (b, c) although rotations are still prohibited.

apparatus always move along the same direction with respect to each other, avoiding any out-of-plane motion. Also, any rotation of the grips is prohibited by these guide plates. Since the guide plates are aligned along the loading axis of the universal testing machine, the measurement of the vertical force is not influenced.

By rotating the Arcan grips with respect to the guide plates, the biaxial loading angle can be varied in steps of 5 degrees from 0 to 90 degrees. Additionally, the sign of the loading force can be changed, i.e. any combination of combined tension/shear and combined compression/shear can be applied by the EAA. Only the guide plates were machined from aluminum, all other components of the present apparatus were made out of steel. The integrated load cell (Model 31, Sensotec Inc., Columbus, OH) was designed to measure loads as high as 2.5 kN. Local strains along the significant section may be measured directly with digital image correlation analysis (e.g. Bastawros *et al.*, 2000). However, it must be noted that the current applications do not require accurate displacement or strain measurements. Both initial plastic yield and failure can be exclusively defined in the stress space.

2.4 Experiments on butterfly-shaped specimens under combined loading

2.4.1 Material and specimen

The hexagonal honeycomb chosen for the current study was fabricated and supplied by Hexcel Corporation, Dublin, CA. The cell walls of the honeycomb were made up of aluminum 5056-H39. For the honeycomb tested we have: $t \approx 33$ μm, $h \approx 2.4$ mm, $l \approx 3.1$ mm and $\theta \approx 40^{\circ}$ (refer to Fig. 1 for the notation of the hexagonal cellular microstructure). The nominal density of the honeycomb was 47 kg/m^3, which represents a relative density of about 1.8% compared to the fully-dense aluminum alloy.

In order to test the above honeycomb with the EAA, a flat specimen of approximately one full cell width is required. In addition to the L- and W-directions, there is another direction (denoted as K in the schematic of Fig. 1) at $\phi \approx 61.5^{\circ}$ with respect to the W-direction that allows for a straight cut along the honeycomb cells. Note that the W- and L-directions correspond to the orthotropy axes of the honeycomb and thus, testing of the honeycomb in the T-W or the T-L plane corresponds to testing the honeycomb in its weakest or strongest directions, respectively. In order to obtain representative results for the out-of-plane behavior, we chose to test the honeycomb in the T-K plane. The honeycomb was sliced into layers of thickness $w \approx 7.9$ mm, corresponding to one cell by cutting the honeycomb parallel to the K- and T-directions from a honeycomb block with EDM. Figure 11 shows the photographs of a typical specimen. It can be seen that the specimen is made up of a single row of 6 cells along the significant section (the 'boxed' region in Fig. 11(a)). The exact shape of the butterfly-specimens was chosen according to the results of the stress uniformity analysis by Arcan *et al.* (1978).

After cutting, the specimens were prepared for bonding to roughened steel holding grips (see Fig. 11(b) and (c)). The specimens were bonded to the holding grips with toughened Epoxy (Lord 410A/B) allowing the glue to penetrate the honeycomb cells to some extent for superior bond strength.

2.4.2 Testing

The prepared specimen was connected to the EAA with its holding grips. Figure 12 shows the photograph of the EAA aligned to test the honeycomb specimen at 60° loading angle. The EAA was attached to a universal testing machine (Model 45G, MTS Systems, Eden Prairie, MN) with a screw driven crosshead, which was then used to apply a displacement on the apparatus (see the white arrow and label 1 in Fig. 12). The vertical loads F_V were measured by a 10kN MTS load cell. Load and displacement responses were acquired with the MTS TestWorks software and exported for further analysis.

Several butterfly-shaped specimens were tested with the EAA at different loading angles: $\alpha = 0°$, 10°, 20° 30°, 45°, 60°, 65°, 70°, 80° and 90°. Positive and negative resultant displacements were applied on the specimens in order to gain insight into both the compression/shear and tension/shear behavior of the honeycomb. The 90° loading angle represents uniaxial tension or compression along the T-direction depending on the sign of the applied displacement. Further, observe from Eqs. (31) and (32), that the 0° loading angle does not represent a state of pure shear as long as the specimen is connected to the integrated load cell, i.e. as long as $F_y \neq 0$. In order to perform a pure shear test with the EAA, the butterfly-shaped specimen is detached from the integrated load cell at 0° loading, thus guaranteeing that $F_y = 0$ (Fig. 10). Typically, four tests were conducted for each loading path to achieve a satisfactory statistical confidence level of the measurements. In this section, we shall qualitatively describe the observed deformation modes and their effects on the load-displacement responses.

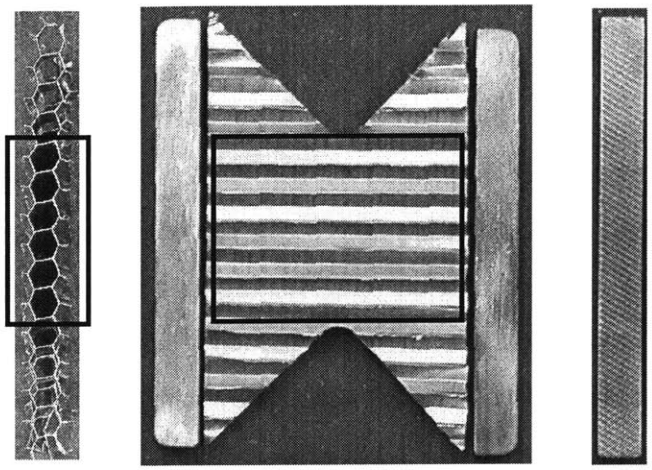

Fig. 11. Photograph of the T-K honeycomb butterfly specimen: (a) cross-section of the specimen, (b) side view of the specimen holding grips, (c) roughened surface of holding grips.

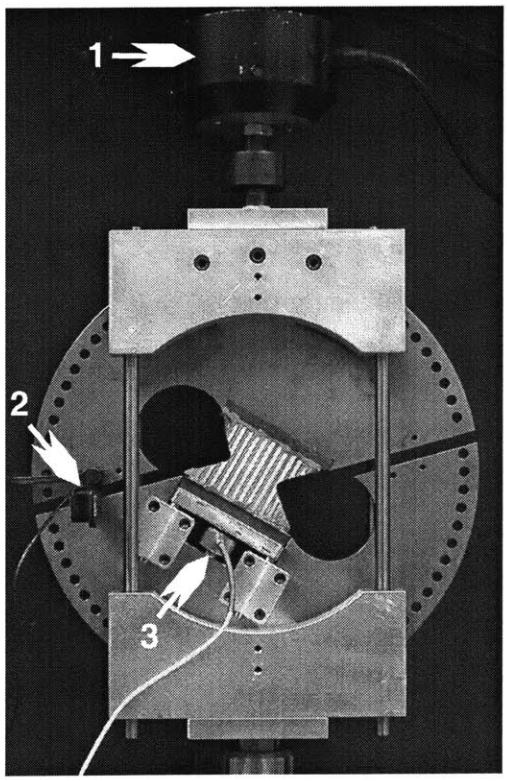

Fig. 12.A photograph of the test-setup showing the EAA with a honeycomb specimen for testing at 60°loading angle: 1-universal load cell, 2-extensometer, 3-integrated load cell.

2.4.3 Observations

Uniaxial compression

The characteristic load-displacement response of the honeycomb under compression in the T-direction is shown in Fig. 13 for four different specimens. The normal load increases linearly with displacement until a peak load is reached and the load drops. The behavior of the honeycomb microstructure during out-of-plane compression is documented photographically in Fig. 14 for one of the specimens. The example photographs were taken at positions labeled A and P in the load-displacement plot in Fig. 14. At the intermediate position of loading, A, the specimen has already developed several regular buckles (of some wavelength λ) while the load keeps increasing. When the load is increased beyond the peak load, the cells collapse plastically along the significant section.

Uniaxial tension

The tensile load-displacement responses of four honeycomb specimens in the T-direction are presented in Fig. 15. Note that the current testing method emphasizes force measurements rather than displacement measurements. The represented displacements correspond to the crosshead position and thus include both the deformation of the specimen as well as of that of the apparatus and joints. The history of one specimen during loading is followed as shown by the highlighted load-displacement plot. Since the uniaxial tension test on a honeycomb can be seen as a uniaxial tension test on aluminum foil, the onset of non-linearity (denoted by 'Y' in Fig. 15) is associated with the plastic yield of cell wall material. Upon further loading to position B, sudden cracks occur in the honeycomb specimen, probably due to local necking preceding ductile fracture of the cell wall material (Fig. 16). The observation that the specimen could even fracture in tension without the failure of glue at the holding grips demonstrates the reliability of this testing method.

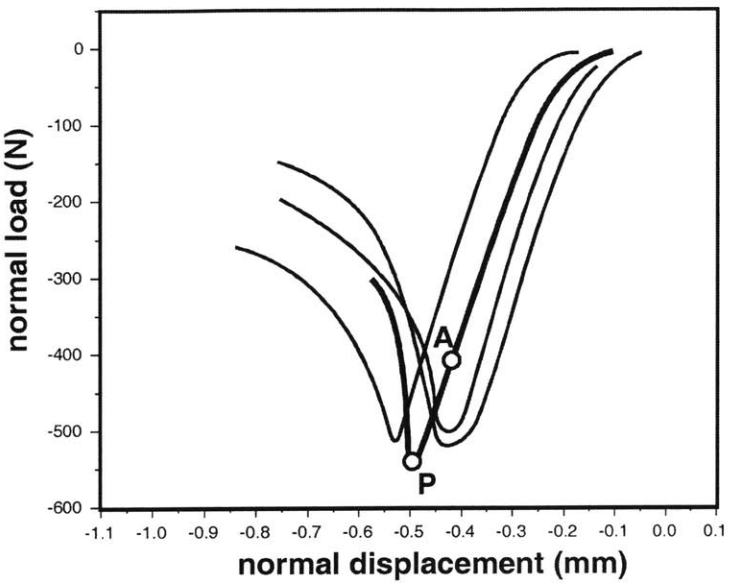

Fig. 13. Uniaxial compressive response of the honeycomb in the T-direction.

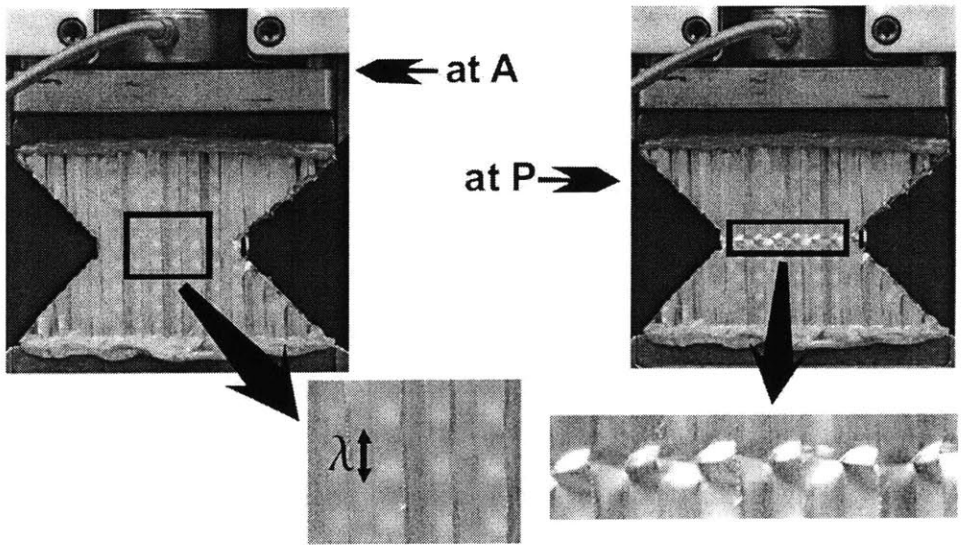

Fig. 14. Photographs of the honeycomb specimen at different points of uniaxial compression in the T-direction

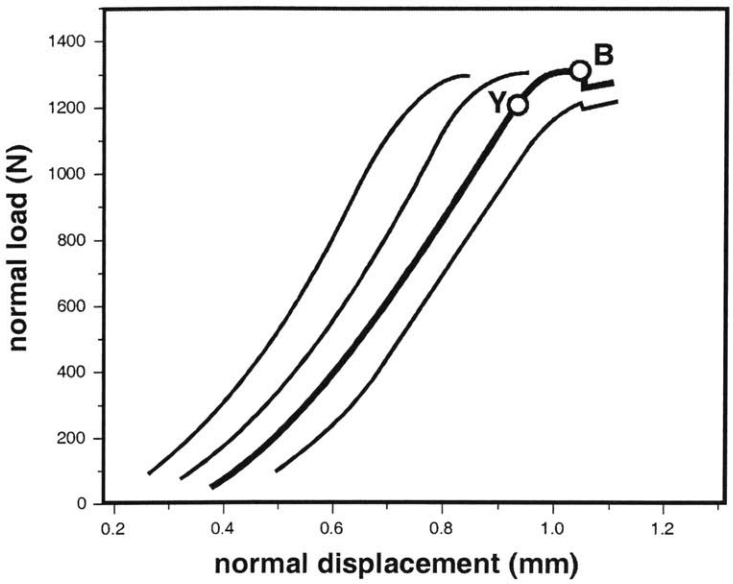

Fig. 15. Uniaxial tensile response of honeycomb in the T-direction

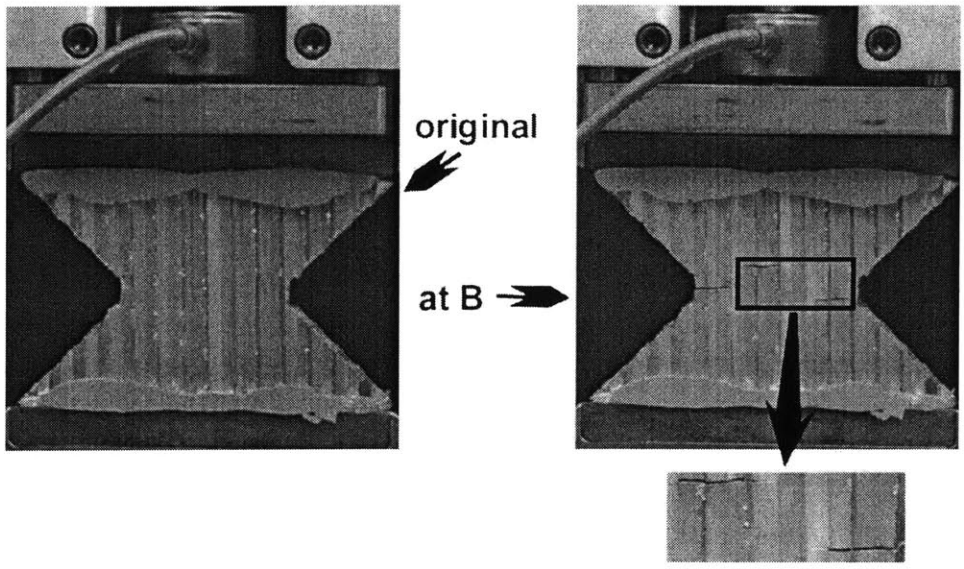

Fig. 16. Photographs of original vs. fractured honeycomb specimen during tensile testing in the T-direction

Pure shear

Figure 17 shows the load-displacement responses for four tested honeycomb specimens subjected to a state of pure shear in the T-K -plane (the integrated load cell has been disconnected for these tests). After a peak load is reached at point P, the load remains approximately constant with displacement. This is demonstrated with one highlighted load-displacement curve for one of the specimens in the plot. A post peak load photograph of the specimen taken at position C is shown in Fig. 18. The pure shear failure mode involves small parallel and regular folds with oblique orientations to the T-direction.

Combined compression and shear

Transverse load vs. normal load responses for the honeycomb specimens subjected to a negative displacement loading at 60 degrees is shown in Fig. 19. The different starting points of the loading curves reveal differences in the pre-loading of the specimens. The magnitude and direction of the pre-load was not chosen by any criteria, but was rather a consequence of the slight variations in the length of the specimens. Typically, the transverse load increases almost linearly with the normal load until some point P after which the transverse load decreases while the normal load remains roughly constant. A photograph of the specimen taken at point D (Fig. 20) shows evolution of short regular folds obliquely orientated to the T- direction.

Combined tension and shear

Under a combination of tension and shear, a well-defined turning point is observed in the transverse-normal load plane. This is shown exemplary in Fig. 21 for one of the four specimens subjected to positive resultant displacement at a loading angle of 60 degree. Beyond point P, the transverse load remains constant while the normal load continues to increase. Note that this is a reverse behavior as compared to that under compression and shear, where the normal load remained constant whereas the transverse load carrying capacity decreased. Fig. 22 shows photographs of the specimen taken at points P and E.

At point *P*, distinct folds oriented almost parallel to the T- direction of the cell structure have been evolved. Upon further loading to point *E,* fracture of the cell wall material occurs.

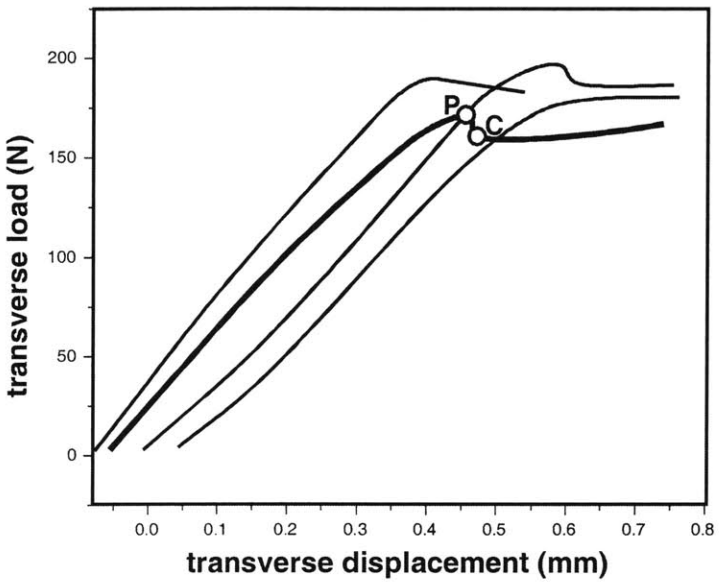

Fig. 17. Response of honeycomb under pure shear in the T-K plane

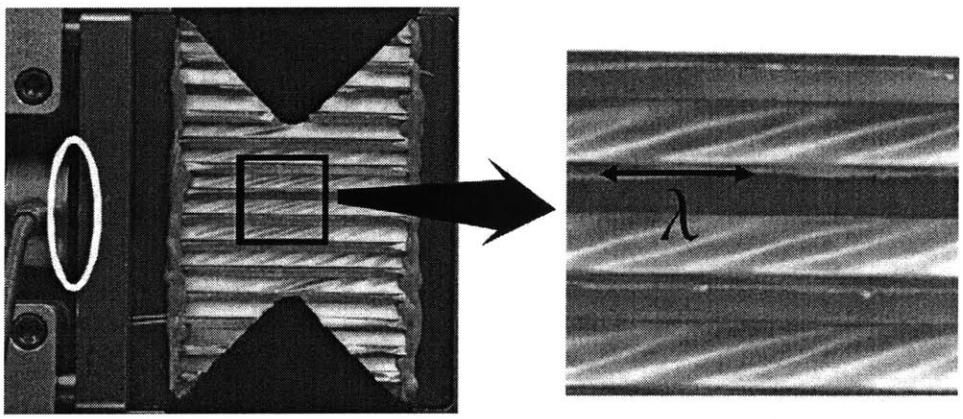

Fig. 18. Representative photograph of the honeycomb specimen at point C during pure shear loading in the T-K plane. The white ellipse is drawn to emphasize that the integrated load cell is disconnected from the specimen holder for pure shear testing without being detached from the apparatus.

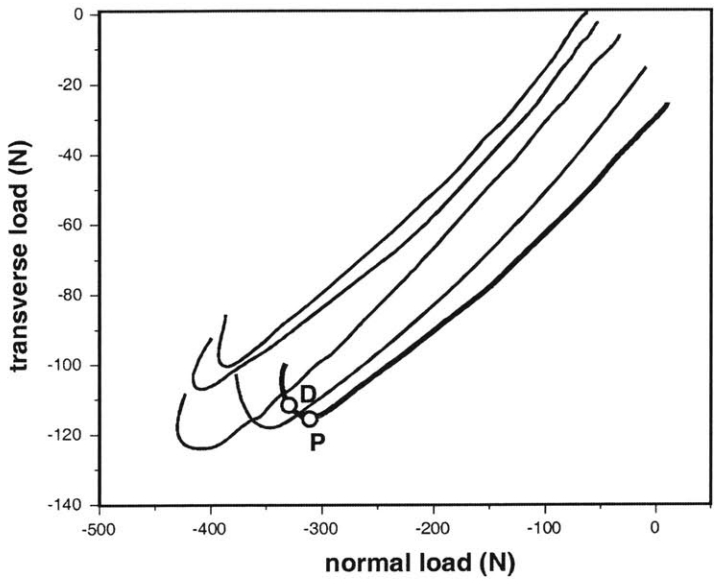

Fig. 19. Response of honeycomb under combined compression and shear at 60° loading in the T-K plane.

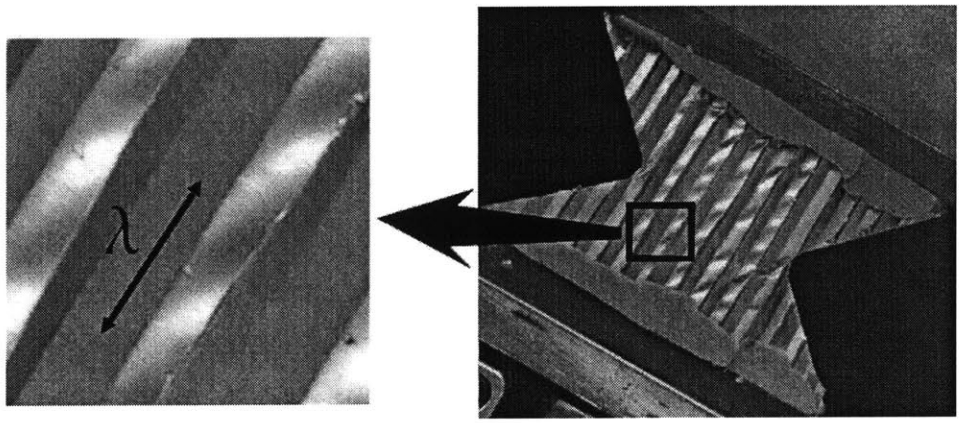

Fig. 20. Photograph of deformed honeycomb specimen at point P under combined compression and shear at 60° loading.

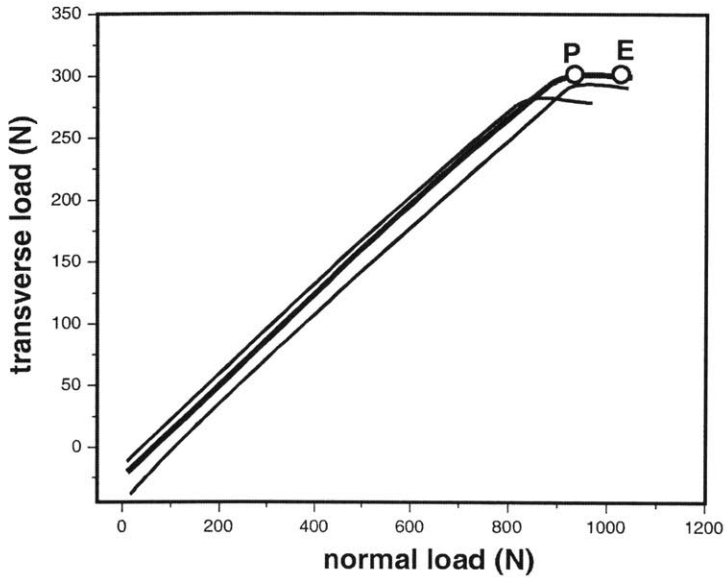

Fig. 21. Response of the T-K honeycomb specimen under combined tension and shear at 60° loading.

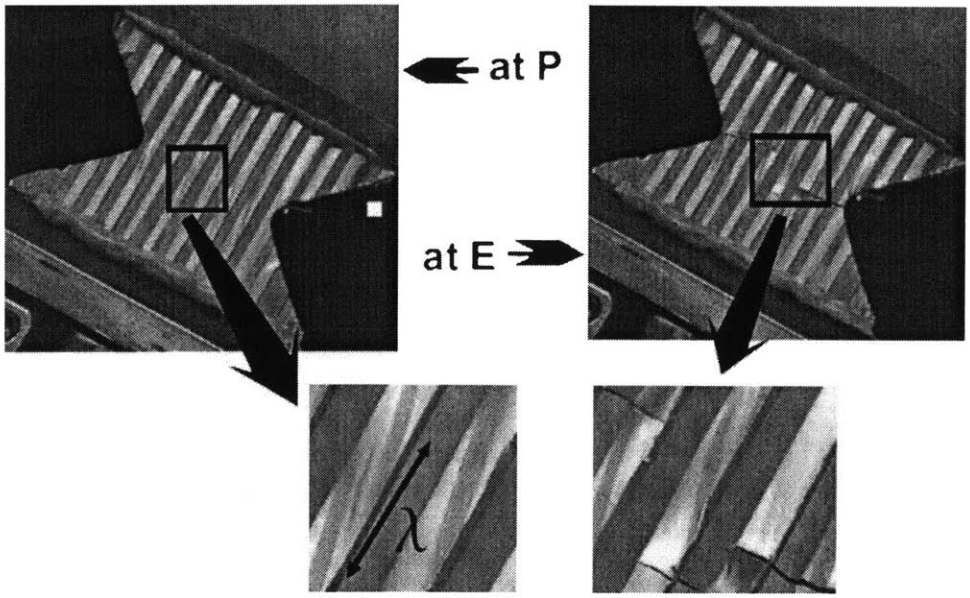

Fig. 22. Photographs of the deformed honeycomb specimen under combined tension and shear at different points during 60° loading.

2.4.4 Macroscopic yield envelope

Following the above observations on the behavior of the tested honeycomb specimens under combined out-of-plane loading, we define 'macroscopic yield' according to the following microstructural mechanisms:

1. Plastic collapse of the honeycomb cell wall structure: The occurrence of a regular buckling pattern prior to the peak load indicates that the honeycomb cell walls buckled elastically. Analogously to the plastic collapse of thin plates (see e.g. von Kármán *et al*, 1932) the honeycomb reached its maximum load carrying capacity as plastic deformation occurred locally in the buckled cell walls. In terms of the average macroscopic stresses σ and τ along the significant section of the butterfly specimen, this microstructural mechanism is associated with a change of the sign of the slope in stress space. We therefore define the macroscopic yield point corresponding to the plastic collapse mechanism as

$$\left.\frac{\partial \tau}{\partial \sigma}\right|_P = 0. \tag{33}$$

2. Plastic yield of the cell wall material: in the case when no folds are generated during testing, we assume that plastic yield of the cell walls lessen the increase or even limits the load carrying capacity of the honeycomb. By contrast to the plastic collapse mechanism, plastic yield of the cell walls occurs without premature microstructural stability failure. We therefore define the onset of yield as a significant change of slope of the corresponding normal-shear stress curve.

In other words, under combined compression and shear the macroscopic yield is taken as the point at which plastic folds are generated in the specimen. We have seen that this point, labeled P in the load response curves represents a distinct turning point in the transverse load vs. normal load space. However, under a combination of tension and shear both mechanisms are present: plastic folds are observed up to a loading angle of 60

degrees, indicating that plastic collapse of the microstructure is still the dominant yielding mechanism at this angle. However, for higher loading angles such as 70 or 90 degrees, the macroscopic yield is associated with conventional yield of the cell walls.

Macroscopic normal and shear stresses at the point of macroscopic yield are calculated from the measured vertical and normal forces according to Eqs. (31) and (32) respectively. The measured macroscopic yield points in terms of the macroscopic stresses along the significant section of the butterfly specimen are presented in Table 2 for different loading conditions. The macroscopic tensile yield strength for the honeycomb in the T-direction, denoted by σ^+, is found to be $\sigma^+ = 7.0 \pm 0.1 MPa$. While the macroscopic compressive yield strength in the T-direction, represented by σ^-, is equal to $\sigma^- = 3.0 \pm 0.1 MPa$. Thus, the tensile strength for this 1.8% relative density aluminum honeycomb specimen in the T-direction is about 2.3 times the compressive strength.

Loading state	Loading angle	Failure stresses: (σ, τ) (MPa)
compression	90	(-2.95,0); (-3.07,0); (-2.96,0); (-2.86,0)
tension	90	(7.08,0); (6.90,0); (7.16,0); (6.98,0)
pure shear	0	(0,0.99); (0,1.09); (0,1.08); (0,0.98); (0,1.04)
compression and shear	0	(-0.05,1.09); (-0.05,1.12); (-0.03,0.98);(-0.06,-1.05); (-0.05,-0.95); (-0.04,-0.98), (-0.01,-1.08)
compression and shear	10	(-0.13,-0.98); (-0.02,-0.95); (-0.51,-0.63); (-0.22,-0.77); (-0.23,-0.94); (-0.31,-1.00)
compression and shear	20	(-0.9,-0.84); (-0.61,-0.77); (-0.61,-0.88); (-0.9,-0.9); (-0.71,-0.71); (-0.19,-0.94); (-0.11,-0.89); (-0.19,0.99); (-0.14,-0.98)
compression and shear	30	(-1.28,-0.89); (-0.61,-0.77); (-1.41,-0.67); (-1.22,-0.82); (-1.09,-0.76); (-1.42,-0.83); (-0.89,-0.63); (-0.53,-0.87)
compression and shear	45	(-1.09,-0.95); (-1.26,-1.08); (-1.27,-1.01); (-1.29,-1.01); (-1.13,-1.00)
compression and shear	60	(-2.21,-0.69); (-1.92,-0.67); (-2.00,-0.55); (-1.62,-0.61); (-1.74,-0.47)
tension and shear	0	(0.1,1.15); (0.1,-1.06); (0.09,1.12); (0.06,1.1); (0.59,1.12); (0.25,1.07); (0.12,1.07); (0.23,1.10); (0.06,1.10)
tension and shear	10	(0.44,1.23); (0.34,1.03); (0.35,1.18); (0.08,1.09); (0.63,1.12); (0.14,-0.79)
tension and shear	20	(0.86,1.00); (0.96,1.16); (0.98,1.21); (0.89,1.23)
tension and shear	30	(1.16,1.16); (1.29,1.20); (1.32,1.31); (1.18,1.19); (1.35,1.30); (1.5,1.26)
tension and shear	45	(1.75,1.13); (2.35,1.38); (1.77,1.28); (2.45,1.38); (1.84,1.22)
tension and shear	60	(5.11,1.67); (5.06,1.58); (5.43,1.72)
tension and shear	65	(6.00,1.42); (5.91,1.43)
tension and shear	70	(6.31,0.73); (6.11,1.01); (6.07,1.05); (6.16,0.74)
tension and shear	80	(6.63,0.47); (6.53,0.31); (6.96,0.57); (6.69,0.88); (6.93,0.44)

Table 2. Macroscopic yield (failure) stresses for the hexagonal aluminum 5056-H39 honeycomb measured from butterfly specimens in the T-K-plane.

Finally, the macroscopic shear yield strength of the honeycomb in the T-K-plane, denoted by τ^0, is measured to be $\tau^0 = 1.0 \pm 0.05 MPa$.

The macroscopic normal and shear yield stresses are normalized by the compressive and shear strengths respectively and the results are plotted in Fig. 23. According to the identified microstructural mechanisms associated to macroscopic yield, two distinct regimes appear in the stress space. Thus, the yielding of a honeycomb under out-of-plane loading is best described by a multi-surface model. In other words, we assume that the elastic domain of a honeycomb is bounded by two intersecting yield surfaces. Careful analysis of the present data reveals that the phenomenological yield envelope corresponding to the plastic collapse of the honeycomb microstructure of a butterfly specimen is given by the parabolic function:

$$f^P = \left(\frac{\tau}{\tau^o}\right)^2 - \frac{\sigma}{\sigma^-} - 1 = 0 \tag{34}$$

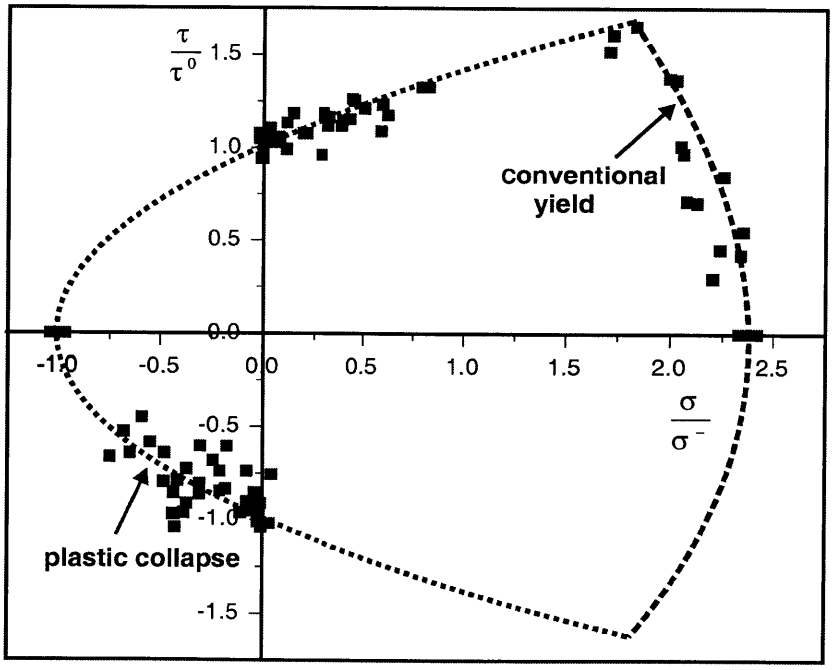

Fig. 23. Macroscopic yield envelope for honeycomb butterfly specimens under combined loading in the T-K-plane.

With respect to the second mechanism, i.e. conventional yield of the cell wall material, we propose an elliptical criterion:

$$f^{Y} = \kappa^2 \left(\frac{\tau}{\tau^o} \right)^2 + \left(\frac{\sigma}{\sigma^+} \right)^2 - 1 = 0 \tag{35}$$

The best agreement with the present data is found for $\kappa = 0.42$.

2.5 Concluding remarks

- Based on the experience of Sutcliffe and Petras (2000), Chen and Fleck (2001), and Doyoyo and Wierzbicki (2000; 2003), we use the Arcan apparatus in its clamped configuration to perform biaxial tests on aluminum honeycomb. In this setup, experimental problems associated with the intrinsic localization of deformation in cellular solids are overcome by controlling displacements and rotations at the specimen boundaries.
- Theoretical analysis reveals: the use of the Arcan apparatus in the clamped configuration requires the measurement of the 'horizontal force' in addition to the standard force measurement. Until now, researchers omitted this important measurement of the horizontal force. It is shown that the resultant error in stresses may be significant. At the same time, a procedure is suggested to correct erroneous experimental data.
- The Enhanced Arcan Apparatus (EAA) is developed incorporating an additional load cell to measure the horizontal force. Experiments on butterfly-shaped aluminum honeycomb specimens demonstrate the reliability of this new testing method.

- Under compression and shear, the macroscopic yield of the tested honeycomb is associated with plastic collapse of the cellular honeycomb microstructure. Short folds characterize the deformation pattern of the load carrying cell walls. The same mechanism is observed under a combination of shear and tensile stresses. However, at large loading angles, when tensile stresses become dominant, macroscopic yield is observed as the cell wall material yields without premature microstructural failure.

- The plastic collapse mechanism occurs over a wide range of normal and shear stresses and the corresponding macroscopic yield envelope is found to be parabolic in the shear-normal stress space. However, when the normal stresses approached the tensile strength and conventional yielding became the governing microstructural mechanism, an elliptical yield envelope was observed intersecting the parabolic surface.

Chapter 3

Determination of the crushing response of a honeycomb sandwich core using the Universal Biaxial Testing Device (UBTD)

3.1 Introduction

The Enhanced Arcan Apparatus (EAA) is suitable for testing butterfly shaped specimens. The overall stress field in butterfly-shaped specimens is heterogeneous, but locally, at the so-called 'significant section', it is well-defined and homogeneous (e.g. Arcan *et al.*, 1978; Hung and Litchie, 1999). This type of specimen allows for the determination of characteristic material properties of fiber-reinforced composites (Voloshin and Arcan, 1980) as well as metallic foams (Doyoyo and Wierzbicki, 2003). However, in the case of aluminum honeycomb, the experimentally observed mechanisms indicated that the mechanical response of a butterfly-shaped honeycomb specimen is characterized by emerging folds covering the entire specimen. Thus, we believe that the out-of-plane behavior of butterfly-shaped honeycomb specimens is not only determined by the stress state along the significant section, but also by the stress state away from the significant section. Given the overall heterogeneous stress state in butterfly-shaped specimens, it is desirable to modify the specimen such that the stress field is homogenous within the

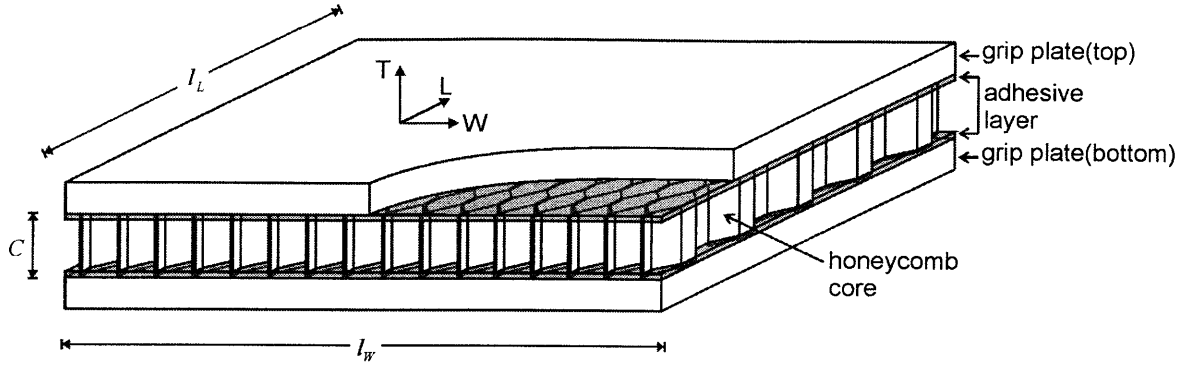

Fig. 24. Schematic of the sandwich specimen.

entire specimen. The simplest shape approximately satisfying this condition is a 'rectangular sandwich specimen' (Fig. 24) as suggested in the ASTM C-273 standard for shear testing of sandwich core materials (ASTM, 1994). Wierzbicki's (1997) experimental investigation has shown that response of sandwich specimens depends on the specimen height. With sandwich applications in mind, we limit our attention to so-called 'thin specimens'. This restriction applies to the present series of experiments and may also limit the applicability of the results of this thesis to honeycomb cores of sandwich structures.

In this chapter, we develop and use the Universal Biaxial Testing Device (UBTD) to perform tests on honeycomb sandwich specimens. The design of the UBTD is much stiffer than the one of the EAA. The maximum allowable transverse force is about 20,000N as compared to about 500N for the EAA. Also the maximum stroke was increased from $\pm 2mm$ to $\pm 10mm$ and an LVDT was built-in for standard displacement measurement. Furthermore, the new design allows for the variable specimen thicknesses, i.e. the EAA restriction on the specimen thickness (8mm, equivalent to one cell layer) no longer applies. Similarly to the experiments performed with the EAA, we conduct fully displacement-controlled combined compression and shear tests over a range of biaxial

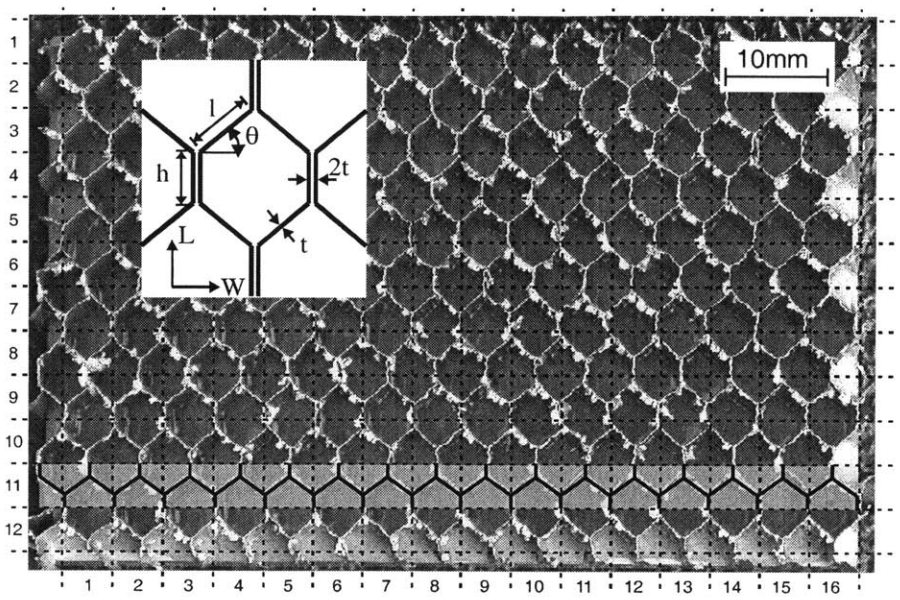

Fig. 25 Top view of the sandwich specimen before being bonded to the second grip plate. The insert shows a schematic of a single honeycomb cell. The shaded rectangle highlights the nature of the microstructure.

loading angles. We evaluate the macroscopic stress-strain curves and discuss the experimental observations. In addition to initial yield, we draw our attention to the post-yield behavior of metallic honeycombs.

3.2 Material and specimen

The material tested is the same as for the previous experiments using the EAA: Aluminum 5056-H39 honeycomb, single cell wall thickness $t=33\mu m$, cell wall widths $h=2.4mm$ and $l=3.1mm$, expansion angle $\theta = 40^o$, initial density $\rho_0 = 46.5kg/m^3$ (see insert in Fig. 25).

We perform combined compression and shear tests on sandwich specimens. In this configuration, a honeycomb core of constant height is sandwiched between two

faceplates (Fig. 24). The faceplates serve as grips to mount the specimen onto the testing device. An epoxy adhesive (Lord 310A/B) is used to bond the honeycomb onto roughened aluminum grip plates. The specimen width of $l_W = 80mm$ is predefined by the size of the biaxial testing device. This corresponds to about 16 honeycomb cells along the W-direction. The width along the ribbon direction, $l_L = 52.8mm$, is chosen according to the recommendation of ASTM C273. Two opposite aspects are taken into account for the choice of the specimen height: As a result of the bonding technique employed, the cell walls are embedded into an adhesive layer; thus, to minimize the influence of the adhesive layer on the test results, the specimen height should be large as compared to the up to $1mm$ thick bond line. On the other hand, under shear loading, a large width to height ratio l_W / C (i.e. a small specimen height) is desirable to guarantee a homogeneous stress field along the W-direction. Here, a height of $C=15mm$ is chosen for the sandwich specimen, which corresponds to an aspect ratio l_W / C of about 5.

Figure 26 shows the shear stress-strain curves for shear loading for different specimen geometries as obtained from virtual experiments (details of the underlying finite element model for the honeycomb microstructure are given in Chapter 4). Both sandwich specimens are $C=15mm$ high, but their widths along the ribbon direction are chosen such that their aspect ratios correspond to the dimensions of the UBTD-specimen ($l_W / C = 5$) and the ASTM C-273 specimen ($l_W / C = 12$), respectively. Furthermore, a simulation of a butterfly specimen under pure shear loading in the T-W-plane is performed. Clearly, the response of the butterfly specimen is quantitatively different, while the curve for the UBTD-specimen is close to the one for the ASTM-approved shear specimen, strongly supporting the choice of the UBTD-specimen geometry and dimensions. According to the results of Wierzbicki (1997), the UBTD-specimen may be typified as 'thin specimen'. Wierzbicki (1997) showed that the shear deformation mode of honeycomb specimens depends on the specimen height: thin specimens showed a uniform microstructural deformation pattern, while higher honeycomb specimens develop local patterns of non-uniform compression. This deformation mode for high honeycomb blocks is schematically shown in Fig. 27; Wierzbicki (1997) also showed tests on high specimens that developed diagonal shear bands.

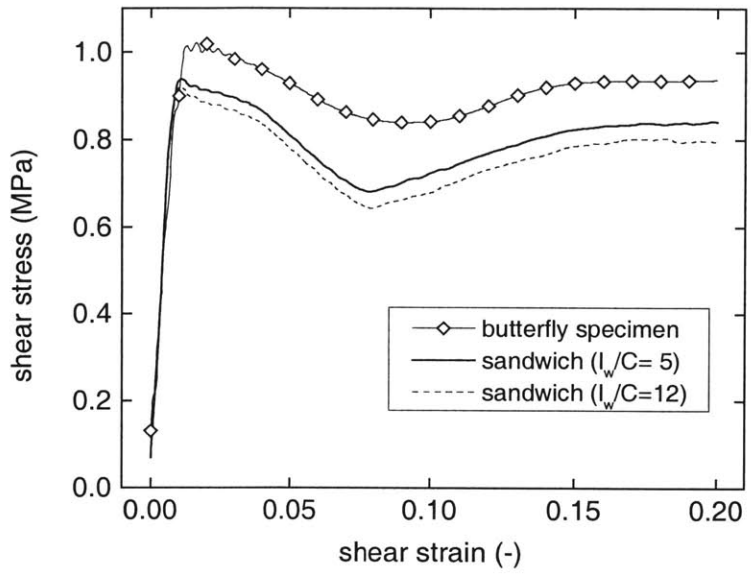

Fig. 26. Shear stress-strain curves for different specimen aspect ratios.

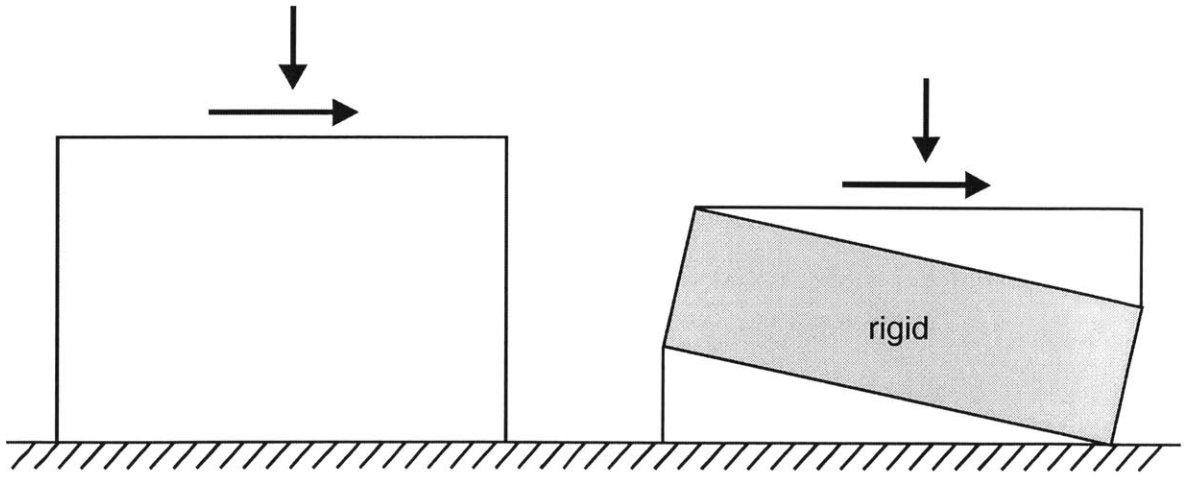

Fig. 27. Sketch of the deformation mode assumed in Wierzbicki's model (1997) for thick honeycomb block specimens.

3.3 Experimental procedure

The Universal Biaxial Testing Device (UBTD) is used to apply combinations of large compressive and shear displacements to the boundaries of a honeycomb specimen. All tests are performed under quasi-static loading conditions.

3.3.1 Mechanical details

A schematic of the UBTD is given in Fig. 28. The specimen is placed between the fixed and movable parts of the apparatus. The movable part is allowed to slide along the vertical direction (y-axis) only. All other degrees of freedom of the movable part including rotations are restricted. The inclination of the specimen with respect to the vertical axis determines the combination of applied shear and normal displacements. This inclination is measured by the biaxial loading angle α (Fig. 28). The corresponding

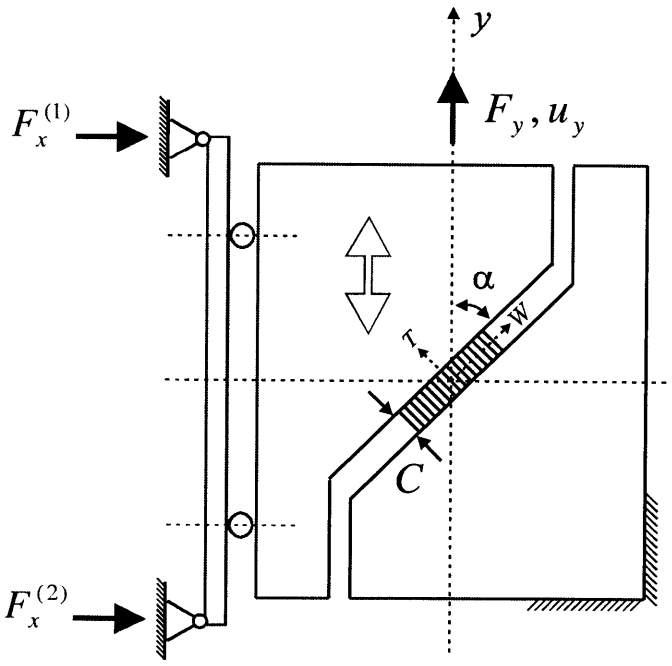

Fig. 28. Schematic of the Universal Biaxial Testing Device (UBTD).

normal and shear displacements are

$$u_T = u_y \sin\alpha \tag{36}$$

$$u_W = u_y \cos\alpha \tag{37}$$

where u_y denotes the vertical displacement. In other words, the biaxial displacement field on the top boundary of the specimen is uniquely characterized by the biaxial loading angle and the resultant displacement. Note that the biaxial testing angle is fixed throughout testing, whereas the resultant displacement is prescribed, which limits the experimental capabilities to linear loading paths in terms of displacements. The macroscopic strains are directly obtained by normalizing the displacement components at the specimen boundaries (u_T, u_W) with respect to the specimen height C. The normal strain in the T-direction, ε, and the engineering shear distorsion in the T-W-plane, γ, read

$$\varepsilon = \frac{u_T}{C} \tag{38}$$

and

$$\gamma = \frac{u_W}{C} \tag{39}$$

The UBTD monitors three force components throughout testing: the horizontal forces $F_x^{(1)}$ and $F_x^{(2)}$, and the vertical force F_y (Fig. 28). From the free body diagrams for individual components of the UBTD, we find the normal and shear force components, F_T and F_W, acting on the sandwich specimen:

$$F_T = F_y \sin\alpha - \left(F_x^{(1)} + F_x^{(2)}\right)\cos\alpha \tag{40}$$

$$F_W = F_y \cos\alpha + \left(F_x^{(1)} + F_x^{(2)}\right)\sin\alpha \tag{41}$$

The engineering stresses are calculated by dividing the force components by the cross-sectional area $A_0 = l_W l_L$ of the sandwich specimen. We have the normal stress

$$\sigma = \frac{F_T}{A_0} \tag{42}$$

and the shear stress

$$\tau = \frac{F_W}{A_0} \tag{43}$$

3.3.2 Technical details

A picture of the UBTD is shown in Fig. 29. Throughout the following description, we denote the part numbers according to the part labels in Fig. 29 in parentheses. The movable part of the device (1 to 5) slides vertically on four ball bearings (5) along two fixed guidance rods (8). Parts (7) to (13) belong to the fixed portion of the device. The bottom plate (12) is rigidly connected to the table of a universal testing machine (MTS, Model G45, Eden-Prarie, MN). A universal joint (2) connects the movable grip (1) to the screw-driven crosshead of the universal testing machine. A set of removable clamps (4, 10) positioned the specimen in the center between the movable and fixed part of the device. Four screws on either side provided sufficient clamping pressure. The inclination of the specimen (6) is set prior to testing by rotating the specimen holders (3, 9). Tests can be performed at any biaxial loading angle between 0 and 90 degrees, with an increment of one degree.

A linear variable differential transformer (13) built into the UBTD measures the relative displacement between the movable and fixed portion of the device. This measurement provides the resultant displacement acting on the specimen, u_y, assuming the UBTD to be rigid as compared to the honeycomb specimen. Displacements ranging from $-10mm$ to $+10mm$ are allowed by the current design. The vertical force F_y is recorded by the standard load cell (14) of the universal testing machine (200kN MTS

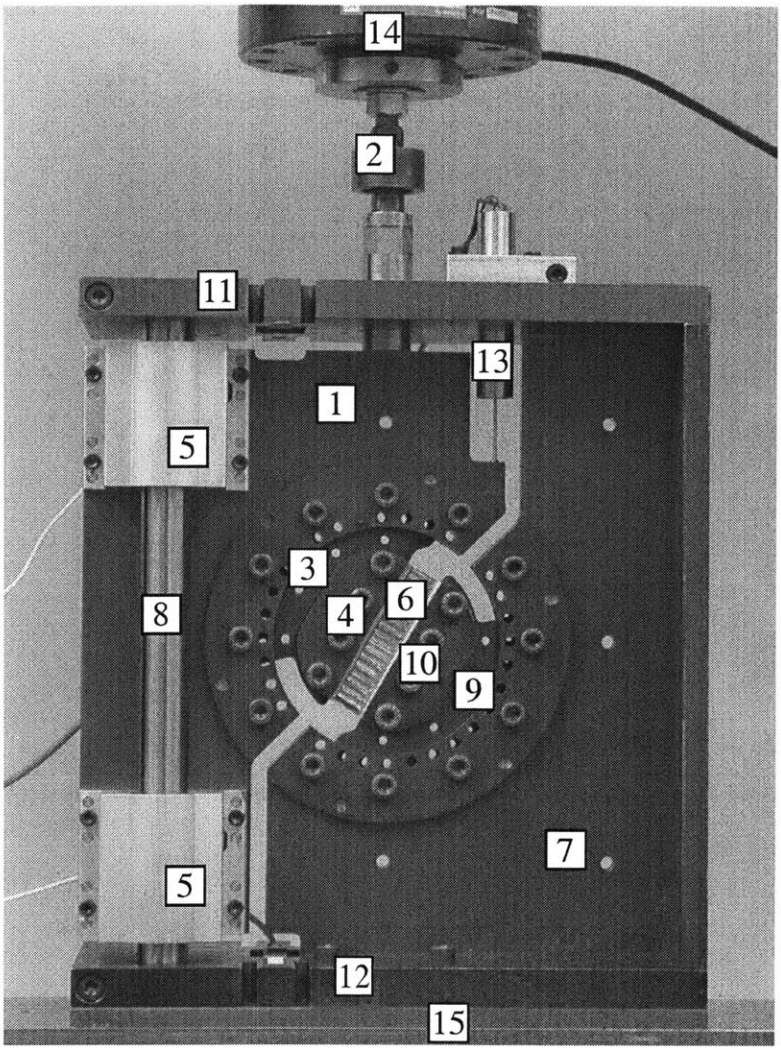

Fig. 29. Photograph of the UBTD (front view): 1-movable grip plate, 2-universal joint, 3-rotating specimen holder (top), 4-positioning clamp (top), 5-roller bearing, 6-sandwich specimen, 7-fixed grip plate, 8-vertial guidance rod, 9-rotating specimen holder (bottom), 10-positioning clamp (bottom), 11-top plate, 12-bottom plate, 13-LVDT, 14-vertical load cell (movable crosshead), 15-table of fixed cross-head.

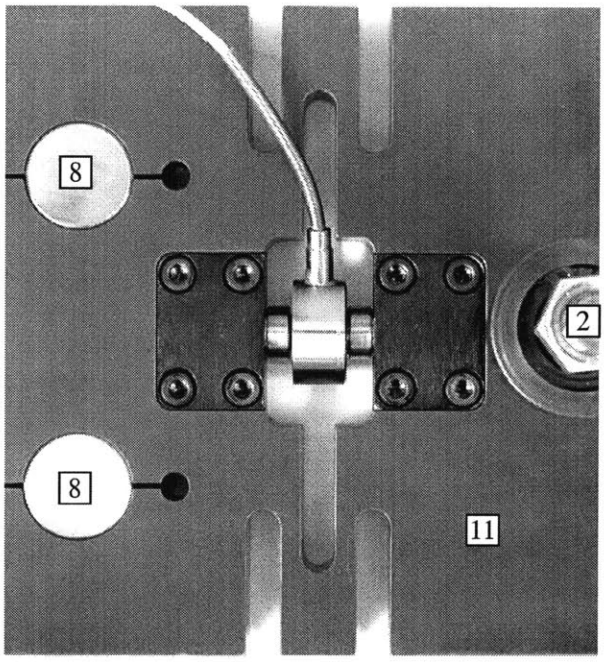

Fig. 30. Detail of how the horizontal load cell is integrated into the top plate (labels are consistent with the captions of Fig. 29).

load cell). The horizontal forces are measured by two DC-DC load cells (Sensotec, Model 31) integrated into the top (11) and bottom plates (12) of the fixed portion of the UBTD. Fig. 30 shows details of the integrated horizontal load cell. The load cells have been calibrated as built-in for a total horizontal load of up to 3kN. The accuracy of the horizontal load measurement at room temperature is $\pm 2\%$.

3.3.3 Sample tests

We present the results from tests at 60° to illustrate the testing procedure. Recordings of the vertical force and the two horizontal forces are shown in Figs. 31 and 32. All force readings are set to zero before the sandwich specimen is placed between the adjusted

rotating specimen holders. Compressive stresses arise (predominantly) along the T-direction as the clamping pressure is applied to the short sides of the specimen grip plates. This may be explained by constrained Poisson's deformation in the grip plates. After clamping, the crosshead was adjusted such that the vertical load was zero (Fig. 31). However, from the nature of the testing method, an initial offset in the horizontal force measurement is inevitable. For the present 60° tests, the horizontal preload load ranges from 170 to 300N (see the encircled region in Fig. 32). All tests are performed at a constant crosshead velocity of 1mm/min. Pictures are taken at different stages during testing. The tests were paused for image acquisition, which generated small relaxation drops in the load (Fig. 31). Furthermore, two unloading/reloading cycles are typically performed at large strains.

Comparison of the horizontal force measurements reveals that, after the vertical load is applied, a difference develops between the two horizontal force components. Under compressive loading, the force acting on the bottom load cell is higher than the force acting on the top load cell. This observation is explained as follows: Suppose that the resultant reaction force in the deforming specimen acts at the geometric center of the specimen. At the same time, note that, throughout testing, the geometric center of the specimen moves with respect to the mechanical center of the testing device. The latter is defined by the intersection of the testing axis (y-axis) with the centerline between the horizontal load cells (dashed horizontal line in Fig. 28). Thus, due to this motion, an eccentricity of the resultant force with respect to the load cells emerges. As a result, a torsion moment acts on the horizontal bearings, which is counterbalanced by a pair of horizontal forces, reducing the load on the top load cell and increasing the load on the bottom load cell. Also heterogeneity of deformation inside the specimen is expected to contribute to the torsion moment. However, this effect has no influence on the total horizontal force $F_x^{(1)} + F_x^{(2)}$, which appears in the expressions for the average shear and normal stresses (see Eqs. (40) and (41)).

It must be noted that the present experiments are very repeatable - irrespective of the biaxial loading angle. As exemplary shown by the two representative tests in Fig. 31 and Fig. 32, only little scatter is observed in the force-displacement curves. Characteristic

features of those curves including force extrema or local changes in slope are almost identical for different specimens. This consistency emphasizes the overall reliability of the present experimental procedure including specimen dimensions and preparation.

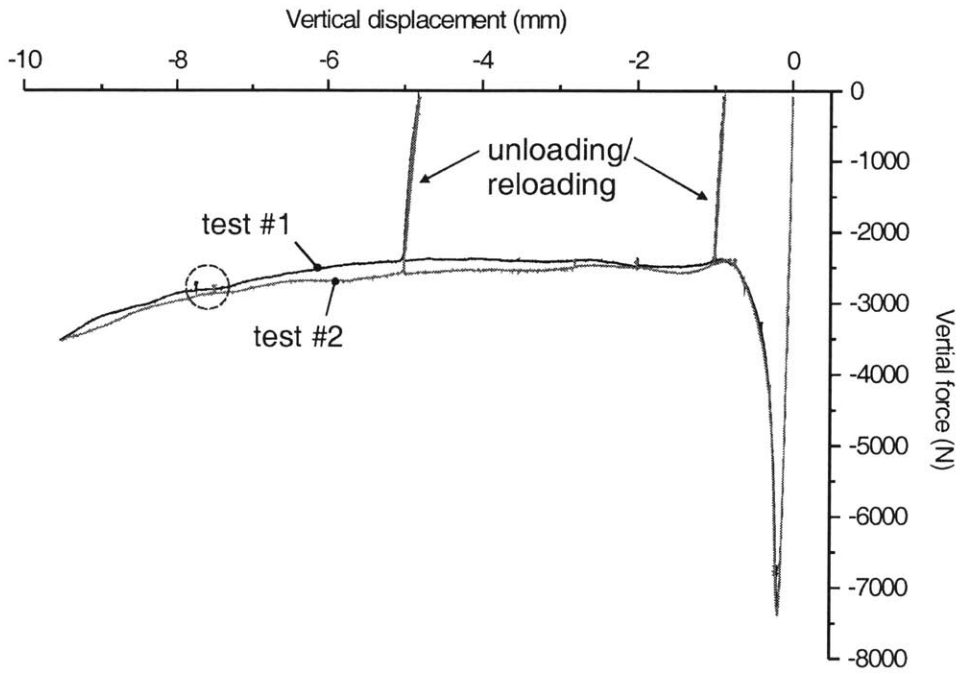

Fig. 31. Vertical force (MTS load cell) vs. vertical displacement (LVDT) for tests under 60 degrees loading. The encircled region highlights an example for minor drops in the load curve while the test was paused for image acquisition.

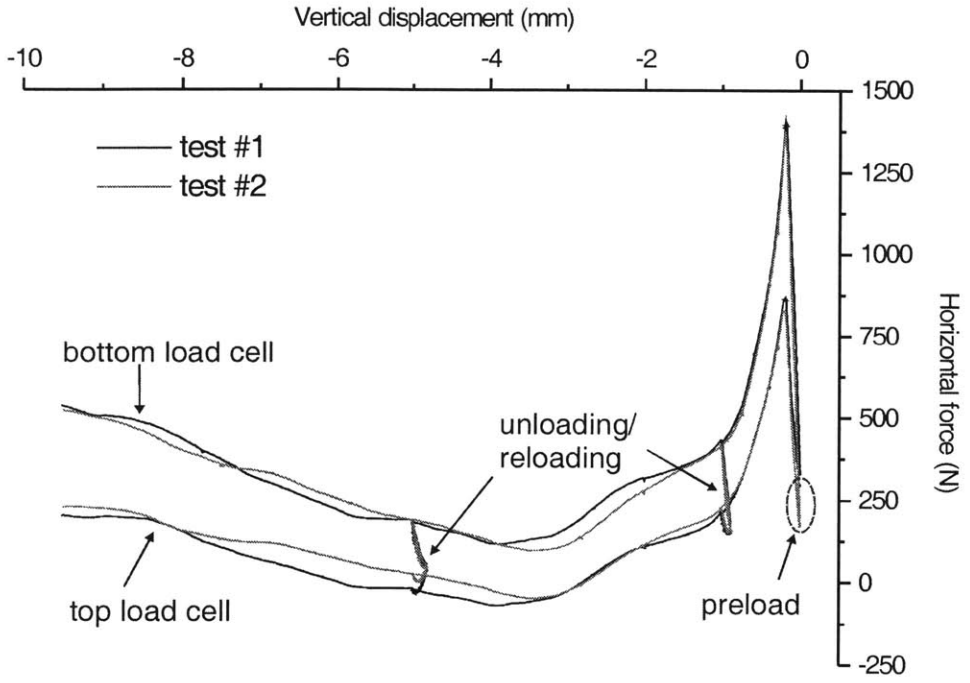

Fig. 32. Plots of the horizontal forces measured during tests under 60° loading. Note the two groups of curves: The upper and lower groups represent the recording of the horizontal force in the bottom plate and top plate, respectively.

3.4 Experimental observations

Tests are performed on the honeycomb with the UBTD at 0, 10, 30, 40, 50, 60, 70, 80 and 90 degrees loading. Large displacements are applied in the negative y-direction. Recall that from the nature of the experimental setup, strain paths remain constant throughout each test. In other words, the normal strain is proportional to the shear strain, and the proportionality factor is determined by the biaxial loading angle from the relation $\varepsilon = \gamma \tan\alpha$. All macroscopic strain paths are in the quadrant of negative normal strains and negative shear strains. Consequently, all elastic stress states are in the compression-shear quadrant of the stress space. However, under large (compressive) strains, tensile stresses develop for small loading angles. The generation of tensile stresses at small testing angles may be explained as follows. Consider the total stretch $\chi = \sqrt{(1+\varepsilon)^2 + \gamma^2}$ that expresses the ratio of current to initial length of a fiber initially aligned with the T-direction. We anticipate that tensile stresses occur if $\chi > 1$, and analogously, compressive stresses occur if $\chi < 1$. The transition curve $\chi = 1$ along with the various strain paths is plotted in Fig. 33. According to this consideration, tests at loading angles above 45° should only generate compressive stresses whereas tests at lower loading angles should exhibit compressive stresses first before tensile stresses build up. We therefore split our upcoming discussion into two parts: The first part focuses on the observations made for tests at large biaxial loading angles where the stress state is exclusively in the compression-shear quadrant, while the second part describes the observations for tests at small loading angles where tensile stresses emerge at large displacements.

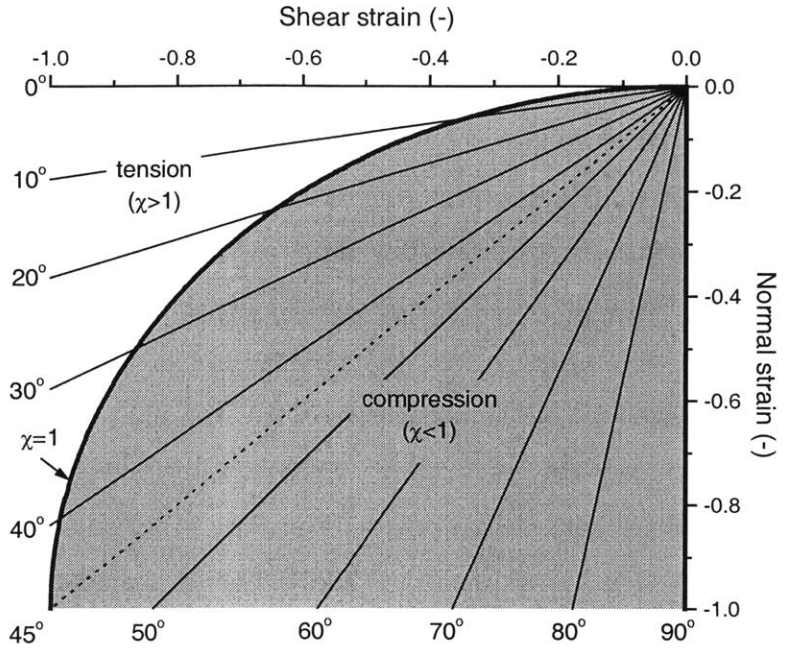

Fig. 33. Linear strain paths for various biaxial loading angles. The transition curve labeled $\chi = 1$ cuts the domain into the expected compression and tension regimes.

3.4.1 Compression-dominated crushing

Figures 34 to 36 show the mechanical response curves for large biaxial loading angles. We discuss the results from tests under 60° and 80° loading as examples of crushing under compression and shear stresses. A sequence of photographs taken during both tests is shown in Figs.37 and 38. In the mechanical response curves, the corresponding picture points are denoted by symbols labeled by small roman letters. The undeformed specimen configuration is denoted as *a*, while successive deforming configurations are denoted as *b*, *c*, *d*, *e*, and *f* respectively.

First, consider the normal stress-strain curves in Fig. 34. Initially, the compressive stress rises linearly with strain (labeled as *elastic I*), until the response becomes slightly non-linear as it can be seen from a continuous decrease in slope in the regime labeled as *elastic II*. Pictures taken at point *b* show a pattern of shallow buckles that developed in the elastic II regime (Fig. 37(b), Fig. 38(b)). As the peak stress is reached (labeled as *nucleation*), the compressive stress steadily drops with strain. This phase denoted as *softening* is associated with the stable plastic collapse of the cellular microstructure under compressive loading. We emphasize that plastic collapse is a stable event. Mechanically, this stability is manifested by the small scatter on the measured nucleation stresses and the maintaining of a constant stress level when the tests were paused for image acquisition in the softening phase (see points '*c*' in Fig. 34). One can observe from the acquired photographs (Fig. 37(d) and Fig. 38(d)) that a characteristic collapse band becomes visible in the honeycomb microstructure throughout the softening phase. Consequently, we refer to the peak stress as a nucleation stress for collapse bands in the mircostructure. For loading angles 60°, 70°, 80° and 90°, the compressive stress drops to a local minimum at $\varepsilon^* = -0.05 \pm .005$ and $\sigma^* = -0.6 \pm .05 MPa$. Then the compressive stress remains either constant (for 60°) or increases to attain a constant plateau level, which is a property of the *crushing regime*. The plateau level is reached at a normal strain of approximately $2\varepsilon^*$.

The shear stress-strain curves show similar characteristics (Fig. 35). Both the elastic I and elastic II regimes are identifiable before the peak shear stress is reached. Furthermore, all the shear stress-strain curves exhibit significant softening between the nucleation point and the local minimum before a stable crushing regime is reached at a more or less constant stress level. However, in contrast to the nature of the compressive stress-strain curves, the minimum shear stress reached at the end of the softening regime varies significantly with the loading angle.

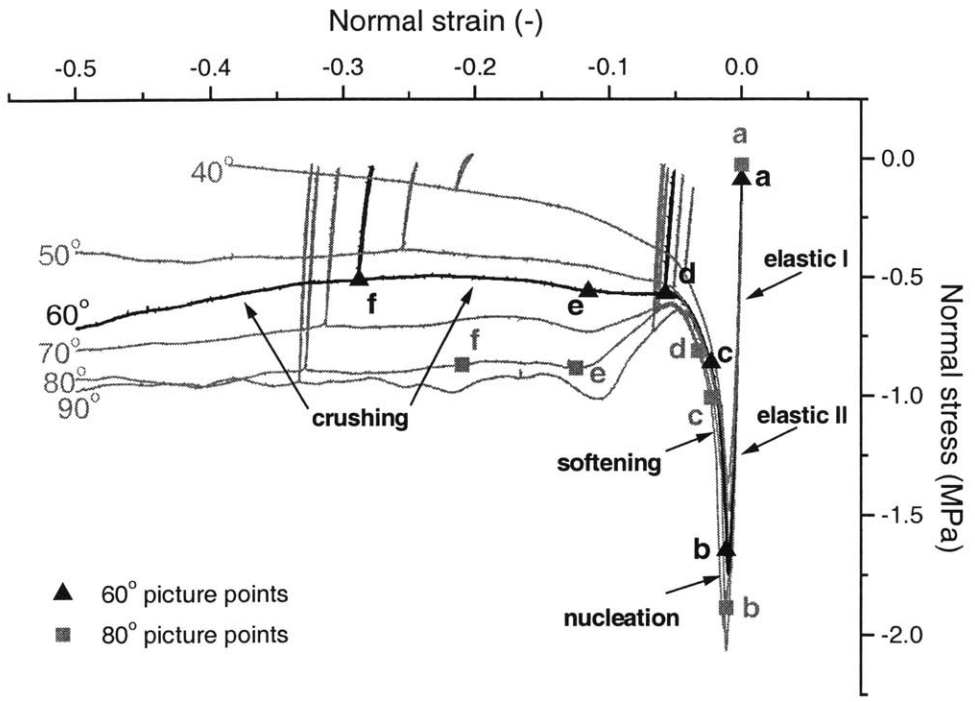

Fig. 34. Normal stress-strain curve for large biaxial loading angles. The corresponding pictures for 60° and 80° are shown in Fig. 37 and Fig. 38, respectively.

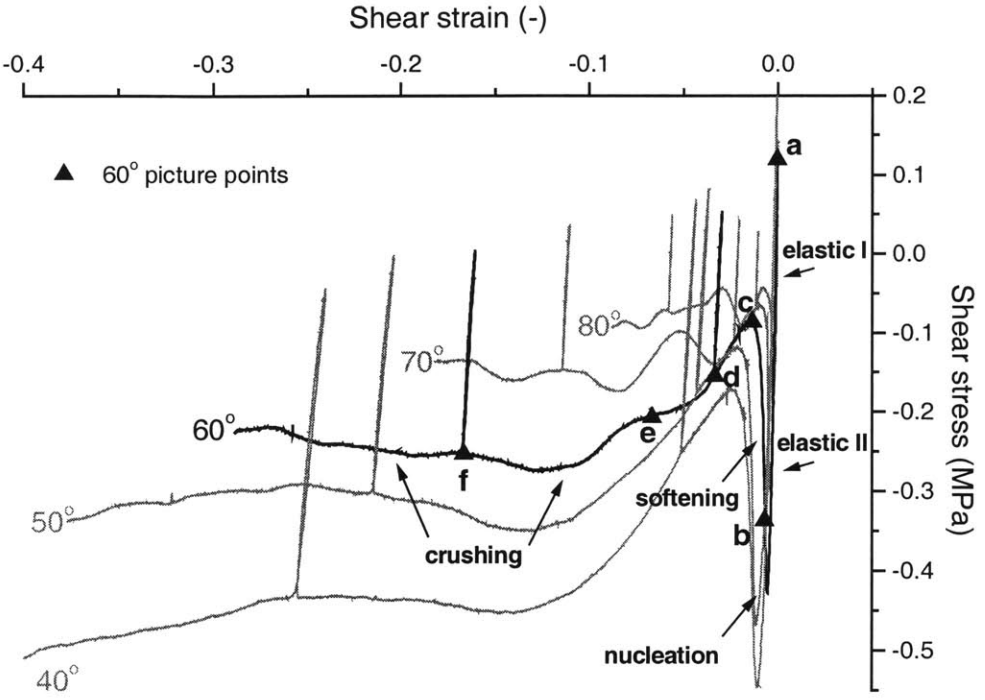

Fig. 35. Shear stress-strain curve for large biaxial loading angles. The corresponding pictures for 60º are shown in Fig. 37.

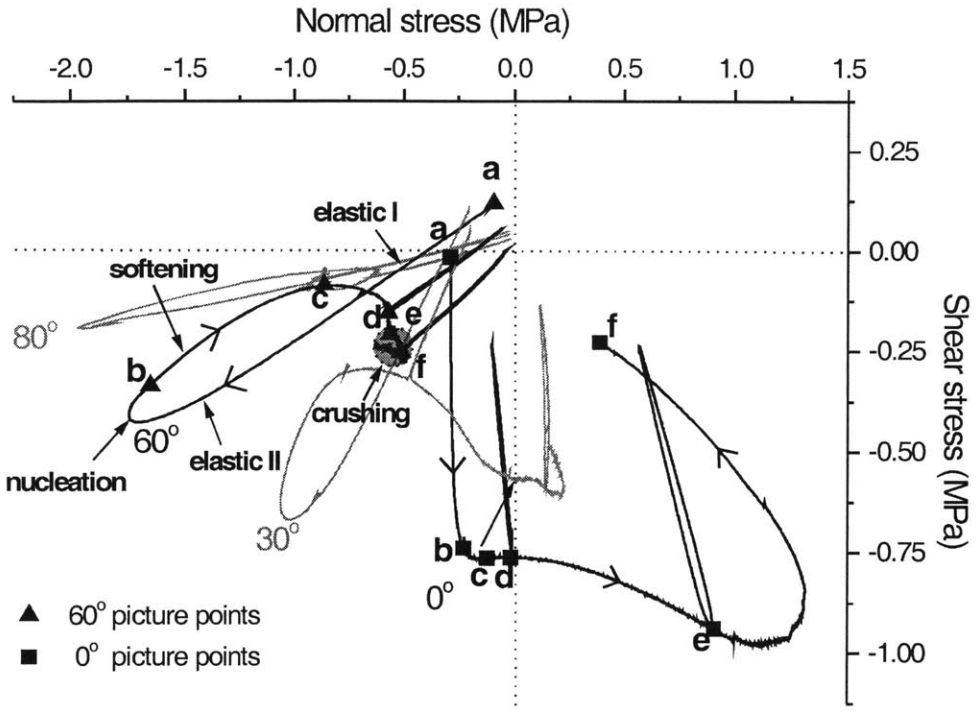

Fig. 36. Shear stress vs. normal stress curve for selected large (60°, 80°) and low (0°, 30°) biaxial loading angles.

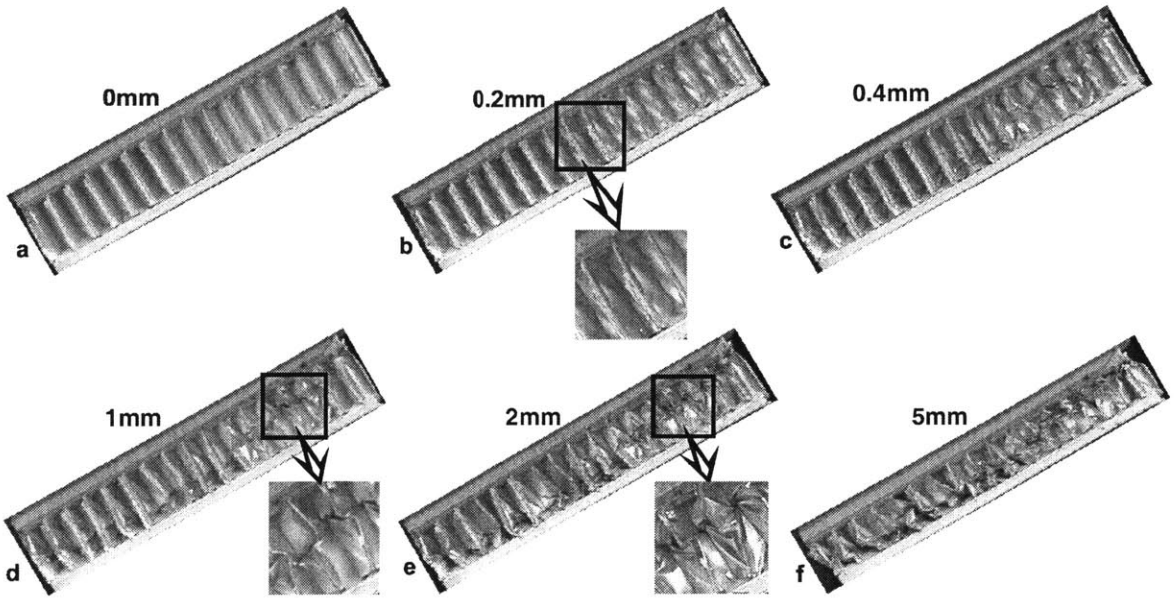

Fig. 37. A sequence of photographs of hexagonal aluminum honeycomb during biaxial loading at 60° angle at different resultant displacements. Note the development of collapse bands into plastic folds under load. The measurements next to each figure represent the magnitudes of the resultant displacement at each picture point.

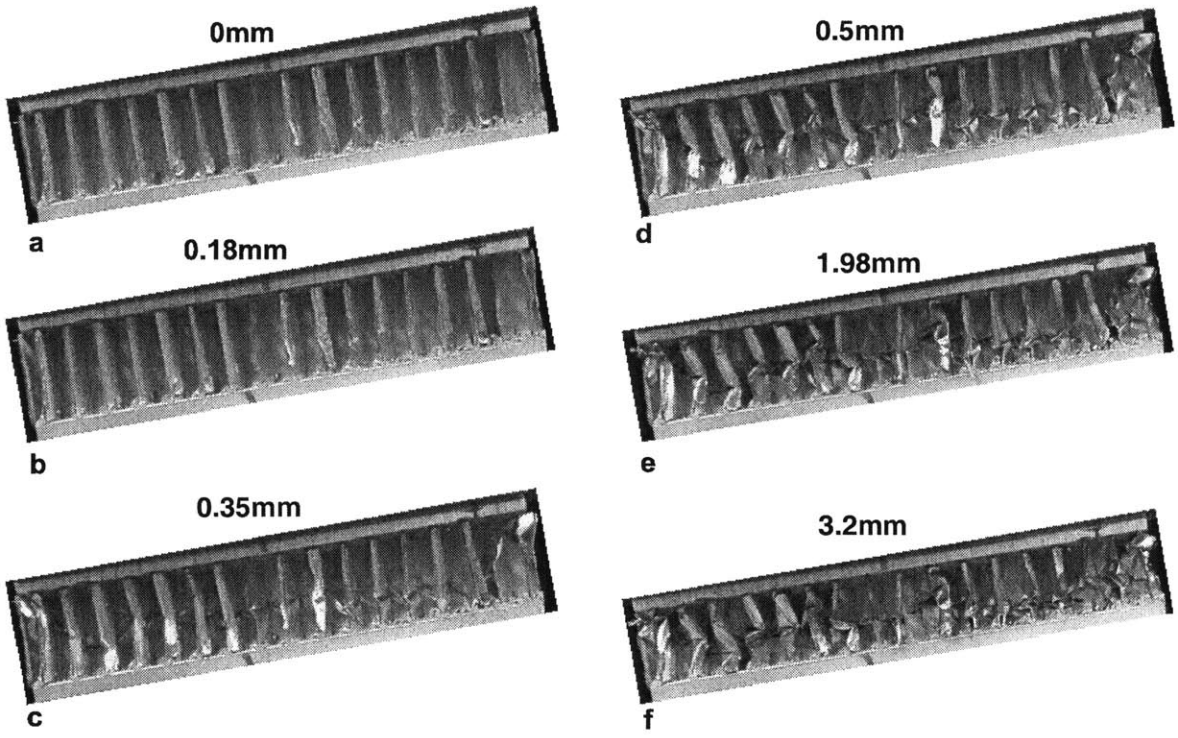

Fig. 38. A sequence of photographs of hexagonal aluminum honeycomb during biaxial loading at 80° angle at different resultant displacements. Note the development of collapse bands into plastic folds under load. The measurements next to each figure represent the magnitudes of the resultant displacement at each picture point.

Figure 36 shows the loading paths in the normal and shear stress space. Consider the plots for 60° and 80° that describe the mechanical response at large loading angles. The sharp turning point in Fig. 36 shows that both the compressive and shear stresses decease almost simultaneously. To be exact, note that the loop turns clockwise, which implies that the shear stress decreases before the compressive stress reaches its maximum magnitude. The same conclusion is drawn for the next turning point: the shear stress reaches its minimum (point '*c*') ahead of the compressive stress (point '*d*'). The shaded circle at the end of the 60° curve in Fig. 36 highlights the crushing regime. Specifically, the center of the shaded circle corresponds to the mean crushing stresses whereas the diameter can be interpreted as the maximum amplitude of fluctuations in stress relative to the mean value in the crushing regime.

3.4.2 Tension-dominated crushing

The mechanical response curves for low biaxial loading angles (0°, 10° and 30°) are shown in Figs. 39 and 40. The normal stress-strain curve (Fig. 40) clearly shows that the normal stress changes from compression to tension at large strains. This compressive-to-tensile stress transition occurs right from the beginning of the test under 0° loading (note that point '*b*' lies above point '*a*' in Fig. 40). For 10° and 30° loading, the compressive stress initially increases to a peak value and then decreases with strain as the transition to tensile stressing takes place at larger strains. The increase of the compressive stress to a peak value is analogous to the mechanical response at large loading angles. However, the subsequent softening phase is not bounded by some local minimum because the compressive stress continues to decrease until the normal stress becomes tensile. Thus, the normal stress-strain curves cross the abscissa axis denoting that the tensile stress is generated during crushing at small loading angles.

Now consider the shear stress-strain curves for small testing angles (Fig. 39). Again, we distinguish between the elastic I and elastic II regimes as the initial response becomes nonlinear. In contrast to all the other tests, the shear stress-strain curve for 0° loading does

not exhibit a softening regime, but instead, it remains constant first and then increases monotonically until fracture of the cell walls limits the load carrying capacity of the specimen. At point '*b*' shear buckles have formed in the microstructure (Fig. 41(b)). However, for a total stretch $\chi > 1$, the cell walls aligned in the L-direction are stretched rather than folded, thereby providing a significant contribution to the shear strength of the microstructure. Fracture of the cell walls occurs in the vicinity of the bond line between the specimen and the grip (see ellipse in Fig. 41(f)).

The shear stress-strain curve under 30° loading is similar to the response for large loading angles (Fig. 39). A pronounced peak stress is observed before a collapse band forms in the softening regime (Fig. 42(c)) and the shear stress level remains approximately constant in the crushing regime (Fig. 39). The shear response to 10° loading includes combined features of the responses at small and large loading angles: the shear stress curve shows a peak value and a softening phase similar to large angle testing, but it gradually increases without ever reaching a plateau value until fracture occurs just like during the 0° testing (Fig. 39).

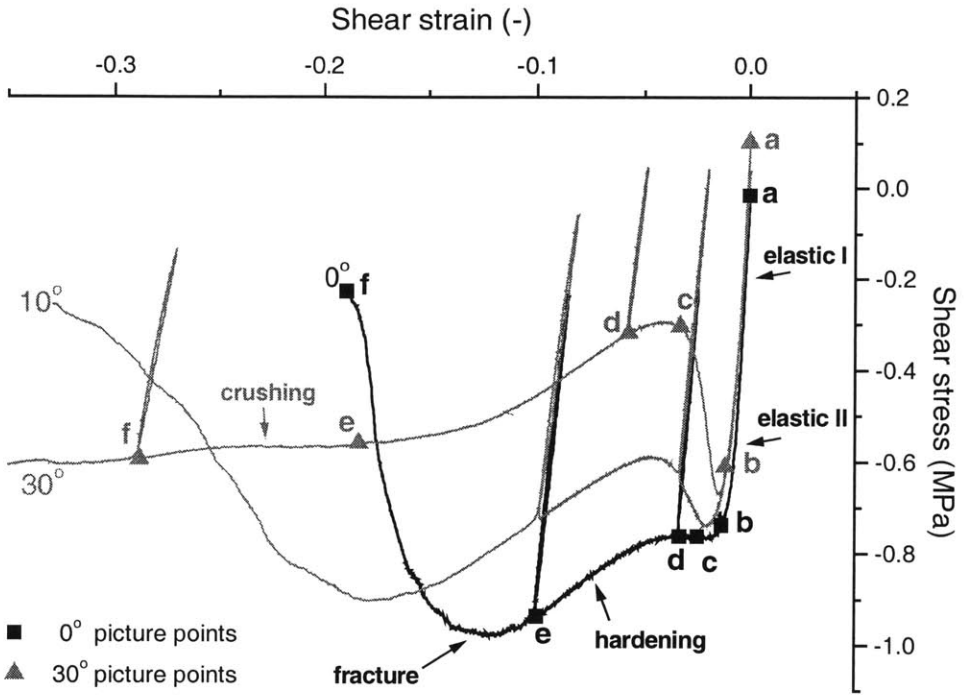

Fig. 39. Shear stress-strain curve for low biaxial loading angles. The corresponding pictures for 0° and 30° are shown in Figs. 41 and 42, respectively.

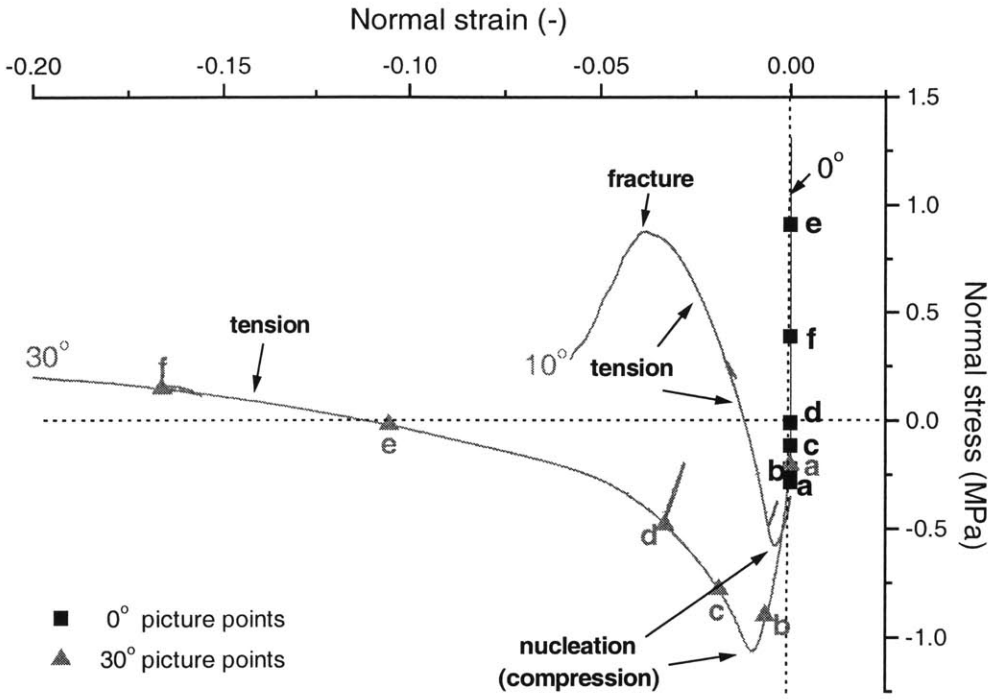

Fig. 40. Normal stress-strain curve for low biaxial loading angles. Note that all data points for 0° lie on the ordinate axis. The corresponding pictures for 0° and 30° are shown in Figs. 41 and 42, respectively.

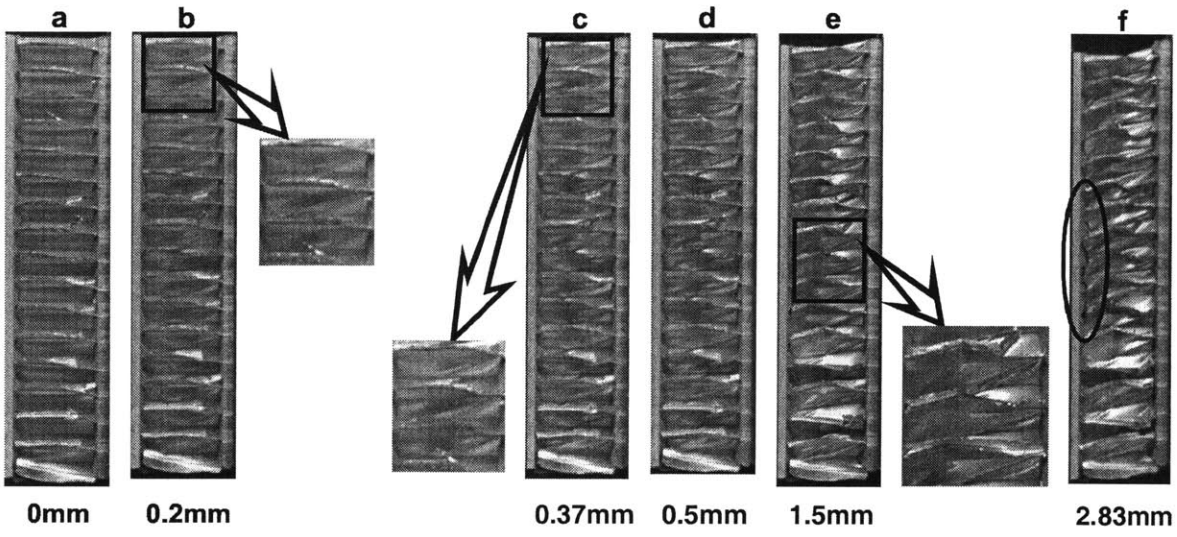

Fig. 41. A sequence of photographs of hexagonal aluminum honeycomb during biaxial loading at 0° angle at different resultant displacements. The measurements next to each figure represent the magnitudes of the resultant displacement at each picture point.

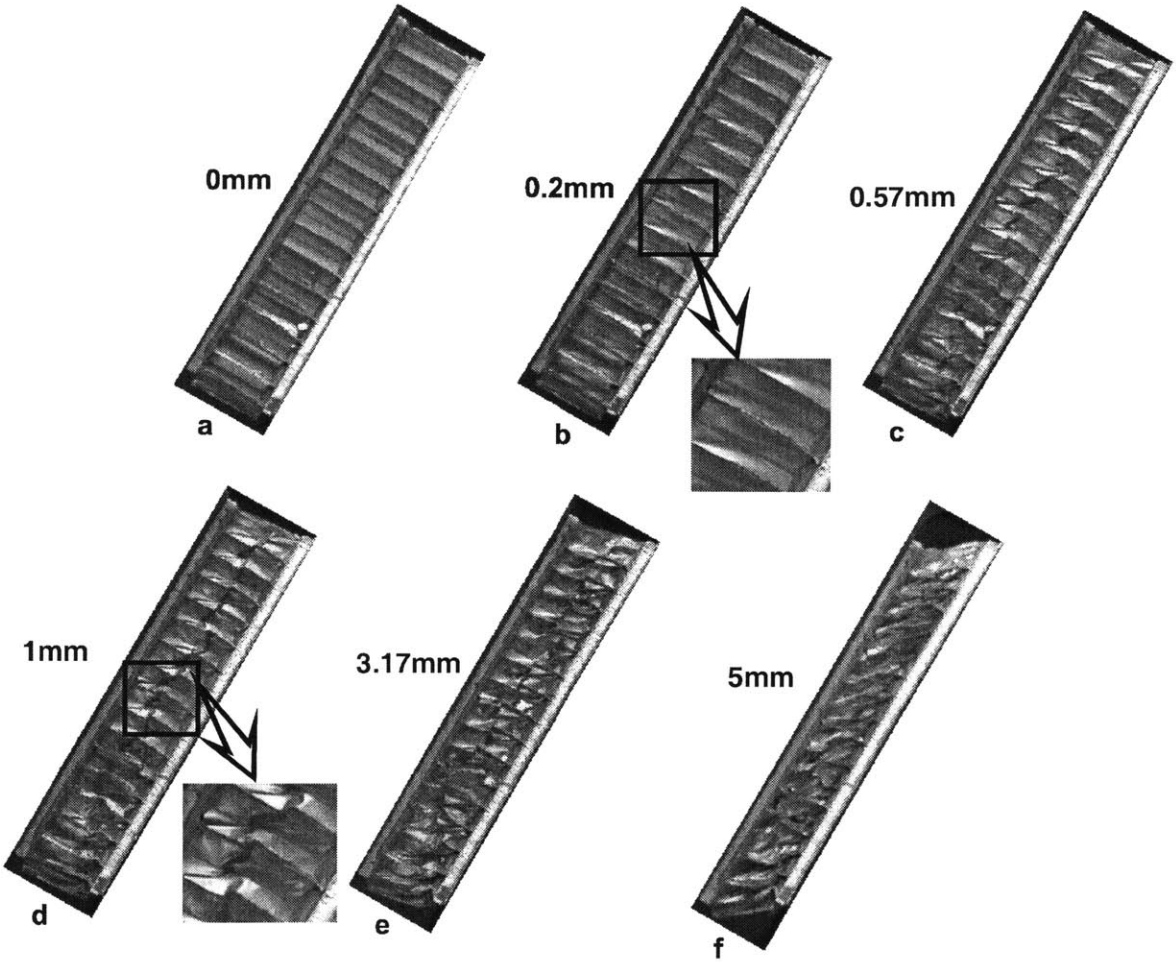

Fig. 42. A sequence of photographs of hexagonal aluminum honeycomb during biaxial loading at 30° angle at different resultant displacements. The measurements next to each figure represent the magnitudes of the resultant displacement at each picture point.

3.5 Phenomenology

The focus in this section is on the phenomenological analysis of compression-dominated crushing. This choice is made with practical applications in mind: for example, one would expect the honeycomb core in a sandwich panel to experience largely a combination of compressive and shear stresses rather than that of tensile and shear stresses. The initial yield envelope defining the onset of plastic collapse in terms of macroscopic stresses is presented. To describe the mechanical response in the crushing regime, we introduce a crushing envelope along with a flow rule.

Honeycomb elasticity as well as the transition from initial collapse to the crushing regime (that is, softening) are not addressed from a phenomenological point of view. We refer to the textbook by Gibson and Ashby (1997) for a description of orthotropic elasticity of the statistically homogeneous honeycomb microstructure. Under large deformations however, the elastic moduli evolve and most importantly, the elastic material behavior changes from transversely-orthotropic to fully-anisotropic. In other words, coupling effects between elastic shear strains and normal stresses and vice versa come into play and require special attention. At the same time, most engineering applications of honeycomb either exploit its orthotropic elastic behavior or its crushing behavior, where elastic strains are small as compared to the total strains and are thus negligible. The later argument also partially justifies why the phenomenological description below does not include the transition from the nucleation envelope to the crushing envelope. The other argument for omitting a discussion of this transition phase is the lack of experimental evidence.

3.5.1 Initial yield envelope

We ignore irreversible deformation in the honeycomb microstructure prior to collapse and define the initial yield envelope by the onset of plastic collapse of the honeycomb microstructure. The corresponding collapse stresses are defined by the initial peak

stresses of the macroscopic stress-strain curves. A plot of the data points found from the present experiments is shown in Fig. 43. It appears that an elliptical yield envelope provides the best description for the onset of plastic collapse:

$$f_0(\sigma,\tau)=\left(\frac{\sigma}{\sigma_0}\right)^2+\left(\frac{\tau}{\tau_0}\right)^2-1=0 \tag{44}$$

From a fit of Eq. (44) to the data, we find the yield stress under uniaxial compression $\sigma_0=-2.08MPa$ and the shear yield stress under pure shear $\tau_0=0.76MPa$. It follows from the morphological orthotropy of the undeformed microstructure that the initial yield envelope must be symmetric with respect to shear. However, Eq. (44) is only valid for compressive stresses ($\sigma\leq 0$). Under tensile stresses, the microstructural deformation mode is expected to change, which might require a different phenomenological description on the macroscopic level.

A direct comparison of the results from the experiments using sandwich specimens (this Chapter) with those using butterfly-shaped specimens (Chapter 2) cannot be made. The latter considered combined loading in the T-K-plane (see Fig. 1), while the present sandwich tests characterize the response to combined loading in the T-W-plane. The tests on butterfly-shaped specimens suggested a parabolic yield surface by contrast to the elliptic surface that has been found from the present experiments on sandwich specimens.

3.5.2 Crushing behavior

In our discussion of the experimental observations, the crushing phase is characterized by more or less constant normal and shear stress levels. We define the plateau stresses $\overline{\sigma}$ and $\overline{\tau}$ as the mean stress level in crushing regime:

$$\overline{\sigma}=\frac{1}{\varepsilon_{\max}-2\varepsilon^*}\int_{2\varepsilon^*}^{\varepsilon_{\max}}\sigma\mathrm{d}\varepsilon \tag{45}$$

and

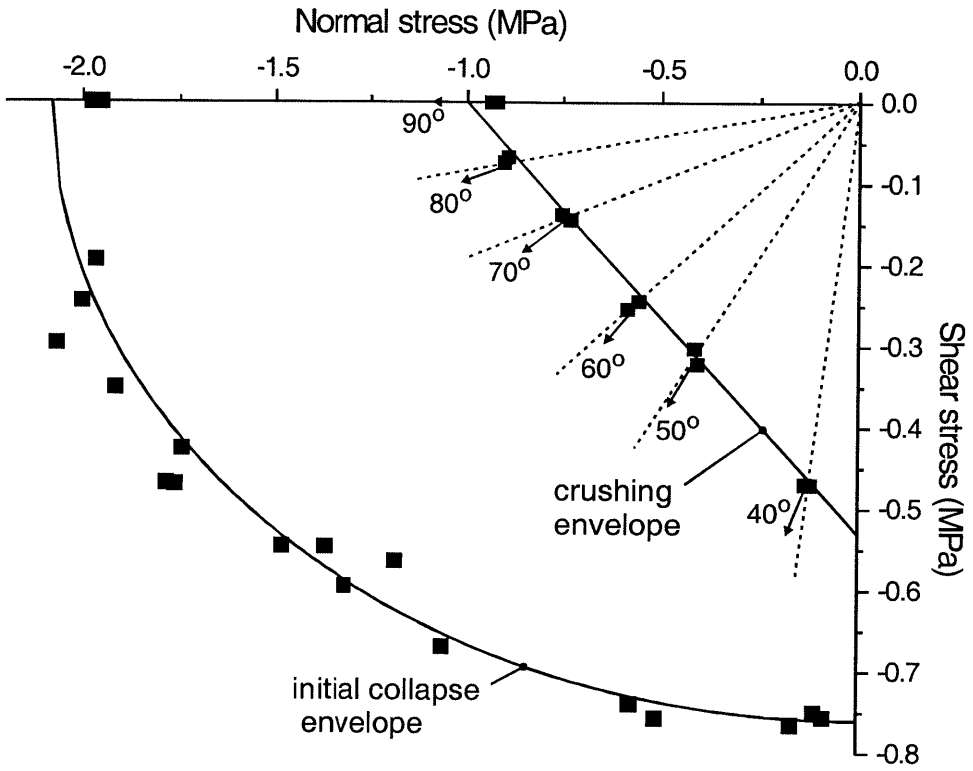

Fig. 43. Initial collapse and crushing envelopes in stress space. The square dots are experimental data points. The vectors indicate the direction of plastic flow during crushing, whereas the dashed straight lines starting from the origin prescribe the direction of plastic flow according to the simplified flow rule given by Eq. (48).

$$\bar{\tau} = \frac{1}{\gamma_{\max} - 2\gamma^*} \int_{2\gamma^*}^{\gamma_{\max}} \tau \mathrm{d}\gamma \tag{46}$$

The characteristic interval $[2\varepsilon^*, \varepsilon_{\max}]$ determines the length of the crushing phase. Based on the experimental results, we suggest $2\varepsilon^* = -0.1$ and $\varepsilon_{\max} = -0.5$. The corresponding shear strain interval $[2\gamma^*, \gamma_{\max}]$ is found from the relation $\gamma = \varepsilon / \tan\alpha$. A plot of the data points $(\bar{\sigma}, \bar{\tau})$ is presented in Fig. 43. It appears that under monotonic loading along a linear strain path the corresponding 'crushing envelope' is an approximately linear function in the shear stress – normal stress plane:

$$f_c(\bar{\sigma}, \bar{\tau}) = \frac{\bar{\sigma}}{\bar{\sigma}_0} + \left| \frac{\bar{\tau}}{\bar{\tau}_0} \right| - 1 = 0 \tag{47}$$

The mean stress under uniaxial compression (so-called 'plateau stress') found from a fit to the experimental data is $\bar{\sigma}_0 = -1.0 MPa$. Again, we restrict the validity of the envelope to compressive stresses only, i.e. $\bar{\sigma} \leq 0$. Recall that tests at small biaxial loading angles developed tensile stresses under large strains and are thus not considered for the evaluation of the compression-dominated crushing behavior. Consequently, the mean shear stress, $\bar{\tau}_0 = 0.53 MPa$, is determined from the extrapolation of the data in Fig. 43 (instead of using the results from the tension-dominated 0° tests). The limitation to the compression-dominated response might appear as a restriction of generality, but in fact, it will be difficult to find a practical problem in which tensile stresses appear.

Further analysis of the data (Fig. 43) suggests that the relationship between the direction of deformation and the location on the crushing envelope may be expressed as follows (flow rule equivalent):

$$\frac{d\varepsilon}{d\gamma} \cong \frac{\bar{\sigma}}{\bar{\tau}} \tag{48}$$

Note that for the present experiments along linear strain paths, the left-hand side corresponds to the tangent of the biaxial loading angle, i.e. it represents the direction of

the strain resultant in the T-W plane. The right hand side represents the direction of the corresponding stress resultant. According to Eq. (48), the strain and stress resultants are parallel in the crushing regime. A more accurate description of the direction of plastic flow will be given in Chapter 5.

3.6 Concluding remarks

- Tests using the EAA have shown: by contrast to FRP or foam specimens, the mechanical behavior of butterfly-shaped honeycomb specimens is not only controlled by the homogeneous stress field along the 'significant section', but it is also influenced by the heterogeneous stress field away from the significant section. Thus, we change specimen shape and use a rectangular sandwich specimen to investigate the yield and post-yield behavior of metallic honeycombs. The stress field in sandwich specimens is statistically homogeneous for reasonably large width to height ratios (see also ASTM C-273 for the shear testing of sandwich core materials).
- A novel Universal Biaxial Testing Device (UTBD) is specifically designed for the testing of sandwich specimens. As compared to the EAA, it is by far more rigid and allows for higher shear and normal loads. Furthermore, large displacements can be applied, which is necessary to study the post-yield behavior. Other additional features include a variable clamping mechanism for different specimen sizes, a built-in displacement measurement device, and two integrated load cells for the measurement of two horizontal force components.
- Changing specimen type and size was also beneficial for the repeatability of the experimental results. Despite the highly complex response of the aluminum honeycomb, characteristic details of the macroscopic stress-strain curves including local fluctuations were accurately reproduced for specimens tested at the same loading angle.

- It is well known that metallic honeycombs exhibit long stress plateaus under uniaxial compression along the T-direction. The present experimental results reveal that the 'concept of plateau stresses' still holds under combined loading. Both normal stress vs. normal strain and shear stress vs. shear strain curves show stress plateaus under biaxial loading.
- The following observations are made on the macroscopic level: (1) an elliptical yield envelope defines the onset of microstructural collapse, (2) a linear inner envelope relates the shear and normal plateau stresses under large deformations and (3) a non-associated flow rule characterizes the relationship between strain increments and the stress state.
- The linear crushing envelope found from the present experiments has been suggested previously by Wierzbicki (1997). Wierzbicki's analytical model for specimens with a large height to width ratio assumes that the deformation localizes at the specimen boundaries while the inner part remains undeformed (see Fig. 27).

Chapter 4

Virtual experiments: Finite element simulations of a metallic honeycomb microstructure under combined out-of-plane loading

4.1 Introduction

Finite element simulations of the microstructural response of a honeycomb have proven to be a powerful means to investigate the mechanical behavior of cellular materials. Grediac (1993) studied the height dependency of the shear modulus using a three-dimensional finite element model of a honeycomb cell; Xu and Qiao (2001) employed a periodic unit cell finite element model in their study on the skin effect. The dynamic in-plane response of elastic-viscoplastic polycarbonate honeycomb was modeled by Papka and Kyriakides (1999) using two-dimensional beam models. This modeling technique was later adopted by Hönig and Stronge (2002) to study the effect of local inertia in aluminum honeycomb at high strain rates. Andrews and Gibson (2001) used two-dimensional beam models to study the fracture behavior of metallic foam. A similar model was used by Chen and Fleck (2002) to investigate size effects in metallic foams.

Here, we go one step further and perform a non-linear three-dimensional finite element analysis of a honeycomb microstructure. Our objective is to gain further insight on the deformation mechanisms at the microstructural level as large macroscopic out-of-plane displacements are applied. The core of the present study is the 'Virtual Honeycomb Specimen (VHS)' that represents the honeycomb microstructure discretized by 3D-shell elements with an elastic-plastic constitutive law. The simulations represent the biaxial testing of a honeycomb in its sandwich configuration, very similar to the experiments using the UBTD. Displacement-controlled simulations are performed for various combinations of normal and shear loading.

4.2 Virtual Experiments

4.2.1 Material

The microstructural geometry and cell wall material properties of the VHS are chosen according to the commercial aluminum honeycomb tested before. The characteristic cross-section of the honeycomb is shown schematically in Fig. 44(a). It has a hexagonal cellular microstructure with a wall thickness of t=33μm, an expansion angle of $\theta = 40^o$, cell wall widths l=3.1mm and h=2.4mm, and a relative density of $\rho/\rho_0 = 1.8\%$. The stress-strain response of the cell wall material has been determined at the Solid Mechanics and Materials Laboratory at MIT. Small dogbone specimens with a gage width of 1mm (Fig. 44(b)) were extracted from the honeycomb cell walls using a custom-made punching device and tested in a force-controlled micro-tensile testing device (Gearing et *al.*, 2002). The cell wall material (aluminum 5056-H39 foil) exhibited an ideal plastic response at a constant engineering stress of $\tilde{\sigma}_y$ = 265 MPa; fracture occurred at an engineering strain of about 8% (Ames, 2003).

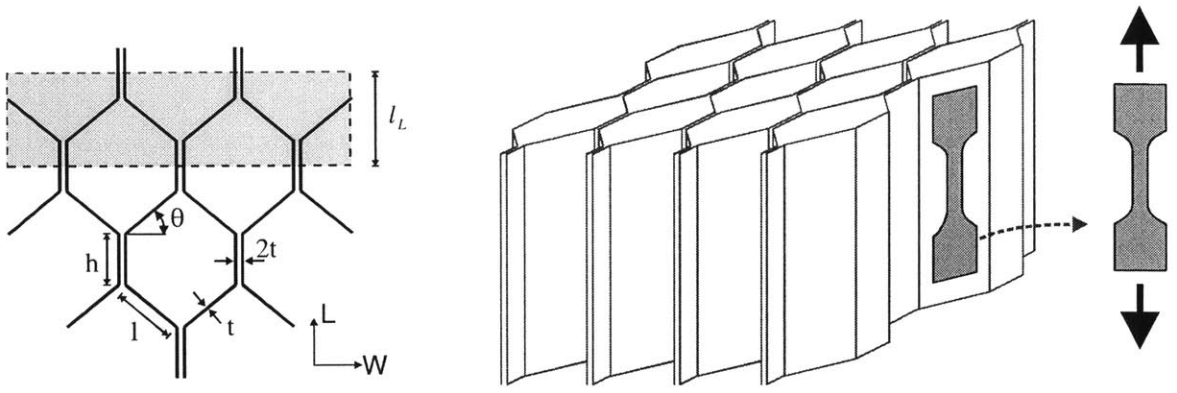

(a) (b)

Fig. 44. (a) Honeycomb geometry in the L-W-plane; the dashed rectangle shows a part of the microstructure that is represented in the VHS; (b) extraction of a micro-tensile dogbone specimen from the honeycomb microstructure (Solid Mechanics and Materials Laboratory, MIT).

4.2.2 Specimen

Fig. 45(a) shows the section of the honeycomb microstructure represented by the VHS. The VHS was $l_W = 38\,\text{mm}$ wide and $C = 7.5\,\text{mm}$ high, which corresponded to a width to height ratio of $l_W / C = 5$. Thus, it represents one quarter of the physical sandwich specimen tested before. We make use of the microstructural periodicity along the L-direction and restrict our model to a representative band of width $l_L = h + l\sin\alpha = 4.4\,\text{mm}$ along the L-direction (Fig. 44(a), Fig. 45(a)). Symmetry boundary conditions are applied to the boundaries in the L-direction (Fig. 46(b)), which, at the macroscopic level, may be interpreted as a plane strain condition along the L-direction. All degrees of freedom are restricted at the bottom of the specimen, whereas a homogeneous displacement field (u_W, u_T) is prescribed at the top boundary (Fig. 46(a)).

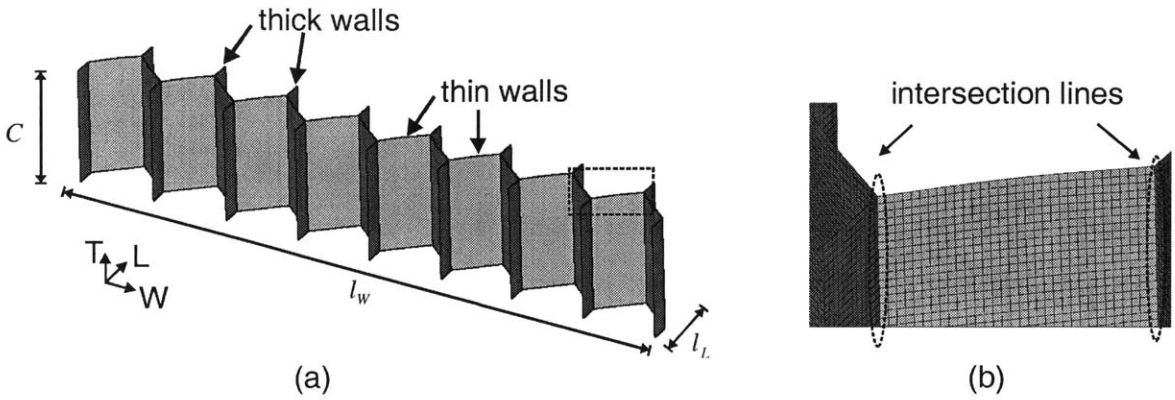

Fig. 45. (a) Schematic of the microstructure of the VHS; the thick walls are aligned with the L-direction; (b) details of the FE-discretization with shell elements; the intersection between the flat walls is labeled as 'intersection line'.

4.2.3 Details of the FE-Model

(i) Spatial discretization of cell wall geometry with 53,700 four-node shell elements (Belytschko-Tsay formulation, reduced in-plane integration, 5 integration points through cell wall thickness, active hourglass control); this corresponded to an average element side length of 0.1mm (see detail in Fig. 45(b)); the mesh of the perfect cell wall geometry is generated using the HYPERMESH preprocessing software. Next, the shape functions of the lowest elastic buckling mode under compressive loading are computed with ABAQUS/standard (HKS, 2002). Based on the shape of this buckling mode, an 'imperfect mesh' is generated and used for the subsequent non-linear analysis. The initial imperfections introduced are of the order of the cell wall thickness.

(ii) Explicit time integration of the non-linear problem using the LS-DYNA v960 solver (LSTC, 2001); by means of automatic density scaling, 200,000 constant time steps of $\Delta t = 2.5ns$ are performed to linearly apply a total displacement of

u=-5mm under a predefined loading angle α (Fig. 46(a)); problem time and time step are carefully chosen such as to guarantee quasi-static loading conditions. This requirement is verified at the macroscopic level by ensuring the kinetic energy to be small as compared to the strain energy.

(iii) The cell wall material is represented by a phenomenological J_2-plasticity model with multi-linear isotropic hardening.

(iv) Penalty formulation for possible cell wall contact; the shell thickness is considered for contact, but thickness changes are neglected.

(v) The resultant force vs. problem time signals at frequencies above 4000Hz are cut-off using a standard SAE-filter.

4.2.4 Limitations

Besides well-known limitations of the mathematical model and its finite element solution, two physical limitations shall be noted:

(i) The double-thickness cell walls in a real honeycomb are typically made of two single-thickness cell walls that are bonded together. Thus, given the finite strength of the thin adhesive bond in a real honeycomb, total or partial delamination may occur between adjacent cell walls. For the case of uniaxial compression along the T-direction, Seggewiss (1996) modeled the adhesive layer as spot-welds and calibrated their shear strength to $150MPa$ in order to achieve satisfactory agreement of simulation and experiments. The successful numerical modeling of adhesive bonds of finite strength requires further research. Due to the lack of reliable modeling technique for delamination, the present simulations are carried out for a monolithic honeycomb, where the double-thickness walls are represented by a single shell element layer of double thickness.

(ii) Cell wall fracture is not included in the model.

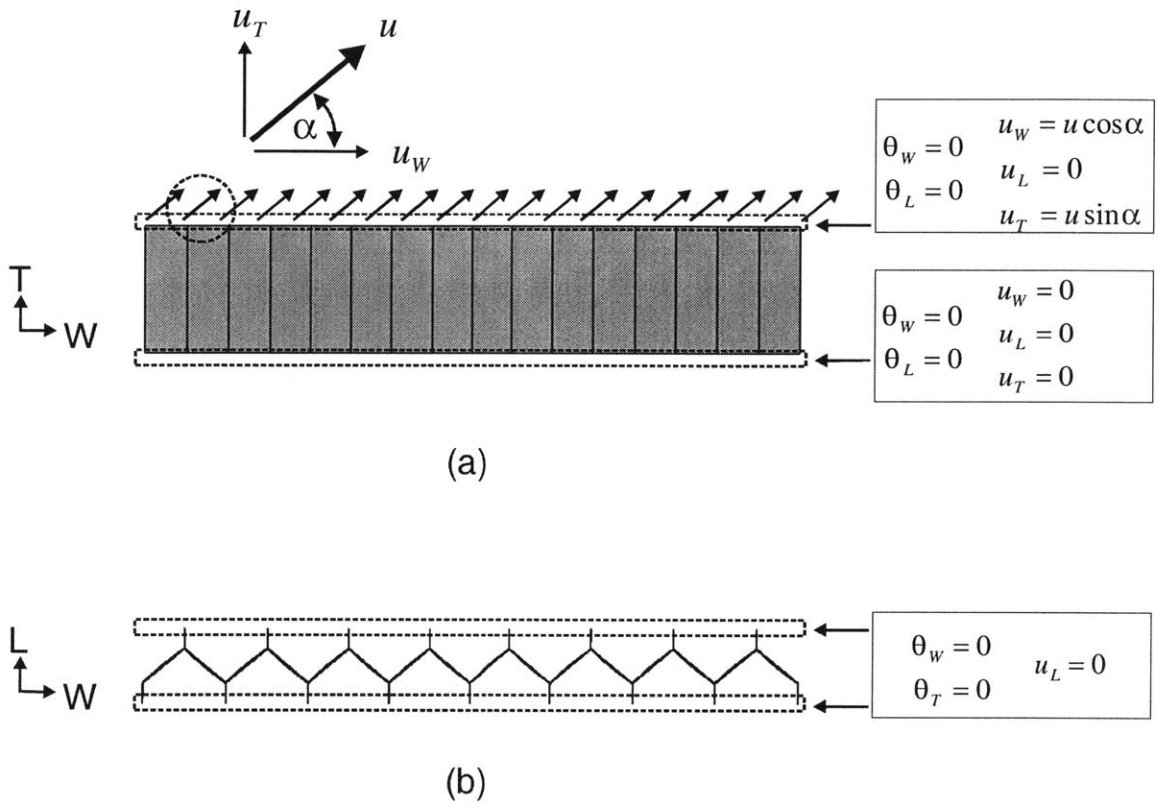

Fig. 46. Boundary conditions of the FE-model on the VHS. θ_i and u_i denote the rotational and translational degrees of freedom of the shell element in the global coordinate system respectively: (a) side view, (b) top view.

4.3 Virtual experimental program

Simulations are performed under various loading conditions. The combined normal and shear displacement loading on the top boundary is characterized by the biaxial loading angle α and the resultant displacement u (Fig. 46(a)). With the exception of the simulation for 'pure shear' loading, the biaxial loading angle is kept constant for individual simulations while a maximum resultant displacement of u=-*5mm* is applied. In terms of normal and shear displacements, u_T and u_W, we have:

$$u_T = u \sin \alpha \tag{49}$$

$$u_w = u \cos \alpha \tag{50}$$

Furthermore, we introduce the macroscopic normal and shear strains, ε and γ, by normalizing the displacements with respect to the specimen height *C*:

$$\varepsilon = \frac{u_T}{C} \tag{51}$$

$$\gamma = \frac{u_W}{C}. \tag{52}$$

The macroscopic strain path is linear and defined by the tangent of the biaxial loading angle: $\varepsilon = \gamma \tan \alpha$. Displacement-controlled simulations are performed for biaxial loading angles of 0°, 10°, 20°, 30°, 40°, 50°, 60°, 70°, 80° and 90°. The corresponding strain paths are shown in Fig. 47.

The resultant force components acting on the top boundary, F_W and F_T, were written as ASCII output from each simulation. The macroscopic shear and normal stresses τ and σ are calculated from the total forces that act on the specimen:

$$\sigma = \frac{F_T}{A_0} \tag{53}$$

$$\tau = \frac{F_W}{A_0} \tag{54}$$

where $A_0 = l_W l_L$ is the cross-sectional area of the VHS. Under pure shear loading, we apply the shear displacement along the W-direction and impose the force boundary condition $F_T = 0$ along the T-direction. As a result, a non-linear strain path is observed (Fig. 47).

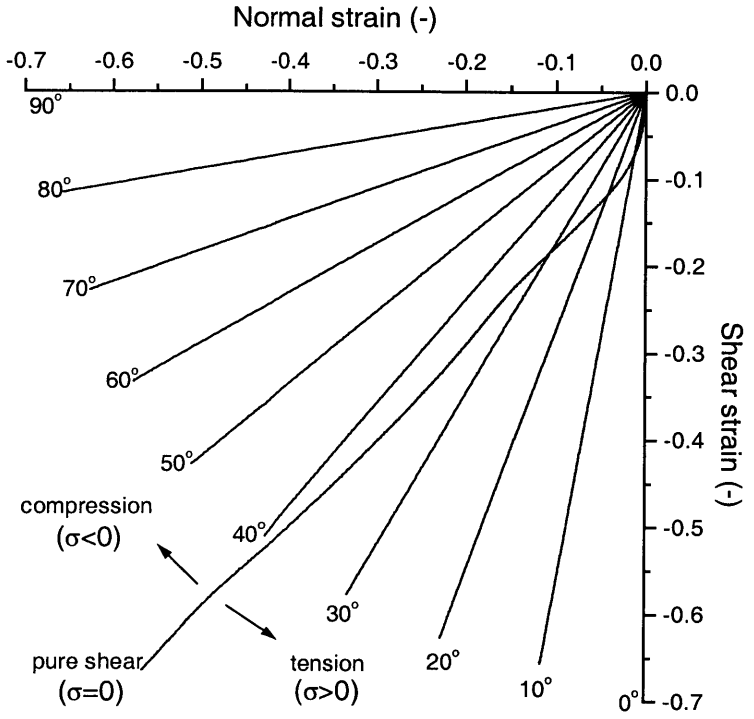

Fig. 47. Strain paths for the biaxial numerical experiment on the VHS.

4.4 Results

A summary of all normal stress vs. normal strain curves and all shear stress vs. shear strain curves is given in Figs. 48 and 49, respectively. A pronounced initial peak stress is observed in the normal stress-strain curves, denoting plastic collapse of the microstructure. After initial collapse, the following observations are noteworthy:

(i) All curves are in hierarchical order: with the exception of the results for pure shear, neither the normal nor the shear stress-strain curves intersect. From small to large loading angles, the normal stress level increases, whereas the shear stress level decreases.

(ii) Tensile stresses develop for loading angles below 40° (Fig. 48). This may be explained by Fig. 47. The curve for pure shear represents the strain path for $\sigma = 0$. As a first approximation, tensile stresses develop when the magnitude of the compressive normal strain applied is smaller than the corresponding normal strain for pure shear.

(iii) As normal tensile stresses develop, the corresponding shear stress-strain curves typically exhibit significant hardening (see 0°, 10°, 20°, 30° in Fig. 49).

(iv) The curve for pure shear shows a more or less constant stress level (Fig. 49). It separates the shear stress-strain curves into two groups: Those comprising strain hardening lie above; the curves for large loading angles (α>40°) lie below.

(v) For large loading angles and large normal strains ($\varepsilon < -0.1$), an almost constant plateau stress is observed in the normal stress-strain curves. This regime is labeled 'crushing' in Fig. 48.

We focus on the behavior under combined compressive and shear stresses with practical applications in mind. For clarity of our discussion, we emphasize the naming of the different parts of the honeycomb microstructure (Fig. 45): The single-thickness walls are referred to as *thin walls*, the double-thickness walls, all aligned in L-direction, are referred to as *thick walls*. The line joint between thick and thin walls is called the *intersection line*. Among the output quantities at the microstructural level, we frequently refer to the *internal energy density*. The internal energy density represents the plastic dissipation per unit volume in a shell element. By contrast to strain or stress components, it is calculated as the mean over the volume of the shell element and thus, independent of the shell thickness coordinate. As a reference, the value of internal energy density at 8% axial strain during uniaxial compression of Al5056-H39 is $21.2 mJ / mm^{-3}$ which

corresponds to a specific energy absorption of $7.8J/g$ (which is calculated as the internal energy density divided by the mass density of the cell wall material).

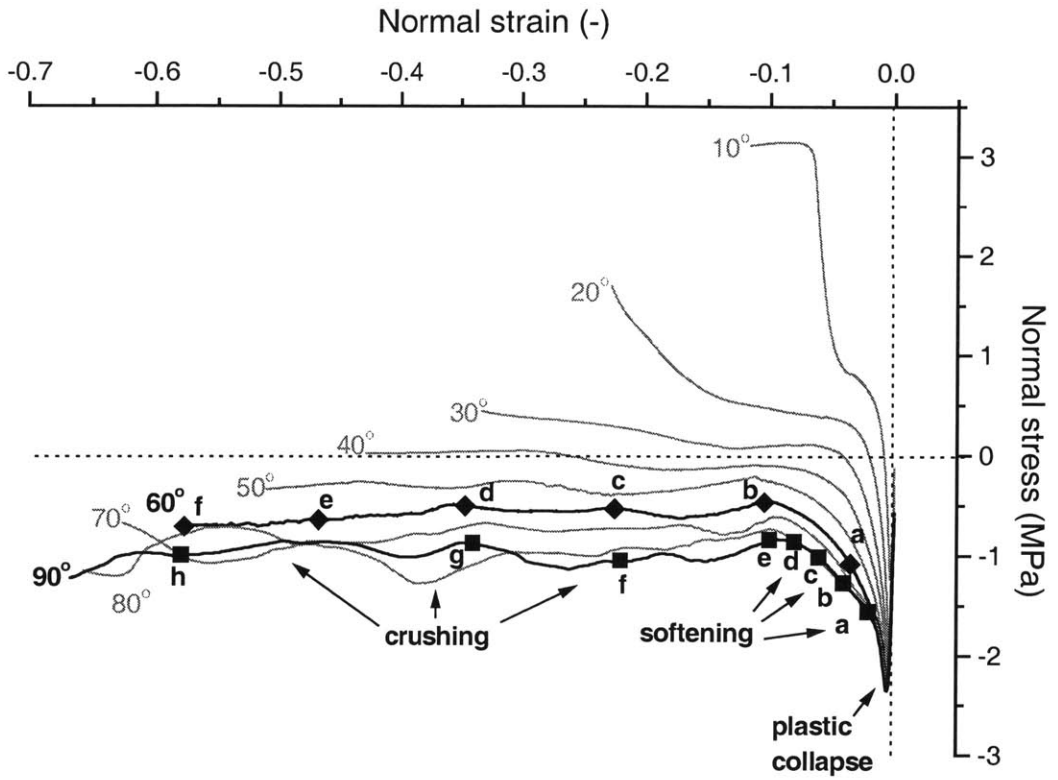

Fig. 48. Macroscopic compressive stress-strain curves at different loading angles.

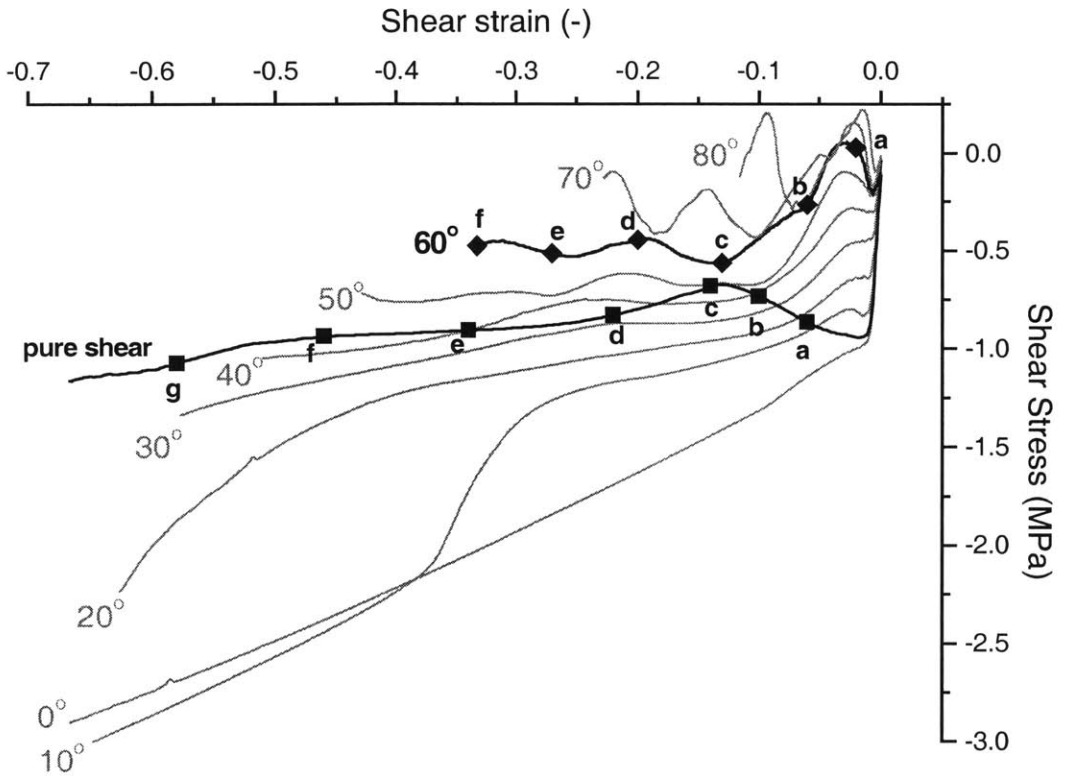

Fig. 49.Macroscopic shear stress-strain curves at different loading angles.

With the exception of 0° loading, all macroscopic normal stress-strain curves show a monotonically increasing macroscopic stress until a pronounced peak stress is reached and the stress level drops. We labeled this point as 'plastic collapse' in Fig. 48. Prior to plastic collapse, elastic buckles form and grow in the honeycomb microstructure, which results in the unloading of cell wall centers and the concentration of stress at the intersection lines. Beyond the initial peak in the macroscopic stress-strain curves, a pronounced softening regime is observed. The development of the first fold takes place in the softening regime. Progressive folding is the dominant microstructural deformation mechanism in the crushing regime. At the same time, the macroscopic stress fluctuates around an almost constant stress level. The progressive folding of honeycombs under uniaxial compression was investigated by various authors and is well understood (McFarland, 1963, Wierzbicki, 1983). Fig. 50 illustrates a side view of progressive folding under uniaxial compression. Note the intense localization of deformation within the microstructure. The honeycomb folds layer by layer, thereby transforming the microstructure from its uncrushed configuration to its crushed configuration. During 90° loading, the folds pile up along the T-direction. A vertical cut through the deformed thin walls confirms this observation (Fig. 53(f)).

Figure 51 (a) shows the deforming microstructure at the end of the softening regime in pure shear. In this figure, the first column is a 3D-view while the second column is the side view of the deforming microstructure. Similarly to the 90° results, the energy dissipation is highly localized within a narrow band in the microstructure. The top and bottom behave rigidly and move relative to each other while the microstructure is highly deformed within the localization band. In the crushing regime, two additional folds form almost simultaneously above and below the first fold (Fig. 51(b)-(d)). At this time, the width of the localization band increases. In other words, the microstructure is transformed from uncrushed to crushed state. The corresponding cut through the thin walls of the deformed microstructure reveals the regular folding pattern in pure shear (Fig. 53(a)). As compared to 90°, the folds are not piled up along the T-direction but accumulated at a much lower angle. Furthermore, note that the folds are three-dimensionally arranged in space and do not touch in the cutting plane (Fig. 53(a)). In a typical side view (second column in Fig. 51), only one fold is seen.

A series of pictures from the 60° simulation shows progressive folding under combined loading. Again, only one fold is seen from the side (second column in Fig. 52), but the three folds become visible in the 3D-view (first column in Fig. 52). Cuts through the deformed microstructures at *u=-5mm* after loading along various stress paths is presented in Fig. 53. A series of folds is typically aligned along a characteristic direction. It must be noted that this direction is not monotonically related to the biaxial loading angle. A full sequence of the cuts throughout loading under 70° is shown in Fig. 54. The first complete fold grows along the T-direction (Fig. 54(b)-(c)), but rotates during the formation of the subsequent fold (Fig. 54(c)-(e)) until it reaches its final position aligned with the other folds.

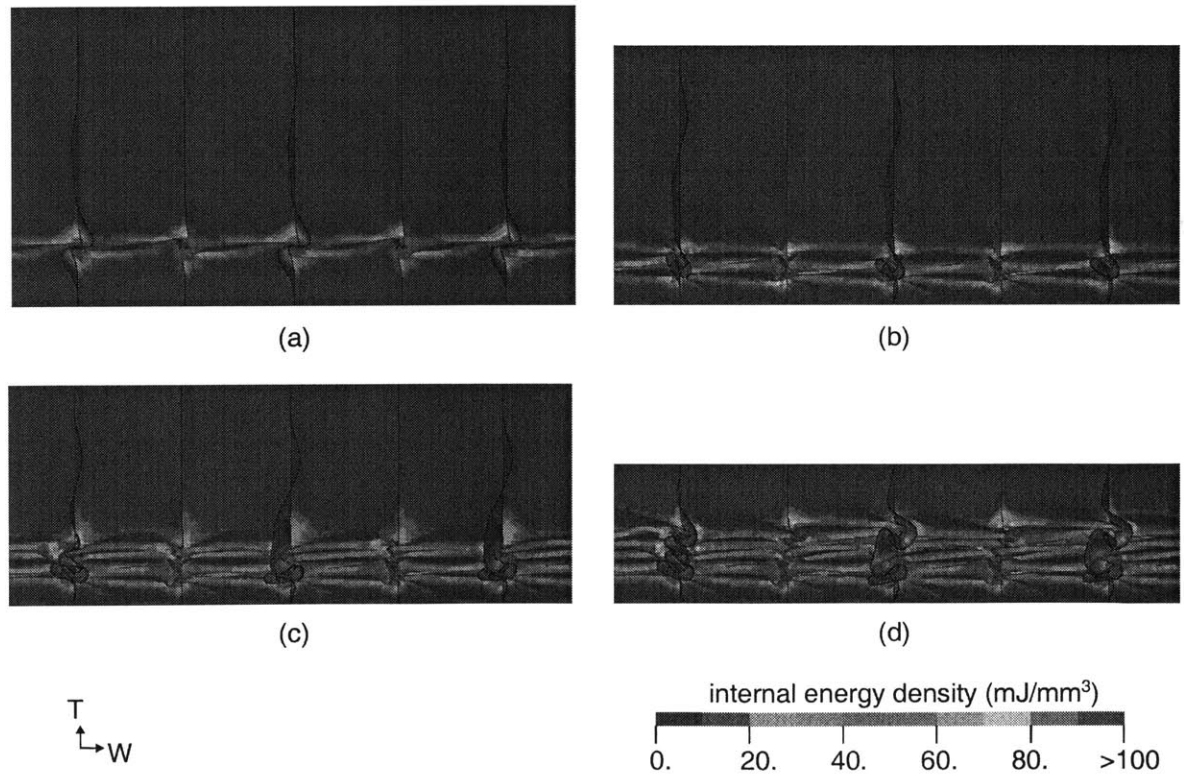

Fig. 50. Deformed microstructure during 90° loading: (a) *u=-0.75mm* [e], (b) *u=-1.65mm* [f], (c) *u=-2.55mm* [g], and (d) *u=-4.35mm* [h]. The letter in square brackets denotes the data point on the stress-strain curve for 90° loading in Fig. 48.

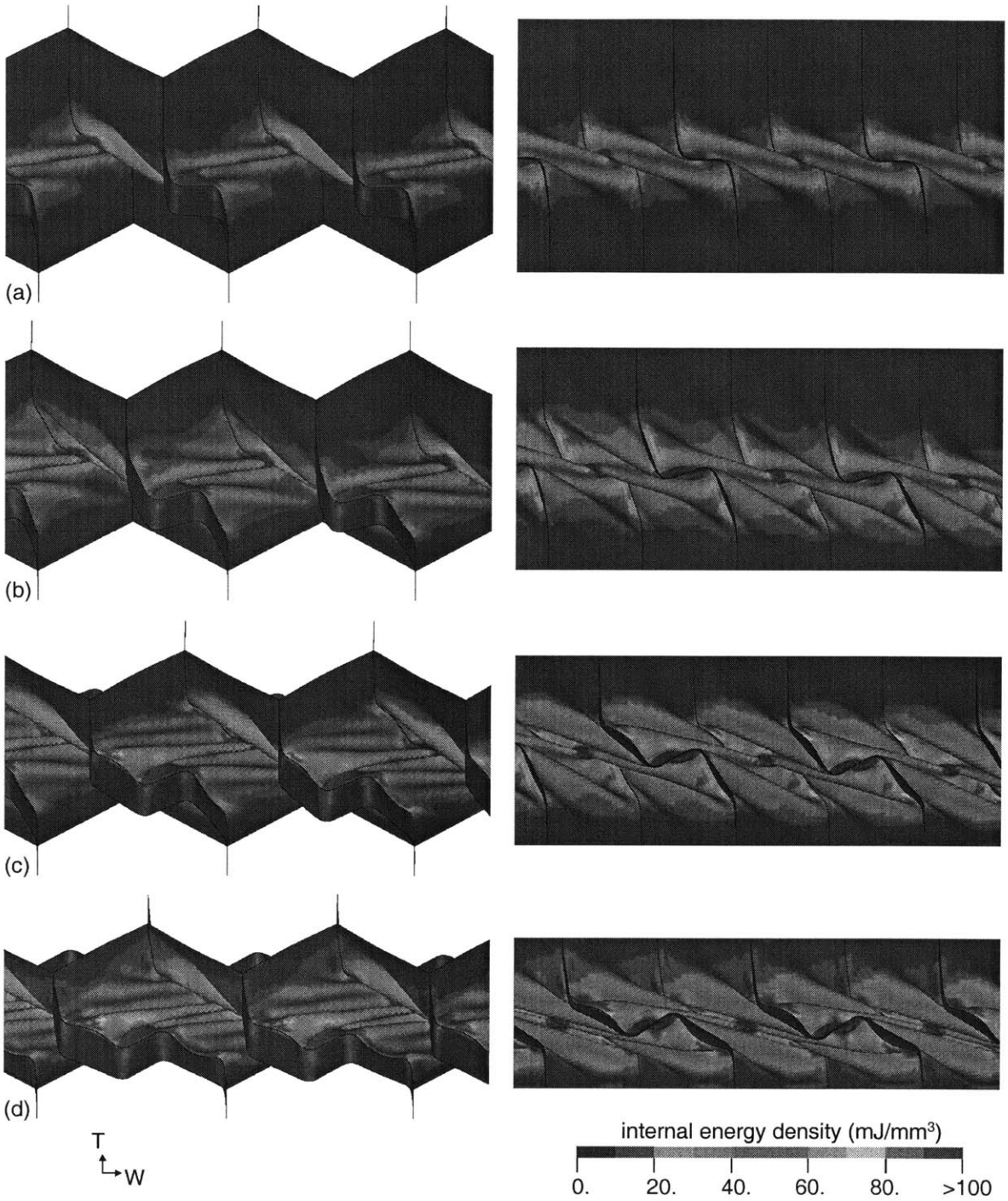

Fig. 51. Deformed microstructure during pure shear loading: (a) *u=-1.65mm* [d], (b) *u=-2.55mm* [e], (c) *u=-3.45mm* [f], and (d) *u=-4.35mm* [g]. The letter in square brackets denotes the data point on the stress-strain curve for pure shear in Fig. 49. In this figure, the first column is a 3D-view while the second column is the side view of the microstructure.

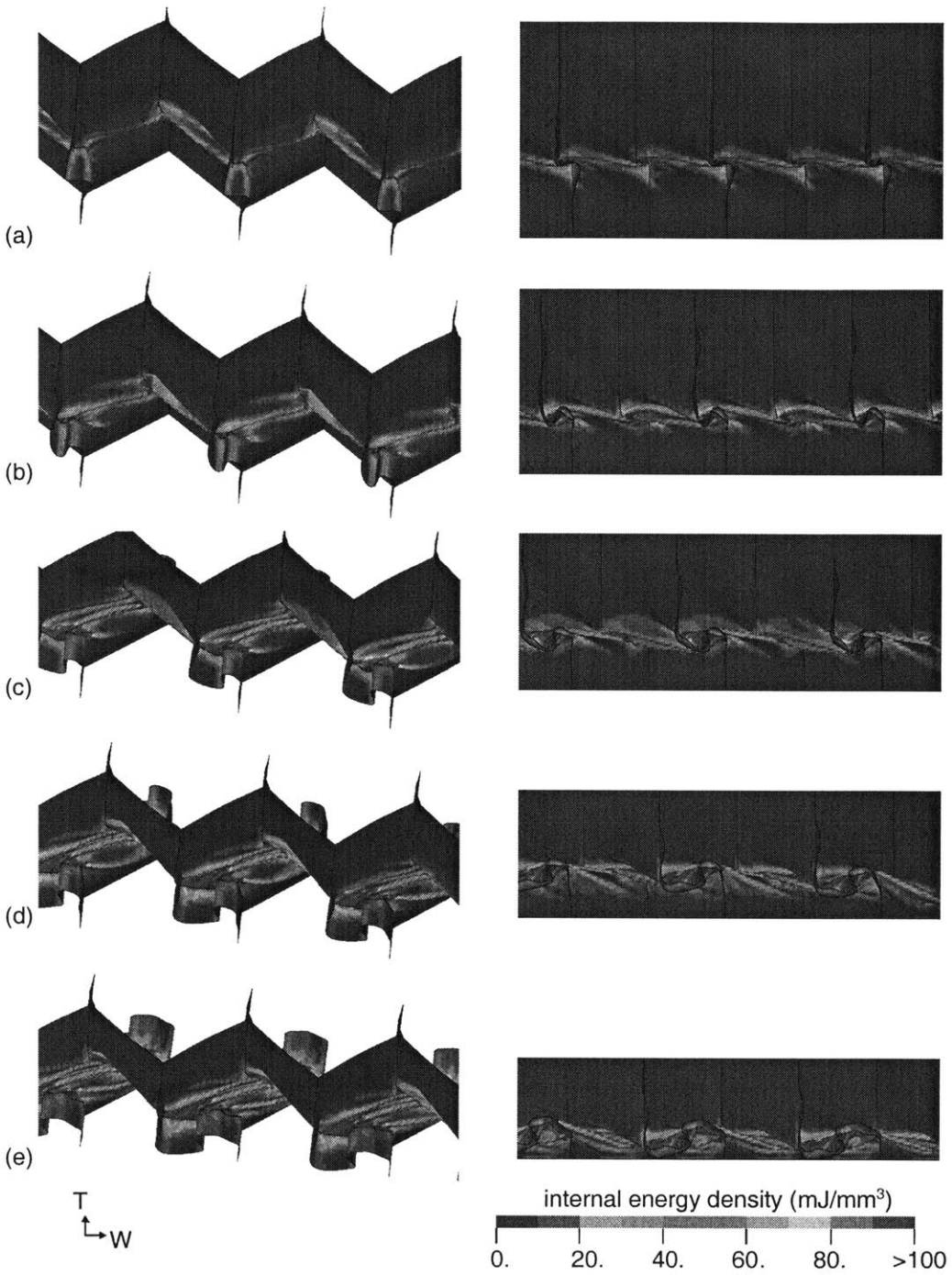

Fig. 52. Deformed microstructure during 60° loading: (a) *u=-0.9mm* [b], (b) *u=-1.95mm* [c], (c) *u=-3.0mm* [d], (d) *u=-4.05mm* [e], and (e) *u=-5.0mm* [f]. The letter in square brackets denotes the data point on the stress-strain curve for 60° loading in Figs. 48 and 49. In this figure, the first column is a 3D-view while the second column is the side view of the microstructure.

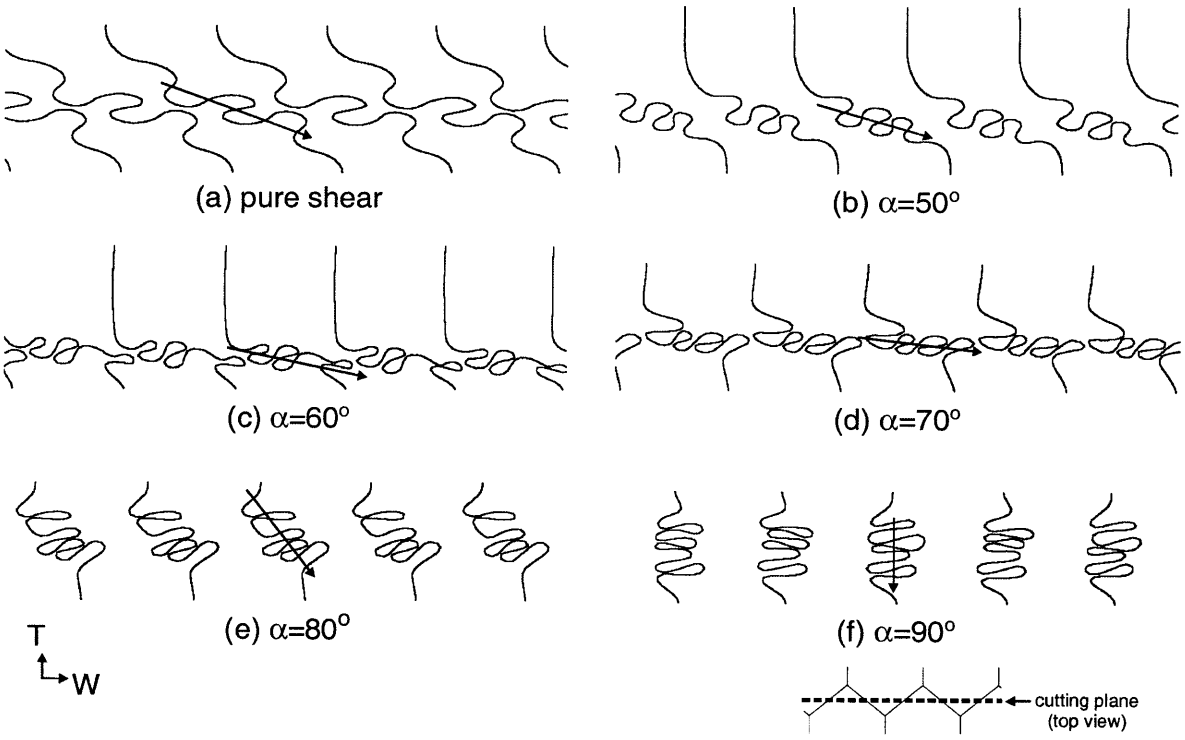

Fig. 53. Cuts through the folding microstructure in the T-W plane for various loading angles at *u=-5mm.* The vector denotes the folding direction.

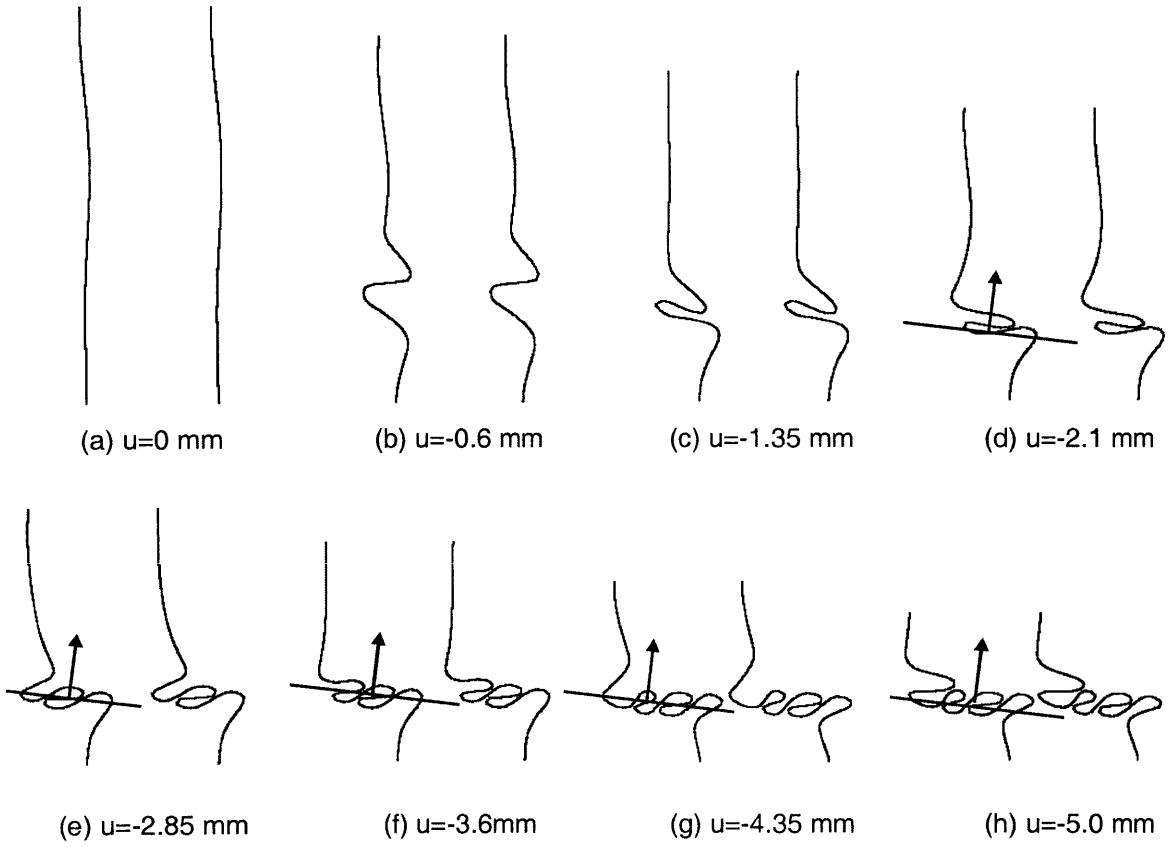

Fig. 54. Cuts through the folding microstructure in the T-W plane during 70° loading.

4.5 Comparison: Virtual versus physical experiments

The macroscopic stress-strain curves of the physical and virtual experiments are remarkably similar. In Fig. 55(a), we plotted the normal stress-strain curves for 90° loading as found from physical and virtual experiments next to each other. Both curves show the same characteristics: initial peak, softening, crushing and densification regimes. But most importantly, numerical simulation and physical experiment are in good quantitative agreement in the crushing regime. The initial peak is lower for the physical experiments than for the virtual experiments, which may be explained by imperfections in a physical specimen. The end of the softening regime, defined as the local stress minimum after the plastic collapse, is reached at a strain $\varepsilon^* \cong -0.05$ in the physical experiment. The corresponding strain in the virtual experiment is $\varepsilon^* \cong -0.1$. This difference may be due to a size effect entering in the strain definition. As we discussed above, the first fold is formed in the softening regime. The completion of the first fold (until contact occurs) requires a displacement u^*, irrespective of specimen size. Thus, the strain $\varepsilon^* = u^* / C$ depends on the specimen height C. The heights of the virtual and physical specimens were $C = 7.5mm$ and $C = 15mm$, respectively, which immediately explains the differences in the strain ε^*.

In the case of shear-dominated loading conditions, significant differences between virtual and physical experiments appear. As an example, we plotted the shear stress-strain curves for 50° loading in Fig. 55(b). The response curves are similar – qualitatively – but different quantitatively. In particular, the plateau shear stress predicted by the simulation is -0.63MPa, while the physical experiment suggests -0.3MPa. We reemphasize one important limitation of the mathematical model underlying the numerical simulations: delamination of the double-thickness cell walls and cell wall fracture are not included. Intercellular delamination dramatically reduces the shear strength of a honeycomb. We performed a finite element simulation for pure shear loading, where the double-thickness cell walls are modeled as two separate (i.e. fully-delaminated) single-thickness cell walls (Fig. 56). The corresponding shear stress-strain curve is shown in Fig. 57, along with the curve obtained from the 'monolithic honeycomb model' that was used for the present finite element study.

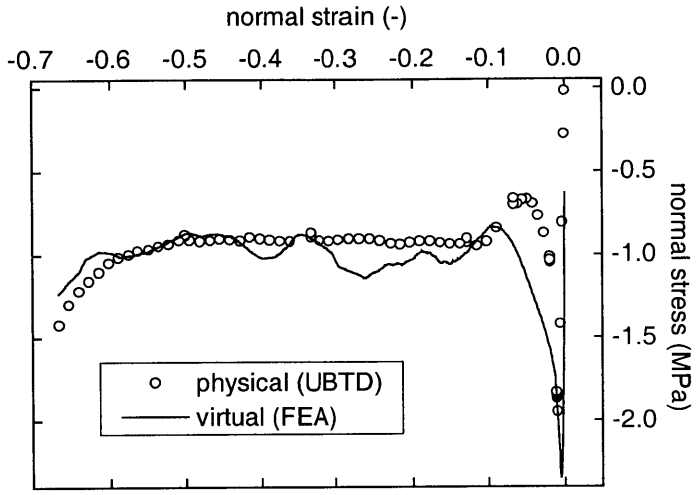

(a)

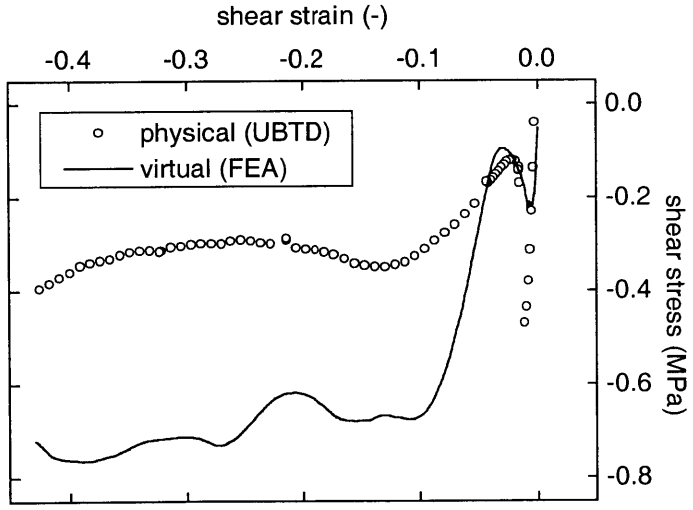

(b)

Fig. 55. Comparison of virtual and physical experiments: (a) normal stress-strain curve for 90° loading, (b) shear stress-strain curve for 50° loading.

Recall that in the monolithic model, we represented the double-thickness cell walls by shell elements with the thickness $2t = 66\mu m$. The curves in Fig. 57 clearly demonstrate that a significant amount of shear strength is lost when the cell walls are separated. Furthermore, note that the plateau stress for the adhesively bonded real honeycomb (found from extrapolation of the results from physical experiments, see Fig. 43) is sandwiched between the curves for the two limiting cases of monolithic and separate cell walls.

Given the differences between the virtual and physical experiments, we consider the results form the virtual experiments as an additional set of experimental data. Consequently, we evaluate the phenomenology for the virtual experiments on monolithic honeycomb, before we develop the constitutive model for metallic honeycomb in Chapter Five.

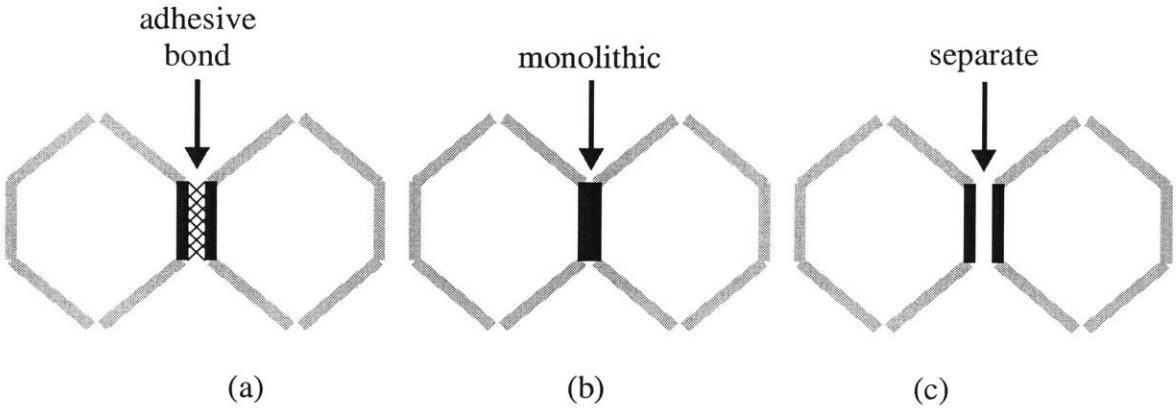

Fig. 56. Modeling of the double-thickness cell walls: (a) two single-thickness walls bonded together (physical experiments), (b) single monolithic double-thickness cell wall (virtual experiments), (c) separate cell walls.

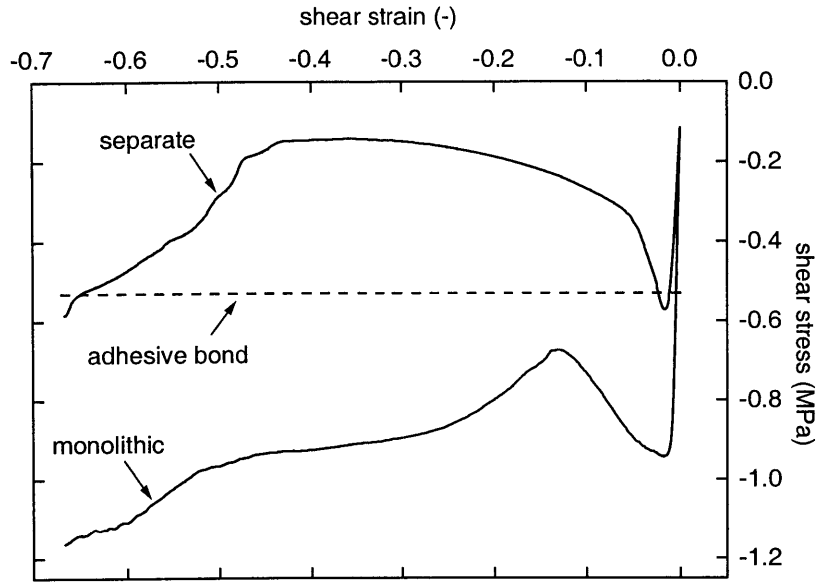

Fig. 57. Shear-stress strain curves for pure shear loading. The dashed line represents the crushing stress for pure shear obtained from the extrapolation of the crushing envelope for the physical experiments. The upper curve is found from numerical simulation assuming two separate cell walls, whereas the lower curve corresponds to the virtual experiment assuming a monolithic microstructure.

4.6 Phenomenology

4.6.1 Plastic collapse

Recall the macroscopic collapse envelope found from the physical experiments (Chaper 3):

$$f_0 = \left(\frac{\sigma}{\sigma_0}\right)^2 + \left(\frac{\tau}{\tau_0}\right)^2 - 1 = 0 \tag{55}$$

where, σ_0 is the macroscopic yield stress under uniaxial compression and τ_0 is the macroscopic yield stress under pure shear. From a fit of Eq. (55) into the simulation data (Fig. 58), we find $\sigma_0 = 2.9\,\text{MPa}$ and $\tau_0 = 0.93\,\text{MPa}$. Clearly, the elliptical form of the plastic collapse envelope also provides a reasonable description of the virtual experiments. (Aside: The simulation data points at plastic collapse were determined as the initial peak stresses from the unfiltered force-time curves. This improves the accuracy of the measurements, while at the same time it explains some minor difference in magnitude between the peaks shown in Figs. 48, 49, and 58).

4.6.2 Crushing regime

The concept of a 'crushing envelope' was introduced in Chapter 3 to describe the behavior under large combined compressive and shear deformation. Given the qualitative similarities of virtual and physical experiments, we calculate the macroscopic plateau stresses $\bar{\sigma}$ and $\bar{\tau}$ according to Eqs. (45(and (46). The corresponding plot of the plateau stress data points $(\bar{\sigma},\bar{\tau})$ is presented in Fig. 58. The straight line in Fig. 58 shows the crushing envelope, defined as

$$f_c(\bar{\sigma},\bar{\tau}) = \frac{\bar{\sigma}}{\bar{\sigma}_0} + \frac{|\bar{\tau}|}{\bar{\tau}_0} - 1 = 0 \tag{56}$$

where we fitted $\bar{\sigma}_0 = -0.99$ MPa for the plateau stress under uniaxial compression and $\bar{\tau}_0 = 0.93$ MPa for the plateau stress under pure shear.

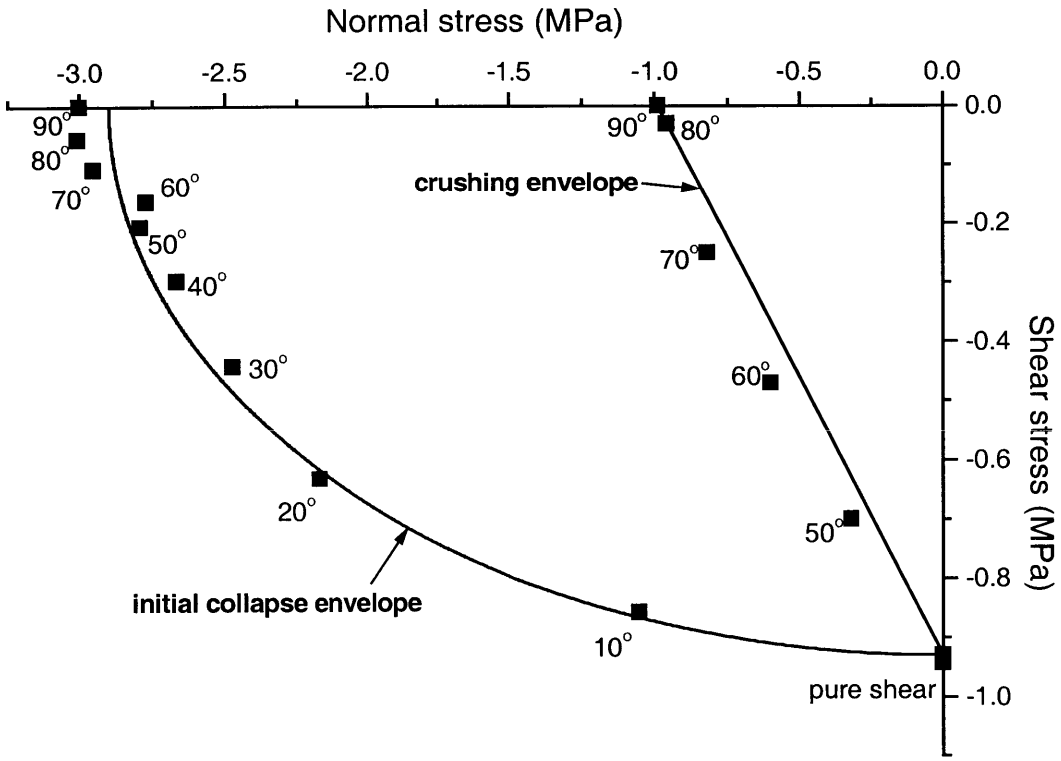

Fig. 58.Characteristic envelopes in the macroscopic shear stress vs. compressive stress plane

4.6.3 Flow rule

The simulations for pure shear indicated that the corresponding strain path is fairly parallel to the strain trajectory for $\alpha = 45^o$ (Fig. 47). In other words, the direction of the strain increment $d\varepsilon / d\gamma$ appears to be close to the direction of the compressive principal macroscopic plateau stress. For a macroscopic stress state of combined compression and shear ($\bar{\sigma} \le 0$, $\bar{\tau} \le 0$), we can calculate the angle χ between the W-axis and the direction of the compressive principal stress:

$$\frac{\pi}{4} \le \chi \le \frac{\pi}{2}: \qquad \tan 2\chi = -\frac{2\bar{\tau}}{\bar{\sigma}} \tag{57}$$

Our hypothesis for the direction of the strain increment reads:

$$\tan \chi = \tan \alpha = \frac{\mathrm{d}\varepsilon}{\mathrm{d}\gamma} \tag{58}$$

We tested this hypothesis for other loading angles and found reasonable agreements (Table 3). Thus, after combining Eqs. (57) and (58), we suggest the following relationship between the stress state and strain increment in the crushing regime:

$$\frac{d\varepsilon}{d\gamma} = \frac{2}{\sqrt{4+\xi^2} - \xi} \tag{59}$$

where $\xi = \bar{\sigma} / \bar{\tau}$ denotes the compressive-shear stress ratio in the crushing regime.

α[°]	45*	50	60	70	80	90
χ[°]	45.0	51.4	61.3	74.3	88.2	90.0

*α=45° assumed for pure shear

Table 3. Direction of strain increment. The upper row shows the biaxial loading angle α, whereas the angle χ in the lower row indicates the direction of the minimum principal macroscopic stress in the crushing regime (both with respect to the W-axis).

4.7 Conclusion

The detailed finite element analysis of the honeycomb microstructure under large biaxial displacement loading provides important insight into the microstructural mechanisms that determine the macroscopic constitutive behavior. Analogous to the results from previous physical experiments, an elliptic envelope in the macroscopic normal vs. shear stress plane describes the onset of plastic collapse, while a linear envelope characterizes the crushing regime. The direction of incremental deformation appeared to be parallel to the direction of the compressive principal stress acting on the honeycomb.

The geometric characteristics of the simulated honeycomb microstructure were identical with the 'real honeycomb' tested with the UBTD (see Chapter 3). The mechanical properties of the cell walls were determined from microtensile tests on dogbone specimens extracted from the cell walls of the real honeycomb (Ames, 2003). However, a quantitative comparison of the results from virtual and physical experiments revealed that delamination between neighboring cell walls plays a key role for the macroscopic shear response.

Chapter 5

Three-dimensional finite-strain rate-independent orthotropic constitutive model

5.1 Introduction

A characterizing feature of a honeycomb microstructure is its strong orthotropy. The initial orthotropy axes may be labeled W, L, and T, where the T-direction is aligned with the axis of the thin-walled tubes; the two in-plane directions (W and L) denote the so-called ribbon and length direction of the hexagonal cross-section (Fig. 59). The elastic in-plane moduli, i.e. the stiffnesses in the W- an L-directions as well as the stiffness for shear loading in the W-L-plane, are typically by one to two orders of magnitude lower than the moduli for out-of-plane loading (that includes normal loading in the T-direction and shear loading in the T-W and T-L-planes). The stress level under plastic loading may be described in a similar manner. For illustration, we summarized characteristic mechanical properties of the aluminum honeycomb considered in the previous Chapters in Table 4. This honeycomb deforms plastically in the W-direction when a stress of 0.02MPa is applied. However, a stress of about 0.9MPa is required to crush the honeycomb along the T-direction. This observation leads to an essential assumption in

in-plane properties					
E_{WW} (MPa)	E_{LL} (MPa)	G_{WL} (MPa)	σ^{y}_{WW} (MPa)	σ^{y}_{LL} (MPa)	τ^{y}_{WL} (MPa)
0.11	0.27	0.02	0.02	0.03	0.05
out-of-plane properties					
E_{TT} (MPa)	G_{TW} (MPa)	G_{TL} (MPa)	σ^{y}_{TT} (MPa)	τ^{y}_{TW} (MPa)	τ^{y}_{TL} (MPa)
1253.	156.	315.	0.93	0.53	n.a.

Table 4. Mechanical properties of 1.8% relative density hexagonal aluminum 5056-H39 honeycomb.

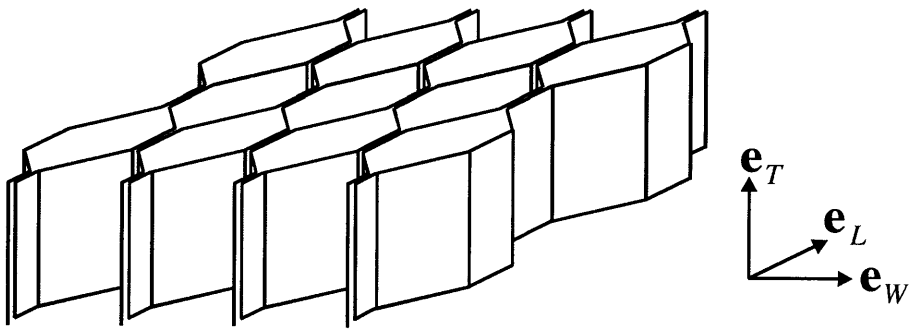

Fig. 59. Microstructural geometry of a hexagonal honeycomb.

the present model: the internal energy variation under in-plane loading be negligibly small as compared to the variation under out-of-plane loading. In other words, we ignore the modeling of the in-plane behavior and limit our attention to the modeling of the out-of-plane behavior.

Schreyer *et al.* (1995) proposed a three-dimensional anisotropic plasticity model for honeycombs. Using the results from uniaxial compression experiments along the W-, L- and T-direction, Schreyer *et al.* assumed a spherical yield surface in the principal stress space, while the center of the yield surface is shifted in the stress space. However, biaxial tests clearly disprove this assumption (Fig. 60). Widely used heuristic constitutive models for honeycombs that are built into commercial finite element programs such as PamCrash (model 41, ESI, 1999) neglect the interaction between the shear and normal stresses. They comprise six separate fully-uncoupled one-dimensional constitutive equations for each component of the stress tensor. The corresponding crushing envelope in the normal-shear stress plane is a rectangle (Fig. 60). The experimental results presented in Chapter 3 reveal that the use of such models may overestimate the plastic work by as much as 100% when the honeycomb is subjected to combined normal and shear loading in the T-W-plane.

Based on previous experimental observations, we develop a phenomenological constitutive model for metallic honeycomb to describe its mechanical behavior in the crushing and densification regimes (Fig. 61). The central assumptions are: (1) the in-plane strains are small, (2) the in-plane stresses are small as compared to the out-of-plane stresses, and (3) the concept of plateau stresses applies, i.e. the assumption of constant normal and shear stress plateaus in the crushing regime provides a satisfactory approximation of the complex stress-strain response. The yield surface is conical in the shear-normal stress space, while plastic flow is non-associated. We employed a backward-Euler integration scheme to implement the constitutive model into a finite element program and used it to simulate uniaxial and multiaxial experiments on aluminum honeycomb. The reasonable agreement of the model predictions and the experimental results encourages the use of the model for applications involving large plastic out-of-plane deformation.

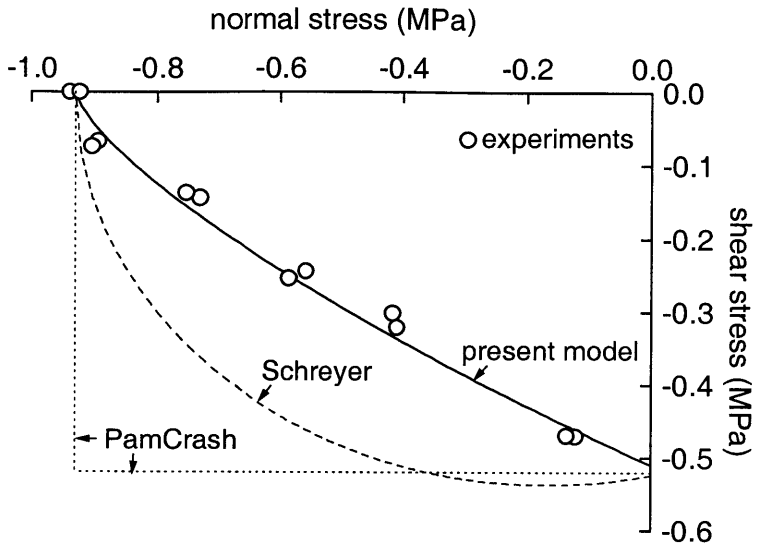

Fig. 60. Comparison of yield surfaces: The dotted rectangle indicates the yield surface in the PamCrash (model 41) and the dashed line shows the elliptic envelope by Schreyer et al.(1995). Each open circle represents an experimental data point as obtained from tests with the UBTD, while the solid line shows the crushing envelope that is assumed by the present model.

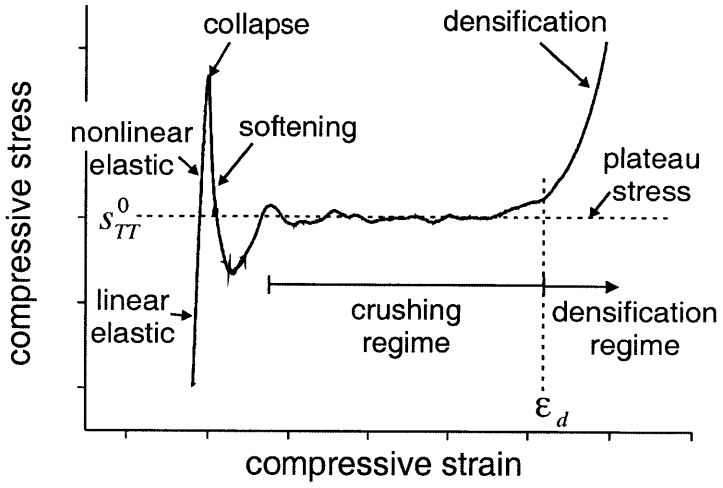

Fig. 61. Characteristic stress-strain curve for metallic honeycomb under uniaxial compression along the T-direction.

5.2 Phenomenological constitutive model

Our constitutive equations are specifically tailored for metallic honeycombs right from the beginning. This is done to keep the formulation as transparent as possible and to guarantee the physical interpretation of the individual components. In particular, we define the stresses and finite strain measures such that they are identical to the engineering stress and strain measures that have been used in the previous Chapters. The constitutive equations could also by formulated using other stress and strain measures such as the Cauchy stress tensor along with the rate-of-deformation tensor or the second Piola-Kirchhoff stress tensor along with Lagrangian strains. In particular, a different choice of stress and strain measures might be beneficial to the computational efficiency of the corresponding integration algorithm. However, the present choice is ideal in order to establish a clear link between the model assumptions and experimental observations.

Throughout our presentation, we shall use the notation of modern continuum mechanics (e.g. Gurtin, 1981). Specifically, $\mathbf{a}\cdot\mathbf{b}$ denotes the scalar (inner) product of two vectors $\mathbf{a}$ and $\mathbf{b}$; $\mathbf{a}\otimes\mathbf{b}$ denotes the dyadic (tensor) vector product, that yields a linear transformation defined as $(\mathbf{a}\otimes\mathbf{b})\mathbf{c}=(\mathbf{c}\cdot\mathbf{b})\mathbf{a}$, where $\mathbf{c}$ is a vector of the same length as $\mathbf{a}$ and $\mathbf{b}$. Vectors with the components $\{1,0,0\}^T$, $\{0,1,0\}^T$, and $\{0,0,1\}^T$ are denoted respectively as $\mathbf{e}_1$, $\mathbf{e}_2$, and $\mathbf{e}_3$. (Note: the superscript 'T' denotes the transpose of a vector or matrix, whereas the subscript 'T' indicates the coordinate axis T).

5.2.1 Material coordinate system

The constitutive model is formulated in material coordinates. The material coordinate system is attached to the orthotropy axes of the initial configuration of the honeycomb material. Given the unit vectors $(\mathbf{e}_W^g,\mathbf{e}_L^g,\mathbf{e}_T^g)$ of the three orthotropy axes in global coordinates (Fig. 59), we can express the coordinate system transformation by the tensor $\mathbf{B}$:

$$\mathbf{B} = \mathbf{e}_W^g \otimes \mathbf{e}_1 + \mathbf{e}_L^g \otimes \mathbf{e}_2 + \mathbf{e}_T^g \otimes \mathbf{e}_3 \tag{60}$$

In other words, a vector $\mathbf{a}$ given in global coordinates is expressed in material coordinates as:

$$\mathbf{a}^g \rightarrow \mathbf{a}^m = \mathbf{B}\mathbf{a}^g \tag{61}$$

where the superscripts 'g' and 'm' refer to the corresponding 'global' and 'material' coordinate systems. Accordingly, the coordinate system transformation of the deformation gradient tensor $\mathbf{F}$ reads

$$\mathbf{F}^g \rightarrow \mathbf{F}^m = \mathbf{B}\mathbf{F}^g\mathbf{B}^T \tag{62}$$

and analogously, we have the transformation of the Cauchy stress tensor $\mathbf{T}$ from global to material coordinates:

$$\mathbf{T}^g \rightarrow \mathbf{T}^m = \mathbf{B}\mathbf{T}^g\mathbf{B}^T \tag{63}$$

Conversely, the transformation from material to global coordinates is given as

$$\mathbf{T}^m \rightarrow \mathbf{T}^g = \mathbf{B}^T\mathbf{T}^m\mathbf{B} \tag{64}$$

In the following, we omit the superscript that indicates the coordinate system. All tensors and vectors are given in material coordinates, i.e. $\mathbf{F} := \mathbf{F}^m$ and $\mathbf{T} := \mathbf{T}^m$.

5.2.2 Kinematics of finite strain

We decompose the deformation gradient into a stretch tensor $\mathbf{U}$ and a rotation tensor $\mathbf{R}$:

$$\mathbf{F} = \mathbf{R}\mathbf{U} \tag{65}$$

This decomposition is typically performed according to the fundamental rotation theorem, which implies that $\mathbf{R}$ represents an orthogonal rotation tensor and $\mathbf{U}$ is a symmetric positive-definite tensor (e.g. Malvern, 1969). In the present model, we also assume that $\mathbf{R}$ is an orthogonal rotation tensor, but we use a physical argument for the decomposition, which yields a non-symmetric stretch tensor $\mathbf{U}$. Here, we chose $\mathbf{R}$ such that is describes the rotation of the W-L-plane. In other words, the deformation field

described by the stretch tensor $\mathbf{U}$ is free from any rigid body rotation of the W-L-plane. The sketch in Fig. 62 illustrates this decomposition. As a result, the engineering strain tensor is given by the simple expression:

$$\mathbf{E} = \mathbf{U} - \mathbf{1} \tag{66}$$

where the components

$$E_{13} = \mathbf{E} \cdot (\mathbf{e}_1 \otimes \mathbf{e}_3) = \gamma_{TW} \tag{67}$$

$$E_{23} = \mathbf{E} \cdot (\mathbf{e}_2 \otimes \mathbf{e}_3) = \gamma_{TL} \tag{68}$$

$$E_{33} = \mathbf{E} \cdot (\mathbf{e}_3 \otimes \mathbf{e}_3) = \varepsilon_{TT} \tag{69}$$

correspond to the engineering strains γ_{TW}, γ_{TL} and ε_{TT} that are typically measured in experiments (see Fig. 63). Mathematically, we write the rotation $\mathbf{R}$ as

$$\mathbf{R} = \hat{\mathbf{e}}_W \otimes \mathbf{e}_1 + \hat{\mathbf{e}}_L \otimes \mathbf{e}_2 + \hat{\mathbf{e}}_T \otimes \mathbf{e}_3 \tag{70}$$

where the vector $\hat{\mathbf{e}}_T$ denotes the normal to the W-L-plane in the rotated deformed configuration and $\hat{\mathbf{e}}_W$, $\hat{\mathbf{e}}_L$ are the corresponding rotated in-plane directions:

$$\begin{aligned} \hat{\mathbf{e}}_W &= \frac{\mathbf{F}\mathbf{e}_W}{\|\mathbf{F}\mathbf{e}_W\|} \\ \hat{\mathbf{e}}_L &= \frac{\mathbf{F}\mathbf{e}_L}{\|\mathbf{F}\mathbf{e}_L\|} \end{aligned} \tag{71}$$

The vectors $\hat{\mathbf{e}}_W$ and $\hat{\mathbf{e}}_L$ are not necessary perpendicular in the deformed configuration, but we demand that the in-plane distortion be small, i.e.

$$\hat{\mathbf{e}}_W \cdot \hat{\mathbf{e}}_L \cong 0 \tag{72}$$

The third unit vector, $\hat{\mathbf{e}}_T$, is defined perpendicular to the rotated W-L-plane

$$\hat{\mathbf{e}}_T = \frac{\hat{\mathbf{e}}_W \times \hat{\mathbf{e}}_L}{\|\hat{\mathbf{e}}_W \times \hat{\mathbf{e}}_L\|} \tag{73}$$

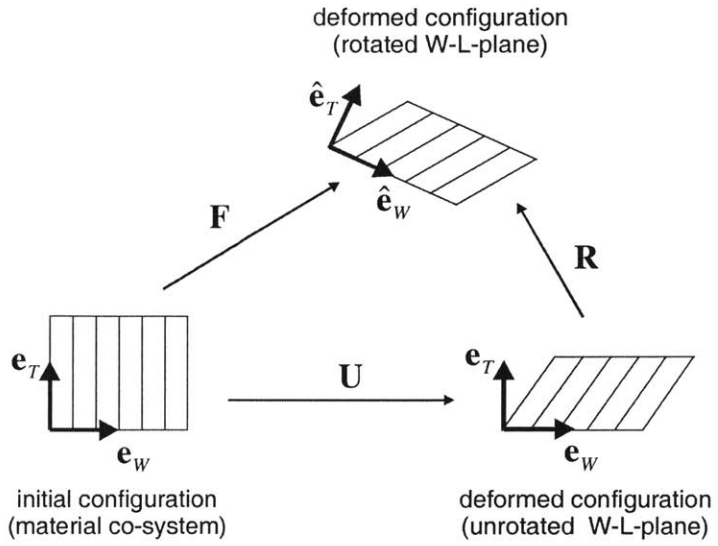

Fig. 62. Kinematics.

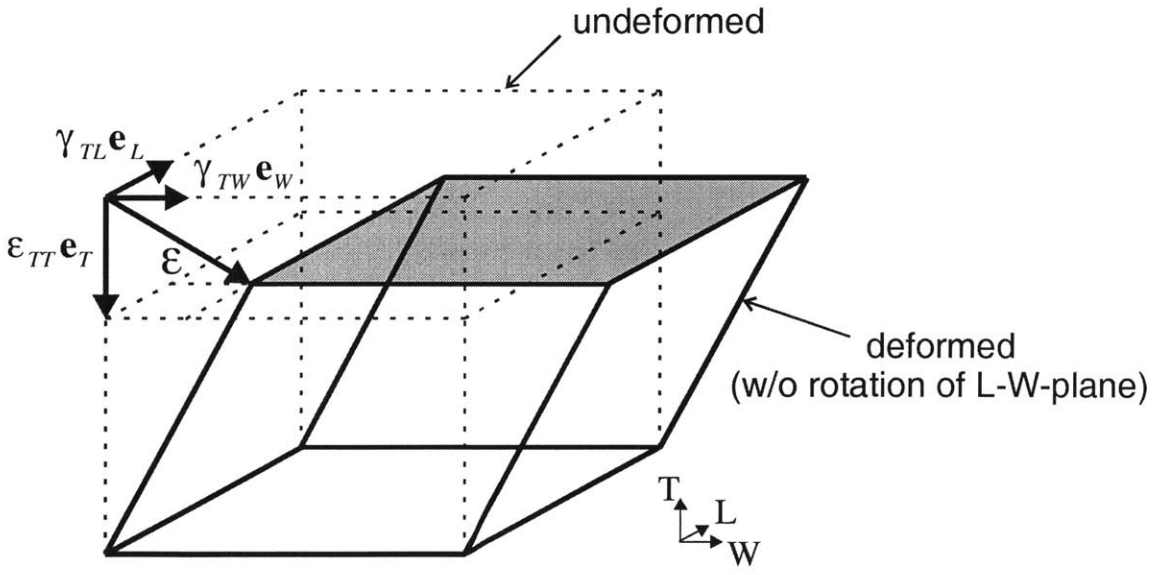

Fig. 63. Homogeneous out-of-plane deformation of a unit cube from the undeformed configuration (dashed lines) to the deformed configuration (solid lines).

And finally, in order to ensure the exact orthogonality of the base vectors, we recalculate $\hat{\mathbf{e}}_L$ from the cross product of the $\hat{\mathbf{e}}_W$ and $\hat{\mathbf{e}}_T$ vectors:

$$\hat{\mathbf{e}}_L = \hat{\mathbf{e}}_T \times \hat{\mathbf{e}}_W \tag{74}$$

Thus, the rotation tensor $\mathbf{R}$ is uniquely determined by Eqs (70), (71), (73) and (74), and we can compute the non-symmetric engineering strain tensor as

$$\mathbf{E} = \mathbf{R}^T\mathbf{F} - \mathbf{1} \tag{75}$$

5.2.3 Thermodynamic framework

According to the Clausius-Duhem inequality for isothermal conditions, the rate of dissipation, φ, must be positive:

$$\varphi = W - \dot{\psi} \geq 0 \tag{76}$$

where W denotes the stress power and ψ denotes the Helmholtz free energy, both defined per unit initial volume. Evaluating the stress power provides the engineering stress tensor $\mathbf{T}^*$ that is work conjugate to the engineering strain tensor $\mathbf{E}$ defined by Eq. (75). Starting point is the expression of the stress power in terms of the Cauchy stress tensor $\mathbf{T}$ and the rate-of-deformation tensor $\mathbf{L} = \dot{\mathbf{F}}\mathbf{F}^{-1}$:

$$\begin{aligned} \mathrm{W} &= (\det\mathbf{F})\mathbf{T}\cdot\mathbf{L} = (\det\mathbf{F})\mathbf{T}\cdot\dot{\mathbf{F}}\mathbf{F}^{-1} \\ &= (\det\mathbf{U})\mathbf{T}\cdot\dot{\mathbf{R}}\mathbf{R}^{\mathrm{T}} + (\det\mathbf{U})\mathbf{T}\cdot\mathbf{R}\dot{\mathbf{U}}\mathbf{U}^{-1}\mathbf{R}^{\mathrm{T}} \\ &= (\det\mathbf{U})\mathbf{R}^{\mathrm{T}}\mathbf{T}\mathbf{R}\mathbf{U}^{-\mathrm{T}}\cdot\dot{\mathbf{U}} \\ &= \mathbf{T}^*\cdot\dot{\mathbf{E}} \end{aligned} \tag{77}$$

where the work conjugate engineering stress tensor reads

$$\mathbf{T}^* = (\det\mathbf{U})\mathbf{R}^T\mathbf{T}\mathbf{R}\mathbf{U}^{-T} \tag{78}$$

Core assumption of this model is the neglect of the work done by the in-plane stresses. Thus, the expression for the stress power reduces to

$$
\begin{aligned}
W &= \mathbf{T}^* \cdot \dot{\mathbf{E}} \\
&\cong T_{13}^* \dot{E}_{13} + T_{23}^* \dot{E}_{23} + T_{33}^* \dot{E}_{33} \\
&= \tau_{TW} \dot{\gamma}_{TW} + \tau_{TL} \dot{\gamma}_{TL} + \sigma_{TT} \dot{\varepsilon}_{TT} = \boldsymbol{\sigma} \cdot \dot{\boldsymbol{\varepsilon}}
\end{aligned} \tag{79}
$$

where we introduced the engineering stress vector

$$
\boldsymbol{\sigma} = \begin{Bmatrix} T_{13}^* \\ T_{23}^* \\ T_{33}^* \end{Bmatrix} = \begin{Bmatrix} \tau_{TW} \\ \tau_{TL} \\ \sigma_{TT} \end{Bmatrix} \tag{80}
$$

and the engineering strain vector $\boldsymbol{\varepsilon}$

$$
\boldsymbol{\varepsilon} = \begin{Bmatrix} E_{TW} \\ E_{TL} \\ E_{TT} \end{Bmatrix} = \begin{Bmatrix} \gamma_{TW} \\ \gamma_{TL} \\ \varepsilon_{TT} \end{Bmatrix} \tag{81}
$$

The constitutive model will describe the relationship between the stress vector $\boldsymbol{\sigma}$ and the strain vector $\boldsymbol{\varepsilon}$ for an arbitrary loading path.

We consider the additive decomposition of the strain vector into its elastic part $\boldsymbol{\varepsilon}^e$ and its plastic part $\boldsymbol{\varepsilon}^p$

$$
\boldsymbol{\varepsilon} = \boldsymbol{\varepsilon}^e + \boldsymbol{\varepsilon}^p \tag{82}
$$

and we define the free Helmholtz energy as a function of the elastic strain vector.

$$
\psi = \hat{\psi}(\boldsymbol{\varepsilon}^e) \tag{83}
$$

Combining Eqs. (76), (79) and (83) yields

$$
\varphi = \left(\boldsymbol{\sigma} - \frac{\partial \hat{\psi}}{\partial \boldsymbol{\varepsilon}^e} \right) \cdot \dot{\boldsymbol{\varepsilon}}^e + \boldsymbol{\sigma} \cdot \dot{\boldsymbol{\varepsilon}}^p \geq 0 \tag{84}
$$

Under the absence of plastic evolution, i.e. $\dot{\boldsymbol{\varepsilon}}^p = \mathbf{0}$, the dissipation must be zero, which leads to the constitutive equation for the stress:

$$
\boldsymbol{\sigma} = \frac{\partial \hat{\psi}}{\partial \boldsymbol{\varepsilon}^e} \tag{85}
$$

Moreover, when plastic evolution occurs, the rate of dissipation must be positive:

$$\varphi = \boldsymbol{\sigma} \cdot \dot{\boldsymbol{\varepsilon}}^p \geq 0 \tag{86}$$

which imposes an important thermodynamic restriction on the flow rule that prescribes the plastic rate-of-deformation $\dot{\boldsymbol{\varepsilon}}^p$.

5.2.4 Hyperelasticity

We assume a quadratic form of the free Helmholtz energy:

$$\hat{\psi} = \tfrac{1}{2}\boldsymbol{\varepsilon}^e \cdot \boldsymbol{\mathcal{C}}\boldsymbol{\varepsilon}^e \tag{87}$$

and thus according to Eq. (85)

$$\boldsymbol{\sigma} = \boldsymbol{\mathcal{C}}\boldsymbol{\varepsilon}^e \tag{88}$$

while the second-order elasticity tensor $\mathcal{C}$ denotes the diagonal matrix of the elastic moduli:

$$\mathbf{C} = \begin{bmatrix} G_{TW} & 0 & 0 \\ 0 & G_{TL} & 0 \\ 0 & 0 & E_{TT} \end{bmatrix} \tag{89}$$

The elastic moduli can be found from micromechanical analysis (Kelsey *et al.*, 1958, Grediac, 1993, Gibson and Ashby, 1997). The underlying assumption is that, even for large deformations, the material resides orthotropic and the elastic moduli remain constant. The simple elasticity model adopted here is predominantly for numerical purpose. A more detailed description requires further research on the evolution of the elastic properties under large plastic deformation.

5.2.5 Yield surface

Results from biaxial experiments on metallic honeycomb in the T-W-plane are typically represented by two characteristic envelopes in terms of τ_{TW} and σ_{TT}: (1) the initial collapse envelope and (2) the crushing envelope. Both envelopes represent the behavior under out-of-plane compression and shear, a loading condition that shall also be the focus

of the present work. The collapse envelope describes the initial peak stress observed in the stress-strain curves under combined compression and shear. It determines the elastic domain for the initial, undeformed honeycomb microstructure that is free from any plastic loading history. Once plastic deformation occurred in the honeycomb under compression, the initial collapse envelope may not be recovered. In other words, the collapse envelope is important for problems dealing with the onset of plastic deformation such as the damage evaluation of sandwich components after accidental loading. In the case of large plastic deformation, the crushing envelope is of greater importance. The stress-strain curves exhibit long plateau regimes where the stresses fluctuate around their so-called plateau values. In the T-W-plane, the relationship between the shear and normal plateau stresses is described by the crushing envelope:

$$\frac{\sigma_{TT}}{s_{TT}^0} + \left|\frac{\tau_{TW}}{s_{TW}^0}\right|^m = 1 \tag{90}$$

where s_{TT}^0 and s_{WT}^0 denote the plateau stresses under uniaxial compression and pure shear loading, respectively. A first approximation suggested a shear exponent $m = 1.0$. Here, we extend this experimentally observed concept of a crushing envelope to the three-dimensional case and suggest the following yield surface to describe the boundary of the elastic domain under large out-of-plane deformation:

$$f(\boldsymbol{\sigma}, \mathbf{s}) = \frac{\sigma_{TT}}{s_{TT}} + \left[\left(\frac{\tau_{TW}}{s_{TW}}\right)^2 + \left(\frac{\tau_{TL}}{s_{TL}}\right)^2\right]^{\frac{m}{2}} - 1 = 0 \tag{91}$$

The vector $\mathbf{s}^T = \{s_{TW}, s_{TL}, s_{TT}\}$ denotes the deformation resistance. It is constant in the crushing regime, but increases in the densification regime as described later. Note that for $\tau_{TL} = 0$ we recover the crushing envelope in the T-W-plane. The elliptic interaction in the shear plane was chosen such that the yield surface represents a transversely isotropic material for the special case $s_{TL} = s_{TW}$.

5.2.6 Flow rule

Denoting the direction of plastic flow by the unit vector $\mathbf{r} = \mathbf{r}(\boldsymbol{\sigma})$, the flow rule reads:

$$d\varepsilon^p = d\lambda \mathbf{r} \tag{92}$$

where the plastic multiplier $d\lambda$ obeys the loading/un-loading conditions:

$$d\lambda \geq 0 \quad \text{and} \quad f d\lambda = 0 \tag{93}$$

Virtual experiments on metallic honeycomb indicated that the plastic flow in a honeycomb under compression and shear loading is almost coaxial with the direction of the minimum principal stress (see Section 4.5.2). Recall that the honeycomb microstructure is composed of thin plates. When combinations of shear and normal stresses are applied to a single thin plate, buckles form perpendicular to the compressive principal stress (Fig. 64b). Under large deformations, these buckles transform into deeper folds; in order to minimize the membrane stretching, the plate shortens macroscopically as the material 'flows into the fold' (Fig. 64c). This simple mechanism suggests an explanation as to why the plastic flow in a honeycomb is fairly close to the direction of the macroscopic compressive principal stress.

To incorporate this phenomenological flow rule in our present model, we calculate the direction of the principal stress based on the stress vector $\boldsymbol{\sigma}$. The direction of the principal stress is found from the spectral decomposition of the corresponding stress tensor into its eigenvalues σ_I, σ_{II}, σ_{III} and its eigenvectors $\mathbf{t}^I$, $\mathbf{t}^{II}$, $\mathbf{t}^{III}$:

$$\begin{aligned} &\tau_{TW}(\mathbf{e}_1 \otimes \mathbf{e}_3 + \mathbf{e}_3 \otimes \mathbf{e}_1) + \tau_{TL}(\mathbf{e}_2 \otimes \mathbf{e}_3 + \mathbf{e}_3 \otimes \mathbf{e}_2) + \sigma_{TT}(\mathbf{e}_3 \otimes \mathbf{e}_3) \\ &= \sigma_I \mathbf{t}^I \otimes \mathbf{t}^I + \sigma_{II} \mathbf{t}^{II} \otimes \mathbf{t}^{II} + \sigma_{III} \mathbf{t}^{III} \otimes \mathbf{t}^{III} \end{aligned} \tag{94}$$

After ordering the eigenvalues such that $\sigma_I \leq \sigma_{II} \leq \sigma_{III}$, the direction of plastic flow is given by the eigenvector $\mathbf{t}^I = \mathbf{t}^I(\boldsymbol{\sigma})$ corresponding to the smallest eigenvalue:

$$\mathbf{r} = -sign(t_3^I)\mathbf{t}^I(\boldsymbol{\sigma}) \tag{95}$$

The sign correction guarantees that the vector $\mathbf{r}$ points away from the yield surface. Fig. 65 compares the direction of plastic flow according to Eq. (95) with the experimental

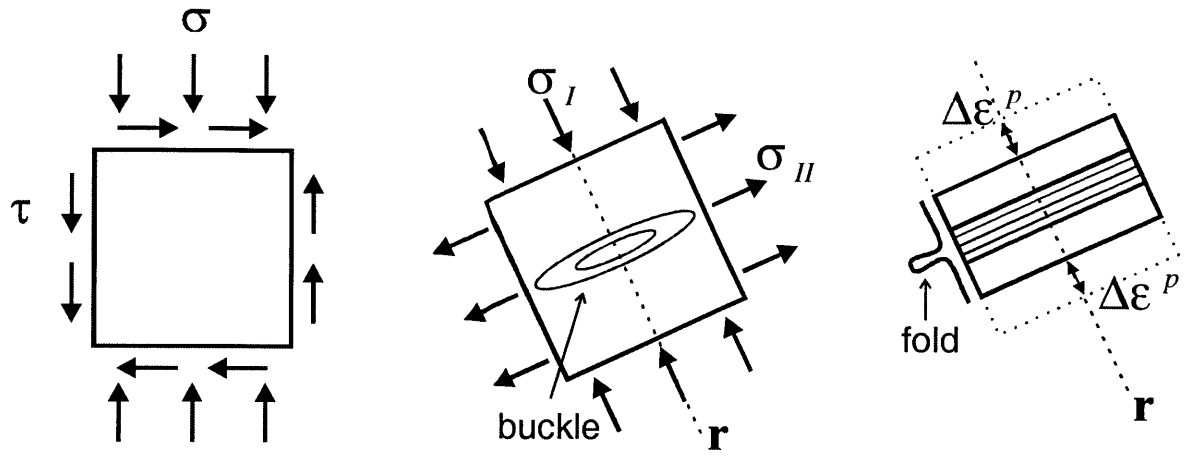

(a) (b) (c)

Fig. 64. Single plate under combined compression and shear: (a) stress state in terms of shear and normal stress, (b) corresponding principal stress state, (c) post-buckling response.

results as well as with the prediction for the normality flow rule. The assumption of plastic flow in the direction of the minimum principal stress yields satisfactory results for the behavior of the 'monolithic honeycomb' that was considered in the virtual experiments. However, in a real honeycomb, the microstructural deformation mechanisms are perturbed by the intercellular delamination between neighboring cell walls as well as local cell wall fracture. Such microstructural effects change the driving stress state in the cell walls. In our model, this effect is taken into account by introducing the flow rule parameter $\Delta\sigma_r$ into the flow rule. It allows for the adjustment of the direction of plastic flow. Instead of using the stress state described by the stress vector $\boldsymbol{\sigma}$, we use the perturbed stress vector $\boldsymbol{\sigma}+\Delta\sigma_r\mathbf{e}_3$ as basis for the calculation of the direction of plastic flow. Formally, we rewrite Eq. (95):

$$\mathbf{r}(\boldsymbol{\sigma}) = -sign(t_3^I)\mathbf{t}^I(\boldsymbol{\sigma}+\Delta\sigma_r\mathbf{e}_3) \tag{96}$$

The calibration of the flow rule parameter $\Delta\sigma_r$ is discussed in Section 5.3.1. Regarding thermodynamics, it must be noted that the present combination of flow rule and yield surface fulfills the non-negativity requirement for the intrinsic dissipation. However, the

model may not be applied in loading situations with normal tensile loads ($\sigma_{TT} > 0$). Firstly, the mechanisms change under tension along the T-direction and consequently both the yield surfaces as well as the flow rule no longer apply. Secondly, as the plastic strain rate is always negative according to our flow rule $d\varepsilon_{TT}^{p} \leq 0$, the product of normal stress and normal strain rate is negative for tension ($d\varepsilon_{TT}^{p}\sigma_{TT} \leq 0$). Thus, depending on the shear dissipation, the total plastic dissipation might become negative which would violate the non-negativity requirement for the intrinsic dissipation (Eq. (86)).

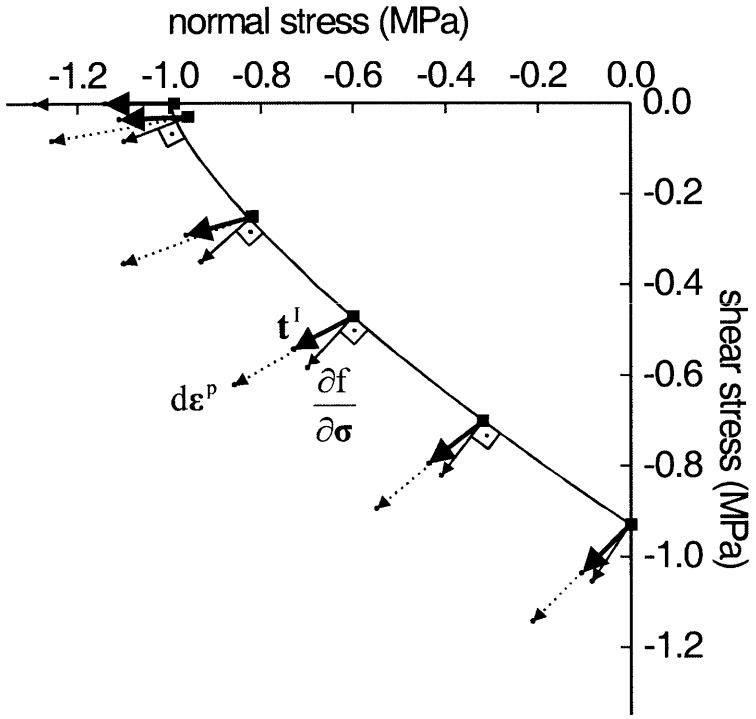

Fig. 65. Direction of plastic flow at various points on the yield surface (virtual experiments). The dashed vectors show the experimentally measured direction $d\boldsymbol{\varepsilon}^{p}$, the thin solid vectors $\partial f / \partial \boldsymbol{\sigma}$ represent the prediction according to normality flow rule, while the thick solid vectors indicate the direction of the minimum principal stress $\mathbf{t}^{I}$.

5.2.7 Strain hardening - densification

The deformation resistance remains constant throughout the crushing regime where the components of the deformation resistance vector correspond to the plateau stresses, $\mathbf{s}^0 = \{s_{TW}^0, s_{TL}^0, s_{TT}^0\}^T$. Significant strain hardening is characteristic for the densification regime, where cell wall contact within the microstructure continually rises the load carrying capacity of the honeycomb. We extend the results from uniaxial experiments to the multiaxial case by relating the strain hardening to the plastic strain along the T-direction, ε_{TT}^p and by assuming a geometrically self-similar evolution of the yield surface. The evolution equation for the deformation resistance vector $\mathbf{s}$ reads:

$$d\mathbf{s} = d\lambda \mathbf{q} \tag{97}$$

where we have the initial condition

$$\mathbf{s}(\varepsilon_{TT}^p = 0) = \mathbf{s}^0 \tag{98}$$

and

$$\left.\begin{aligned} \mathbf{q} &= \mathbf{0} && \text{for } \varepsilon_{TT}^p \geq \varepsilon_d \\ \mathbf{q} &= \frac{h_d}{1+\varepsilon_{TT}^p}\frac{r_3}{s_{TT}^0}\mathbf{s}^0 && \text{for } \varepsilon_{TT}^p < \varepsilon_d \end{aligned}\right\} \tag{99}$$

h_d is the densification modulus. The factor $h_d / 1+\varepsilon_{TT}^p$ is introduced based on the results from uniaxial experiments (Mohr and Doyoyo, 2003).

5.2.8 Consistency condition

We write the consistency condition formally as:

$$df = 0 \tag{100}$$

The consistency condition allows for the determination of the plastic multiplier $d\lambda$.

5.2.9 Objectivity

A change of observer does not affect the present formulation as all equations are given in material coordinates. Thus, we limit our attention to the verification of objectivity under rigid body rotations. Under a rigid body rotation $\mathbf{Q}$, the deformation gradient transforms as

$$\mathbf{F} \rightarrow \mathbf{QF} \tag{101}$$

According to the decomposition of the deformation gradient defined in Eq. (65), we have

$$\mathbf{R} \rightarrow \mathbf{QR} \tag{102}$$

$$\mathbf{U} \rightarrow \mathbf{U} \tag{103}$$

and hence

$$\mathbf{E} \rightarrow \mathbf{E} \tag{104}$$

which implies that the elastic and plastic strain vectors remain invariant under rigid body rotation:

$$\boldsymbol{\varepsilon}^e \rightarrow \boldsymbol{\varepsilon}^e \tag{105}$$

$$\boldsymbol{\varepsilon}^p \rightarrow \boldsymbol{\varepsilon}^p \tag{106}$$

The Cauchy stress tensor transforms objectively under rigid body rotation

$$\mathbf{T} \rightarrow \mathbf{QTQ}^T \tag{107}$$

while the engineering stress tensor remains unaltered:

$$\mathbf{T}^* \rightarrow (\det \mathbf{U})(\mathbf{QR})^T \mathbf{QTQ}^T (\mathbf{QR})\mathbf{U}^{-T} = (\det \mathbf{U})\mathbf{R}^T \mathbf{TRU}^{-T} = \mathbf{T}^* \tag{108}$$

In what follows that the engineering stress vector is frame-indifferent as well:

$$\boldsymbol{\sigma} \rightarrow \boldsymbol{\sigma} \tag{109}$$

The objectivity of the computational model is shown in Appendix B.

5.3 Application

A user-subroutine for the finite element code Abaqus/explicit (HKS, 2001) has been developed to utilize the present constitutive model in structural applications. Details of the numerical integration of the constitutive equations are presented in Appendix A. In this section, we use the constitutive model to perform finite element simulations of various experiments on metallic honeycomb and compare the response curves with experimental data.

5.3.1 Identification of model parameters

The elastic moduli G_{TW}, G_{TL}, and E_{TT} are directly determined from the micromechanical models that are summarized in the textbook by Gibson and Ashby (1997). The plateau normal stress s_{TT}^0, the densification strain ε_d, and the hardening modulus h_d are conveniently found from a uniaxial compression test (Fig. 61). The identification of the remaining plastic properties, namely the plateau shear stresses s_{TW}^0 and s_{TL}^0, the shear exponent m, and the flow rule parameter $\Delta\sigma_r$ requires tests under combined normal and shear loading or, if $m = 1.0$ is assumed, at least one shear test is necessary. The model calibration involves two steps:

1. Fit of the yield surface to the experimental data (determination of s_{TW}^0, s_{TL}^0, m)
2. Fit of the flow rule to the experimental data (determination of $\Delta\sigma_r$)

The first step is a standard data fitting procedure. The correct fitting of the flow rule parameter on the other hand requires careful analysis of the experimental data. Consider combined shear and normal loading in the T-W-plane ($\boldsymbol{\sigma} = \tau_{TW}\mathbf{e}_1 + \sigma_{TT}\mathbf{e}_3$) along a linear monotonic strain path under compression in the crushing regime along ($\sigma_{TT} \le 0, d\lambda > 0$):

$$\frac{d\varepsilon_{TT}}{d\gamma_{TW}} = -sign(\tau_{TW})\tan\alpha \qquad \text{and} \qquad \gamma_{TL} = 0 \tag{110}$$

where $\alpha \in [0, \pi/2]$ denotes the biaxial loading angle. In the crushing regime, we have steady state conditions, characterized by

$$\left.\begin{aligned} d\boldsymbol{\sigma} &= \mathbf{0} \\ d\mathbf{s} &= \mathbf{0} \end{aligned}\right\} \tag{111}$$

It follows from the elastic constitutive equation (Eq. (85)) that $d\boldsymbol{\sigma} = \boldsymbol{C}(d\boldsymbol{\varepsilon} - d\boldsymbol{\varepsilon}^p)$ and hence $d\boldsymbol{\varepsilon} = d\boldsymbol{\varepsilon}^p$. Thus, the stress state $\boldsymbol{\sigma}$ is determined by the following equations:

$$\mathbf{r}(\boldsymbol{\sigma}) = \frac{d\boldsymbol{\varepsilon}}{d\lambda} = \frac{d\boldsymbol{\varepsilon}^p}{d\lambda} \tag{112}$$

$$f(\boldsymbol{\sigma}) = 0 \tag{113}$$

In other words, under steady state conditions, the solution $\boldsymbol{\sigma}$ is the point on the yield surface for which the direction plastic flow $\mathbf{r}(\boldsymbol{\sigma})$ coincides with the direction of the applied total strain increment $d\boldsymbol{\varepsilon}$. This coaxiality is achieved by adjusting the flow rule parameter $\Delta\sigma_r$. For combined loading in the T-W-plane, the direction of plastic flow reads

$$\mathbf{r} = sign(\tau_{TW})\cos\chi\mathbf{e}_1 - \sin\chi\mathbf{e}_3 \tag{114}$$

where the angle χ between the W-axis and the direction of flow is given by

$$0 \le \chi < \pi/2: \qquad \tan 2\chi = \frac{2|\tau_{TW}|}{\sigma_{TT} + \Delta\sigma_r} \tag{115}$$

Figure 66 shows the direction of plastic flow as a function of the stress state. According to the sign function in Eq. (114), the right quadrant applies to negative shear stresses, whereas the left quadrant must be considered for positive shear stresses. For $0 < \chi < \pi/4$, we have tension and shear, while the interval $\pi/4 < \chi < \pi/2$ applies to combined compression and shear. The limiting cases $\chi = 0$, $\chi = \pi/4$, and $\chi = \pi/2$ correspond to uniaxial tension, pure shear, and uniaxial compression, respectively. To continue our discussion, we rewrite Eq. (114), which yields

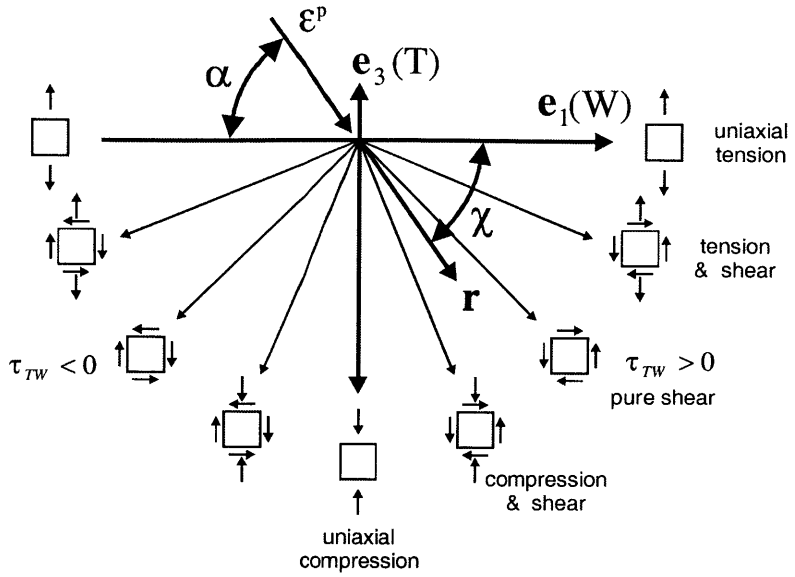

Fig. 66. Direction of the minimum principal stress under combined loading in the T-W-plane ($\mathbf{e}_1$=W-direction, $\mathbf{e}_3$=T-direction)

$$\frac{r_3}{r_1} = -sign(\tau_{TW}) \tan \chi \tag{116}$$

Furthermore, it follows from Eq. (112) that

$$\frac{r_3}{r_1} = \frac{d\varepsilon_{TT}}{d\gamma_{TW}} \tag{117}$$

Now, applying Eqs. (110), (116) and (117), we find:

$$\tan \chi = \tan \alpha \tag{118}$$

Figure 67 illustrates the equations above. Consider the experimental data point $(\sigma^*_{TT}, \tau^*_{TW})$ for a biaxial test at a fixed loading angle $\alpha^* = 50^o$. It lies on the yield surface described by Eq. (91) and thus fulfills Eq. (113). To satisfy Eq. (112), we calculated the stress paths for which the direction of flow given by Eq. (114) coincides with the loading direction. Combining Eqs. (115) and (118), we have

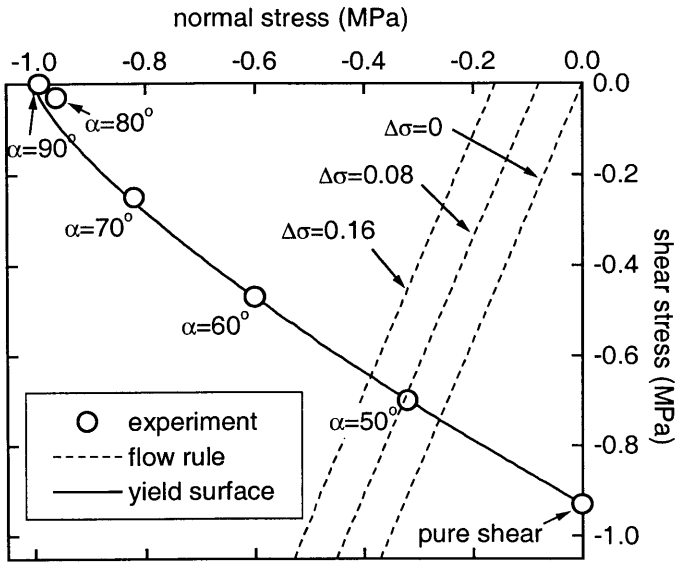

Fig. 67. Model calibration from the results of the virtual experiments in the crushing regime. The labels next to the open circles denote the biaxial loading angle. The units of the shift stress $\Delta\sigma$ are MPa.

$$|\tau_{TW}| = \tfrac{1}{2}(\sigma_{TT} + \Delta\sigma_r)\tan 2\alpha^* \tag{119}$$

in what follows:

$$\Delta\sigma_r = \frac{2|\tau^*_{TW}|}{\tan 2\alpha^*} - \sigma^*_{TT} \tag{120}$$

We plotted Eq. (119) for different $\Delta\sigma_r$ in Fig. 67. The plot for $\Delta\sigma_r = 0$ shows the result for the mechanism-based assumption of plastic flow along the direction of the minimum principal stress. The corresponding dashed line intersects the yield envelope at a normal stress slightly higher than in the experiment. However, introducing a perturbation of $\Delta\sigma_r = 0.08MPa$ changes the direction of flow such that the model prediction coincides with the experimental data point, whereas the use of $\Delta\sigma_r = 0.16MPa$ would result in an underestimation of the normal stress under 50° loading.

In the case of pure shear in the T-W-plane ($\boldsymbol{\sigma} = \tau_{TW}\mathbf{e}_1$), the flow rule parameter affects the shear-induced dilatation along the T-direction. We introduce the dilatancy parameter β_{TW} to express the ratio of normal and shear strains under pure shear loading ($d\boldsymbol{\sigma} = d\tau_{TW}\mathbf{e}_1$):

$$\beta_{TW} := \frac{d\varepsilon_{TT}^p}{\left|d\gamma_{TW}^p\right|} = -\tan\chi \qquad \text{and} \qquad \tan 2\chi = \frac{2\left|\tau_{TW}\right|}{\Delta\sigma_r} \tag{121}$$

For $\Delta\sigma_r = 0$, we have $\chi = 45^o$ and thus $\beta_{TW} = -1$ (shear-induced compaction). In other words, the amount of shear and compressive deformation are identical under pure shear loading. For $\Delta\sigma_r < 0$, we increase the amount of shear-induced normal deformation, whereas for $\Delta\sigma_r > 0$, it is reduced. In analogy with Eq. (121), the shear dilatancy parameter β_{TL} may be introduced for the case of pure shear loading in the T-L-plane.

5.3.2 Uniaxial compression

We simulate the uniaxial compression experiments on hexagonal aluminum 5056-H39 honeycomb, where block specimens (195x195x200mm) have been subjected to quasi-static loading along the T-direction (Mohr and Doyoyo, 2003). The honeycomb had a cell size $D = 4.75mm$, a single cell wall thickness $t = 33\mu m$, and 1.8% relative density. Fig. 68 shows the force displacement curves for the experiment and for the numerical simulation with the model parameters $s_{TT}^0 = 0.92MPa$, $\varepsilon_d = 0.82$ and $h_c = 10.2MPa$ (Table 5). The part of the model to be verified by this simulation is the evolution law for the deformation resistance (Eq. (99)). The good correlation of the experimental and numerical results in the densification regime supports the choice of the densification law.

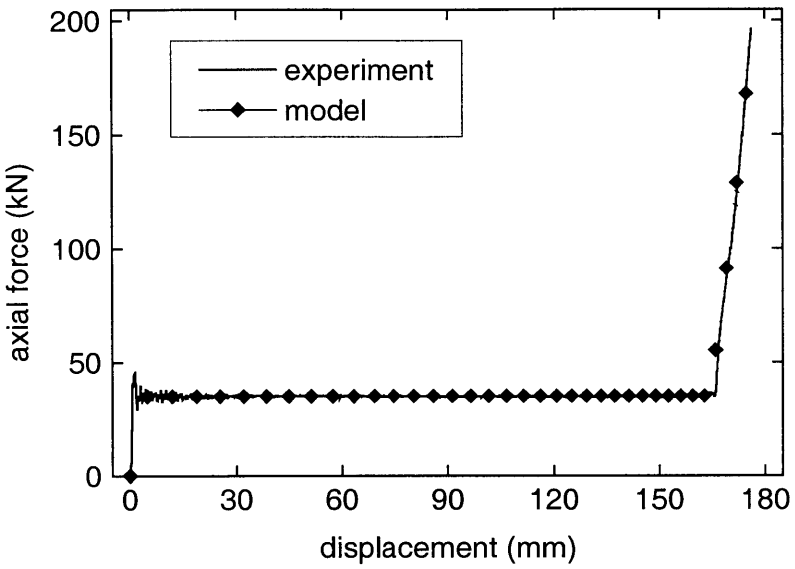

Fig. 68. Axial force (compression) vs. displacement in a uniaxial compression experiment of cubic specimens.

experiment type	s^0_{TW} (MPa)	s^0_{TT} (MPa)	m (-)	ε_d (-)	h_d (MPa)	$\Delta\sigma$ (MPa)
uniaxial (physical)	-	-0.93	-	0.82	10.7	-
combined (virtual)	0.93	-1.0	1.35	0.82	10.7	0.08
combined (physical)	0.51	-0.93	1.40	0.82	10.7	0.30

Table 5. Material properties and model parameters.

5.3.3 Combined compression and shear

Here, we simulate experiments where the honeycomb is loaded along a constant strain path in the T-W-plane and the corresponding stress states in the crushing regime are combined compression and shear ($\sigma_{TT} \leq 0$). The schematic in Fig. 69 illustrates this loading condition. It is characterized by the biaxial loading angle α (see Eq. (110)). We use two sets of experimental data for the validation of the constitutive model. The first is taken from physical experiments (see Chapter 3) performed on the same aluminum honeycomb that was used in the uniaxial compression tests. The second data set was obtained from so-called 'virtual experiments' (see Chapter 4). In virtual experiments, the entire cellular microstructure of a honeycomb specimen is discretized with three-dimensional shell elements; subsequently a non-linear finite element analysis is performed to determine its mechanical behavior under various loading conditions. The honeycomb considered in the virtual experiments is the monolithic version of the physically tested aluminum 5056-H39 honeycomb. Note that the manufacture of honeycombs in the expansion process requires a bond line between neighboring cell walls aligned with the L-direction. This bond partially fails under large deformations and thus

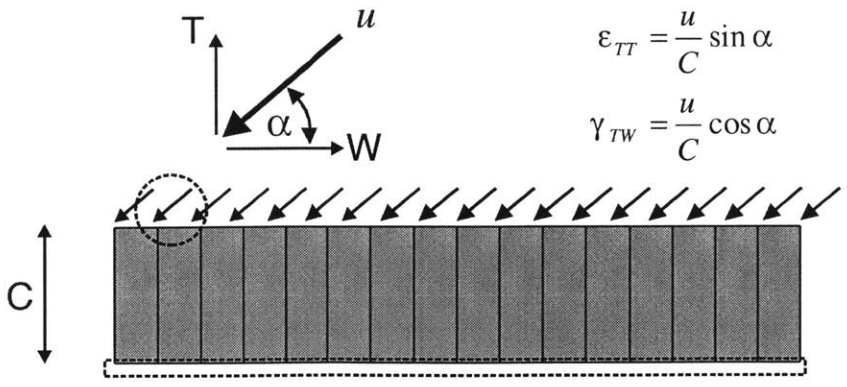

Fig. 69. Schematic of biaxial test.

reduces the macroscopic strength of the honeycomb. The honeycomb considered in the virtual experiments, however, has a perfect bond and hence represents a monolithic honeycomb.

Virtual experiments

Figure 67 depicts the experimental data points for the plateau stresses in the $\sigma_{TT} - \tau_{TW}$ - plane. Each data point represents the result of a virtual experiment under the biaxial loading angle as indicated by its label. The solid line highlights a fit of the yield surface (Eq. (91)) to the data. We have $s_{TT}^0 = -1.0MPa$, $s_{TW}^0 = -0.93MPa$ and $m = 1.35$. As exemplary shown above, we calibrated the flow rule for $\Delta\sigma_r = 0.08MPa$, which corresponds to a shear dilatancy factor of $\beta_{TW} = -0.96$. Note that $\Delta\sigma_r$ is the only fitting parameter for the flow rule, but at the same time Eq. (120) must be satisfied for six different experiments. Here, the shift stress found from a fit for $\alpha = 50^o$ also presents a satisfactory approximation for the remaining data. According to the definition of the plateau stresses, the model correctly describes the mean shear stress under pure shear loading (Fig. 70(a)). The constitutive model assumes a constant shear dilatancy ratio. This assumption agrees well with the experiments at large shear strains, but cannot capture the initial non-linearity in the experimental shear vs. normal strain curve (Fig. 70(b)). The results for larger biaxial loading angles are summarized in Fig. 71(a)-(h). The initial peaks observed in experiments are not present in the model results as they are not part of the constitutive formulation. Experiments and simulations agree well in the crushing regime; the mean stress level that is determined by the interaction of yield surface and flow rule is successfully represented. The results are poor for loading angles where the concept of plateau stresses does not fully apply. For instance, observe that the shear response under 80° loading shows significant fluctuations with respect to its mean value.

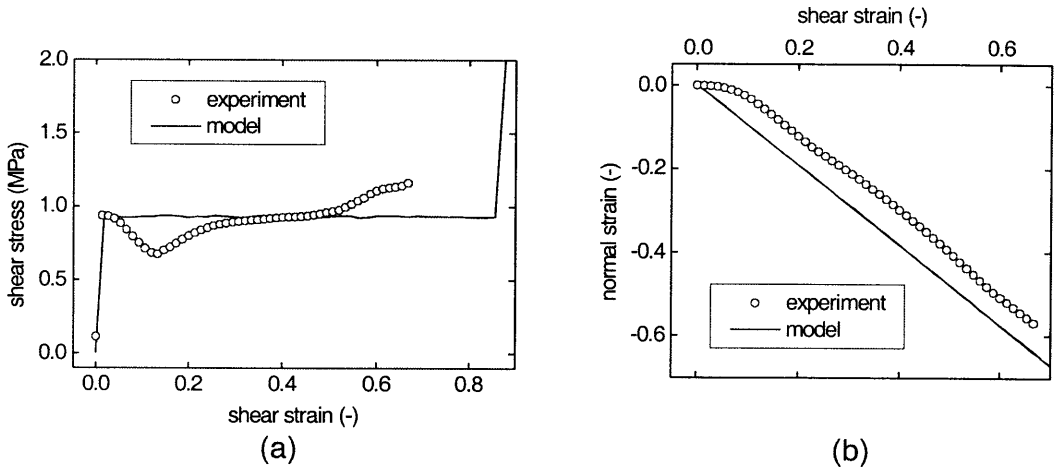

Fig. 70. Simulation of the virtual experiments for pure shear loading ($\sigma_{TT} = 0$). (a) shear stress vs. shear strain, (b) normal strain vs. shear strain.

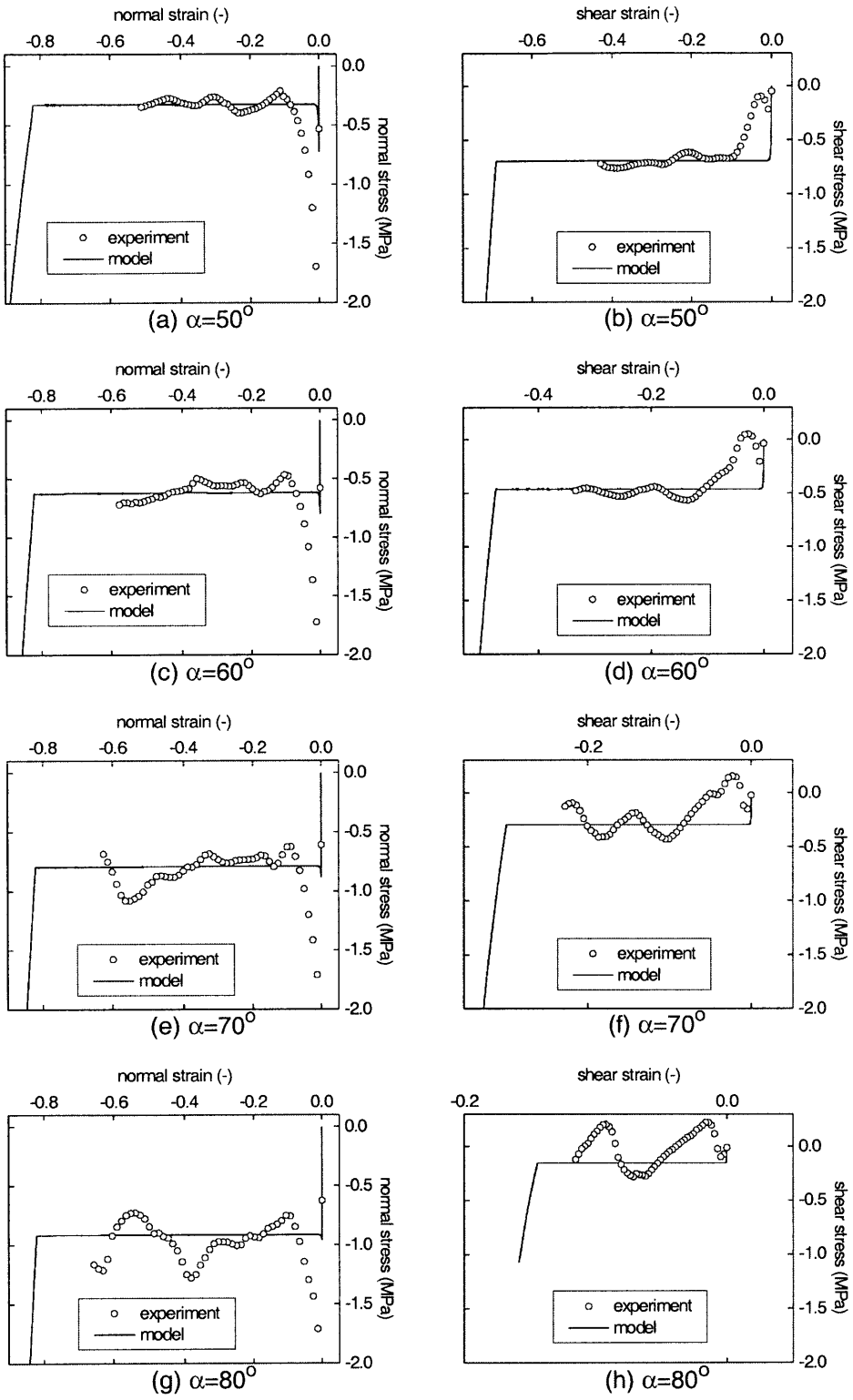

Fig. 71. Simulation of the virtual experiments under combined loading.

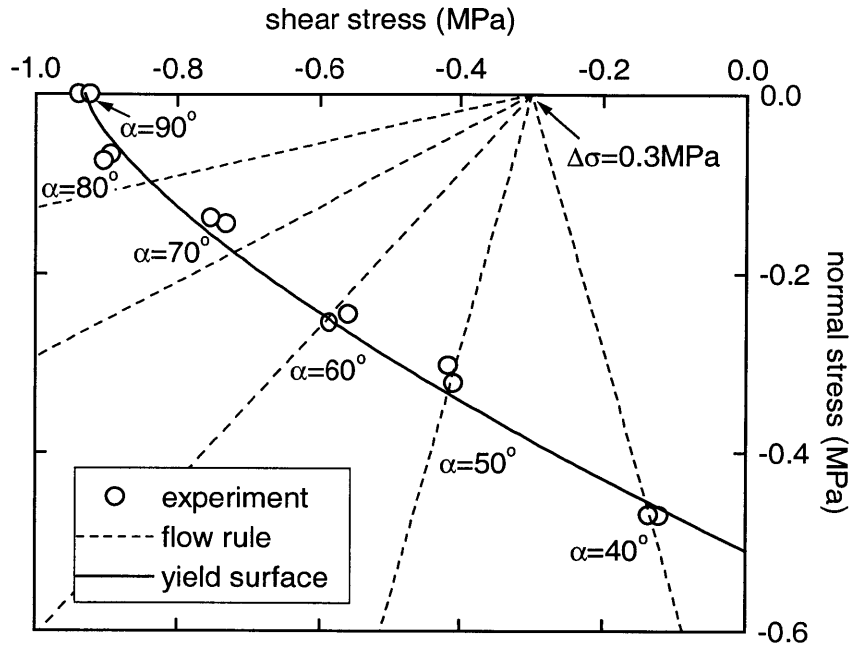

Fig. 72. Model calibration for the physical experiments.

Physical experiments

The plateau stresses determined from biaxial tests under 40°, 50°, 60°, 70°, and 80° loading are depicted in Fig. 72. The yield envelope is described by $s_{TT}^{0} = -0.93MPa$, $s_{TW}^{0} = 0.51MPa$ and $m = 1.40$. Best overall fit of the flow rule is found for $\Delta\sigma = 0.3MPa$, that is $\beta_{TW} = -0.75$. The dashed lines in Fig. 72 represent the flow rule as described by Eq. (119). The intersection points of the dashed lines with the yield envelope provide the model prediction corresponding to the nearest experimental data points. Again, we emphasize that we have five independent tests, but only one model fitting parameter for the flow rule.

Figure 73 demonstrates the excellent agreement of the experimental results and model predictions. As compared to the stress-strain curves for the virtual honeycomb, the fluctuation in the response curves of the physical experiments are smaller and thus, the concept of plateau stresses yields a good approximation for all loading angles.

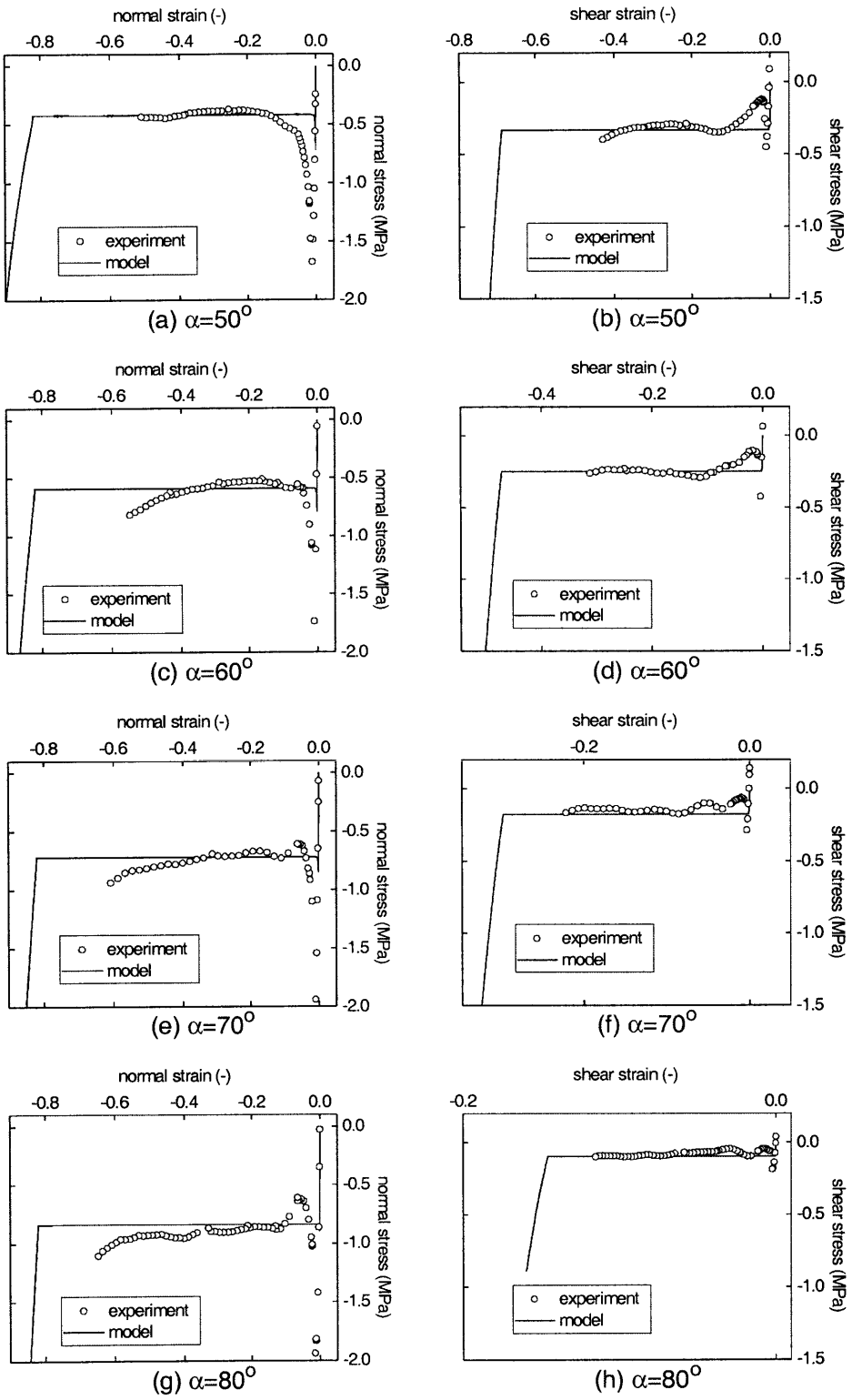

Fig. 73. Simulation of the physical experiments for combined loading.

5.3.4 Limitations

The generic term 'metallic honeycomb' stands for a large family of cellular materials with two-dimensional periodic microstructures. One example is the hexagonal thin-walled aluminum honeycombs that was investigated here. The backbone of the present constitutive model is the concept of plateau stresses. Throughout the empirical development of the phenomenological constitutive model, we used the results from the virtual and physical experiments presented above. The benefit of the present model in different applications must be shown in the future. There are various known and anticipated limitations of the present constitutive model that are noteworthy:

- *Tension.* The model does not provide reliable predictions when tensile stresses are applied along the T-direction. The experiments described in Chapter 2 have shown that the constitutive response under tension is dramatically different from that under compression. For simplicity, we did not include the tensile behavior. Moreover, most practical applications do not include tension as it is rather rare that out-of-plane tensile loads are applied to a honeycomb.

- *Fracture.* For example, impact honeycomb barriers for passenger car crash tests frequently show fracture. As for other engineering materials, fracture of honeycomb requires special treatment in terms of modeling. In particular, the influence of large in-plane deformation is expected to come into play.

- *Strain rate effects.* Strain rate effects on the macroscopic level are expected at high loading velocities where the lateral inertia of the folding cell walls influences the folding mechanics of the microstructure. The applicability of the concept of plateau stresses must be carefully examined for high loading velocities.

- *Deformation-induced anisotropy and evolving elastic moduli.* Recall the assumptions made in the elastic part of the constitutive equations. Metallic honeycomb becomes fully anisotropic under large deformations, which goes along with a change of its elastic moduli. Thus, the simple hyperelastic law adopted here does not allow for an analysis of the wave propagation or other

phenomena that require an accurate description of the variation of the elastic strain energy.

5.4 Conclusion

A three-dimensional finite-strain orthotropic rate-independent constitutive model for thin-walled metallic honeycomb has been developed. The foundation of the model is the experimental observation of plateau stresses in the crushing regime of the honeycomb under large displacements. The constitutive model comprises a conical yield surface in the shear normal stress space along with a non-associated flow rule. The model has been incorporated into a finite element code and has been successfully employed to predict the mechanical response of physical and virtual honeycomb specimens under various loading conditions. The limitations of the model have also been discussed in detail.

Chapter 6

Crashworthiness of sandwich structures

6.1 Introduction

Standard sandwich technology focuses on engineering applications where the total thickness of sandwich core and facings ranges from several millimeters to several decimeters. Examples include façade elements for high-rise buildings, blast mitigation systems for battle ships, or ultra-light composite sandwich panels in aircrafts. The underlying structural concept is to separate two face sheets by a light core material, thereby significantly increasing the overall bending stiffness per unit weight. The core material contributes only little to the overall sandwich bending stiffness, but controls the sandwich deflection due to shear loading. Thus, optimized sandwich core materials must typically provide a required shear stiffness at a minimum weight. In automotive engineering, *thin* sandwich sheet materials with a total thickness of about one millimeter provide possible alternatives to sheet metals. The high specific bending stiffness of sandwich sheets may be beneficial for large shell structures of the car body, such as the roof, hood or floor panels. However, requirements with regard to their acoustic performance are seldom met because of sound transmission at joints. Within this study, we focus on thin-walled prismatic components assembled from thin sandwich profiles. Fig. 74 shows the cross-section of a double-cell sandwich profile. The sandwich design

objective is different from the traditional stiffness-based design: here, the sandwich material is introduced to increase the specific crashworthiness of the component.

First, we characterize the mechanical properties of the Hybrid Stainless Steel Assembly (HSSA), a thin sandwich sheet with a low density stainless steel fiber core. Double-cell profiles are built from this sandwich material and crushed under quasi-static loading. Based on previous work (Alexander, 1960; Wierzbicki and Abramowicz, 1983; Abramowicz and Wierzbicki, 1989), a theoretical model is developed, providing insight into the crushing mechanics of sandwich profiles. This model gives an explanation for the short folding wavelength that describes the crushing of soft-core sandwich profiles. The model also indicates that the crashworthiness of sandwich structures depends on the shear crushing strength of the core material, which leads to the subsequent conceptual comparative study on the specific shear crushing strengths of sandwich core materials such as the HSSA fiber core or metallic honeycombs. It appears that with respect to their specific energy absorption under large shear deformation, hexagonal metallic honeycombs outperform fiber cores - irrespective of their relative density or

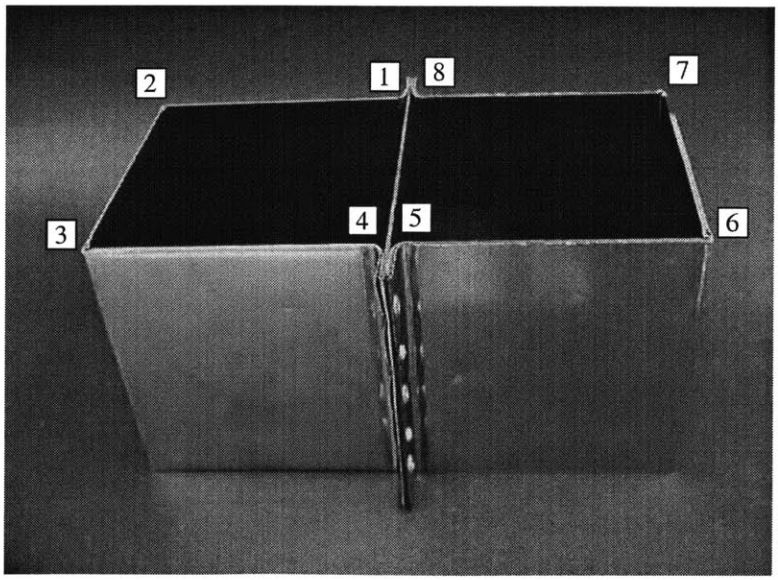

Fig. 74. HSSA double-cell profile after manufacturing. The eight 90-degree corners of the cross-section are labeled by roman numbers.

microstructural geometry.

An example is shown, where we propose a novel thin sandwich sheet with a 10% relative density micro-cell honeycomb core as weight-equivalent competitor to the HSSA sheet. We apply the modeling techniques developed in Chapters 4 and 5 of this thesis: the mechanical properties of the micro-cell honeycomb are estimated from virtual experiments, the constitutive model is calibrated and then used to simulate the crushing response of a prismatic profile made of the thin honeycomb sheet. The numerical results demonstrate a superior mechanical performance on the structural level: the predicted specific energy absorption found for the thin micro-cell honeycomb sheet is twice as high as for the same structure made of the HSSA sheet.

6.2 HSSA sandwich material properties

Flat prototype sheets of the Hybrid Stainless Steel Assembly (HSSA) were provided to us by HSSA Sweden AB. This novel sandwich material consists of two thin stainless steel faceplates (Type 304, AvestaPolarit, Sweden) that are connected by a fiber core (e.g. Gustafsson, 2000). The prototype samples that were used for this study had a facing thickness of $t_f = 0.2mm$ and a fiber core thickness of $C=0.8mm$ (Fig. 75). Thus, the total sandwich thickness was $1.2mm$. The basic elements of the core are stainless steel fibers of $25\mu m$ diameter, cut to $0.8mm$ length. Using an electrostatic field, these fibers are oriented perpendicular to the facings. A thin layer of adhesive (Betamate, Dow Automotive AG, Switzerland) bonds the oriented fibers to either facing. The density of the fiber core (including the adhesive) is approximately $\rho^*=0.78\ g/cm^3$. With respect to the density of the solid stainless steel fibers, ρ_s, this corresponds to a relative density of $\rho^*/\rho_s=10\%$.

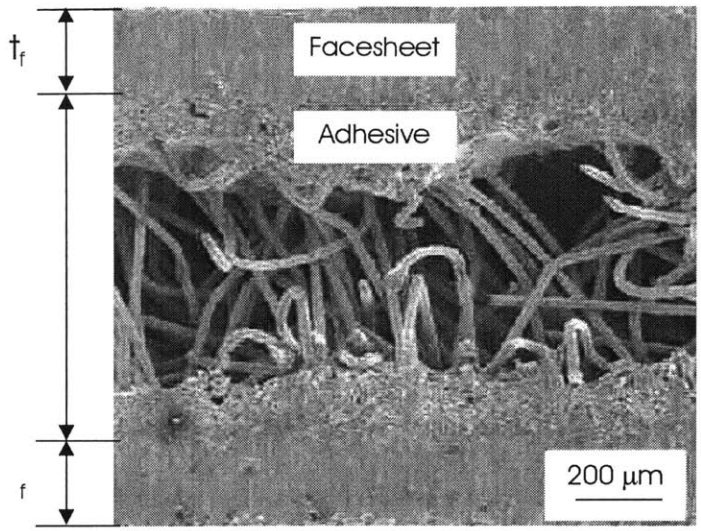

Fig. 75. Micrograph of the Hybrid Stainless Steel Assembly (HSSA); Courtesy of Markaki and Clyne, Cambridge University.

6.2.1 Facing tensile properties

There are two ways to determine the (in-plane) tensile properties of a sandwich material. One can either test the whole sandwich sheet under uniaxial tension or determine the tensile properties of the sandwich from separate tests on the core and facings. Here, the results from tensile tests on the sandwich sheet as well as on the facings were similar, indicating that the oriented microstructure of the HSSA fiber core contributes only little to the tensile properties of the sandwich sheet. Fig. 76 shows the stress-strain curve as obtained from tension tests on flat dogbone specimens.

The yield stress of the stainless steel facings is σ_y=*290MPa* and the uniaxial engineering strain at failure is $\varepsilon_f = 0.47$ (Fig. 76). For subsequent crush calculations, we determine the energy equivalent yield stress, σ_0, defined as

$$\sigma_0 = \frac{1}{\varepsilon_f}\int_0^{\varepsilon_f} \sigma(\varepsilon)d\varepsilon \,. \tag{122}$$

For the ductile, strain hardening stainless steel facings, we find $\sigma_0 = 591MPa$ by integrating the stress-strain function shown in Fig. 76.

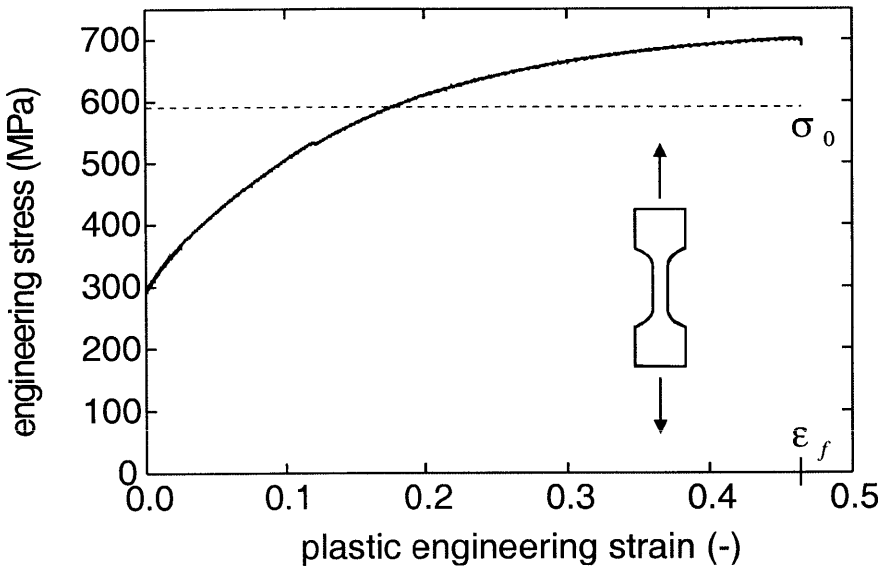

Fig. 76. Stress-strain curve of the stainless steel face sheets. The dashed line corresponds to the energy equivalent yield stress, σ_0.

6.2.2 Fiber-core shear properties

The shear properties of the HSSA fiber core play an important role on the mechanical behavior of structures built from HSSA sheets. In particular for the subsequent crush analysis it is important to determine the response to large shear distortions. The Enhanced Arcan Apparatus (EAA), developed for the biaxial testing of cellular solids, was used to measure the shear properties of the HSSA fiber core. The enhanced Arcan jig applied a

displacement loading parallel to the facings of the HSSA core, whereas the displacement normal to the facings was not restricted, i.e. the corresponding stress resultant was zero. Fig. 77 illustrates the displacement loading and shows the resultant forces that acted on the HSSA shear specimen.

Assuming a homogeneous stress distribution, we evaluate the shear stress

$$\tau = \frac{F_s}{A}, \tag{123}$$

where $A = 105mm^2$ is the cross-sectional area of the shear specimen. As work conjugate shear distortion, we introduce

$$\gamma = \frac{u_s}{C}, \tag{124}$$

where u_s denotes the shear displacement that is applied by the apparatus. Fig. 78 shows the shear stress as a function of the engineering shear distortion. The shear stress increases almost linearly until the load attains its maximum at a shear distortion of about $\gamma = 0.4$. Subsequently, the shear carrying capacity decays monotonically due to fracture and pull-out of individual fibers. Analogously to the energy equivalent yield stress of the facings, we introduce the concept of the 'energy equivalent shear stress' τ_0 for the core material, using the following definition:

$$\tau_0 = \int_0^1 \tau(\gamma) d\gamma \tag{125}$$

Conceptually, the core is fully shear crushed at a distortion of $\gamma = 1$. Therefore, τ_0 can be considered as the mean shear stress throughout the shear crushing of the core material. From our tests, we find $\tau_0 = 0.8MPa$.

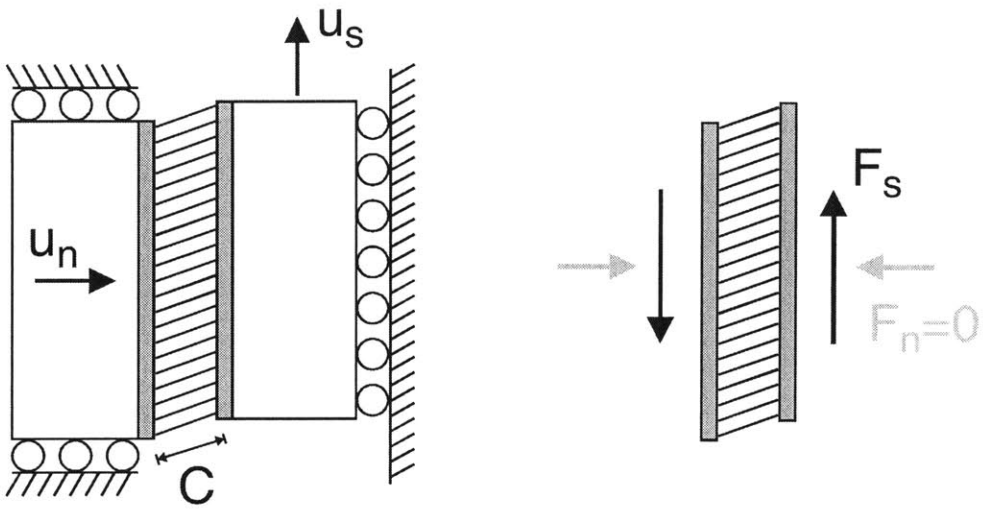

(a) (b)

Fig. 77. Schematic of the shear test on the HSSA fiber core; (a) displacement loading, (b) stress resultants acting on the HSSA fiber core.

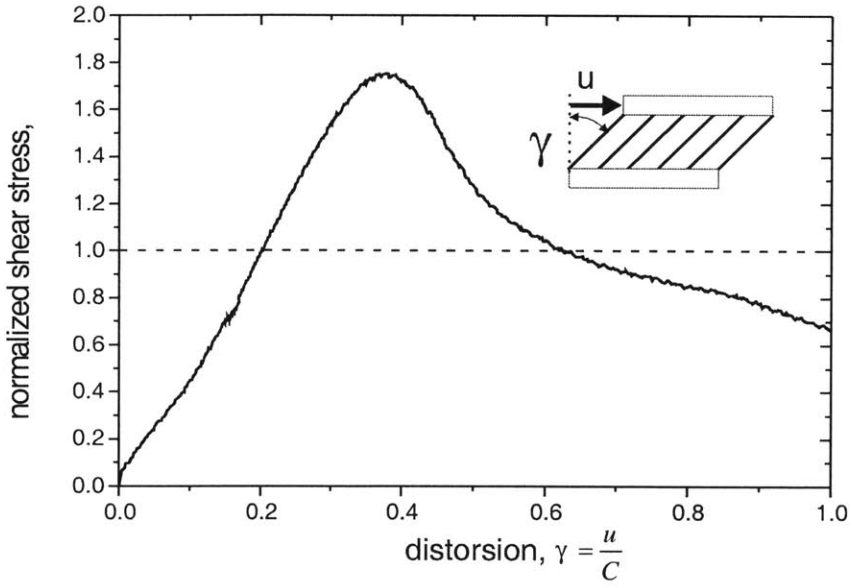

Fig. 78.Shear stress τ, normalized by the energy equivalent shear stress τ_0, plotted as a function of the energy conjugate distortion γ.

6.2.3 Sandwich sheet bending properties

Another important sandwich property that determines the crushing behavior of sandwich structures is the fully plastic bending moment of the cross-section. The fully plastic bending moment of sandwich beams is commonly defined as

$$M_0^{rigid} = \sigma_0 t_f (C + t_f) . \tag{126}$$

The definition given in Eq.(126) must be used with care when shear forces are present. The underlying assumption of the above definition is a shear-rigid core behavior (Fig. 79(a)), i.e. cross-sections remain plane and perpendicular to the mid-plane of the profile walls (Kirchhoff-Love hypothesis). However, due to the finite shear strength of sandwich core materials, large shear distortions can dramatically reduce the fully plastic bending moment of a sandwich beam. In the case of shear-soft core behavior (Fig. 79(b)), the plastic bending moment is given by the sum of the fully plastic bending moments of either facing,

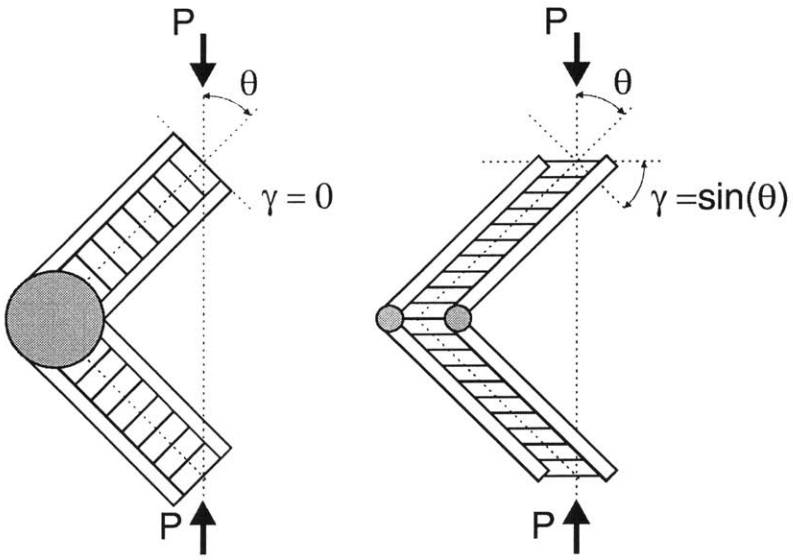

(a) (b)

Fig. 79. Sandwich folding modes as a function of the core properties. (a) shear-rigid core and (b) shear-soft core.

$$M_0^{soft} = 2 \cdot \tfrac{1}{4}\sigma_0 t_f^2 = \tfrac{1}{2}\sigma_0 t_f^2 , \tag{127}$$

which is associated with large shear deformations of the core material. The 'real' fully plastic bending moment of a sandwich beam, M_0, is expected to lie between these two limiting cases of shear-soft and shear-rigid behavior,

$$M_0^{soft} \le M_0 \le M_0^{rigid} . \tag{128}$$

For the given HSSA sandwich, we have $11.8\,Nm/m \le M_0 \le 118.2\,Nm/m$. The actual fully plastic bending moment is determined experimentally from tests on wide HSSA beams. As an alternative to simple beam bending tests, we chose uniaxial compression tests on HSSA strips that allow for the determination of the plastic bending moment and, at the same time, illustrate the characteristic buckling behavior of the HSSA sandwich. Rectangular strips were extracted from the flat HSSA panels. The width of the *1.2mm* thick specimens was $w = 12.8\,mm$. Mechanically roughened grips fixed the specimen on either end. The *free length*, i.e. the initial distance between the top and bottom fixture was $l = l_1 + l_2 = 70\,mm$ (Fig. 80). The axial displacement was applied at a constant crosshead velocity of *1mm/min*.

Fig. 81 shows a representative force-displacement curve for this test. After buckling in the elastic regime, the load decreased rapidly. The L-shape of the deformed specimen in the post-buckling regime (Fig. 80) corresponds to a shear type of failure mode (see e.g. Vinson, 1986). Throughout the *shear folding* of the HSSA strip, the rate of energy dissipated is the sum of the energy dissipation rate along plastic hinge lines, $\dot{E}_b^{beam}$, and the energy dissipation rate due to shear crushing of the core, $\dot{E}_s^{beam}$:

$$\dot{E}_{int}^{beam} = \dot{E}_b^{beam} + \dot{E}_s^{beam} = wM_0 \sum_i \dot{\theta}_i + wC\tau_0 \sum_i \dot{\gamma}_i l_i \tag{129}$$

Equating $\dot{E}_{int}^{beam}$ to the rate of external work, which is given by the product of the axial force F and the corresponding displacement rate,

$$\dot{E}_{ext}^{beam} = F\dot{u} \tag{130}$$

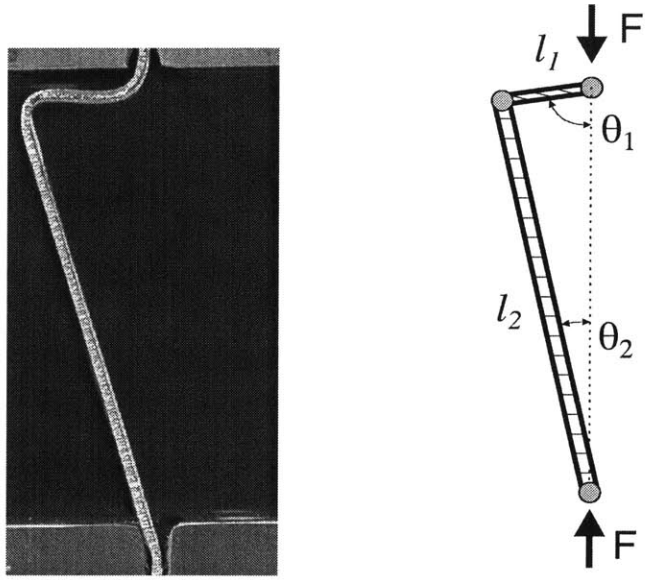

(a) (b)

Fig. 80. Shear folding of a sandwich beam under uniaxial compression, (a) experiment, (b) folding model.

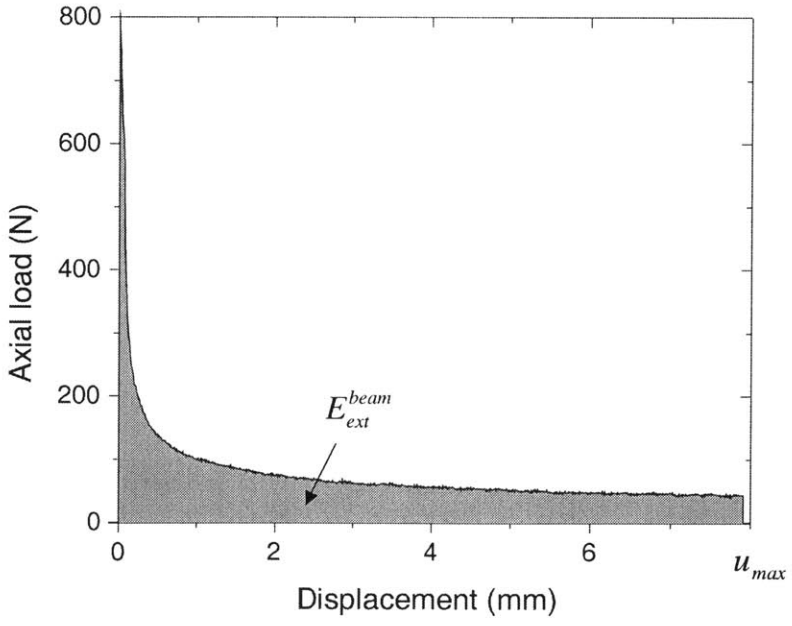

Fig. 81. Representative axial force vs. displacement curve for a HSSA beams under compression.

and integrating over the interval $[0, u_{max}]$, where u_{max} denotes the maximum displacement that was applied during the test, yields

$$\int_0^{u_{max}} F(u)du = wM_0 \sum_i \theta_i + wC\tau_0 \sum_i \gamma_i l_i \tag{131}$$

where the parameters θ_i, l_i and $\gamma_i = \sin\theta_i$ are measured from the tested specimens (see Fig. 80(b) and Table 6).

	l_1 (mm)	l_2 (mm)	θ_1 (deg.)	θ_2 (deg.)
specimen #1	8.2	61.8	78	6
specimen #2	12.3	57.7	81	7
specimen #3	9.9	60.1	82	7
specimen #4	10.6	59.4	80	6

Table 6. Deformed geometry of the HSSA bean specimens

Hence, based on Eq. (131), an expression for the fully plastic bending moment per unit width of the sandwich strip can be given:

$$M_0 = \frac{E_{ext}^{beam} - E_s^{beam}}{w\sum_i \theta_i} = \frac{\int_0^{u_{max}} F(u)du - wC\tau_0 \sum_i \gamma_i l_i}{w\sum_i \theta_i} \tag{132}$$

Upon evaluation for the present tests, we find $M_0 = 12.0\ Nm/m$ and thus $M_0 \cong M_0^{soft}$. It appears that the presence of the fiber core has no impact on the energy dissipated in the facings. In other words, the two face sheets deform independently from each other, whereas the sandwich core is crushed in a shear mode ($\gamma_i = \sin\theta_i$). This can be explained by the fact that the resultant shear force transmitted between the core and the facings is small as compared to the fully plastic normal force of a facing, $O(\tau_0 l_i) << O(\sigma_0 t)$.

An alternative way of presenting the results of the beam compression tests is as follows. Based on the assumption of shear-soft core behavior, beam compression tests can be used as an experimental method to determine the energy equivalent shear stress of the core material. Again, using Eq. (131), the energy equivalent shear stress can be expressed as

$$\tau_0 = \frac{\int_0^{u_{max}} F(u)du - wM_0^{soft}\sum_i \theta_i}{wC\sum_i l_i\gamma_i} \tag{133}$$

Fig. 82 shows the energy equivalent shear stress as obtained from the beam compression tests as well as directly measured from the shear tests. The data of both tests have an average for the energy equivalent shear stress of about $\tau_0 = 0.85MPa$.

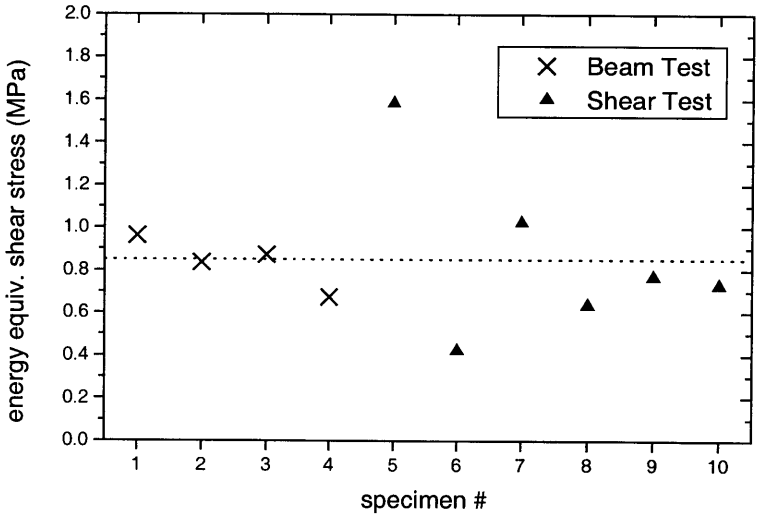

Fig. 82. Energy equivalent shear stress of the HSSA fiber core as found from shear tests on the HSSA core and compression tests on HSSA beams.

6.3 Experiments on the crushing of HSSA sandwich double-cell profiles

Three double-cell profiles were manufactured from flat HSSA sheets. Each double-cell profile was composed of two identical HSSA channel-profiles (U-profiles) and a flat HSSA diaphragm (Fig. 74). For ease of manufacturing, we applied a simple edge-bending technique to bend all eight 90°-corners of the U-profiles (Fig. 74). However, prior to bending, a cylindrical indenter (diameter *6mm*) was used to locally reduce the core thickness along the corner lines to be bent. The U-profiles had each two *F=20mm* wide lips to allow for a rivet joint to connect the two U-profiles with the diaphragm. A rivet line of equally spaced $\frac{1}{8}$'' semi-rivets was chosen. The joint was designed such that the rivets had only a minor influence on the folding mode. Using this assembly technique, three double-hat profiles were built from the prototype material. All profiles had a height of 100mm. The widths B of the square cells of the double-cell profiles were 70, 85, and 103mm for the small, medium, and large specimen, respectively. For the following analysis, it is helpful to define the corresponding *cross section path length L*, defined as

$$L = 7B + 6F, \tag{134}$$

where F denotes the width of the flanges along the rivet line. For the above three specimens the cross-section path lengths were *L=609, 716* and *840mm*. It must be noted that no triggering was placed on the specimens.

We used a standard test set-up for the axial crushing. The double-cell profile was placed between two massive steel plates (250x250x20mm) with rough surfaces (Fig. 83). The axial loading was applied by the moving crosshead of a screw-driven universal testing machine (Model 45G, MTS Corporation, Eden Prairie, MN). A 200kN load cell measured the axial force. The constant crosshead velocity throughout these quasi-static tests was *2 mm/min*. During the crushing, the load-displacement curves were acquired with the MTS TestWorks software.

The structural deformation mode was similar for all tested HSSA double-cell profiles. The initial fold formed at either the top or bottom of the column. Subsequent

folds formed along a crushing front that traveled down the specimen. The observed folding process was progressive. A well-defined crushing front separated the folded and the (almost) undeformed part of the tested profile (Fig. 83). As seen in the previous pilot study on the HSSA material (Mohr and Wierzbicki, 2000), notably short folding wavelengths were observed throughout all tests.

The recorded force-displacement curves are presented in Fig. 84. One notes that, although the specimens were not triggered, the onset of the folding process did not require a significantly higher force than needed for the formation of subsequent folds. It is believed that this is caused by initial imperfections due to the manufacturing technique. Furthermore, the force-displacement curve did not show clear periodicity, as it was expected for a progressive folding process. A perfect periodicity of the force-displacement curve requires that the folding of all corners of the profile occurred simultaneously. But the imperfections introduced by the manufacturing process and the joining technique are already sufficient to cause the folding of various corners at different

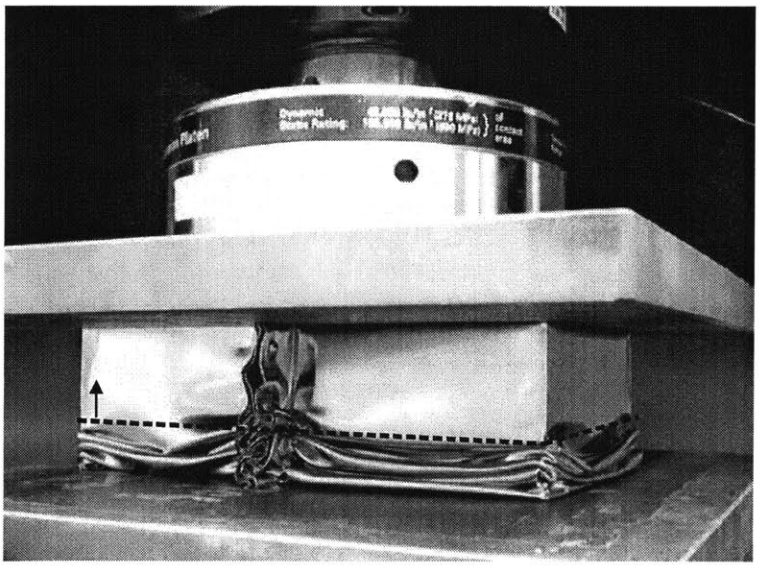

Fig. 83. Crushing of a HSSA double-cell profile. The dashed line indicates the traveling crushing front, separating the crushed from the undeformed part.

times. Consequently, the periodicity of the force-displacement curve as well as the periodicity in the folding pattern was disturbed. However, the periodicity of the folding mode is clearly seen in Fig. 87(a).

As a reference, a fourth double-cell profile was made from a solid-section stainless steel sheet. The profile dimensions were similar to the small HSSA column (*B=70mm*, *L=609mm*). The sheet thickness was $t_s = 0.4mm$ which is equal to the sum of the thicknesses of the two HSSA facings, i.e. $t_s = 2t_f$. Furthermore, the solid-section column and the HSSA facing were made of the same material. Due to the absence of the fiber core, this solid-section specimen was 17% lighter than the corresponding HSSA profile. The force-displacement curve for the solid-section specimen is compared with those of HSSA columns in Fig. 84, while the corresponding final views of the crushed specimens are shown in Fig. 85.

Since there was no significant force peak at the beginning of the crushing, we determined the mean crushing forces by dividing the area under the force-displacement curve by the maximum crosshead displacement. The mean crushing forces were respectively 14.6kN, 16.4kN and 19.0kN for the small, medium and large HSSA specimens and 9.0kN for the solid-section profile. The corresponding specific energy absorptions, defined as the ratio of the absorbed energy and the mass of the crushed material, were 4.0, 4.3, 4.5 and 2.2 kJ/kg.

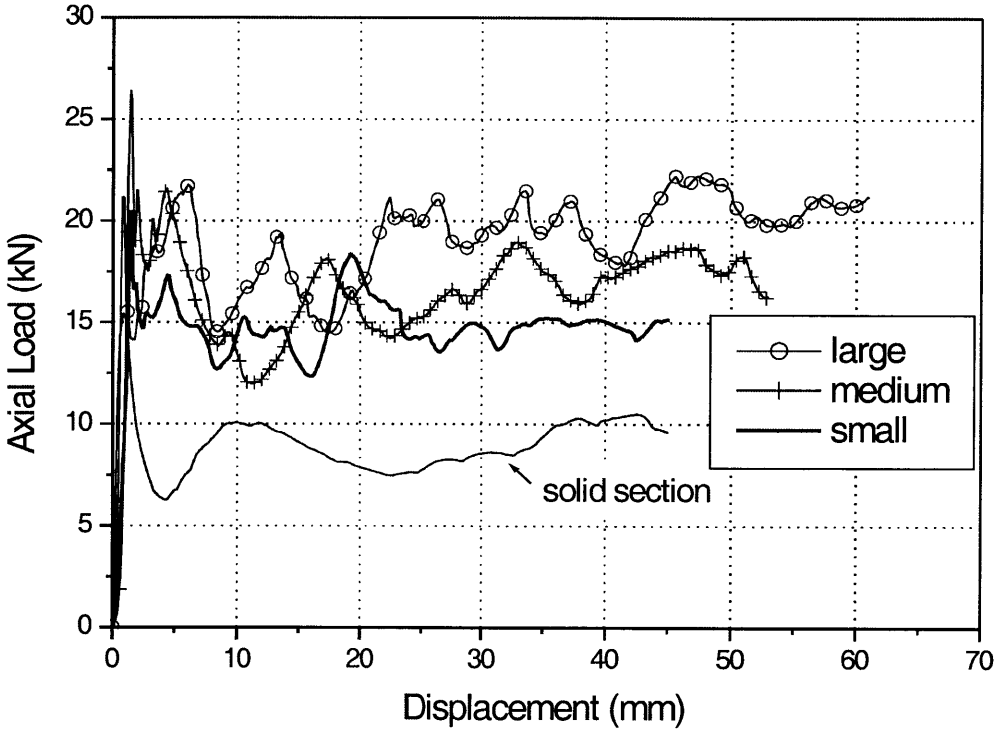

Fig. 84. Force-displacement curves for HSSA double-cell profiles under axial crush loading. The corresponding profile widths were B=70, 85 and 102 mm for the curves labeled as small, medium and large, respectively. Additionally, the response of a small column (B=70mm) built from a solid-section stainless steel sheet is shown.

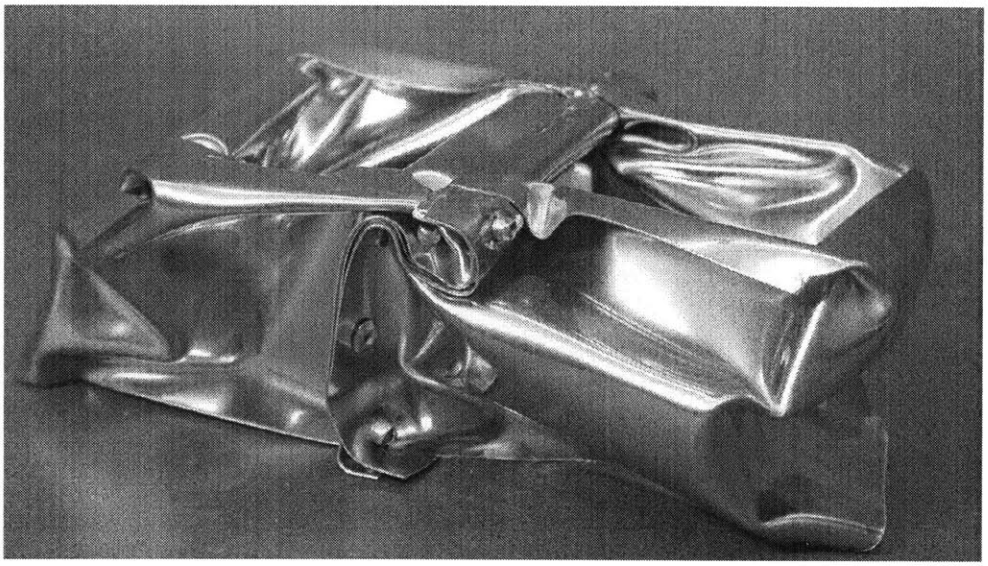

(a)

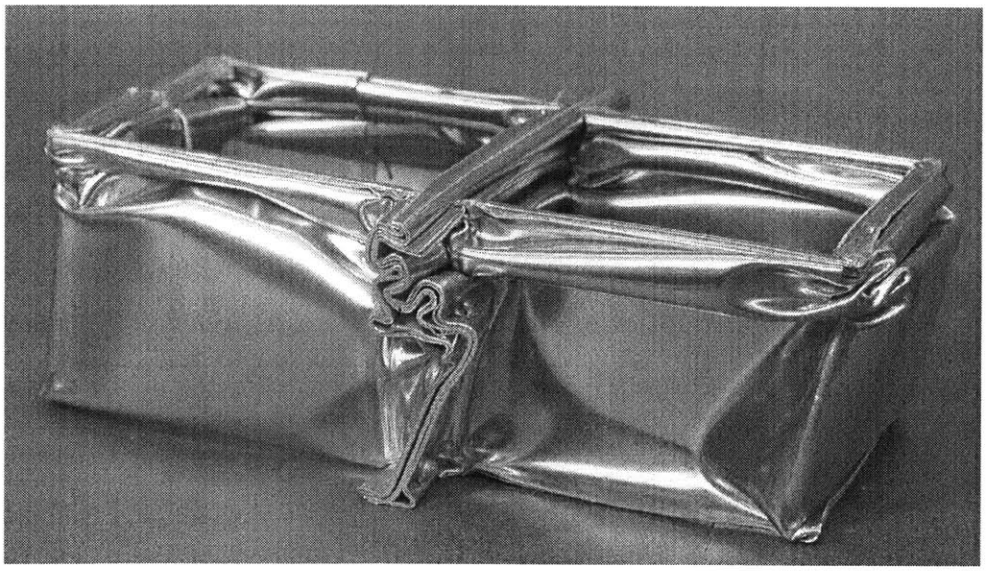

(b)

Fig. 85. Deformed double-cell profiles after crushing, built from (a) solid-section stainless steel sheet and (b) from the HSSA sandwich sheet. Both columns had similar profile dimensions and were crushed over the same distance.

6.4 Shear-folding model

6.4.1 Theoretical analysis

For the theoretical analysis of the crushing process, we adopt the same methodology as commonly used to analyze the crushing of thin-walled structures (see e.g. Alexander (1960), Wierzbicki and Abramowicz (1983), Abramowicz and Wierzbicki (1989)). The central point of the analysis is the evaluation of the energy balance equations based on a kinematically admissible folding mechanism for a representative corner element. A schematic of the folding mechanism is shown in Fig. 86. Assuming a rigid-perfectly plastic behavior of the skin material, the energy dissipation is concentrated along plastic hinge lines and is localized around the corners of the structure, where the material is predominantly stretched. In addition, there is energy dissipated by the shear crushing of the sandwich core. Thus, the rate of energy dissipated can be written as follows:

$$\begin{aligned} \dot{E}_{int} &= \dot{E}_b + \dot{E}_c + \dot{E}_s \\ &= \int_L M_0 \dot{\theta} dl + \int_{A_c} N_0 \dot{\lambda} dA + \int_{A_s} Q_0 \dot{\gamma} dA \end{aligned} \tag{135}$$

where L is the cross section path length (see Eq. (134)), A_c and A_s denote the areas as highlighted in Fig. 86. The meaning of the three terms is as follows. $\dot{E}_b$ is the rate of energy dissipation along the plastic hinge lines and can be expressed by the product of the plastic bending moment per unit length, M_0, and the corresponding rate of rotation $\dot{\theta}$. The second term, $\dot{E}_c$, accounts for the energy dissipation due to the stretching of the material in the profile corners. N_0 denotes the fully plastic membrane force and $\dot{\lambda}$ refers to the corresponding (plastic) membrane stretch rate. $\dot{E}_s$ denotes the rate of energy dissipated by shear crushing of the sandwich core. The transverse shear crushing force Q_0 is introduced as

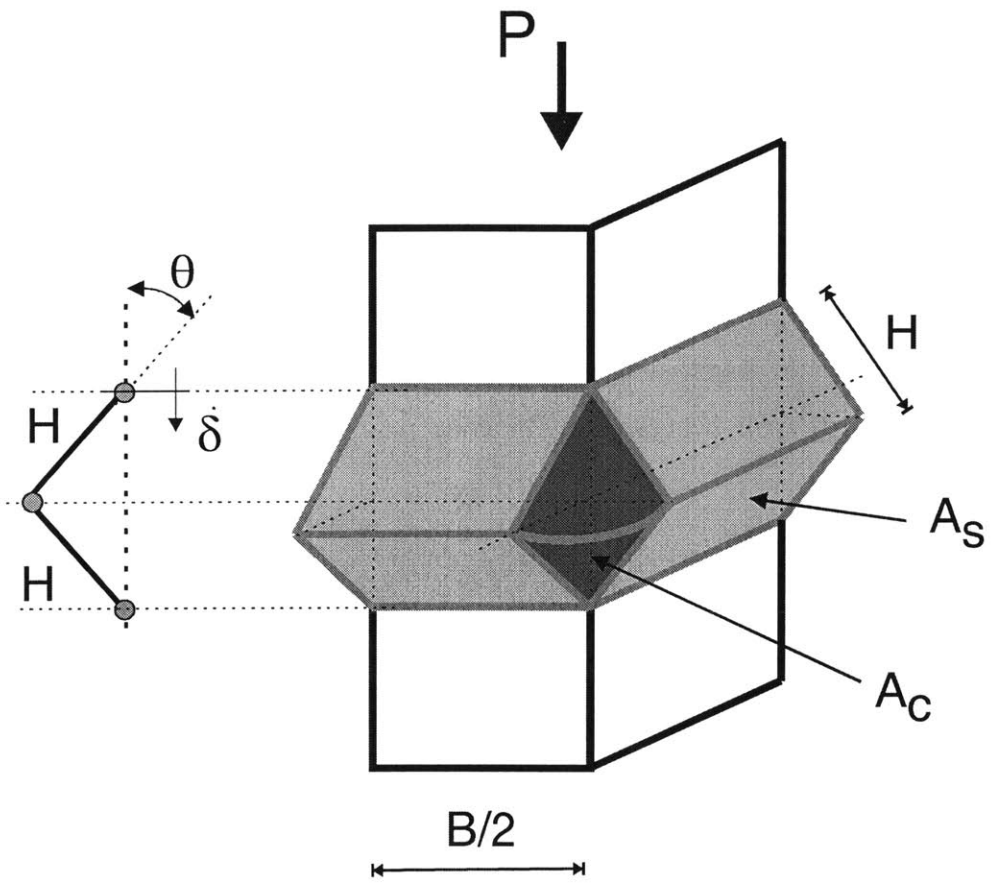

Fig. 86. Global geometry of the basic folding mechanism.

$$Q_0 = C\tau_0 \tag{136}$$

and $\dot{\gamma}$ is the rate of shear strain.

The rate of external work done by compressing the corner element is

$$\dot{E}_{ext} = P\dot{\delta} = 2PH(\sin\theta)\dot{\theta}, \tag{137}$$

where P is the instantaneous crushing force and $\dot{\delta}$ is the rate of displacement that acts in the direction of P. As illustrated by Fig. 86, the folding wavelength is denoted by $2H$. Neglecting the elastic strain energy, it follows from the theorem of power expended that the rate of external work and the rate of energy dissipation must be equal, $\dot{E}_{ext} = \dot{E}_{int}$. Equation (137) includes the folding (half-)wavelength H as geometric unknown. To determine the folding (half-)wavelength, the concept of a mean crushing force, P_m, is introduced as

$$P_m(H) = \frac{1}{2H}\int_0^{2H} P(\delta)d\delta = \frac{1}{2H}\int_0^T P\dot{\delta}dt = \frac{1}{2H}\int_0^T \dot{E}_{int}dt. \tag{138}$$

Following Alexander (1960), it is postulated that the folding wavelength adjusts itself as to minimize the mean crushing force. Therefore, we seek for the minimum of the expression above and thus, obtain an equation that determines the folding wavelength as well as the mean crushing force:

$$P_m = \min_{H>0} P_m(H) \tag{139}$$

6.4.2 Solution and Evaluation

We now evaluate the mean crushing force for multi-cell sandwich profiles. The geometry of such profiles is characterized by the number of 90-degree corners, n, and the total cross-section path length L. As schematically shown in Fig. 86, the kinematically

admissible displacement field assumes a constant folding wavelength along the cross-section path. Thus, as compared to the experimental deformation pattern (Fig. 87(b)), we neglect the transition of large folds in the middle of the column sides into shorter folds around the corner region. The folding mode of the sandwich profiles cannot be clearly identified as mode I or mode II (for definition see Abramowicz and Jones, 1984). It was found from evaluation of the mean crushing force that the assumption of a fully extensional folding mechanism (mode II) provides the best agreement of theoretical prediction and experimental results.

Thus, throughout the completion of a single fold, the energy dissipated by plastic stretching of the material in the n profile corners of a multi-cell profile, E_c, reads

$$E_c = n\int_0^T dt \int_{A_C} N_0 \dot{\lambda} dA = n\sqrt{2} N_0 H^2 . \tag{140}$$

We assume that the core is crushed to its maximum shear distortion ($\gamma = 1$). In what follows, that the dissipation related to core shear crushing can be written as

$$E_s = L\int_0^T dt \int_{A_C} Q_0 \dot{\gamma} dA = 2\tau_0 LHC . \tag{141}$$

The integration of the plastic dissipation along the plastic hinge lines gives:

$$E_b = L\int_0^T dt \int_l M_0 \dot{\theta} dl = 2\pi M_0 L \tag{142}$$

Next, evaluating Eq. (135) and (138) leads to an expression for the mean crushing force:

$$P_m = \frac{L\pi}{H} M_0 + \frac{n}{\sqrt{2}} H N_0 + \tau_0 LC \tag{143}$$

The minimum of P_m with respect of H exists and occurs at

$$H = \sqrt{\frac{\sqrt{2}\pi L M_0}{n N_0}} , \tag{144}$$

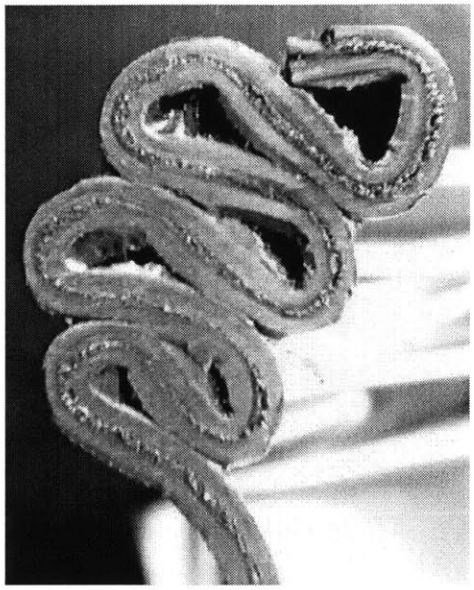

(a)

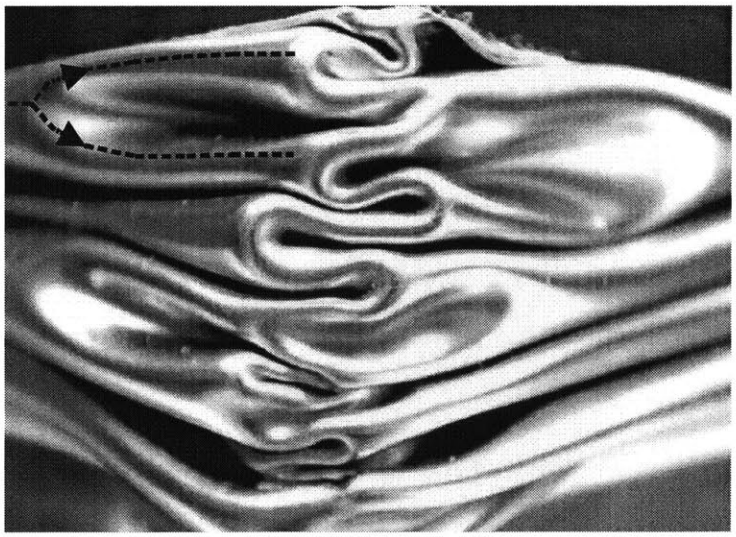

(b)

Fig. 87. (a) longitudinal cut through the folded wall of a crushed double-cell profile, (b) corner of a crushed double-cell profile. The dashed lines in (b) illustrate the transition from long folds into shorter folds.

or, for a soft-core sandwich profile,

$$H = \sqrt{\frac{\pi}{2\sqrt{2n}}}\sqrt{Lt_f}\ , \tag{145}$$

Finally, we substitute H back into Eq. (143) and, in order to account for the effective crushing distance, we multiply the solution by a factor of $\frac{4}{3}$:

$$P_m = \frac{4}{3}\left(\sqrt{2\sqrt{2}\pi nLM_0N_0} + \tau_0 LC\right) \tag{146}$$

As recommended by Abramowicz and Wierzbicki (1989), the factor $\frac{4}{3}$ is commonly used for profiles with homogeneous walls. This assumption implies that the ratio of current to initial height of the crushed part (Fig. 83) was $\frac{3}{4}$, which could be confirmed by measurements on the deformed HSSA columns.

Theoretical predictions of the mean crushing force based on the present model compare very well with the experimental data (Fig. 88). The maximum deviation between the theoretical and experimental results is about 5%. Fig. 88 also shows the prediction of the mean crushing force assuming a shear-rigid core behavior, as suggested earlier by Santosa (1999). Based on this assumption, the force level is overestimated by up to 200%. The folding wavelengths $2H$ as predicted by the theory were 8.3, 9.0 and 9.7 mm for the small, medium and large column, respectively. The corresponding estimates based on measurements on the crushed profiles are 7.3, 8.0 and 8.5mm. Note that in the case of the tested specimens the folding wavelength varied along the cross-section path.

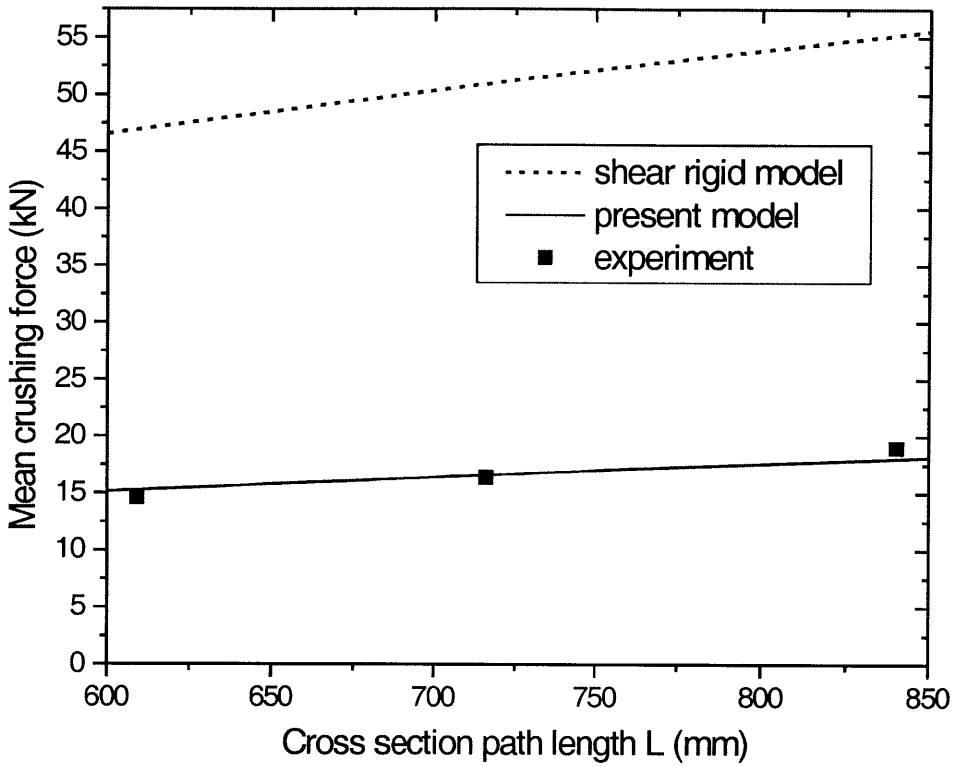

Fig. 88. Mean crushing force as function of the cross-section path length [see Eq. (13) for definition]. The three discrete points show the experimental results. The upper dotted curve is found assuming a shear-rigid core behavior, whereas the solid lower curve is calculated on the basis of the present model (shear-soft core behavior).

6.5 Computational modeling of honeycomb sandwich sheets

Our objective is to model honeycomb sandwich sheets under large deformations. Computational models for sandwich panels and shells can be classified in three distinct categories (Noor *et al.*, 1996):

(i) *Detailed models.* The cell walls of the honeycomb microstructure are discretized by several shell elements; also, the face sheets are treated as shell (e.g. Ogasawara *et al.*, 1999). An example for is shown in Fig. 89(a).

(ii) *Continuum models.* The sandwich core is represented as homogenous continuum. In other words, solid elements along with a constitutive model for the sandwich core are employed. The face sheets are modeled with shell elements. An example is shown in Fig. 89(b).

(iii) *Shell models.* Assumptions are made that characterize the sandwich behavior along its thickness direction. The kinematics of the sandwich mid-plane is described along with additional degrees of freedom/element variables (e.g. the cross-section rotation or transverse stress components in mixed/hybrid elements). This class of models includes so-called 'global approximation models' where the heterogeneous sandwich is replaced by a quasi-homogeneous single layer shell, and 'discrete-layer models', where the sandwich is considered as a three-layer laminate.

Detailed models cannot be recommended for structural applications that involve large deformations of the honeycomb core. Under large deformations, reliable modeling of the core behavior requires very fine meshes on the microstructural level. In the example shown in Fig. 89(a), 5400 shell elements with five through the thickness integration points represent $2.7mm^2$ of a $0.8mm$ thick micro-cell honeycomb core. The numerical simulation of the structural behavior of a small honeycomb sandwich sheet of 100x100mm and would require about 20,000,000 shell elements for the core material, which exceeds the capabilities of state of the art for high performance FE-codes and supercomputers (about one million elements).

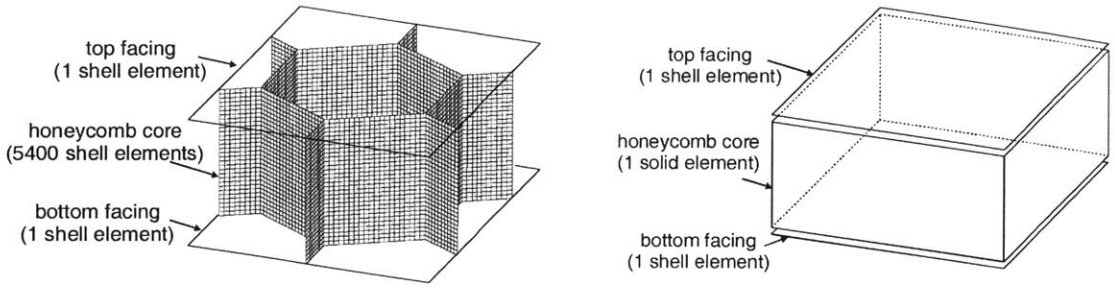

(a) (b)

Fig. 89. Honeycomb sandwich modeling: (a) detailed model, (b) continuum model.

However, the use of a continuum model provides an attractive solution to this problem. Using this technique, we can replace the 5,400 shell elements for the sandwich core by a single reduced-integration solid element, where we use a constitutive model for honeycombs to perform the stress update at the integration point. Thus, the size of the computational problem is dramatically reduced. Furthermore, a larger time step may be chosen in simulations with explicit time integration, since the size of the smallest element has been increased by several orders of magnitude (while the elastic wave propagation speed remained more or less the same).

The success of the third approach, i.e. the use of shell models, relies on the details of the sandwich shell formulation. As per the best knowledge of the author, existing 'special sandwich elements' are not designed for the simulation of large plastic deformation in honeycomb cores (see Mackerle (2002) for a bibliography review on special sandwich elements). Extensive literature is available on sandwich elements for elastic analysis, but only little has been published on the modeling of their inelastic behavior under large deformations. Here, we omit the formulation of a special sandwich element for large deformations and suggest the use of continuum models.

Finally, we comment on the modeling of the kinking of sandwich beams and plates. Two types of sandwich facing instabilities characterize the onset of kinking: (i) face

wrinkling (Fig. 90a), and (ii) face dimpling (Fig. 90b). In the case of face wrinkling, the honeycomb core is locally indented, whereas in the case of face dimpling, the length of the wrinkle is smaller than the honeycomb cell size and thus the buckle can form without deforming the core material (intracell buckling). In sandwich literature, wrinkling is treated as a purely elastic phenomenon (e.g. Plantema, 1966; Allen, 1969; Zenkert, 1995). Analytical formulations propose a beam on an elastic foundation as mechanical model to predict face winkling. In the continuum model, the solid elements for the core material represent the elasto-plastic foundation for the shell mesh of the facings. Given the analogy between the analytical and continuum model, it may be concluded that wrinkling can be predicted by the current modeling approach. The second mode of kinking initiation, face dimpling, is not captured by the continuum model. Modeling of face dimpling requires either a detailed core model with a fine mesh for the facings or the implementation of a dimpling criterion. An example using the latter approach can be found in Starlinger and Rammerstorfer (1990).

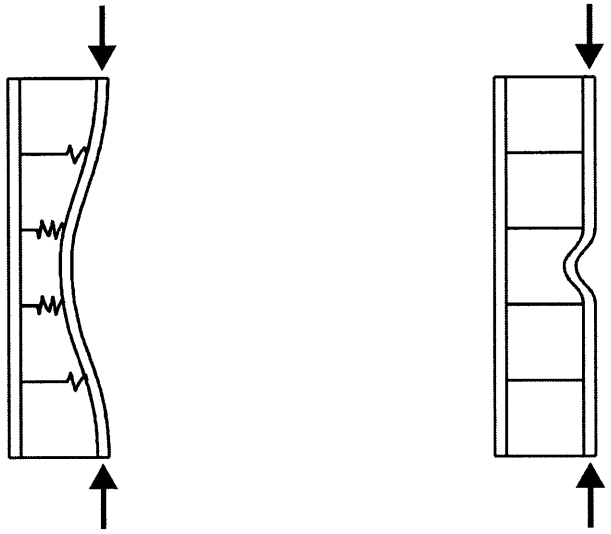

Fig. 90. Kinking modes: (a) face sheet wrinkling, (b) face sheet dimpling.

6.6 Comparison of the specific shear crushing strength of sandwich core materials: Metallic honeycomb versus HSSA

The analysis of the crushing of soft-core sandwich profiles has shown that the response of a sandwich core material to large (out-of-plane) shear deformation is of foremost importance for the crushing behavior of prismatic sandwich profiles. The HSSA fiber core described above belongs to a class of core materials where beams are the characteristic microstructural elements. Conversely, thin plates represent the characteristic microstructural elements of honeycombs. Here, we briefly discuss these two low density core material concepts with respect to their mechanical performance under large shear deformation. First, we derive approximate analytical expressions for the shear response of an HSSA fiber core and a metallic honeycomb core, before we compare their weight specific 'shear crushing strengths'. We use the terminology 'shear crushing' in this context as at the microstructural level, large macroscopic shear deformation of either core material involves the crushing of its metallic microstructure.

6.6.1 Shear-crushing of the HSSA fiber core

We closely follow the crushing analysis by Teng and Wierzbicki (2002). A beam with circular cross-section is chosen as mechanical model for a single fiber (Fig. 91). The beam length corresponds to the sandwich core height C; the fiber diameter is denoted as D. Furthermore, we represent the fiber material behavior as ideal plastic, characterized by the von Mises yield stress σ_y. Refer to Teng and Wierzbicki (2002) for an exact solution including strain-hardening.

Under large macroscopic shear deformation, two plastic hinges form at the clamped beam boundaries. The beam length is assumed to remain constant throughout the crushing (inextensibility). Upon evaluation of the plastic work balance, we have:

$$F du_s = 2M_0 d\alpha \tag{147}$$

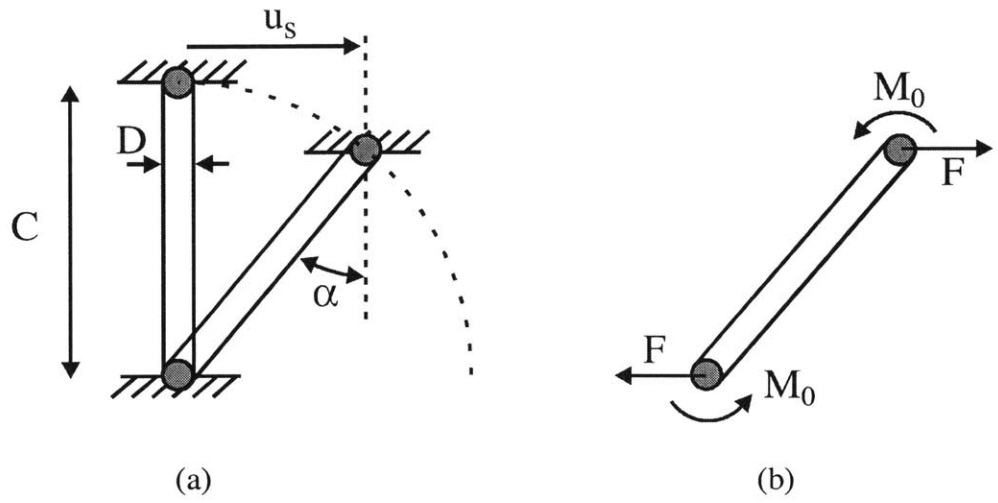

Fig. 91. Mechanical model for a single HSSA fiber

where F and u_s denote the shear force and shear displacement at the top boundary. The plastic bending moment of the circular cross-section reads

$$M_0 = \tfrac{1}{6}\sigma_y D^3 \tag{148}$$

Furthermore, the kinematic relationship between the rotation α and the shear displacement is given by

$$\sin\alpha = \frac{u_s}{C} \tag{149}$$

or, in terms of increments

$$d\alpha\cos\alpha = \frac{du_s}{C} \tag{150}$$

Combining Eqs. (147) and (150), we find

$$F(\alpha) = \frac{2M_0}{C\cos\alpha} \tag{151}$$

Equivalently, we can express the shear force as a function of the shear displacement:

$$F(u_s) = \frac{2M_0}{\sqrt{C^2 - u_s^2}} \tag{152}$$

The shear force of $F = 2M_0 / C$ must be overcome to initiate the shear crushing, but the shear force increases monotonically towards infinity for $u_s \to C$. However, the plastic work required to fully crush a single fiber is finite:

$$\int_0^C F du_s = \pi M_0 \tag{153}$$

Thus, the energy equivalent shear stress can be calculated. Given the fiber diameter D and the relative density of the fiber core, ρ / ρ_s, we have the number of fibers per unit area of the fiber core

$$n = \frac{4}{\pi D^2} \frac{\rho}{\rho_s} \tag{154}$$

At the same time, the macroscopic shear stress is defined as the total shear force per unit area (of the fiber core), in what follows

$$\tau(\gamma) = nF(u_s) = \frac{2nM_0}{C\sqrt{1-\gamma^2}} \tag{155}$$

where we introduced the engineering shear strain $\gamma = u_s / C$. Applying the definition for the energy equivalent shear stress τ_0 (Eq. 125) yields

$$\tau_0 = \int_0^1 \tau(\gamma) d\gamma = \frac{n}{C} \int_0^C F du_s = \frac{n\pi}{C} M_0 \tag{156}$$

And finally, after combining Eqs. (148), (154) and (156), we find

$$\tau_0 = \frac{2}{3} \frac{D}{C} \frac{\rho}{\rho_s} \sigma_y \tag{157}$$

6.6.2 Shear-crushing of metallic honeycomb

The analysis below yields the same result as the earlier derivation by Reuter (1996) and Wierzbicki (1997). We limit our attention to the shear crushing of hexagonal honeycomb cores in the T-W-plane. Furthermore, we describe the cell wall material as ideal plastic (von Mises yield stress σ_y). The stress distribution in the initially flat elastic cell walls of a honeycomb subjected to macroscopic shear loading has been investigated by Kelsey *et al.* (1958). Fig. 92 depicts the shear distribution as found from Kelsey's analysis. Note that for infinitesimal strains, the double-thickness cell walls are theoretically stress free under pure shear loading in the T-W-plane. The microstructural stress state in the single-thickness cell walls is pure shear. In this case, the relationship between the shear stress in a single wall, τ_{sg}, and the macroscopic shear stress acting on the honeycomb core, τ, reads

$$\tau_{sg} = \left(\frac{h}{t} + \frac{l}{t}\sin\theta\right)\tau \tag{158}$$

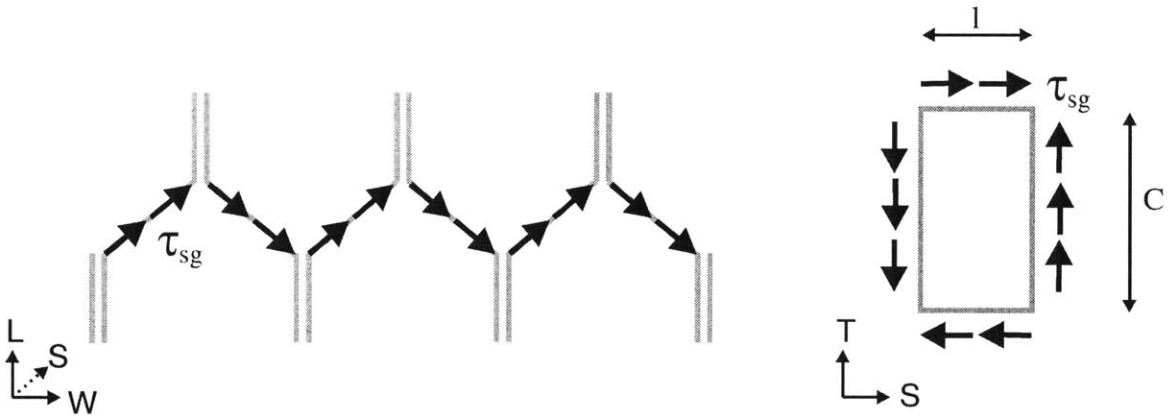

(a) (b)

Fig. 92. Shear flow in a honeycomb under pure shear loading in the T-W-plane (Kelsey *et al.*, 1958).

where h and l denote the cell wall widths, t is the cell wall thickness and θ is the cell wall expansion angle. To calculate a first approximation of the macroscopic shear stress in the plateau regime, we assume that the stress state in the cell walls (a) remains pure shear, and (b) satisfies the von Mises yield condition.

These assumptions are made based on the results of an in-depth analysis of the shear crushing of plates by Wierzbicki and Price (1992): their experimental and analytical results indicated that the plastic limiting load for the flat plate provides a reasonable approximation for the energy equivalent shear stress that describes the highly complex crushing mechanics of a plate under shear loading. Following this simple model, we have $\tau_{sg} = \sigma_y / \sqrt{3}$ and thus, the work equivalent shear stress, τ_0, of a honeycomb reads

$$\tau_0 = \frac{\sigma_y}{\sqrt{3}\left(\frac{h}{t} + \frac{l}{t}\sin\theta\right)} \tag{159}$$

For example, in the case of the aluminum honeycomb described in the virtual experiments, we determined $\tau_0 = 0.93MPa$ from numerical simulation. Evaluating Eq. (159) for $\sigma_y = 265MPa$, $t = 0.033mm$, $h = 2.4mm$, $l = 3.1mm$ and $\theta = 40^0$ yields $\tau_0 = 1.1MPa$.

In the subsequent comparison with the HSSA core, we consider perfectly hexagonal honeycombs. Both single and double-thickness walls have the same width $(h = l)$, and the expansion angle equals $\theta = 30^0$. For this geometry, we have the relative density

$$\frac{\rho}{\rho_s} = \frac{\frac{h}{l} + 1}{\cos\theta\left(\frac{h}{t} + \frac{l}{t}\sin\theta\right)} \tag{160}$$

and thus

$$\frac{h}{t} + \frac{l}{t}\sin\theta = \frac{2}{\cos\theta}\frac{\rho_s}{\rho} = \frac{4}{\sqrt{3}}\frac{\rho_s}{\rho} \tag{161}$$

Making use of Eq. (161) in Eq. (159), we may rewrite the shear plateau stress as a function of the relative density ρ / ρ_s:

$$\tau_0 = \frac{1}{4}\frac{\rho}{\rho_s}\sigma_y \tag{162}$$

6.6.3 Comparison

We compare the energy equivalent shear stress of the HSSA fiber core with the shear plateau stress of a honeycomb. Both quantities provide a good measure for the plastic work done throughout the shear crushing of the core material. In the following, we refer to either stress as 'shear crushing strength'. Fig. 93 shows a plot of Eqs. (157) and (162). Note that for both core materials, the shear crushing strength is proportional to the von Mises yield stress of its metallic base material. Therefore, we chose the dimensionless shear crushing strength τ_0 / σ_y and the relative density ρ / ρ_s as ordinate and abscissa, respectively.

According to Eq. (162), the dimensionless shear crushing strength of a honeycomb depends on the relative density only. In the case of the HSSA core, the dimensionless shear crushing strength also depends on the microstructural configuration. It is inversely

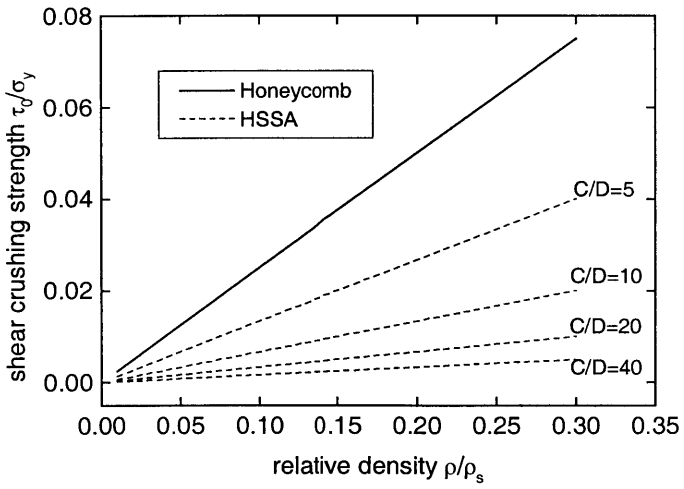

Fig. 93 . Dimensionless shear strength vs. relative core density for honeyocmb and HSSA.

proportional to the fiber slenderness ratio, i.e. the ratio of sandwich core height to fiber diameter (C/D). For the same relative density, fiber cores with slender fibers have a lower shear crushing strength than fiber cores with stocky fibers. Consequently, the curves for large ratios of C/D in Fig. 93 lie below the curves for small ratios of C/D. Eqs. (157) and (162) also allow us to calculate the slenderness ratio of HSSA fibers, for which the core shear crushing strengths of HSSA and honeycomb are theoretically equal. Upon evaluation, we find the slenderness ratio $C/D = 2.7$, which appears to be incompatible with the HSSA fiber core concept (see e.g. Gustafsson (1998) for details on the HSSA manufacturing technology).

Based on this conceptual comparison, we claim that hexagonal honeycomb cores provide a higher shear crushing strength than HSSA fiber cores of the same density and the same metallic base material.

6.7 Example: Crushing of a thin sandwich profile with a micro-cell honeycomb core

Here, we propose a new micro-cell honeycomb sandwich sheet as an example for future sandwich technology. It has the bending stiffness, total thickness and weight as the HSSA sheets, but excels in crashworthiness applications.

6.7.1 Stainless steel micro-cell honeycomb core

The core thickness $C = 0.8mm$ and the relative density $\rho/\rho_s = 0.1$ are chosen in analogy with the HSSA fiber core. Furthermore, we select stainless steel as base material for the cell walls. We limit our attention to 'perfectly hexagonal' microstructures with $\theta = 30^o$ and $h = l$. Thus, the relative density is inversely proportional to the width to thickness ratio of the single-thickness cell walls (Eq. (160)):

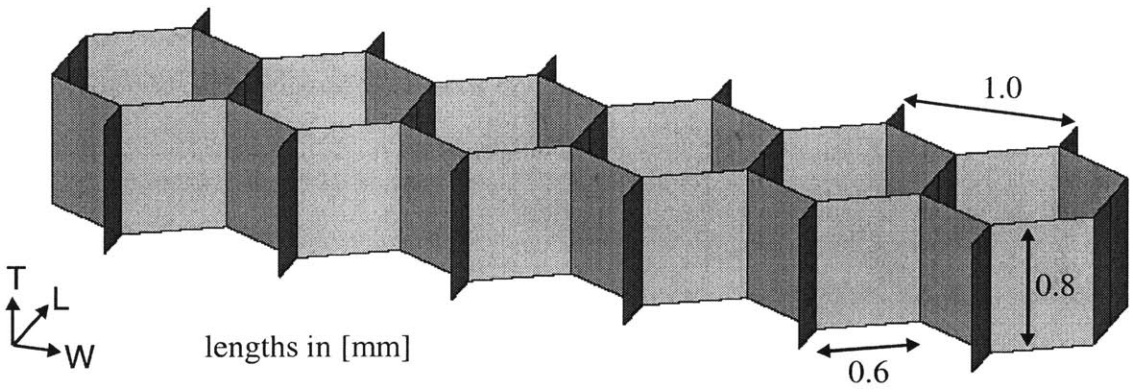

Fig. 94. Geometry of honeycomb specimen used in the numerical simulation. The single cell wall thickness was t=0.04mm.

$$\frac{\rho}{\rho_s} = 1.54\frac{t}{l} \tag{163}$$

The requirement of 10% relative density may be translated into the requirement of a width to thickness ratio of $l/t = 15.4$. With respect to practical applications, a small cell size is desirable to guarantee a quasi-continuous support of the sandwich facings. Here we chose $t = 40\mu m$ for the thickness of the cell walls and a cell wall width of $l = 0.6mm$.

The mechanical properties of this honeycomb are determined from microstructural simulations. As for the virtual experiments performed on aluminum honeycomb (see Chapter 4), the microstructure is discretized with three-dimensional shell elements and the displacement loading is applied to the top boundary of the specimen under quasi-static conditions. The specimen microstructure is shown in Fig. 94. In the J2-plasticity model for the cell wall material, we chose a constant von Mises yield stress of $\sigma_y = 500MPa$ to represent a ductile low-strength stainless steel. Virtual experiments are performed under pure shear loading in the T-W-plane and uniaxial compression along the T-direction. The corresponding macroscopic stress-strain curves are shown in Fig. 95 and Fig. 96, while Fig. 97 shows the shear-induced normal dilatation under pure shear loading. The same figures also show the calibration of the honeycomb constitutive model. The shear crushing strength predicted by Eq. (162) is $\tau_0 = 12.5MPa$, whereas the virtual

experiments suggest $\tau_0 = 18.4MPa$. A summary of the constitutive model input parameters is given in Table 7. Note that we will model the honeycomb as transversely isotropic, i.e. $G_{TL} = G_{TW}$ and $s^0_{TL} = s^0_{TW}$. This assumption underestimates the energy absorbed during shear crushing in the T-L-plane.

G_{TW} (MPa)	G_{TL} (MPa)	E_{TT} (MPa)	s^0_{TW} (MPa)	s^0_{TL} (MPa)	s^0_{TT} (MPa)	m (-)	ε_d (-)	h_d (MPa)	$\Delta\sigma$ (MPa)
770	770	2053	18.4	18.4	-49.6	1.0	0.65	45.0	18.2

Table 7. Material model paramaters for 10% stainless steel honeycomb.

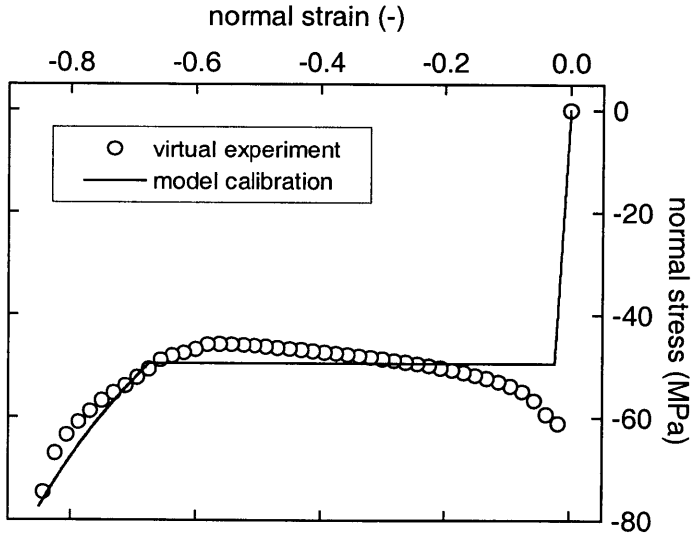

Fig. 95. Normal stress-strain curve for 90° loading.

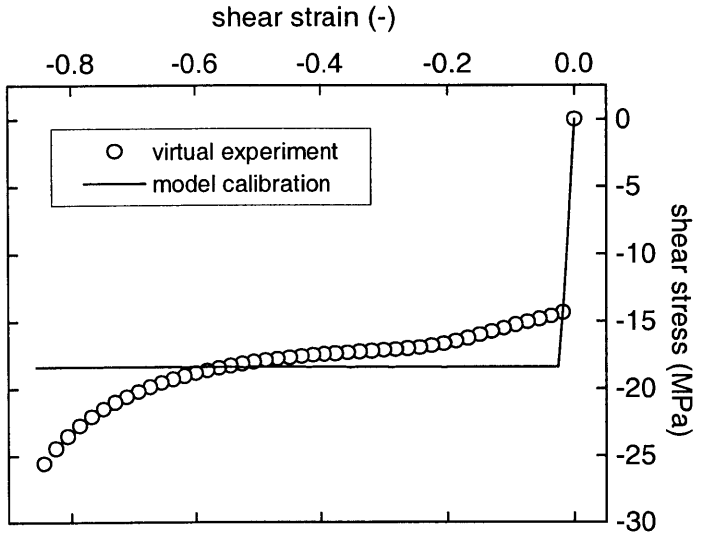

Fig. 96. Shear stress-strain curve for pure shear loading.

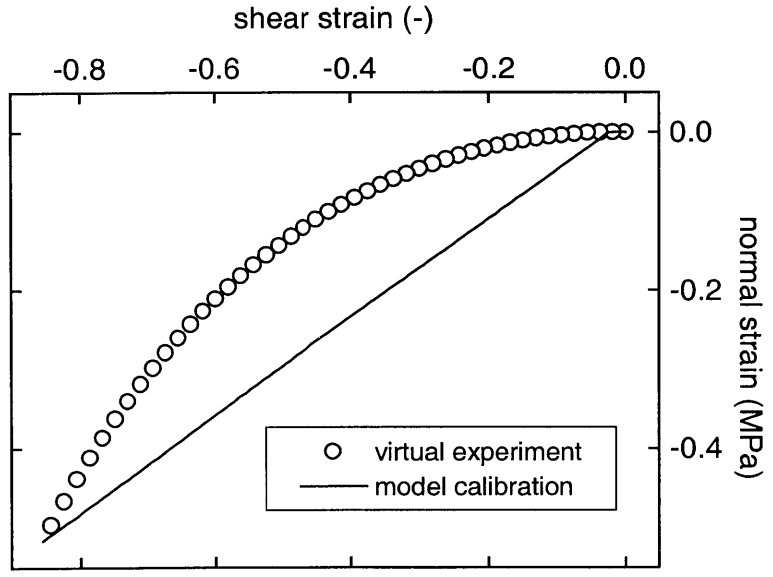

Fig. 97. Normal strain vs. shear strain under pure shear loading.

6.7.2 Numerical simulation of the crushing of a thin honeycomb sandwich profile

To illustrate the crashworthiness of thin honeycomb sandwich structures, we conduct a finite element simulation of the crushing of a corner element (Fig. 98). The response of corner elements is representative for the crushing behavior of prismatic thin-walled structures. The corner element analyzed is $H = 50mm$ high and has a side length of $B/2 = 35mm$. The sandwich structure is modeled by 4,000 six-node hexagonal solid elements for the honeycomb core (Abaqus/explicit element C3D6) and 4,000 four-node shell elements for the two facings (Abaqus/explicit element S4R). The six node solid element is chosen to circumvent hourglass problems with the reduced-integration eight-node solid element (Abaqus/explicit element C3D8R). Fig. 98(b) also shows the material coordinate axes for the honeycomb core. The T-direction is perpendicular to the facings, whereas the W-direction is aligned with the length (height) direction of the corner element.

Rigid shell elements (Abaqus/explicit element R3D4) at the top and bottom represent the loading platens of a testing machine. Kinematic contact is defined between all surfaces. 400,000 explicit time steps are performed as a total axial displacement of $u_{max} = 40mm$ is quasi-statically applied to the top boundary (time step $\Delta t = 200ns$ enforced by active mass scaling). Fig. 100 shows deformed configurations of the mesh during crushing. A detail of the folding process is shown in Fig. 101. Observe the thinning of the sandwich core throughout the crushing. Thinning is a characteristic sandwich property that has been reported from experiments on sandwich columns (Wierzbicki and Mohr, 2000). This characteristic feature is captured by the present honeycomb constitutive model as it accounts for the shear-induced dilatation, which produces the sandwich thinning on the structural level.

To evaluate the specific energy absorption of the honeycomb sandwich structure, we calculate the mean crushing force P_m from the area under the force-displacement curve in Fig. 99:

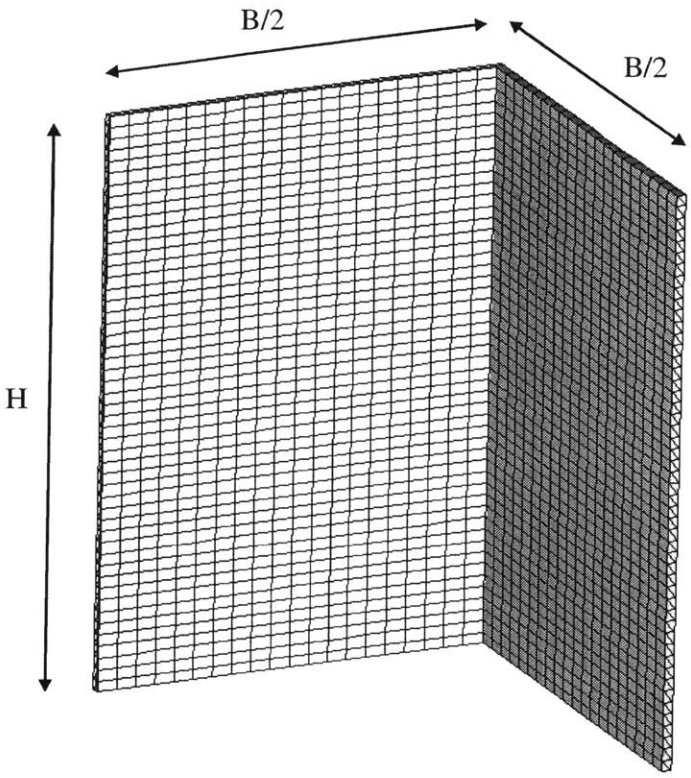

(a)

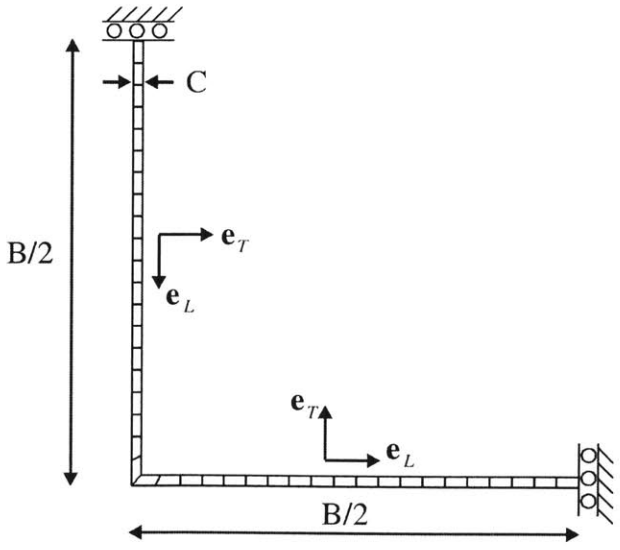

(b)

Fig. 98. Mesh for the corner element with a honeycomb core: (a) 3D view, (b) top view with material coordinate systems for sandwich core.

$$P_m = \frac{1}{u_{\max}} \int_0^{u_{\max}} P(u)du \tag{164}$$

Upon evaluation, we find $P_m = 3.7kN$ which corresponds to a specific energy absorption of $SEA = 11.3kJ/kg$. For comparison, we calculate the corresponding mean crushing force for the HSSA based on Eq. (146). Using $n = 1$, $L = 70mm$, $M_0 = 12.0Nmm/mm$, $N_0 = 236N/mm$, $\tau_0 = 0.8MPa$, and $C = 0.8mm$, we find $P_m^{HSSA} = 1.8kN$. In other words, using the thin micro-cell honeycomb sheet instead of the HSSA sheet doubles the mean crushing force as well as the specific energy absorption (!).

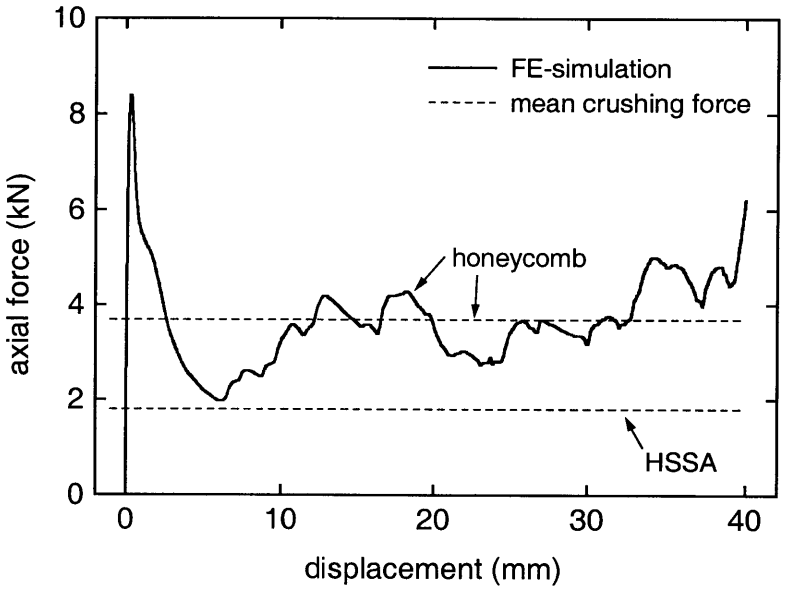

Fig. 99. Axial force vs. displacement curve for a sandwich profile with a 10% relative density stainless steel honeycomb core (numerical simulation). The dashed lines indicate the mean crushing forces $P_m = 3.7kN$ for the honeycomb sheet and $P_m = 1.8kN$ for the HSSA sheet of similar weight.

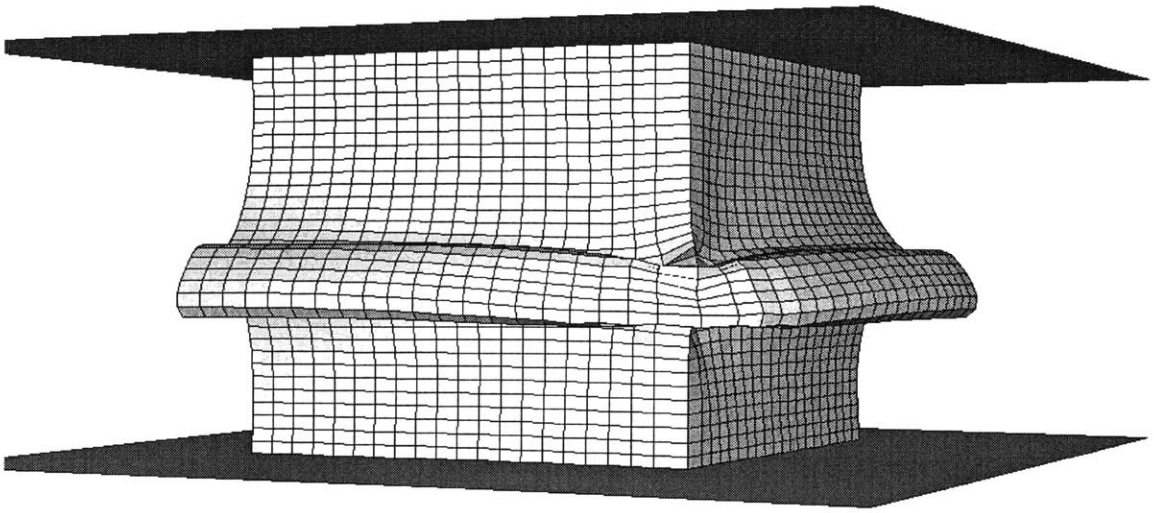

(a)

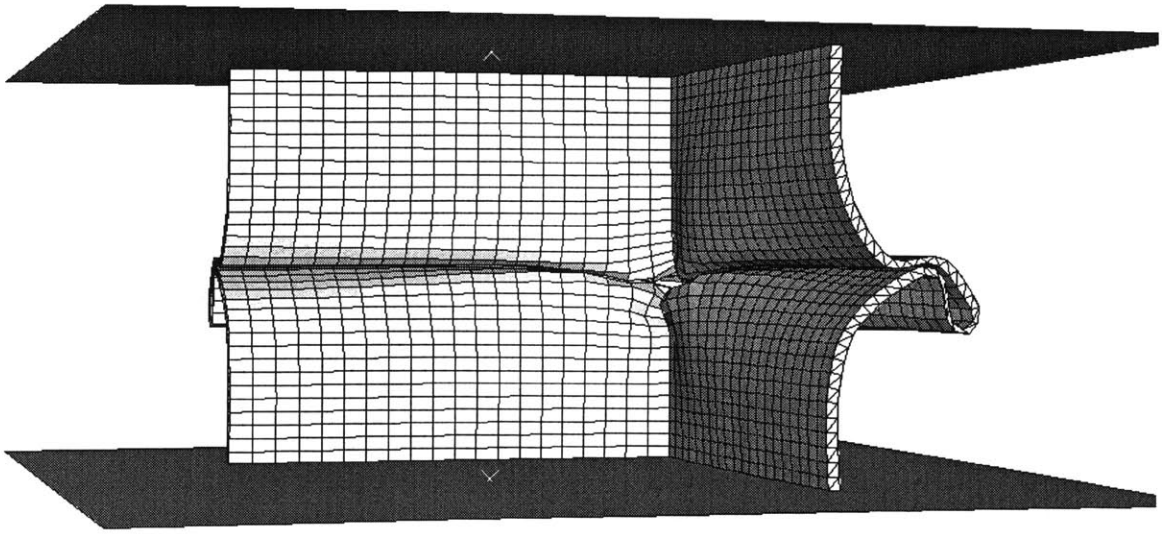

(b)

Fig. 100. Different views of the deformed mesh during the crushing of a honeycomb sandwich profile.

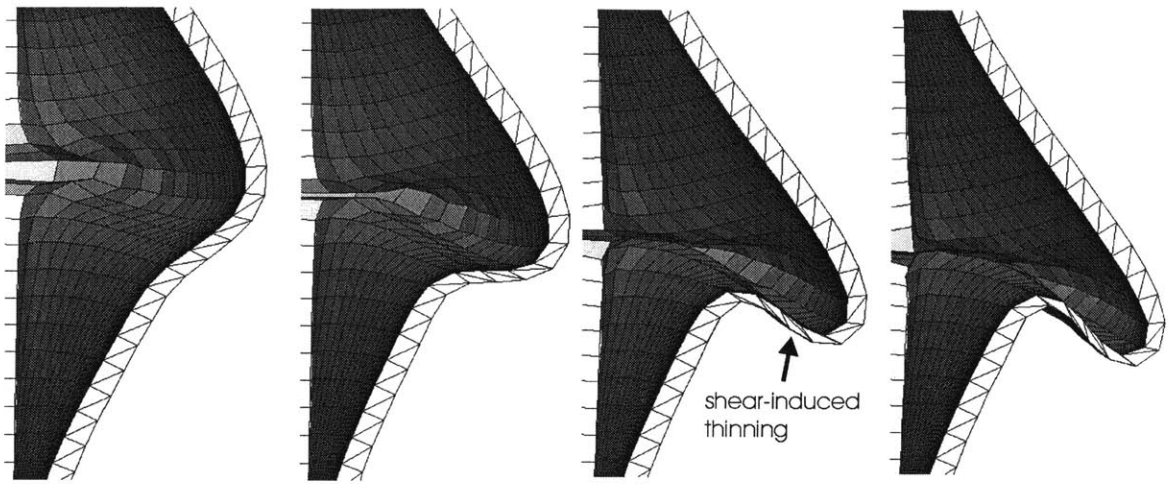

Fig. 101. Illustration of the shear-induced thinning of the sandwich core.

6.8 Concluding remarks

- The folding mechanism of thin-walled prismatic structures made of *thin* sandwich sheets (about $1mm$ total sheet thickness) is different from the one of solid-section thin-walled structures. When subjected to axial crush loading, short folds form, while the low-density core material is crushed in a shear mode.
- A new shear-folding model for sandwich profiles was derived, accounting for the shear crushing of the sandwich core material. The work by Alexander (1960), Wierzbicki and Abramowicz (1983), and Abramowicz and Wierzbicki (1989) provided the theoretical framework for the development of the current model. A good agreement of the theoretical predictions for the mean crushing force with the experimental data was found by assuming a fully-extensional mode.
- The shear crushing of the core has two opposite effects on the overall energy dissipation: (1) additional energy is dissipated throughout the shear crushing, involving relative motion of the face sheets; (2) the plastic bending moment of the

entire sandwich section cannot be fully developed because the necessary shear forces cannot be transmitted by the soft core. As a result, the energy dissipated throughout plastic bending decreases.

- The second effect also has a significant impact on the folding pattern. As indicated by Eq. (144), the folding wavelength scales with the fully plastic bending moment but is independent of the dissipation due to shear crushing. Thus, the crushing of soft-core profiles is characterized by a very short folding wavelength. This is an important feature in crashworthiness applications because in the case of longer columns, transition from the progressive axial compression to overall bending may occur much later (Abramowicz and Jones, 1997).

- The tested prototype version of the HSSA sheets, which was not optimized for crush, exhibit 60% increase in the mean crushing force compared to its solid-section counterpart.

- The model also indicates that the crashworthiness of sandwich structures depends on the shear crushing strength of the core material. Based on a theoretical comparison, we claim that hexagonal honeycomb cores provide a higher shear crushing strength than HSSA fiber cores - irrespective of their relative density or microstructural geometry.

- We propose a novel thin sandwich sheet with a 10% relative density micro-cell stainless steel honeycomb core as weight-equivalent competitor to the HSSA sheet. The numerical simulation of the crushing of a prismatic profile made of this thin honeycomb sheet demonstrates the potentially superior mechanical performance on the structural level: the predicted specific energy absorption found for the thin micro-cell honeycomb sheet is *twice as high* as for the same structure made of the HSSA sheet. However, as discussed in Chapter 4, the theoretical and numerical predictions for the honeycomb core are only valid if the adhesive bond between neighboring cell walls provides sufficient shear strength.

Chapter 7

Summary

Experimental techniques for the testing of metallic honeycomb under large combined out-of-plane deformation were developed in this thesis. The microstructural response of a thin-walled aluminum honeycomb was examined in detail and its underlying mechanisms were explained. Based on the experimental results, a three-dimensional orthotropic finite-strain rate-independent phenomenological constitutive model was developed, numerically integrated and incorporated into a commercial finite element program. Furthermore, the crushing mechanics of thin-walled structures made of thin soft-core sandwich sheets were investigated experimentally, theoretically and numerically.

Key to success in testing cellular solids is the full control of the displacement fields at the specimen boundaries. By this, the characteristic localization of deformation inside cellular specimens no longer affected the measurement of the resultant forces and displacements at the specimen boundaries. The Arcan apparatus in the clamped configuration was employed to perform biaxial tests on aluminum honeycomb butterfly specimens. It was shown by theoretical analysis that the clamping of the Arcan grips, i.e. the control of the rotational component of the displacement field, generates an additional reaction force that must be measured. Consequently, an additional load cell was implemented into the Enhanced Arcan Apparatus (EAA). A first series of biaxial tests on

butterfly shaped out-of-plane honeycomb specimens was successfully completed using the EAA. The experimental results clearly indicated different microstructural mechanisms for combined tension and shear, and combined compression and shear. Conventional yield of the flat cell walls determines the onset of inelastic behavior under the presence of large tensile stresses, whereas microstructural collapse determines the elastic limit of a honeycomb under combined compression and shear. Phenomenologically, two distinct intersecting surfaces were determined to describe the initial yield envelope in the stress space.

The Universal Biaxial Testing Device (UBTD) was developed to investigate the post-yield behavior of metallic honeycombs under combined compression and shear. Using the UBTD, three force components can be measured as a biaxial displacement field is applied to a honeycomb sandwich specimen. The microstructural stress field in a butterfly-shaped specimen is homogeneous within the central section of the specimen, whereas the stress field within a sandwich specimen is more or less homogeneous throughout the entire specimen. The experimental results obtained from tests with the UBTD were remarkably repeatable and provided an excellent basis for the development of the phenomenological constitutive model. In addition to the physical experiments with the UBTD, so-called virtual experiments were performed. This involved the discretization of the honeycomb microstructure of a sandwich specimen with shell elements and the numerical simulation of the biaxial tests for various loading angles. The numerical results were similar to those of the physical experiments, but revealed that the shear response of a honeycomb strongly depends on the strength of the adhesive bond between neighboring cell walls.

The response of a honeycomb to uniaxial compression in the T-direction was described as follows: the stress-strain curve is initially linear, but then becomes non-linear due to elastic buckling of the cellular microstructure. Similarly to von Kármán's theory on the strength of thin plates, the honeycomb microstructure collapses as the local stresses in the cell walls exceed the yield threshold. Globally, a peak stress is observed, followed by a short softening regime until the crushing regime is reached. The cell walls are progressively folded in the crushing regime, which is macroscopically characterized by small stress fluctuations around a constant plateau stress. The crushing regime persists

over a wide range of strains until the entire microstructure is folded and the stress rises as the folded microstructure is densified. A similar response was observed under combined compression and shear, which led to the introduction of the concept of plateau stresses. Although the stress level depends on the biaxial loading angle, the qualitative response is comparable: both the normal and shear stress-strain exhibit long stress plateaus.

The phenomenological constitutive model for metallic honeycomb was formulated for large deformations and focuses on the out-of-plane behavior in the crushing and densification regimes. The central assumptions are: (1) the in-plane strains are small, (2) the in-plane stresses are small as compared to the out-of-plane stresses, and (3) the concept of plateau stresses applies, i.e. the assumption of constant normal and shear stress plateaus in the crushing regime provides a satisfactory approximation of the complex stress-strain response. The yield surface is conical in the shear-normal stress space, while the direction of plastic flow was assumed to be parallel to the direction of the compressive principal stress. A standard return-mapping scheme along with an Euler backward time integration scheme was employed to implement the constitutive model into a finite element program. It was used to simulate uniaxial and multiaxial experiments on aluminum honeycomb. The reasonable agreement of model predictions and experimental results encourages the use of the model for applications involving large plastic out-of-plane deformation.

Crush experiments on thin-walled prismatic structures revealed that the folding wavelength of structures made of thin sandwich sheets is significantly shorter than for traditional sheets with monolithic cross-section. A new shear-folding model was developed explaining this sandwich-characteristic behavior by shear crushing (large shear deformation) of the sandwich core material. The shear crushing of the core also has two opposite effects on the energy dissipation: (1) additional energy is dissipated throughout the shear crushing, involving relative motion of the face sheets; (2) the plastic bending moment of the entire sandwich section cannot be fully developed because the necessary shear forces cannot be transmitted by the soft core. As a result, the energy dissipated throughout plastic bending decreases. Thin sandwich sheets with a total thickness of about $1mm$ are currently available with a stainless steel fiber core (HSSA sheets). However, theoretical analysis showed that the mechanical performance of honeycombs is

superior to the one of fiber cores of the same density. As an example, a $0.8mm$ thick stainless steel micro-cell honeycomb was suggested as competitor to the 10% relative density HSSA fiber core. After calibrating the phenomenological constitutive model, a finite element simulation of the crushing of a sandwich structure demonstrated the advantages of honeycombs on the structural level: the specific energy absorption of the prismatic structure increased by 100% as the HSSA fiber core was replaced by the micro-cell honeycomb core. A general recommendation of thin sandwich sheets as replacement for traditional sheet metal in crash relevant structural components should not be made as the mechanical performance also depends on other design constraints such as the overall structural dimensions, the structural bending stiffness, or the total force level.

Future testing technology should provide a simple device for the shear testing of cellular sandwich core materials, similar to the EAA set-up for pure shear, but specifically designed for sandwich specimens and with readout for the shear-induced normal displacements. The ASTM Standard C 273 should be revised in this context. Reliable interface models including fracture are needed to improve the prediction of the macroscopic behavior of metallic honeycombs by means of finite element simulations on the microstructural level. Interface models for adhesives would also enable the virtual design and optimization of honeycomb microstructures. Alternatively, intercellular delamination under shear loading could be prevented by improving the bond strength or by redesigning the microstructure such that the shear force between neighboring cell walls is distributed over wider area.

The constitutive model should be validated for non-proportional and non-monotonic loading paths, which requires further experiments. The analysis of the behavior of metallic honeycomb under dynamic loading was also left to future research. The evolution of the elastic moduli should be taken into account as well as inertia effects at the microstructural level that might manifest as strain rate effects on the macroscopic level. Other applications might require the exact modeling of the transition from the plastic collapse to the crushing regime, which can be done using the data and virtual testing techniques published in this thesis.

Furthermore, there might be the need to classify honeycombs according to their microstructural composition. The same way as the mechanics of thin-walled structures differs from the one of thick-walled structures, the mechanical behavior of metallic honeycombs is expected to vary from one metallic honeycomb to the other, both quantitatively and qualitatively.

References

Abramowicz, W. and Jones, N. (1997). Transition from initial global bending to progressive buckling of tubes loaded statically and dynamically, *International Journal of Impact Engineering*, 19(5-6), 415-437.

Abramowicz, W. and Wierzbicki, T. (1988). Axial crushing of foam-filled columns. *International Journal of Mechanical Sciences*, 30(3-4), 263-271.

Abramowicz, W. and Wierzbicki, T. (1989). Axial crushing of multicorner sheet metal columns. *Journal of Applied Mechanics*, 56, 113-120.

Alexander, J. M. (1960). An approximative analysis of the collapse of thin cylindrical shell under axial loading. *Q. J. Mech. Appl. Math.*, 13(1), 10-15.

Allen, H.G. (1969). *Analysis and design of structural sandwich panels*, Pergamon Press, Oxford, UK.

Ames, N. M. (2003). *Private communication.*

Anand, L. and Gu, C. (2000). Granular materials: constitutive equations and strain localization, *Journal of the Mechanics and Physics of Solids*, 48, 1701-1733.

Andrews, E.W., Gioux, G., Onck, P. and Gibson, L.J. (2001). Size effects in ductile cellular solids. Part II: experimental results. *International Journal of Mechanical Sciences*, 43, 701-713.

Arcan, M., Hashin, Z. and Voloshin, A. (1978). A method to produce uniform plane-stress states with applications to fiber-reinforced materials. *Experimental Mechanics*, 18, 141-146

ASTM C273 (1994). Standard Test Method for Shear Properties of Sandwich Core Materials, Annual Book of ASTM Standards.

Bastawros, A.F., Bart-Smith, H. and Evans, A.G. (2000). Experimental analysis of deformation mechanisms in a closed-cell aluminum alloy foam. *Journal of the Mechanics and Physics of Solids*, 48, 301-322.

Chen C. and Fleck N.A. (2002). Size effects in the constrained deformation of metallic foams. *Journal of the Mechanics and Physics of Solids*, 50(5), 955-977.

Chen W. (2001). Crashworthiness optimization of ultralight metal structures. Ph.D. Thesis, Massachusetts Institute of Technology.

Chen, W. and Wierzbicki, T. (2001), Weight optimization of foam-filled thin-walled crash members. Design Optimization International Journal for Product and Process Improvements. submitted for publication.

Doyoyo, M. and Mohr, D. (2003). Microstructural response of aluminum honeycomb to combined out-of-plane loading. *Mechanics of Materials*, 35(9), 865-876.

Doyoyo, M. and Wierzbicki, T. (2000). Tests on combined normal and shear loading of cellular solids. *Impact and Crashworthiness Laboratory Report #40.*

Doyoyo, M. and Wierzbicki, T. (2002). Measurement of the failure surfaces for ductile and brittle aluminum foams. In: *Plasticity, damage and fracture at macro, micro and nano scales.* Editors: Khan, A.S. and Lopez-Pamies, O., Neat Press, Fulton, MD, 114-116.

Doyoyo, M. and Wierzbicki, T. (2003). Experimental studies on the yield behavior of ductile and brittle aluminum foams. *International Journal of Plasticity*, 19(8), 1195-1214.

ESI (2000), Engineering Systems International, PamCrash reference manuals.

François, D., Pineau, A. and Zaoui, A. (1998). *Mechanical Behaviour of Materials, Volume I: Elasticity and Plasticity*, Kluwer Academic Publishers.

Gearing, B.P., Gudlavalleti, S. and Anand, L., (2003). Novel testing apparatuses for mechanical testing at the small scale. *Experimental Mechanics*, to be submitted.

Gibson, L.J. and Ashby, M.F. (1997). *Cellular solids: structure and properties*, 2nd edn., Cambridge University Press.

Grediac, M. (1993). A finite element study of the transverse shear in honeycomb cores. *International Journal of Solids and Structures*, 30(13), 1777-1788.

Gurtin, M.E. (1981). An introduction to continuum mechanics. Academic Press, New York.

Gustafsson RNG (1998). HSSA Base Patent, US application no. 09/214,333.

Gustafsson R.N.G. (2000). Ultralight Stainless steel sandwich materials – HSSA, In: Meyer-Piening HR, Zenkert D. Sandwich construction 5, EMAS, 169-176.

Hanssen, A.G. (2000). Validation of constitutive models applicable to foams. Ph.D. Thesis. Norwegian University of Science and Technology, Norway.

Hexcel Corporation (1997), *private communication.*

HKS (2001). ABAQUS Reference Manuals, Version 6.1, Hibbitt, Karlsson & Sorensen Inc, Pawtucket, RI.

Hönig, A. and Stronge W.J. (2002). In-plane dynamic crushing of honeycomb. Part I: crush band initiation and wave trapping, *International Journal of Mechanical Sciences*, 44, 1665-1696.

Hung, S.-C. and Liechti, K.M. (1999). Finite element analysis of the Arcan specimen for fiber reinforced composites under pure shear and biaxial loading. *Journal of Composite Materials* 33, 1288-1316.

Kármán, T. von, Sechler, E.E. and Donnell, L.H. (1932). The strength of thin plates in compression. *Transactions of ASME*, 54, 53-63.

Kelsey, S., Gellatly, R.A. and Clark, B.W. (1958). The shear modulus of foil honeycomb cores. *Aircraft Engineering*, 30, 294-302.

Kim, H.-S. (2001). Crash behavior of three-dimensional thin-walled structures under combined loading, Ph.D. Thesis, Massachusetts Institute of Technolgy.

Klintworth, J.W. and Stronge, W.J. (1988). Elasto-plastic yield limits and deformation laws for transversely crushed honeycombs. *International Journal of Mechanical Sciences*, 30, 273-292.

LSTC (2001), Livermore Software Technology Corporation, LS-DYNA reference manuals.

Mackerle, J. (2002). Finite element analyses of sandwich structures: a bibliography (1980-2001). *Engineering Computations*, 19(2), 206-245.

Malvern, L.E. (1969). *Introduction to the Mechanics of a Continuous Medium*, Prentice-Hall.

McFarland, R.K. (1963). Hexagonal cell structure under post-buckling axial load. *AIAA Journal* 1, 1380-1385.

Meguid, S.A., Cheon, S.S. and El-Abbasi, N. (2002). FE modelling of deformation localization in metallic foams, *Finite Elements in Analysis and Design*, 38(7), 631-643.

Mohr, D. and Doyoyo, M. (2002). Analysis of the Arcan apparatus in the clamped configuration, *Journal of Composite Materials*, 36 (22), 2583-2594.

Mohr, D. and Doyoyo, M. (2003). Nucleation and Propagation of Plastic Collapse Bands in Aluminum Honeycomb, *Journal of Applied Physics*, 94(4). 2262-2270.

Mohr, D. and Wierzbicki, T. (2000). Pilot study on axial and bending crushing of HSSA profiles. Impact and Crashworthiness Laboratory Report #47.

Mohr, D. and Wierzbicki, T. (2003). Shear Folding of Soft-core Sandwich Profiles. *International Journal of Mechanical Sciences*, 45(2), 253-271.

Noor, A.K., Burton, W.S. and Bert, C.W. (1996). Computational models for sandwich panels and shells. *Applied Mechanics Review*, 49(3), 155-199.

Ogasawara, N., Shiratori, M., Yu, S. and Miyano, A. (1999). Elastic-plastic analysis of honeycomb sandwich panel by using honeycomb element. *JSME International Journal Series A*, 42(3), 381-387.

Papka, S.D. and Kyriakides, S. (1999). Biaxial crushing of honeycombs – Part I: Experiments, *International Journal of Solids and Structures*, 36, 4367-4396.

Papka, S.D. and Kyriakides, S. (1999). Biaxial crushing of honeycombs – Part II: Analysis, *International Journal of Solids and Structures*, 36(29), 4397-4423.

Petras, A. and Sutcliffe, M.P.F. (2000). Indentation failure analysis of sandwich beams, *Composite Structures*, 50(3), 311-318.

Petras, A. (1998). Design of Sandwich Structures. PhD Thesis, Cambridge University, Engineering Department (1998).

Plantema, F.J. (1966). *Sandwich construction*, John Wiley & Sons, New York.

Price, S.R. (1992). Plastic shear buckling of ship hull plating induced by grounding. MS Thesis, Massachusetts Institute of Technology.

Reuter, I. (1996). Experimental and theoretical investigation of a honeycomb structure under combined compression/shear loading. MS Thesis (in German), Universität der Bundeswehr München.

Rice, J.R. (1976). The localization of plastic deformation, In: *Theoretical and applied mechanics*, Editor: Koiter, W.T., North-Holland, 207-220.

Santosa S.P. (1999). Crashworthiness analysis of ultralight metal structures. Ph.D. Thesis, Massachusetts Institute of Technology.

Santosa, S.P., Hanssen, A.G., Wierzbicki, T. and Langseth, M. (2000). Experimental and numerical studies of axially crushing of foam-filled sections, *International Journal of ImpactEngineering*, 24, 509 – 534.

Santosa, S.P. and Wierzbicki, T. (1998). Crash behavior of box columns filled with aluminum honeycomb or foam, *Computers & Structures*, 68, 343 – 367.

Santosa, S.P. and Wierzbicki, T. (1999). The concept of double-walled sandwich columns for energy absorption, *International Journal of Crashworthiness*, 4(2), 175–197.

Schreyer, H.L., Zuo, Q.H. and Maji, A.K. (1994). Anisotropic plasticity model for foams and honeycombs. *Journal of Engineering Mechanics*, 120(9), 1913-1930.

Seggewiss, P. (1996). Numerical investigation of honeycomb structures made of aluminum foil. MS Thesis (in German), Universität der Bundeswehr München.

Shaw, M.C. and Sata, T. (1966). The plastic behavior of cellular materials. *International Journal of Mechanical Sciences*, 8, 469-478.

Starlinger, A. and Rammerstorfer, F.G. (1990). Berücksichtigung von lokalem kurzweiligen Deckschichtbeulen in speziellen finiten Sandwich-Schalenelementen, *Zeitschrift für angewandte Mathematik und Mechanik*, 71(6), T619-T623.

Swanson, S.R. (1997). Introduction to design and analysis with advanced composite materials. Prentice Hall, Inc.

Teng, X. and Wierzbicki, T. (2002). Exact solution for a full crush of a single stainless steel fiber. *Impact and Crashworthiness Laboratory Report #64*.

Triantafillou, T.C., Zhang, J., Shercliff, L.J., Gibson, L.J. and Ashby, M.F. (1989). Failure surfaces for cellular materials under multiaxial loads-II. Comparison of models with experiment. *International Journal of Mechanical Sciences*, 31, 665-678.

Vinson J.R. (1986). Optimum design of composite honeycomb sandwich panels subjected to uniaxial compression. *AIAA Journal*, 24(10), 1690-1696.

Voloshin, A. and Arcan, M. (1980). Failure of unidirectional fiber-reinforced materials – new methodology and results. *Experimental Mechanics*, 280-284.

Weber, G.G., Lush, A.M., Zavaliangos, A. and Anand, L. (1990). An objective time-integration procedure for isotropic rate-independent and rate-dependent elastic-plastic constitutive equations. *International Journal of Plasticity*, 6, 701-744.

Wierzbicki T. and Mohr D. (2000). Crush response of double-walled sandwich columns with a honeycomb core. In: Meyer-Piening HR, Zenkert D. Sandwich construction 5, EMAS, 607-616.

Wierzbicki, T. (1983). A crushing analysis of metal honeycomb. *International Journal of Impact Engineering*, 1, 157-174.

Wierzbicki, T. (1997). Experimental, numerical, and analytical study of honeycomb material. Impact and Crashworthiness Laboratory Report #1.

Wierzbicki, T. and Doyoyo, M. (2003). Determination of the local stress-strain response for foams. *Journal of Applied Mechanics*. 70(2), 204-211.

Wierzbicki, T. and Abramowicz W. (1983). On the crushing mechanics of thin-walled structures. *Journal of Applied Mechanics*, 50, 727-739.

Xu F.X. and Qiao P. (2002). Homogenized elastic properties of honeycomb sandwich with skin effect. *International Journal of Solids and Structures*, 39(8), 2153-2188.

Zaslawsky, M. (1973). Multiaxial stress studies on rigid polyurethane foam. *Experimental Mechanics,* 13, 70-76.

Zenkert, D. (1995). *An introduction to sandwich construction*. The Chameleon Press Ltd., London, UK.

Appendix A

Integration Algorithm for the Constitutive Equations

We briefly describe the algorithm for the update of the state variables from time t to $\tau = t + \Delta t$. Given the deformation gradients $\mathbf{F}(t)$ and $\mathbf{F}(\tau)$ along with the plastic strains $\boldsymbol{\varepsilon}^p(t)$, we compute the Cauchy stress tensor $\mathbf{T}(\tau)$, the plastic strain vector $\boldsymbol{\varepsilon}^p(\tau)$ and the deformation resistance vector $\mathbf{s}(\tau)$.

Step 1. Perform transformation from global to material coordinates

Step 1a. Assemble $\mathbf{B}$

$$\mathbf{B} = \mathbf{e}_1 \otimes \mathbf{e}_W + \mathbf{e}_2 \otimes \mathbf{e}_L + \mathbf{e}_3 \otimes \mathbf{e}_T$$

Step 1b. Calculate the deformation gradient in material coordinates

$$\mathbf{F}^m(\tau) = \mathbf{B}\mathbf{F}(\tau)\mathbf{B}^T$$

Step 2. Calculate the rotation $\mathbf{R}(\tau)$.

Step 2a. Calculate the base vectors of the corotational coordinate system (in material coordinates)

$$\hat{\mathbf{e}}_W = \frac{\mathbf{F}^m \mathbf{e}_1}{\left\| \mathbf{F}^m \mathbf{e}_1 \right\|}$$

$$\hat{\mathbf{e}}_T = \frac{\mathbf{F}^m \mathbf{e}_1 \times \mathbf{F}^m \mathbf{e}_2}{\left\| \mathbf{F}^m \mathbf{e}_1 \times \mathbf{F}^m \mathbf{e}_2 \right\|}$$

$$\hat{\mathbf{e}}_L = \hat{\mathbf{e}}_T \times \hat{\mathbf{e}}_W$$

Step 2b. Assemble $\mathbf{R}(\tau)$

$$\mathbf{R} = \hat{\mathbf{e}}_W \otimes \mathbf{e}_1 + \hat{\mathbf{e}}_L \otimes \mathbf{e}_2 + \hat{\mathbf{e}}_T \otimes \mathbf{e}_3$$

Step 3. Calculate the strain vector $\boldsymbol{\varepsilon}(\tau)$

Step 3a. Calculate the strain tensor $\mathbf{E}(\tau)$

$$\mathbf{E} = \mathbf{R}^T \mathbf{F}^m - \mathbf{1}$$

Step 3b. Extract the strain vector $\boldsymbol{\varepsilon}(\tau)$

$$\boldsymbol{\varepsilon}(\tau) = [\mathbf{E}]_{13} \mathbf{e}_1 + [\mathbf{E}]_{23} \mathbf{e}_2 + [\mathbf{E}]_{33} \mathbf{e}_3$$

Step 4. Calculate trial stress

$$\boldsymbol{\sigma}^{trial} = \mathbf{C}\left(\boldsymbol{\varepsilon}(\tau) - \boldsymbol{\varepsilon}^p(t)\right)$$

Step 5. Check yield condition

$$f^{trial} = \frac{\sigma_3^{trial}}{s_3(t)} + \left[\left(\frac{\sigma_1^{trial}}{s_1(t)} \right)^2 + \left(\frac{\sigma_2^{trial}}{s_2(t)} \right)^2 \right]^{\frac{m}{2}} - 1$$

IF $f^{trial} \leq 0$ THEN time step elastic:

$$\boldsymbol{\sigma}(\tau) = \boldsymbol{\sigma}^{trial}$$

$$\boldsymbol{\varepsilon}^p(\tau) = \boldsymbol{\varepsilon}^p(t)$$

$$\mathbf{s}(\tau) = \mathbf{s}(t)$$

GOTO Step 8

ELSE CONTINUE

Step 6. Return mapping

$$h = \begin{cases} 0 & if \quad \varepsilon_{TT}(t) > \varepsilon_d \\ \dfrac{h_c}{1+\varepsilon_{TT}(t)} & if \quad \varepsilon_{TT}(t) \le \varepsilon_d \end{cases}$$

Iterate $i \leftarrow i+1$ until $\left|\mathbf{r}^i \cdot \mathbf{r}^{i+1} - 1\right| < TOL$

Starting point: $\boldsymbol{\sigma}^{i=0} = \boldsymbol{\sigma}^{trial}$

$\mathbf{r}^i = MINPRINCDIR\left(\boldsymbol{\sigma}^i + \Delta\sigma\mathbf{e}_3\right)$ where the function $MINPRINCDIR(\mathbf{a})$ computes the unit vector of the direction of the minimum principal stress corresponding to the stress state defined by the stress vector $\mathbf{a}$.

$$\left.\frac{\partial \tau_{TW}}{\partial \Delta\lambda}\right|_i = -G_{TW} r_1^i$$

$$\left.\frac{\partial \tau_{TL}}{\partial \Delta\lambda}\right|_i = -G_{TL} r_2^i$$

$$\left.\frac{\partial \sigma_{TT}}{\partial \Delta\lambda}\right|_i = -E_{TT} r_3^i$$

$$\left.\frac{\partial s_{TW}}{\partial \Delta\lambda}\right|_i = h r_3^i \frac{s_{TW}^0}{s_{TT}^0}$$

$$\left.\frac{\partial s_{TL}}{\partial \Delta\lambda}\right|_i = h r_3^i \frac{s_{TL}^0}{s_{TT}^0}$$

$$\left.\frac{\partial s_{TT}}{\partial \Delta\lambda}\right|_i = h r_3^i$$

Iterate $k \leftarrow k+1$ until $\left|f^k(\tau)\right| < TOL$

$$\lambda^{k=0} = 0$$

Starting point: $\boldsymbol{\sigma}^{k=0} = \boldsymbol{\sigma}^{i}$

$$\mathbf{s}^{k=0} = \mathbf{s}(t)$$

$$f^k = \frac{\sigma_{TT}^k}{s_{TT}^k} + \left[\left(\frac{\tau_{TW}^k}{s_{TW}^k} \right)^2 + \left(\frac{\tau_{TL}^k}{s_{TL}^k} \right)^2 \right]^{\frac{m}{2}} - 1$$

$$\frac{\partial f^k}{\partial \tau_{TW}} = m \frac{\tau_{TW}^k}{\left(s_{TW}^k\right)^2} \left[\left(\frac{\tau_{TL}^k}{s_{TL}^k} \right)^2 + \left(\frac{\tau_{TW}^k}{s_{TW}^k} \right)^2 \right]^{\frac{m}{2}-1}$$

$$\frac{\partial f^k}{\partial \tau_{TL}} = m \frac{\tau_{TL}^k}{\left(s_{TL}^k\right)^2} \left[\left(\frac{\tau_{TL}^k}{s_{TL}^k} \right)^2 + \left(\frac{\tau_{TW}^k}{s_{TW}^k} \right)^2 \right]^{\frac{m}{2}-1}$$

$$\frac{\partial f^k}{\partial \sigma_{TT}} = \frac{1}{s_{TT}^k}$$

$$\frac{\partial f^k}{\partial s_{TW}} = -m \frac{\tau_{TW}^k}{\left(s_{TW}^k\right)^3} \left[\left(\frac{\tau_{TL}^k}{s_{TL}^k} \right)^2 + \left(\frac{\tau_{TW}^k}{s_{TW}^k} \right)^2 \right]^{\frac{m}{2}-1}$$

$$\frac{\partial f^k}{\partial s_{TL}} = -m \frac{\tau_{TL}^k}{\left(s_{TL}^k\right)^3} \left[\left(\frac{\tau_{TL}^k}{s_{TL}^k} \right)^2 + \left(\frac{\tau_{TW}^k}{s_{TW}^k} \right)^2 \right]^{\frac{m}{2}-1}$$

$$\frac{\partial f^k}{\partial s_{TT}} = -\frac{\sigma_{TT}^k}{\left(s_{TT}^k\right)^2}$$

$$\frac{\partial \mathrm{f}^{\mathrm{k}}}{\partial \Delta\lambda} = \frac{\partial \mathrm{f}^{\mathrm{k}}}{\partial \tau_{\mathrm{TW}}} \frac{\partial \tau_{\mathrm{TW}}}{\partial \Delta\lambda}\bigg|_{\mathrm{i}} + \frac{\partial \mathrm{f}^{\mathrm{k}}}{\partial \tau_{\mathrm{TL}}} \frac{\partial \tau_{\mathrm{TL}}}{\partial \Delta\lambda}\bigg|_{\mathrm{i}} + \frac{\partial \mathrm{f}^{\mathrm{k}}}{\partial \sigma_{\mathrm{TT}}} \frac{\partial \sigma_{\mathrm{TT}}}{\partial \Delta\lambda}\bigg|_{\mathrm{i}}$$
$$+ \frac{\partial \mathrm{f}^{\mathrm{k}}}{\partial \mathrm{s}_{\mathrm{TW}}} \frac{\partial \mathrm{s}_{\mathrm{TW}}}{\partial \Delta\lambda}\bigg|_{\mathrm{i}} + \frac{\partial \mathrm{f}^{\mathrm{k}}}{\partial \mathrm{s}_{\mathrm{TL}}} \frac{\partial \mathrm{s}_{\mathrm{TL}}}{\partial \Delta\lambda}\bigg|_{\mathrm{i}} + \frac{\partial \mathrm{f}^{\mathrm{k}}}{\partial \mathrm{s}_{\mathrm{TT}}} \frac{\partial \mathrm{s}_{\mathrm{TT}}}{\partial \Delta\lambda}\bigg|_{\mathrm{i}}$$

$$d\Delta\lambda = -\frac{f^k}{\dfrac{\partial f^k}{\partial \Delta\lambda}}$$

$$\Delta\lambda^{k+1} = \Delta\lambda^{k} + d\Delta\lambda$$

$$\boldsymbol{\sigma}^{k+1} = \boldsymbol{\sigma}^{trial} - \Delta\lambda^{k+1}\mathcal{C}\mathbf{r}^{i}$$

$$\mathbf{s}^{k+1} = \mathbf{s}(t) + \Delta\lambda^{k+1} r_3^i \frac{h}{s_{TT}^0}\mathbf{s}^0$$

RETURN

$$\boldsymbol{\sigma}^{i+1} = \boldsymbol{\sigma}^{k+1}$$

RETURN

Step 7. Update plastic strain $\boldsymbol{\varepsilon}^{p}(\tau) = \boldsymbol{\varepsilon}^{p}(t) + \Delta\lambda\mathbf{r}(\tau)$

Step 8. Compute the Cauchy stress tensor $\mathbf{T}(\tau)$

Step 9a. Calculate the stretch tensor $\mathbf{U}(\tau)$

$$\mathbf{U} = \mathbf{R}^{T}\mathbf{F}$$

Step 9b. Calculate the rotated Cauchy stress tensor $\tilde{\mathbf{T}} = \mathbf{R}^{\mathrm{T}}\mathbf{T}^{\mathrm{m}}\mathbf{R}$:

$$\mathrm{A} = \left\|\mathbf{U}\mathbf{e}_1 \times \mathbf{U}\mathbf{e}_2\right\|$$
$$\tilde{\mathrm{T}}_{13} = \tilde{\mathrm{T}}_{31} = \tau_{\mathrm{TW}} / \mathrm{A}$$
$$\tilde{\mathrm{T}}_{23} = \tilde{\mathrm{T}}_{32} = \tau_{\mathrm{TL}} / \mathrm{A}$$
$$\tilde{\mathrm{T}}_{33} = \sigma_{\mathrm{TT}} / \mathrm{A}$$
$$\tilde{\mathrm{T}}_{11} = \tilde{\mathrm{T}}_{22} = \tilde{\mathrm{T}}_{12} = \tilde{\mathrm{T}}_{21} = 0$$

Step 9c. Calculate the Cauchy stress tensor $\mathbf{T}^{m}(\tau)$ in material coordinates:

$$\mathbf{T}^{\mathrm{m}} = \mathbf{R}\tilde{\mathbf{T}}\mathbf{R}^{\mathrm{T}}$$

Step 9d. Calculate the Cauchy stress tensor $\mathbf{T}(\tau)$ in global coordinates:

$$\mathbf{T}^{g} = \mathbf{B}^{T}\mathbf{T}^{m}\mathbf{B}$$

END

Detail on Step 9b:

$$\mathbf{T}^{*}\mathbf{e}_3 = (\det \mathbf{U})\mathbf{R}^{\mathrm{T}}\mathbf{T}\mathbf{R}\mathbf{U}^{-\mathrm{T}}\mathbf{e}_3 = (\det \mathbf{U})\tilde{\mathbf{T}}\mathbf{U}^{-\mathrm{T}}(\mathbf{e}_1 \times \mathbf{e}_2)$$
$$= \tilde{\mathbf{T}}(\mathbf{U}\mathbf{e}_1 \times \mathbf{U}\mathbf{e}_2) = \left\|\mathbf{U}\mathbf{e}_1 \times \mathbf{U}\mathbf{e}_2\right\|\tilde{\mathbf{T}}\mathbf{e}_3 = \mathrm{A}\tilde{\mathbf{T}}\mathbf{e}_3$$

in what follows:

$$\tilde{\mathbf{T}}_{13} = \mathbf{T}^{*}_{13} / \mathrm{A} = \tau_{\mathrm{TW}} / \mathrm{A}$$
$$\tilde{\mathbf{T}}_{23} = \mathbf{T}^{*}_{23} / \mathrm{A} = \tau_{\mathrm{TL}} / \mathrm{A}$$
$$\tilde{\mathbf{T}}_{33} = \mathbf{T}^{*}_{33} / \mathrm{A} = \sigma_{\mathrm{TT}} / \mathrm{A}$$

Appendix B

Computational objectivity test of the integration procedure

A simulation of a single element subjected to uniaxial compression along the T-direction is performed under superposed rigid body rotations. The procedure is similar to the one by Weber *et al.* (1990) who verified the objectivity of their time integration procedure under simple shear loading. The displacement field expressed by the current position $\mathbf{x}(\mathbf{p},t)$ of a point $\mathbf{p}$ at the time t is given by

$$\mathbf{x} = \mathbf{Q}(t)[\mathbf{p} + p_T \dot{\varepsilon}_{TT} t \mathbf{e}_T]$$

where the rotation $\mathbf{Q}$ reads

$$\mathbf{Q}(t) = (\mathbf{e}_W \otimes \mathbf{e}_W + \mathbf{e}_T \otimes \mathbf{e}_T)\cos(\dot{\theta}t) + (\mathbf{e}_W \otimes \mathbf{e}_T - \mathbf{e}_T \otimes \mathbf{e}_W)\sin(\dot{\theta}t)$$

In our present simulation, we chose $\dot{\varepsilon}_{TT} = -0.5$ and $\dot{\theta} = 360$ over a generic time interval from 0 to 1 at a constant time step of $\Delta t = 10^{-5}$. The explicit simulation with ABAQUS/explicit is performed using single precision and the tolerance parameter for the accuracy of the iterations in the integration procedure (see Appendix A) was set to $TOL = 10^{-5}$. The rotation was prescribed in 1000 linear increments. Fig. 102 illustrates the motion that was applied. The corresponding stresses computed at the integration point of the reduced-integration solid element (C3D8R) are shown in Fig. 103. Both curves

show the characteristics that are expected from analytical solution: (1) the normal stress is constant (plateau regime) and (2) the shear stress is zero (uniaxial compression). In other words, the superposed rigid body rotation does not affect the computational procedure. A very small oscillation of a maximum amplitude of 0.02 is observed in the shear response. However, this minor oscillation is not necessarily attributed to the algorithmic formulation but may also be due to round off errors or to inertia effects which are present in explicit simulations. It is concluded that the algorithm satisfies the objectivity requirement for integration procedures.

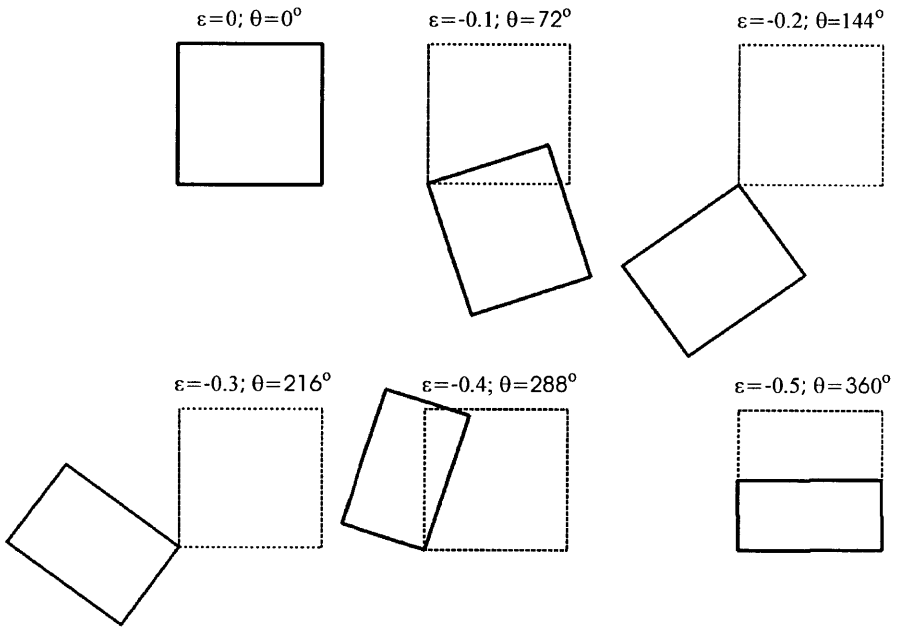

Fig. 102. Configurations during the objectivity test.

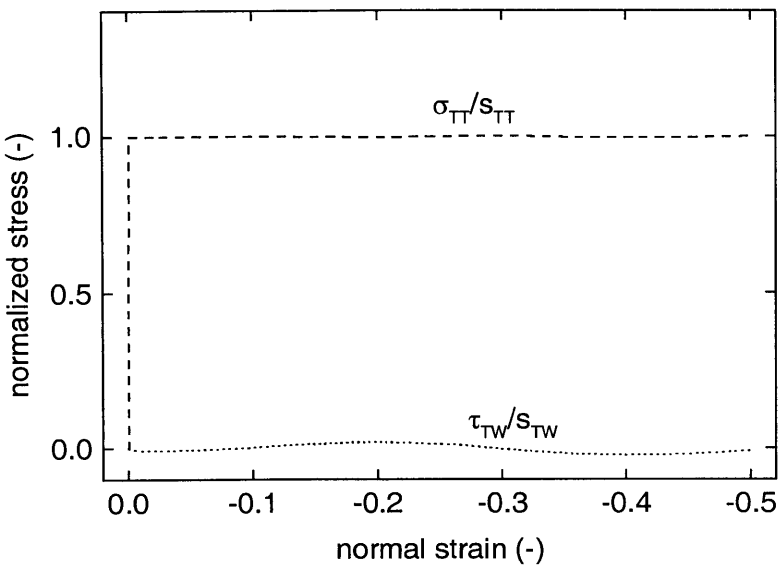

Fig. 103. Results from a numerical simulation of the uniaxial compression of a single element (C3D8R) under superposed rigid body rotation.

Appendix C

Refereed journal publications related to this thesis

Mohr, D. and Doyoyo, M. (2002). Analysis of the Arcan Apparatus in the Clamped Configuration. *Journal of Composite Materials* 36(22), 2583-2594.

Doyoyo, M. and Mohr, D. (2003). Microstructural Response of Aluminium Honeycomb to Combined Normal and Shear Loading. *Mechanics of Materials*, 35(9), 865-876.

Mohr, D. and Doyoyo, M. (2003). A New Method for the Biaxial Testing of Cellular Solids. *Experimental Mechanics*, 43(2), 173-182.

Mohr, D. and Wierzbicki, T. (2003). Shear Folding of Soft-core Sandwich Profiles. *International Journal of Mechanical Sciences* 45(2), 253-271.

Mohr, D. and Doyoyo, M. (2003). Nucleation and Propagation of Plastic Collapse Bands in Aluminum Honeycomb, *Journal of Applied Physics*, 94(4). 2262-2270.

Mohr, D. and Doyoyo, M. (2003). Experimental Investigation on the Plasticity of Hexagonal Aluminum Honeycomb under Multiaxial Loading, *Journal of Applied Mechanics*, (in press).

Mohr, D. and Doyoyo, M. (2003). Deformation-Induced Folding Systems in Thin-Walled Monolithic Hexagonal Metallic Honeycomb, submitted for publication.

Mohr, D. and Doyoyo, M. (2003). Large Plastic Deformation of Thin-Walled Metallic Honeycomb: An Orthotropic Rate-Independent Constitutive Model, submitted for publication.